学位論文

Ultrafast laser-assisted electron scattering and its application: ultrafast response of charge distribution in Xe and instantaneous geometrical structure of CCl_4

（超高速レーザーアシステッド電子散乱とその応用：
Xe 原子内電荷分布の超高速応答と CCl_4 の瞬時的分子構造）

平成 26 年 12 月 博士（理学）申請

東京大学大学院理学系研究科

化学専攻

森本　裕也

Author: Yuya Morimoto
Supervisor: Prof. Kaoru Yamanouchi
Date submitted: 16 December 2014
Date of thesis defense: 27 January 2015

Abstract

When an electron collides with an atom or a molecule inside a laser field, the electron can change its kinetic energy by multiples of the photon energy. This scattering process is called laser-assisted electron scattering (LAES). Because the LAES process occurs only in the presence of a laser field, the LAES process can be used to investigate ultrafast processes occurring in atoms and molecules with a temporal resolution as short as a laser pulse duration. This thesis describes two experimental studies on the LAES process induced by femtosecond intense laser pulses and a development of an apparatus for the observation of an electron impact ionization process which can be induced only in the presence of a laser field.

In the first experiment, the LAES process was measured by using CCl_4 as a sample. In the angular distributions of the observed LAES signals, laser-assisted electron diffraction (LAED) patterns were observed for the first time. The LAED pattern is originating from the interference of the LAES electrons scattered by respective atoms in a molecule. Through a comparison with a numerical simulation, it was demonstrated that LAED can be used to determine instantaneous geometrical structures of gas-phase molecules with high temporal resolution ($\leq$10 fs) simultaneously with high spatial resolution (0.01 Å).

In the second experiment, the LAES signals at small scattering angles ($\geq 0.1^\circ$) were measured by using Xe as a sample. In the angular distribution of the LAES signals, a sharp peak profile was observed at the scattering angle range less than 0.5°. The peak profile is ascribed to the modification of the electron density distribution of atoms induced by the intense laser field, which is known as the light-dressing effect of target atoms. The light-dressing effect of target atoms appearing in the LAES signals has been discussed theoretically for more than 30 years, however, it was observed for the first time in this study. The light-dressing effect can be used for investigating the evolution of the electron density distribution of atoms and molecules in intense laser fields.

Furthermore, an apparatus was designed and constructed in order to observe a characteristic electron impact ionization process in intense laser fields, which is called laser-assisted (e,2e). The laser-assisted (e,2e) process can be used to investigate momentum distributions of atomic and molecular orbitals in the presence of intense laser fields. Two angle-resolved time-of-flight analyzers were specially designed for a coincidence detection of both a scattered electron and an ejected electron which are generated through the laser-assisted (e,2e) process. By conducting a numerical simulation, I confirmed that the sensitivity of the apparatus is high enough to observe the laser-assisted (e,2e) process induced by femtosecond laser pulses.

Contents

1 Introduction

1.1 Electron scattering by atoms and molecules

Scattering of electrons by atoms and molecules has long been a major topic in the collision physics [1, 2] and also an essential tool for the study of atoms and molecules [3]. When an electron approaches to an atom (Fig. 1(a)), the electron experiences a potential $V(\boldsymbol{r})$ which consists of an attractive potential of an atomic nucleus and a repulsive potential of atomic electrons,

$$V(\boldsymbol{r}) = -\frac{1}{4\pi\epsilon_0}\frac{Ze^2}{|\boldsymbol{r}|} + \frac{e^2}{4\pi\epsilon_0}\int \frac{\rho(\boldsymbol{r}')}{|\boldsymbol{r}-\boldsymbol{r}'|}\mathrm{d}\boldsymbol{r}', \tag{1.1}$$

where ϵ_0 is the permittivity of vacuum, e is the unit charge, Z is an atomic number, $\boldsymbol{r}$ is a position vector of the incident electron, and $\rho(\boldsymbol{r})$ is the electron density distribution of the atom. By the potential $V(\boldsymbol{r})$, the projectile electron is deflected by an angle θ, which is called scattering angle. In a typical electron scattering experiment, an atomic beam is irradiated with an electron beam, and an angular distribution of scattered electrons ($I(\theta)$, Fig. 2(a)) is recorded. The angular distribution of the scattered electrons is expressed by the square of the scattering amplitude $f(\theta)$,

$$I(\theta) = |f(\theta)|^2. \tag{1.2}$$

Within the first Born approximation which is discussed in Section 3.1, the scattering amplitude is given by the Fourier transform of the scattering potential $V(\boldsymbol{r})$,

$$f(\theta) = \frac{m_e}{2\pi\hbar^2}\int V(\boldsymbol{r}')e^{\mathrm{i}(\boldsymbol{p}_\mathrm{i}-\boldsymbol{p}_\mathrm{f})\cdot\boldsymbol{r}'/\hbar}\mathrm{d}\boldsymbol{r}', \tag{1.3}$$

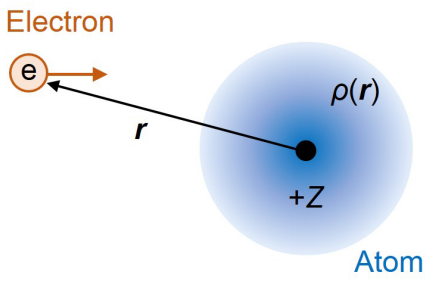

Figure 1: Scattering of an electron by an atom. $\rho(\boldsymbol{r})$ is the electron density distribution of the atom. Z is the atomic number.

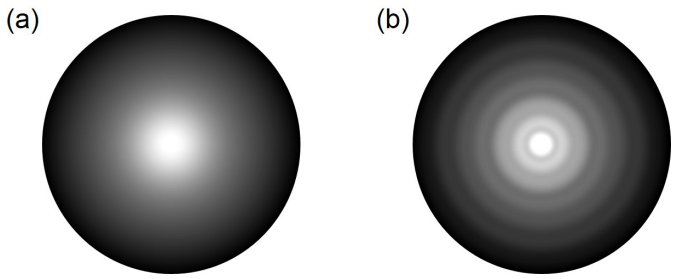

Figure 2: Simulated images of the scattered electrons by atoms (a) and molecules (b). In (b), a clear electron diffraction pattern can be seen. In both images, a distance from a center of the image corresponds to the scattering angle θ.

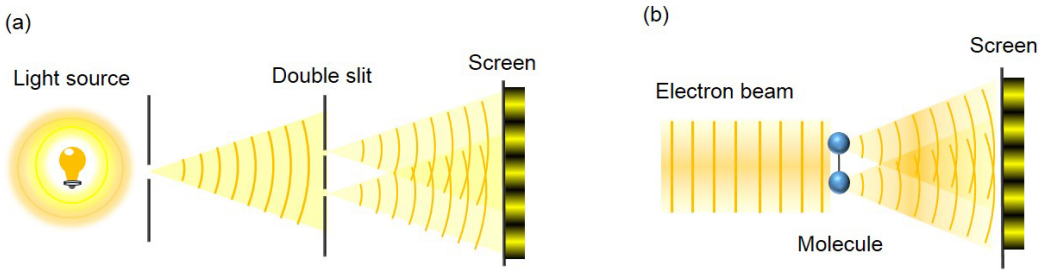

Figure 3: Interference of waves. (a) The Young's double slit experiment. The light waves diffracted by the slits interfere with each other. (b) The electron diffraction by an isolated molecule. The waves scattered by atoms interfere with each other.

where m_{e} is the electron rest mass, $\hbar$ is the reduced Plank constant, and $\boldsymbol{p}_{\mathrm{i}}$ and $\boldsymbol{p}_{\mathrm{f}}$ are the momenta of electrons before and after the scattering, respectively. Consequently, the scattered electrons carry the information of the scattering potential $V(\boldsymbol{r})$ which is determined by the electron density distribution of the atom $\rho(r)$. In 1953, Bartell and Brockway experimentally demonstrated that the radial distribution of atomic electrons ($4\pi r^2\rho(r)$) can be determined from an angular distribution of the scattered electrons [4].

When electrons are scattered by isolated molecules, an electron diffraction pattern appears in the angular distribution of scattered electrons [5] as shown in Fig. 2(b). The appearance of the electron diffraction pattern can be understood by an analogy to the Young's double slit experiment [6]. In the Young's double slit experiment shown in Fig. 3(a), the wave of light diffracted by a slit interferes with that diffracted by another slit. Due to the interference between the two diffracted waves, an interference pattern appears on a screen. The spacing of the bright or the dark fringes are inversely proportional to the distance between the slits. Therefore, by analyzing the observed interference pattern, the distance between the slits can be determined. In the case of the electron scattering by molecules, wavefunctions of an electron scattered by

respective atoms in a molecule interfere with one another, and the electron diffraction pattern appears in the angular distribution of scattered electrons (Fig. 3(b)). As the distance between slits can be determined from the interference pattern measured in the Young's double slit experiment, the distance between atomic nuclei can be determined from the electron diffraction pattern. Because the gas-phase molecules are randomly oriented, the electron diffraction by an ensemble of gas-phase molecules becomes concentric as shown in Fig. 2(b). Detailed theoretical description of the electron diffraction by gas-phase molecules is given in Section 3.1. As in the case of the electron scattering by atoms, the electron density distribution of molecules can also be investigated by analyzing the angular distribution of the scattered electrons [7, 8].

The spatial resolution of the measurements of electron density distributions and internuclear distances depends on the deBroglie wavelength of electrons. The deBroglie wavelength of an electron with a kinetic energy E is given by [9]

$$\lambda_{\mathrm{D}}(\text{Å}) = \sqrt{\frac{150.3}{E(\mathrm{eV})}}. \tag{1.4}$$

For example, the deBroglie wavelengths of 1 keV electrons is 0.39 Å, which is shorter than the size of atoms and the distances between atoms in a molecule ($\sim$ 1 Å). Usually, tens of keV electrons are employed for measuring electron diffraction patterns, and a resolution of 0.01 Å has been achieved [10, 11]. Because of the high spatial resolution, the electron diffraction has been a standard method to determine geometrical structures of gas-phase molecules.

1.2 Ultrafast imaging by lasers and electrons

With the development of the ultrashort laser sources, it is now possible to investigate ultrafast phenomena occurring in atoms and molecules in real-time. The development of ultrashort lasers also enabled the generation of ultrashort electron pulses. By employing the ultrashort electron pulses, the electron scattering described in the previous section can be used to monitor the time evolutions of electron density distributions in atoms and molecules and geometrical structures of molecules. In this section, the progress of ultrafast imaging methods which use laser and electron pulses is briefly introduced.

1.2.1 Investigation of ultrafast processes by ultrashort laser pulses

The most common method used in the study of ultrafast processes is the pump-probe technique with ultrashort laser pulses. The pump laser pulse excites a sample (atoms and molecules), and the probe laser pulse is used to monitor the changes induced in the sample such as the changes in electronic state, vibrational state, rotational state, and molecular structure. By scanning the delay time between the pump and the probe laser pulses, one can follow the time evolution of the sample after the excitation. The temporal resolution of the pump-probe technique is determined

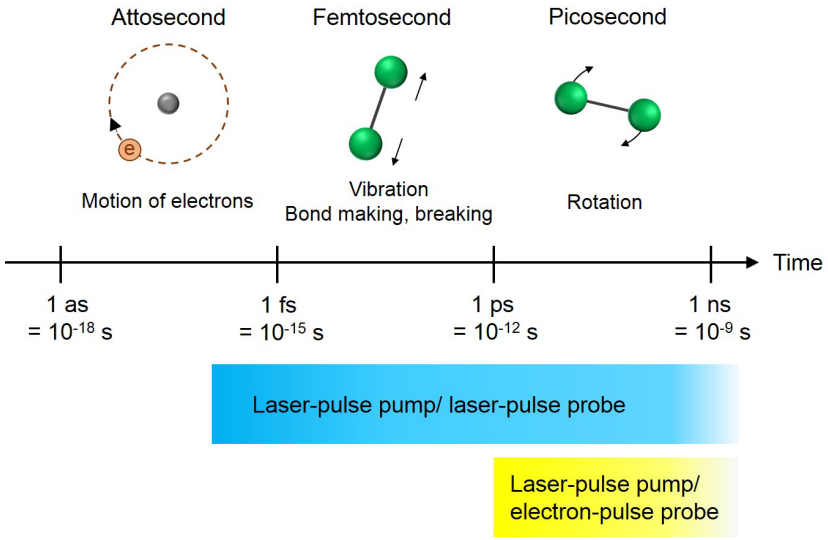

Figure 4: Timescales of the ultrafast dynamics occurring in atoms and isolated molecules [35]. The temporal resolution of the pump-probe technique with laser pulses reaches attosecond. On the other hand, the temporal resolution of the pump-probe technique with laser and electron pulses is limited to picosecond.

by the durations of the laser pulses. The generation of sub-picosecond laser pulses from the dye laser was first reported by Shank and Ippen in 1974 [12], and the pulse duration decreased down to 6 fs until 1986 [13]. The pioneering pump-probe experiments with femtosecond laser pulses were reported by Zewail and coworkers at the end of 1980s [14–16]. Because the durations of the laser pulses they used are comparable to or shorter than the time scales of nuclear motions in molecules (Fig. 4), the pump-probe technique with femtosecond laser pulses enabled the observation of the chemical-bond breaking and formation in real-time [17].

In 2000s, the duration of the laser pulse was further reduced down to attosecond [18–20]. The attosecond laser pulses can be generated through the high-order harmonic generation process [21, 22] which is induced by focusing an intense femtosecond laser pulse into a gas medium. The attosecond pulses whose durations are less than 100 as were obtained so far [23, 24]. The pump-probe measurement with the attosecond lasers is a powerful tool to investigate the attosecond electron dynamics in atomic and molecular systems [25–28]. Because pulse energies of the attosecond lasers were not high enough to use the attosecond laser pulses for both of the pump and probe pulses, most of the attosecond pump-probe experiments were conducted in combination with few-femtosecond laser pulses. However, recent progress in generating high energy attosecond laser pulses [29–33] is making it possible to perform the pump-probe experiment in which attosecond laser pulses are employed for both the pump and probe pulses [34].

1.2.2 Ultrafast imaging by the combination of electron and laser pulses

When the probe laser pulse used in the pump-probe technique with ultrashort laser pulses is replaced by an electron pulse and an angular distribution of scattered electrons is measured, the temporal evolution of the molecular structure [36] and the electron density distribution in atoms and molecules [37, 38] can be explored with high spatial resolution. The temporal resolution of the pump-probe technique depends on the duration of electron pulses. For the generation of ultrashort electron pulses, photocathode-type electron guns [39] are frequently employed. In the photocathode-type electron gun, an electron pulse is generated by an irradiation of an ultrashort laser pulse on the surface of the photocathode which is usually a metallic film formed on a surface of a glass plate. The advantages of using the photocathode-type electron gun are that the pulse duration of the generated electron pulse can be as short as that of the laser pulse, and that the electron pulse is synchronized to the laser pulse with high precision. The precise synchronization between the laser pulse and the electron pulse is important for conducting the pump-probe experiment [39]. By the development of technology for generating ultrashort electron pulses, the temporal resolution for the gas-phase samples has been improved to a few picoseconds (Fig. 4) [40]. However, it is still challenging to achieve the femtosecond temporal resolution which is required to probe the nuclear motion as a snapshot.

1.3 Laser-assisted electron scattering

When an electron is scattered by an atom or a molecule in the presence of a laser field, the kinetic energy of the electron can be shifted by multiples of the photon energy ($nh\nu$, n: integer, h: Planck constant, ν: frequency of the laser field) [41]. This scattering process is called laser-assisted electron scattering (LAES). The first observation of the LAES process was reported by Andrick and Langhans in 1976 [42]. They observed the LAES $n = \pm 1$ processes by employing a continuous-wave CO_2 laser. The observation of the multiphoton ($|n| > 1$) LAES processes was first reported by Weingartshofer *et al.* in 1977 [43]. By employing a microsecond CO_2 laser, they observed the LAES processes up to $|n| = 3$. Since these pioneering works, continuous-wave and microsecond CO_2 lasers have been commonly employed for the observation of the LAES process. The LAES process induced by an ultrashort laser pulse had not been reported until our recent report in which we observed the LAES signals induced by 200 fs laser pulses from a Ti:sapphire laser [44].

Because the LAES process occurs only in the presence of a laser field, it can be used for extracting electrons scattered by atoms and molecules within a duration of the laser pulse by selecting scattered electrons depending on their kinetic energies. By using the ultrafast LAES process as a probe of an ultrafast phenomenon induced by an ultrashort laser pulse, the phenomenon can be investigated with a temporal resolution as short as that of the pump-probe technique with ultrashort laser pulses. Consequently, by taking advantage of the ultrafast LAES process, one can achieve femtosecond or attosecond temporal resolution, which is more than

three orders of magnitude higher than that can be achieved by the pump-probe technique with the combination of laser and electron pulses.

1.4 Present study

As described in Section 1.1, the electron scattering without laser fields can be used to determine geometrical structures of gas-phase molecules and to investigate electron density distributions of atoms and molecules. Therefore, by taking advantage of the LAES process, it will be possible to probe ultrafast evolutions of molecular structures and electron density distributions. In this thesis, I conducted two experiments on the ultrafast LAES process in order to demonstrate that the LAES process can indeed be used to investigate molecular structures and electron density distributions with high temporal resolution. In the first experiment of this study, I report the observation of an electron diffraction pattern appearing in the LAES signals. I show that instantaneous geometrical structures of gas-phase molecules can be determined by analyzing the electron diffraction pattern. In the second experiment, I describe the observation of a characteristic LAES signals which originate from an ultrafast deformation of an electron density distribution of an atom induced by an intense laser field. This experiment paves the way for the ultrafast imaging of electron density distributions of atoms and molecules. This thesis further describes a new apparatus developed for investigating atomic and molecular orbitals in intense laser fields by taking advantage of the laser-assisted electron impact ionization process [45]. Brief summaries of the three topics, i.e., two experiments and a development of the apparatus, are given below.

1.4.1 Laser-assisted electron diffraction

When the LAES process is induced by gas-phase molecules, wavefunctions of the LAES electrons scattered by respective atoms in a molecule interfere with each other, and a gas-phase electron diffraction pattern appears in the angular distribution of the LAES signals. Laser-assisted electron diffraction (LAED) is an ultrafast electron diffraction method which uses the electron diffraction patterns appearing in the LAES signals [44]. Because the LAES process is induced only in the presence of a laser field, the LAED pattern carries the information of the geometrical structure of the molecules only within a duration of the laser pulse used for inducing the LAES process. Even though the LAES process has been studied for more than 30 years, the LAED patterns have not been observed yet. In this study, I report the first observation of the LAED pattern. By measuring 1 keV electrons scattered by gas-phase CCl_4 molecules in a femtosecond laser field ($\lambda = 800$ nm, τ = 520 fs, $I = 6\times10^{11}$ W/cm^2), LAED patterns were observed in the angular distributions of the LAES $n = \pm1$ processes. Through a comparison with a numerical simulation, it is demonstrated that the instantaneous geometrical structure of molecules at the moment of laser irradiation can be determined with 0.01 Å precision by analyzing the LAED patterns. By using LAED, dynamical processes of gas-phase molecules such as breaking and

rearrangement of chemical bonds can be probed with femtosecond temporal resolution.

1.4.2 Light-dressing effect of target atoms in laser-assisted electron scattering

When an atom or a molecule is exposed to an intense laser field, the electron density distribution of the atom or the molecule oscillates in response to the applied electric field of the laser light. The oscillation period of the laser electric field is 2.7 fs when the wavelength is 800 nm. The ultrafast oscillation of the electron density distribution plays a fundamental role in strong-field induced processes [46, 47]. Because the angular distribution of the scattered electrons reflects the electron density distributions of atoms and molecules, the angular distribution of the LAES signals induced by an intense laser field can be modified reflecting the oscillation of the electron density distributions of atoms and molecules. This effect is known as the light-dressing effect of target atoms (molecules) [44]. The light-dressing effect appearing in the LAES signals have been studied theoretically for more than 30 years, and it has been predicted that the light-dressing effect strongly modifies the intensity of the LAES signals scattered at small scattering angles [48]. In this study, by measuring the angular distributions of LAES signals by Xe in an intense laser field ($\lambda = 800$ nm, τ = 970 fs, $I = 1.5\times10^{12}$ W/cm^2), I succeeded in observing the light-dressing effect for the first time. In order to confirm the observation of the light-dressing effect, the experimental result was compared with a numerical simulation. A possibility to determine the spatial distribution of the oscillating electrons from the angular distributions of the LAES signals is discussed.

1.4.3 An apparatus for the observation of laser-assisted (e,2e) process

In order to apply the ultrafast laser-assisted technique to a measurement of the electron impact ionization process or the (e,2e) process by which an electron is ejected from a target atom, I developed a new apparatus. It has been known that the (e,2e) process without laser fields can be used to measure momentum distributions of atomic and molecular orbitals [49, 50]. Therefore, the laser-assisted (e,2e) process can be used to investigate the atomic and molecular orbitals in intense laser fields [51]. Through the laser-assisted (e,2e) process, a sum of kinetic energies of a scattered electron and an ejected electron is shifted by $nh\nu$ [45]. Because of the experimental difficulties in detecting the scattered and ejected electrons in coincidence and with high sensitivity, there are few experimental studies on the laser-assisted (e,2e) process [52]. In this study, in order to observe the laser-assisted (e,2e) process by ultrashort laser pulses, I designed and constructed the apparatus which consists mostly of home-made components. Angle-resolved time-of-flight analyzers were specially designed in order to detect the scattered and ejected electrons with a sensitivity three orders of magnitude higher than that can be achieved by the conventional scanning-type analyzers [53].

1.5 Thesis structure

This thesis consists of six chapters. Chapter 2 gives an introduction of the LAES process and a summary of our recent studies on the observation of the LAES process by femtosecond laser pulses. Chapter 3 describes the experimental study on the laser-assisted electron diffraction. A detailed description of the home-made femtosecond-LAES apparatus is also given in Chapter 3. Chapter 4 deals with the experimental study of the light-dressing effect of target atoms. Chapter 5 gives an account of the apparatus developed for the observation of the laser-assisted (e,2e) process. Finally, Chapter 6 provides a summary of this thesis study.

2 Laser-assisted electron scattering

In this chapter, I give an introduction to the laser-assisted electron scattering (LAES) process through which the kinetic energy of an electron is increased by $nh\nu$ ($n = 0, \pm1, \pm2, \cdots$, h: Planck constant, ν: frequency of a laser field). Because the LAES process can be considered as a transition between continuum states of the electron, the LAES process is also known as free-free transition. Sometimes, this process is also called inverse bremsstrahlung ($n > 0$) or stimulated bremsstrahlung ($n < 0$) due to an analogy to the bremsstrahlung, i.e., the emission of photons induced by an acceleration or a deceleration of a charged particle. The LAES process has long been studied both experimentally and theoretically because of a fundamental interest in the collision physics and its important roles in related physical phenomena such as the infrared opacity of the solar atmosphere [54], the plasma heating [55], and the gas breakdown [56]. The progress in the experimental and theoretical studies on the LAES process is described in books [45, 57–61] and review articles [41, 62–66].

In what follows, I briefly introduce the theoretical and experimental studies on the LAES process. In Section 2.1, I explain the classical mechanism of the LAES process and introduce theoretical formulae which give the differential cross section of the LAES process. Then, in Section 2.2, experimental studies on the LAES process are introduced. Most of the experiments were conducted by using cw- and microsecond-lasers. The experiment of the LAES process by ultrashort laser pulses were recently reported by our group. In Section 2.3, I discuss experimental difficulties to observe the LAES signals by ultrashort laser pulses, and present our recent experimental results on the measurement of the LAES process by femtosecond laser pulses. I also discuss applications of the LAES process induced by femtosecond laser pulses.

2.1 Theory of laser-assisted electron scattering

In this section, classical and quantum theories of the LAES process are introduced. First, the classical theory of the LAES process is introduced in order to consider the origin of the kinetic energy shift of electrons in the LAES process. Then, I introduce two common theories which treat the scattering of electrons quantum mechanically. In a strict sense, the LAES process can occur when an electron is scattered by a potential $V(\boldsymbol{r})$ in a laser field, and the target does not have to be an atom. These two theories give the the cross section of the LAES process in which an electron is scattered by the potential $V(\boldsymbol{r})$. By using the results of the quantum theories, I discuss the laser parameter dependence of the cross section of the LAES process.

2.1.1 Classical theory of laser-assisted electron scattering

Before considering the scattering process, the interaction between a free electron and a laser field is considered. When a free electron interacts with a laser field, the electron experiences the Lorentz force,

$$m_{\mathrm{e}}\frac{\mathrm{d}}{\mathrm{d}t}\boldsymbol{v} = -e\Big(\boldsymbol{F}(\boldsymbol{r},t) + \boldsymbol{v}\times\boldsymbol{B}(\boldsymbol{r},t)\Big), \tag{2.1}$$

where $\boldsymbol{v}$ is the velocity of the electron, $\boldsymbol{r}$ is the position of the electron, m_{e} is the rest mass of electron, $\boldsymbol{F}$ and $\boldsymbol{B}$ are the electric field and the magnetic field of the laser light, respectively. Because of the relationship $|\boldsymbol{F}|/|\boldsymbol{B}| = c$ (c is the speed of light in vacuum), the second term on right-hand side of Eq. (2.1) is much smaller than the first term except when the speed of electron is close to c. Here I only consider the electron whose speed is much slower than c, and thus neglect the second term. By integrating Eq. (2.1) in time t, the velocity of the electron is obtained as follows,

$$\begin{aligned}\boldsymbol{v} &= -\frac{e}{m_{\mathrm{e}}}\int_{t_{\mathrm{i}}}^{t}\boldsymbol{F}(\boldsymbol{r},t')\mathrm{d}t' + \boldsymbol{v}_{\mathrm{i}} \\ &= \frac{e}{cm_{\mathrm{e}}}\boldsymbol{A}(\boldsymbol{r},t) - \frac{e}{cm_{\mathrm{e}}}\boldsymbol{A}(\boldsymbol{r},t_{\mathrm{i}}) + \boldsymbol{v}_{\mathrm{i}},\end{aligned} \tag{2.2}$$

where $\boldsymbol{A}(\boldsymbol{r},t)$ is the vector potential of the laser field, and $\boldsymbol{v}_{\mathrm{i}}$ is the velocity of the free electron at the time of $t = t_{\mathrm{i}}$. When the canonical momentum is defined as follows,

$$\boldsymbol{p} = m_{\mathrm{e}}\boldsymbol{v} - \frac{e}{c}\boldsymbol{A}(\boldsymbol{r},t), \tag{2.3}$$

Eq. (2.2) represents the conservation of the canonical momentum.

Then, based on the discussions in Refs. [67, 68], I consider the scattering of the free electron inside a laser field. The schematic of the scattering process is shown in Fig. 5. At $t = -\infty, +\infty$, the free electron is outside the laser field ($\boldsymbol{A}(\boldsymbol{r}_{\mathrm{i}},-\infty) = \boldsymbol{A}(\boldsymbol{r}_{\mathrm{f}},+\infty) = 0$), and has the (canonical) momenta $\boldsymbol{p}_{\mathrm{i}}$ and $\boldsymbol{p}_{\mathrm{f}}$, respectively. At $t = t_{\mathrm{c}}$, the scattering occurs inside the laser field. Considering the size of the atom (a few Å) and the speed of the free electron (0.2 Å/as for 1000 eV electrons), the scattering takes place instantaneously (within several attoseconds for 1000 eV electron) compared to the oscillation period of the laser field (2.7 fs at the wavelength of λ = 800 nm). Therefore, the vector potential during the scattering can be treated as a constant. Furthermore, I neglect the spatial dependence of the laser field (dipole approximation). This is because the range that the free electron experiences the potential of the target atom is a few Å, and is much smaller than the wavelength of the laser field. By using Eq. (2.2), the instantaneous momenta ($m_{\mathrm{e}}\boldsymbol{v}$) of the electron just before and after the scattering are written as $\boldsymbol{p}_{\mathrm{i}} + e\boldsymbol{A}(t_{\mathrm{c}})/c$ and $\boldsymbol{p}_{\mathrm{f}} + e\boldsymbol{A}(t_{\mathrm{c}})/c$, respectively. Because the scattering proceeds elastically, the absolute value of the momenta ($m_{\mathrm{e}}\boldsymbol{v}$) should be conserved,

$$\left|\boldsymbol{p}_{\mathrm{i}} + \frac{e}{c}\boldsymbol{A}(t_{\mathrm{c}})\right| = \left|\boldsymbol{p}_{\mathrm{f}} + \frac{e}{c}\boldsymbol{A}(t_{\mathrm{c}})\right|. \tag{2.4}$$

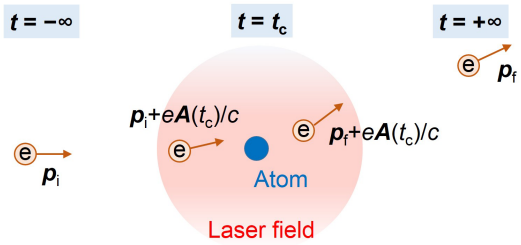

Figure 5: Classical picture of the LAES process. At the time of $t = -\infty$ and $t = +\infty$, the electron is outside the laser field. The momentum ($m_e\boldsymbol{v}$) of the electron is modulated by the interaction with the laser field. The scattering by the atom is completed much faster than the oscillation period of the laser field. Therefore the vector potential ($\boldsymbol{A}$) of the laser field can be considered as a constant during the scattering. At the moment of the scattering ($t = t_C$), the momentum ($m_e\boldsymbol{v}$) of the electron is shifted by $e\boldsymbol{A}(t_C)/c$. Because the scattering proceeds elastically, the absolute value of the instantaneous momentum ($m_e\boldsymbol{v}$) is conserved, and only the propagation direction of the electron is changed. This abrupt change of the propagation direction in the laser field is the origin of the kinetic energy shift of the electron. The origins of the energy shift in processes similar to the LAES process are described in Appendix 1.

From this equation, the energy shift induced by the LAES process is obtained as follows,

$$\begin{aligned} \Delta E &= \frac{p_f^2}{2m_e} - \frac{p_i^2}{2m_e} \\ &= \frac{e}{m_e c}\boldsymbol{A}(t_c)\cdot(\boldsymbol{p}_i - \boldsymbol{p}_f). \end{aligned} \tag{2.5}$$

By defining the scattering vector as

$$\boldsymbol{s} = \frac{\boldsymbol{p}_i - \boldsymbol{p}_f}{\hbar}, \tag{2.6}$$

the energy shift is then expressed as

$$\Delta E = \frac{e\hbar}{m_e c}\boldsymbol{A}(t_c)\cdot\boldsymbol{s}. \tag{2.7}$$

Therefore, the energy shift of electron (ΔE) is determined by the product of the instantaneous vector potential at the moment of the scattering $\boldsymbol{A}(t_c)$, and the scattering vector $\boldsymbol{s}$. Because this formula is obtained by using classical mechanics, ΔE takes continuous values.

Numerical simulation

I conducted classical simulations of an electron scattering process in a laser field. The wavelength, intensity, and pulse duration of the laser field are assumed to be 800 nm, 1×10^{12} W/cm^2, and 10 fs, respectively. The wavelength and the field intensity are almost same as those of the laser field we used in the previous study [69]. The polarization direction of the laser field is perpendicular to the direction of the incoming electron. The scattering potential of the target

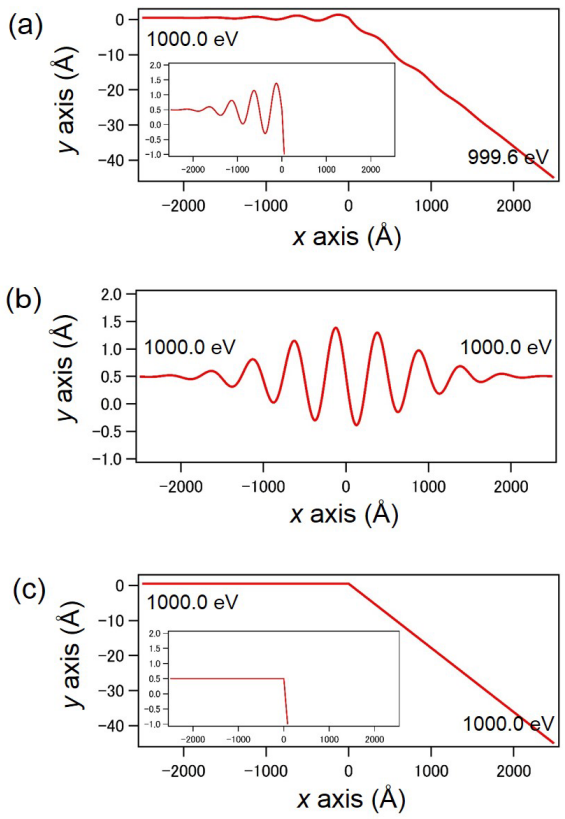

Figure 6: Simulated classical trajectories of free electrons. (a) An electron scattered by an atom in a laser field. (b) An electron in the laser field. (c) An electron scattered by an atom outside the laser field. The values written in these figures are the kinetic energies of the electrons before (left side) and after (right side) the propagation. The polarization direction of the laser field is along the y-axis. Insets in (a) and (c) show the magnified views around $y = 0$. The scattering angle of the electrons in (a) and (c) are about 0.1°.

atom is modeled by the Yukawa potential (screened Coulomb potential) [70],

$$V(r) = -\frac{Ze^2}{4\pi\epsilon_0}\frac{\exp(-r/a)}{r} \tag{2.8}$$

where r is a distance between the free electron and the origin of the potential, Z is the atomic number, and the parameter a is given by $a = a_0/Z^{1/3}$, where a_0 is the Bohr radius. The Yukawa potential is frequently used as a model potential for the scattering of an electron by a neutral atom. In this simulation, I adopted $Z = 1$ (hydrogen). The initial kinetic energy of the free electron is 1000 eV. The trajectories of the free electrons were calculated by the fourth-order Runge-Kutta method [71].

The result of the numerical simulation is shown in Fig. 6(a). Initially, the free electron is

assumed to be at $y = +0.5$ Å and move along the x-axis. The origin of the scattering potential (Eq. (2.8)) is $(x, y) = (0, 0)$. The polarization direction of the laser field is along the y-axis. The vector potential of the laser field has maximum value when the electron is at $x = 0$. In this simulation, the kinetic energy of the electron is shifted by -0.4 eV through the scattering. The amount of the energy shift coincides with the calculated value (-0.4 eV) by using Eq. (2.7).

For comparison, I simulated the classical trajectories of an electron in a laser field without the scattering potential (Fig. 6(b)) and of an electron scattered by the potential without the laser field (Fig. 6(c)). In these cases, the kinetic energies of the electrons were not shifted. In the case of Fig. 6(b), even though the electron is quivered through the interaction with the laser field, the kinetic energy of the electron returns to the initial value after the interaction. This is because the integral of the electric field appearing in Eq. (2.2) becomes zero [45],

$$\lim_{t\to\infty} \int_{-t}^{t} \boldsymbol{F}(t')\mathrm{d}t' \to 0. \tag{2.9}$$

2.1.2 Bunkin-Fedorov and Kroll-Watson approximations

In this subsection, I introduce two theories of the LAES process: Bunkin-Fedorov approximation (BFA) [72] and Kroll-Watson approximation (KWA) [67] in which the scattering of an free electron by a potential is treated quantum mechanically. The derivations of several formulae follow the textbook written by Joachain, Kylstra and Potvliege [45]. The result of BFA provides basic insights about the cross section of the LAES process. The result of KWA is commonly used for the comparison with the experimental LAES signals.

The Hamiltonian of the LAES process is composed of three terms,

$$\hat{H} = \hat{H}_{\mathrm{EL}} + \hat{H}_{\mathrm{TL}} + V_{\mathrm{TE}}, \tag{2.10}$$

where $\hat{H}_{\mathrm{EL}}$ is the Hamiltonian of the free electron in a laser field, $\hat{H}_{\mathrm{TL}}$ is the Hamiltonian of a target (atom) in the laser field, and V_{TE} is the electron-target scattering potential. The theoretical frameworks of BFA and KWA are schematically shown in Fig. 7. In these theories, the interaction between the free electron and the laser field ($\hat{H}_{\mathrm{EL}}$) is included non-peturbatively, whereas the interaction between the target and the laser field ($\hat{H}_{\mathrm{TL}}$) is neglected. As discussed in the next section, the conventional LAES experiments had been conducted by relatively low-intensity laser fields, and therefore the interaction between the laser field and the target was negligibly small. The difference between BFA and KWA lies in the treatment of the electron-atom interaction (V_{TE}). In BFA, V_{TE} is evaluated perturbatively (first Born approximation). On the other hand, in KWA, V_{TE} is treated non-perturbatively.

Before introducing the result of these theories, the wavefunction of a free electron in a laser

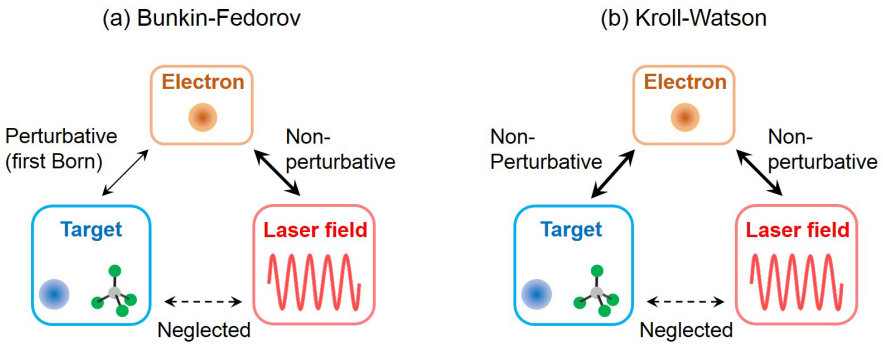

Figure 7: Theoretical frameworks of the LAES process. (a) The Bunkin-Fedorov approximation. (b) The Kroll-Watson approximation. Both approximations treat the interaction between the free electron and the laser field non-perturbatively and neglect the interaction between the target and the laser field. The Bunkin-Fedorov approximation treats the interaction between the free electron and the target by the first Born approximation. On the other hand, the Kroll-Watson approximation treats the electron-target interaction non-perturbatively.

field is discussed quantum mechanically. The Hamiltonian $\hat{H}_{\mathrm{EL}}$ is given by

$$\hat{H}_{\mathrm{EL}}(t) = \frac{1}{2m_{\mathrm{e}}}\left(\boldsymbol{p} + \frac{e}{c}\boldsymbol{A}(t)\right)^2, \tag{2.11}$$

where $\boldsymbol{p}$ is the operator of the canonical momentum. The exact solution of the Schrödinger equation,

$$\mathrm{i}\hbar\frac{\mathrm{d}}{\mathrm{d}t}\chi_{\boldsymbol{p}}(\boldsymbol{r},t) = \hat{H}_{\mathrm{EL}}(t)\chi_{\boldsymbol{p}}(\boldsymbol{r},t), \tag{2.12}$$

is a plane wave which is known as the (non-relativistic) Gordon-Volkov wavefunction [73, 74]

$$\chi_{\boldsymbol{p}}(\boldsymbol{r},t) = \frac{1}{(2\pi\hbar)^{3/2}}\exp\left[-\frac{\mathrm{i}}{\hbar}E_p t + \frac{\mathrm{i}}{\hbar}\boldsymbol{p}\cdot(\boldsymbol{r}-\boldsymbol{\alpha}(t)) + \frac{\mathrm{i}}{\hbar}\frac{e^2}{2m_{\mathrm{e}}c^2}\int_{-\infty}^{t}\boldsymbol{A}^2(t')\mathrm{d}t'\right], \tag{2.13}$$

with

$$E_p = \frac{p^2}{2m_{\mathrm{e}}}, \tag{2.14}$$

and

$$\boldsymbol{\alpha}(t) = \frac{e}{m_{\mathrm{e}}c}\int_{-\infty}^{t}\boldsymbol{A}(t')\mathrm{d}t', \tag{2.15}$$

where $\boldsymbol{\alpha}(t)$ corresponds to the displacement of the classical free electron due to the quiver motion in the laser field. When the laser electric field is written classically as

$$\boldsymbol{F}(t) = F_0\boldsymbol{\epsilon}\sin(\omega t), \tag{2.16}$$

and assuming $F(t=-\infty)=A(t=-\infty)=0$, the position vector of the classical electron is given by

$$\boldsymbol{r}=\boldsymbol{\alpha}_0\sin(\omega t)+\frac{\boldsymbol{p}}{m_\mathrm{e}}t+\boldsymbol{r}_0, \tag{2.17}$$

with

$$\boldsymbol{\alpha}_0=\frac{eF_0}{m_\mathrm{e}\omega^2}\boldsymbol{\epsilon}, \tag{2.18}$$

where ω is the angular frequency of the laser field, $\boldsymbol{r}_0$ is the position vector of the electron at $t=-\infty$. Eq. (2.17) shows that the free electron oscillates with the amplitude of $|\boldsymbol{\alpha}_0|$. As can be seen in Fig. 6(b), the quiver amplitude is about 1 Å under the experimental conditions of this study ($I\sim10^{12}$ W/cm^2, $\lambda=800$ nm).

Bunkin-Fedorov approximation

In BFA, the first Born approximation (FBA) is employed for obtaining the differential cross section of the LAES process. The differential cross section is defined as the ratio of the number of scattered electrons per unit time and unit solid angle to the number of incident electrons per unit time and unit area. The differential cross section can be determined experimentally by measuring intensity of scattered electrons as a function of the scattering angle. In FBA, the differential cross section of LAES process with the energy shift of n-photons is given by

$$\frac{\mathrm{d}\sigma_n^{\mathrm{B1}}}{\mathrm{d}\Omega}=\frac{|\boldsymbol{p}_{\mathrm{f},n}|}{|\boldsymbol{p}_\mathrm{i}|}|f_n^{\mathrm{B1}}(\boldsymbol{p}_\mathrm{i},\boldsymbol{p}_{\mathrm{f},n})|^2, \tag{2.19}$$

where f_n^{B1} is the first Born scattering amplitude which is given by

$$f_n^{\mathrm{B1}}(\boldsymbol{p}_\mathrm{i},\boldsymbol{p}_{\mathrm{f},n})=-2\pi m_\mathrm{e}\int\mathrm{d}t\int\mathrm{d}\boldsymbol{r}\chi^*_{\boldsymbol{p}_{\mathrm{f},n}}(\boldsymbol{r},t)V_{\mathrm{TE}}(\boldsymbol{r})\chi_{\boldsymbol{p}_\mathrm{i}}(\boldsymbol{r},t), \tag{2.20}$$

where $\chi_{\boldsymbol{p}_\mathrm{i}}$ and $\chi_{\boldsymbol{p}_{\mathrm{f},n}}$ are the Gordon-Volkov wavefunctions before and after the scattering. By using the definition of the Gordon-Volkov wavefunction (Eq. (2.13)), the differential cross section becomes

$$\frac{\mathrm{d}\sigma_n^{\mathrm{B1}}}{\mathrm{d}\Omega}=\frac{|\boldsymbol{p}_{\mathrm{f},n}|}{|\boldsymbol{p}_\mathrm{i}|}J_n^2(\boldsymbol{s}\cdot\boldsymbol{\alpha}_0)\frac{\mathrm{d}\sigma_{\mathrm{el}}^{\mathrm{B1}}}{\mathrm{d}\Omega}(\boldsymbol{s}), \tag{2.21}$$

with

$$\frac{\mathrm{d}\sigma_{\mathrm{el}}^{\mathrm{B1}}}{\mathrm{d}\Omega}(\boldsymbol{s})=\left|\frac{m_\mathrm{e}}{2\pi\hbar^2}\int\mathrm{d}\boldsymbol{r}'V_{\mathrm{TE}}(\boldsymbol{r}')\exp(\mathrm{i}\boldsymbol{s}\cdot\boldsymbol{r}')\right|^2, \tag{2.22}$$

where J_n is the n-th order Bessel function of the first kind, $\mathrm{d}\sigma_{\mathrm{el}}^{\mathrm{B1}}/\mathrm{d}\Omega$ is the laser-field free differential cross section of the elastic scattering obtained within FBA. Because the Gordon-Volkov wavefunction is the exact solution of the Schrödinger equation (Eq. (2.12)), the interaction between the free electron and the laser field is included non-perturbatively. Based on this equation (Eq. (2.21)), I discuss the laser parameter dependence and the sum rule of the differential cross section of the LAES process. I also discuss the relationship between the cross section of the

photon-emission ($n < 0$) process and that of the photon-absorption ($n > 0$) process.

In BFA (Eq. (2.21)), the differential cross section of the LAES process depends on the laser parameters only through $\boldsymbol{\alpha}_0$ which appears in the argument of the Bessel function. By expanding the Bessel function in polynomials [75]

$$J_n(x) = \sum_{l=0}^{\infty} \frac{(-1)^l}{l!(n+l)!} \Big(\frac{x}{2}\Big)^{n+2l}, \tag{2.23}$$

and taking the term of $l = 0$, it follows that

$$\begin{aligned} \frac{\mathrm{d}\sigma_n^{\mathrm{B1}}}{\mathrm{d}\Omega} &\sim \frac{(\boldsymbol{s}\cdot\boldsymbol{\alpha}_0)^{2|n|}}{2^{2|n|}(|n|!)^2} \frac{\mathrm{d}\sigma_{\mathrm{el}}^{\mathrm{B1}}}{\mathrm{d}\Omega} \\ &= \frac{F_0^{2|n|}}{\omega^{4|n|}} \Big(\frac{e}{m_{\mathrm{e}}}\Big)^{2|n|} \frac{(\boldsymbol{s}\cdot\boldsymbol{\epsilon})^{2|n|}}{2^{2|n|}(|n|!)^2} \frac{\mathrm{d}\sigma_{\mathrm{el}}^{\mathrm{B1}}}{\mathrm{d}\Omega}. \end{aligned} \tag{2.24}$$

Therefore, the differential cross section of the LAES process with a n-photon energy shift is proportional to $(F_0^2/\omega^4)^{|n|}(\boldsymbol{s}\cdot\boldsymbol{\epsilon})^{2|n|}$. Because the intensity of the laser field (I) is proportional to the square of the amplitude (F_0), and the wavelength of the laser field (λ) is inversely proportional to the frequency ω, the differential cross section is proportional to $(I\lambda^4)^{|n|}$. The term $(\boldsymbol{s}\cdot\boldsymbol{\epsilon})$ indicates that the differential cross section ($n \neq 0$) has a maximum value when the polarization vector of the laser field $\boldsymbol{\epsilon}$ is parallel to the scattering vector $\boldsymbol{s}$, and has a minimum when $\boldsymbol{\epsilon}$ is perpendicular to $\boldsymbol{s}$.

As will be discussed in the next section, the kinetic energy of the electron used for the observation of the LAES process is usually much larger than the photon energy. In this case, the scattering vector s is nearly independent on n, and $|\boldsymbol{p}_{\mathrm{f},n}|/|\boldsymbol{p}_{\mathrm{i}}| \simeq 1$. Then, the summation of the differential cross section over n can be performed by using the sum rule of the Bessel function [76],

$$\sum_{n=-\infty}^{\infty} J_n^2(x) = 1. \tag{2.25}$$

The sum of the differential cross section (Eq. (2.21)) becomes

$$\sum_{n=-\infty}^{\infty} \frac{\mathrm{d}\sigma_n^{\mathrm{B1}}}{\mathrm{d}\Omega} \simeq \frac{\mathrm{d}\sigma_{\mathrm{el}}^{\mathrm{B1}}}{\mathrm{d}\Omega}. \tag{2.26}$$

This equation states that the sum of the differential cross section of the LAES process is almost same as the differential cross section of the elastic scattering in the absence of the laser field.

Moreover, by employing the relationship [75],

$$J_{-n}(x) = (-1)^n J_n(x), \tag{2.27}$$

it follows that

$$\frac{\mathrm{d}\sigma_n^{\mathrm{B1}}}{\mathrm{d}\Omega} \simeq \frac{\mathrm{d}\sigma_{-n}^{\mathrm{B1}}}{\mathrm{d}\Omega}. \tag{2.28}$$

Therefore, the differential cross section of of the photon-emission ($n < 0$) process is nearly identical to that of the photon-absorption ($n > 0$) process when the kinetic energy of the electron is much larger than the photon energy.

Kroll-Watson approximation

In KWA, the scattering of the incident electron by the potential is treated non-perturbatively. KWA adopts the low-frequency approximation in which the photon energy is assumed to be much smaller than the kinetic energy of the electrons [45]. In addition to the original derivation given by Kroll and Watson [67], various derivations of the differential cross section in KWA were reported [77–82]. Here I omit the derivation and only introduce the differential cross section of the LAES process in KWA,

$$\frac{\mathrm{d}\sigma_n}{\mathrm{d}\Omega} = \frac{|\boldsymbol{p}_{\mathrm{f},n}|}{|\boldsymbol{p}_{\mathrm{i}}|} J_n^2(\boldsymbol{s}\cdot\boldsymbol{\alpha}_0) \frac{\mathrm{d}\sigma_{\mathrm{el}}}{\mathrm{d}\Omega}(\boldsymbol{p}_{\mathrm{i}}^*, \boldsymbol{p}_{\mathrm{f},n}^*), \tag{2.29}$$

where

$$\boldsymbol{p}_{\mathrm{i}}^* = \boldsymbol{p}_{\mathrm{i}} + \boldsymbol{\gamma}, \tag{2.30}$$

$$\boldsymbol{p}_{\mathrm{f},n}^* = \boldsymbol{p}_{\mathrm{f},n} + \boldsymbol{\gamma}, \tag{2.31}$$

$$\boldsymbol{\gamma} = \frac{m_{\mathrm{e}} n\omega}{\boldsymbol{s}\cdot\boldsymbol{\alpha}_0}\boldsymbol{\alpha}_0. \tag{2.32}$$

The differential cross section in KWA looks similar to that in BFA (Eq. (2.21)). However, $\mathrm{d}\sigma_{\mathrm{el}}/\mathrm{d}\Omega$ is the exact differential cross section of the elastic scattering that corresponds to the transition from $\boldsymbol{p}_{\mathrm{i}}^*$ to $\boldsymbol{p}_{\mathrm{f}}^*$. Because the momentum shift $\boldsymbol{\gamma}$ depends on the parameters of the laser field, the elastic differential cross section appearing in the formula of KWA can be modified by the parameters of the laser field.

Because the low frequnecy approximation is assumed in KWA, the expressions similar to Eq. (2.26) and Eq. (2.28) hold as follows,

$$\sum_{n=-\infty}^{\infty} \frac{\mathrm{d}\sigma_n}{\mathrm{d}\Omega} \simeq \frac{\mathrm{d}\sigma_{\mathrm{el}}}{\mathrm{d}\Omega}, \tag{2.33}$$

$$\frac{\mathrm{d}\sigma_n}{\mathrm{d}\Omega} \simeq \frac{\mathrm{d}\sigma_{-n}}{\mathrm{d}\Omega}. \tag{2.34}$$

Effect of the momentum shift $\boldsymbol{\gamma}$

The effect of the momentum shift $\boldsymbol{\gamma}$ (Eqs. (2.30) and (2.31)) is discussed. In Fig. 8, the ratio of the momenta, $|\boldsymbol{p}_{\mathrm{i}}^*|/|\boldsymbol{p}_{\mathrm{i}}|$, is plotted as a function of the scattering angle θ. At a scattering angle

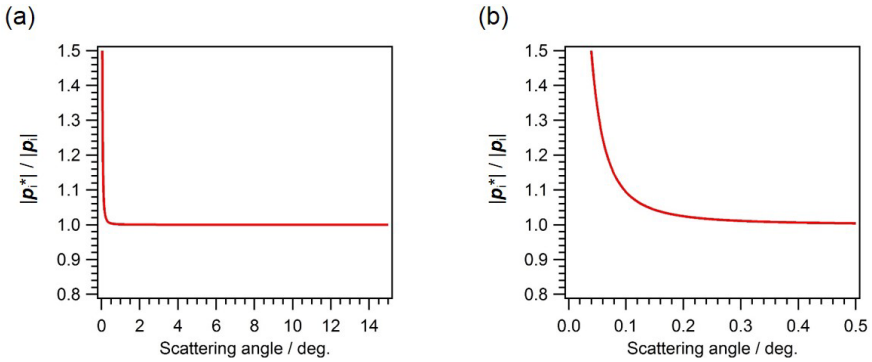

Figure 8: Effect of the momentum shift appearing in the Kroll-Watson approximation under the experimental conditions of the femtosecond LAES experiments. The ratio of the momenta $|\boldsymbol{p}_{\rm i}^*|/|\boldsymbol{p}_{\rm i}|$ is shown. Panel (b) is an expanded view of the small angle range of panel (a).

where the ratio of the momenta is close to 1, the effect of the momentum shift is negligibly small. The simulation was done by assuming that n = 1, the kinetic energy of the incident electrons is 1 keV, the laser field intensity is $I = 2 \times 10^{12}$ W/cm^2, the wavelength of the laser field is $\lambda = 800$ nm, and the laser polarization direction ($\boldsymbol{\epsilon}$) is perpendicular to $\boldsymbol{p}_{\rm i}$. These parameters are similar to the experimental conditions of our previous study [44]. Because $\boldsymbol{s} \cdot \boldsymbol{\alpha}_0$ vanishes at the scattering angle of $\theta \sim 0^\circ$, the ratio of the momenta diverges near the zero scattering angle ($\theta \sim 0^\circ$). However, the ratio of the momenta is almost 1.0 at the scattering angle larger than 0.1°. Even at the small scattering angle of $\theta = 0.1^\circ$, the effect of the momentum shift is less than 10%. I confirmed that the ratio $|\boldsymbol{p}_{\rm f}^*|/|\boldsymbol{p}_{\rm f}|$ shows almost the same curve as that of $|\boldsymbol{p}_{\rm i}^*|/|\boldsymbol{p}_{\rm i}|$. Because the minimum detectable scattering angles in this thesis study are 2° (Chapter 3) and 0.1° (Chapter 4), the momentum shift appearing in the formula of KWA can be neglected. When the momentum shift $\boldsymbol{\gamma}$ is neglected, the formula of KWA becomes

$$\frac{\mathrm{d}\sigma_n}{\mathrm{d}\Omega} = \frac{|\boldsymbol{p}_{\mathrm{f},n}|}{|\boldsymbol{p}_{\rm i}|} J_n^2(\boldsymbol{s} \cdot \boldsymbol{\alpha}_0) \frac{\mathrm{d}\sigma_{\rm el}}{\mathrm{d}\Omega}(\boldsymbol{p}_{\rm i}, \boldsymbol{p}_{\mathrm{f},n}). \tag{2.35}$$

Furthermore, because the kinetic energy of the incident electron (1 keV) is much higher than the photon energy ($h\nu = 1.55$ eV), the absolute value of the momentum after the scattering ($|\boldsymbol{p}_{\mathrm{f},n}|$) is nearly identical with that before the scattering ($|\boldsymbol{p}_{\rm i}|$). By assuming that the absolute value of the momentum of the scattered electron ($|\boldsymbol{p}_{\mathrm{f},n}|$) is the same as that of incident electron ($|\boldsymbol{p}_{\rm i}|$), the differential cross section of KWA can be further approximated by the following formula.

$$\frac{\mathrm{d}\sigma_n}{\mathrm{d}\Omega} = J_n^2(\boldsymbol{s} \cdot \boldsymbol{\alpha}_0) \frac{\mathrm{d}\sigma_{\rm el}}{\mathrm{d}\Omega}(\boldsymbol{p}_{\rm i}, \boldsymbol{p}_{\rm f}), \tag{2.36}$$

where $|\boldsymbol{p}_{\rm f}| = |\boldsymbol{p}_{\rm i}|$. The differential cross section of the elastic scattering appearing in this formula, $\mathrm{d}\sigma_{\rm el}/\mathrm{d}\Omega$, does not depend on either n or the parameters of the laser field. Therefore, the

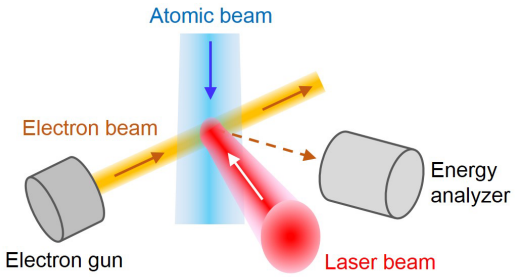

Figure 9: Schematic of the LAES experiment. The electron beam, the atomic beam, and the laser beam should be overlapped with each other.

differential cross section of the elastic scattering used in this formula is the same as that can be measured by an experiment without laser fields. In this study, this formula is used for simulating the differential cross section of the LAES process based on KWA.

2.2 Laser-assisted electron scattering experiments

In order to observe the LAES signals, three beams, i.e., an electron beam, an atomic beam, and a laser beam, should intersect with each other at a spatial point as shown in Fig. 9. When pulsed beams are employed, the temporal overlap between the beams should also be achieved. The kinetic energy distribution of the incoming electron beam (E_i) should be narrow enough to resolve the shift in kinetic energy by a photon energy ($h\nu$).

The experimental studies of the LAES process are summarized in Table 1 in chronological order. Because of the experimental difficulties to conduct the three beam experiment, only a few research groups have succeeded in measuring the LAES processes. The first observation of the LAES process was reported by Andrick and Langhans in 1976 [42]. They employed a cw-CO_2 laser ($\lambda = 10.6$ μm, $h\nu$ = 0.12 eV, $I = 6 \times 10^4$ W/cm^2) and measured the electrons (E_i =11.55 eV) scattered by Ar atoms in the laser field. In the kinetic energy spectrum of the scattered electrons, they observed signals of the LAES processes with the energy shifts of a photon energy ($n = \pm 1$) . The multiphoton LAES processes ($|n| \geq 2$) were first observed by Weingartshofer *et al.* in the next year [43]. In order to observe the multiphoton processes, they employed pulsed-CO_2 laser ($\lambda = 10.6$ μm, τ =2 μs) and achieved the laser field intensity of 10^9 W/cm^2 which is four orders of magnitude higher than that in the experiment done by Andrick and Langhans. By measuring the kinetic energies of the electrons (E_i =11 eV) scattered by Ar in the laser field, they observed multiphoton LAES signals up to $|n|$ = 3. In 1983, Weingartshofer *et al.* observed the multiphoton LAES processes as high as $|n|$ = 11 by employing the pulsed-CO_2 laser ($\lambda = 10.6$ μm, τ =2 μs, $I = 10^8$ W/cm^2) [83].

Table 1: Experimental studies of the LAES process. The experimental works on the LAES process are listed in chronological order. Our reports are shown in red. E_i is the kinetic energy of the incident electron beam.

Year	Authors [Reference]	E_i (eV)	Laser (pulse duration and wavelength)	Field intensity (W/cm^2)	Target (sample)
1976	Andrick, Langhans [42]	11.55	CO_2 (cw, 10.6 μm)	6×10^4	Ar
1977	Weingartshofer *et al.* [43]	11	CO_2 (2 μs, 10.6 μm)	10^9	Ar
1978	Andrick, Langhans [84]	5, 11, 16	CO_2 (cw, 10.6 μm)	2×10^4	Ar
1978	Langhans [85]	11	CO_2 (cw, 10.6 μm)	NA	Ar
1979	Weingartshofer *et al.* [86]	4.2-76.4	CO_2 (2 μs, 10.6 μm)	10^8	Ar, H_2
1983	Weingartshofer *et al.* [83]	9.9-15.8	CO_2 (2 μs, 10.6 μm)	10^8	Ar
1984	Andrick, Bader [87]	19.0	CO_2 (cw, 10.6 μm)	10^5	He
1985	Bader [88]	11	CO (NA, 5.3 μm)	NA	Ar
1986	Bader [89]	11, 16	CO_2 (cw, 10.6 μm)	5×10^4	Ne, Ar
1987	Wallbank *et al.* [90]	10.21	CO_2 ($\sim$ μs, 10.6 μm)	10^8	Ar
1987	Wallbank *et al.* [91]	10.55	CO_2 ($\sim$ μs, 10.6 μm)	2×10^8	Ar
1992	Wallbank *et al.* [92]	19	CO_2 (3 μs, 10.6 μm)	10^8	He
1993	Wallbank, Holmes [93]	9.5	CO_2 ($\sim$ μs, 10.6 μm)	10^8	He
1994	Wallbank, Holmes [94]	6.2-32	CO_2 (4 μs, 10.6 μm)	10^8	He, Ar
1994	Wallbank, Holmes [95]	8-20	CO_2 ($\sim$ μs, 10.6 μm)	10^8	He, Ar
1996	Wallbank, Holmes [96]	0.2-2.5	CO_2 ($\sim$ μs, 10.6 μm)	5×10^7	He
2001	Wallbank, Holmes [97]	1-20	CO_2 ($\sim$ μs, 10.6 μm)	6×10^7	He
2010	Nehari *et al.* [98]	22	CO_2 (3 μs, 10.6 μm)	4×10^8	He
2010	Kanya, Morimoto, Yamanouchi [44]	1000	Ti:Sa (200 fs, 0.8 μm)	2×10^{12}	Xe
2010	Musa *et al.* [99]	3.8, 5.8	CO_2 (3 μs, 10.6 μm)	NA	CO_2
2011	deHarak *et al.* [100]	50-350	Nd:YAG (6 ns, 1.1 μm)	6×10^9	He
2011	Kanya, Morimoto, Yamanouchi [69]	1000	Ti:Sa (50 fs, 0.8 μm)	1×10^{12}	Xe
2014	Morimoto, Kanya Yamanouchi [101]	1000	Ti:Sa (520 fs, 0.8 μm)	6×10^{11}	CCl_4
2014	deHarak *et al.* [102]	30-200	Nd:YAG (8 ns, 1.1 μm)	5×10^9	He

2.3 Ultrafast laser-assisted electron scattering

As described in the previous section, most of the LAES experiments had been conducted by using cw- and microsecond-CO_2 lasers. The LAES process by ultrashort laser pulses had not been observed until our recent study [44]. In this section, I first discuss experimental difficulties to observe the LAES process by ultrashort laser pulses. Then, our recent results on the observation of the LAES process by femtosecond laser fields are presented. At the end of this section, applications of the LAES process induced by ultrashort laser pulses are discussed.

2.3.1 Experimental difficulties to measure laser-assisted electron scattering by ultrashort laser pulses

There are two experimental difficulties to observed the LAES process by ultrashort laser pulses: (i) very weak signal intensity and (ii) intense background signals. According to Eq. (2.24), the signal intensity of the LAES process per unit time is proportional to $(I\lambda^4)^{|n|}$. When the pulsed laser is employed for the measurement of the LAES process, two parameters, the pulse

Table 2: Comparison of the LAES signal intensity in a conventional experiment with a CO_2 laser and that in our experiment with a femtosecond laser.

	Wallbank *et al.* [92]	Our experiment [44]
Laser	CO_2	Ti:Sapphire
Field intensity (I)	10^8 W/cm^2	10^{12} W/cm^2
Wavelength (λ)	10.6 μm	800 nm
Pulse duration (τ)	3 μs	200 fs
Repetition rate (R)	$<$4 Hz	5 kHz
Intensity of LAES ($\|n\| = 1$) signal	1	$\sim 10^{-5}$

duration τ and the repetition rate R, should be taken into account. Because the interaction time between electrons and lasers is given by τR, the LAES signal intensity per unit time becomes proportional to $(I\lambda^4)^{|n|}\tau R$ when these two parameters are considered. By using this relation, I compare the signal intensity of the LAES signal in the case of the CO_2 laser and that of the femtosecond Ti:sapphire laser. In Table 2, the parameters of these two lasers are summarized. The parameters of the microsecond CO_2 laser are adopted from Ref. [92]. The parameters of the femtosecond Ti:sapphire laser are adopted from our recent report [44]. Even though the peak intensity (I) and the repetition rate (R) of our experiment are much higher than those of the conventional LAES experiment with the CO_2 laser, the calculated LAES signal intensity with one-photon energy shift is five orders of magnitude smaller than that of the CO_2 laser. This is because of the large differences in the pulse duration (τ) and the wavelength (λ). Even in the case of the CO_2 lasers, the measurement of the LAES signals requires a long accumulation time, typically a day [83]. Consequently, it is almost impossible to observe the LAES signals by femtosecond laser pulses when the conventional apparatus is employed.

Another difficulty to measure the LAES signals by ultrashort laser pulses is the large background signals originated from the elastic scattering ($\Delta E = 0$). In the LAES experiments with the microsecond CO_2 lasers, the laser pulse duration is much longer than the time required for an electron to pass through the atomic beam. In this case, most of the electron signals are originating from the scattering events which occur inside the laser field. On the other hand, when the duration of the laser pulse is shorter than the time for an electron to pass through the atomic beam, the electron can be scattered before and after the interaction with the laser field. Because the LAES process is induced only in the presence of the laser field, the scattering events which occur outside the laser field give rise to the background elastic scattering signals ($\Delta E = 0$). For example, the 1000 eV electron requires about 50 ps to pass through the 1 mm atomic beam. When a 50 fs laser field is employed for the measurement of the LAES process, only 0.1% of the scattering events occur in the laser field, and the remaining 99.9% of the scattering events occur outside the laser field. Therefore, the LAES signals can be buried under the tail of huge background signals which are centered at $\Delta E = 0$.

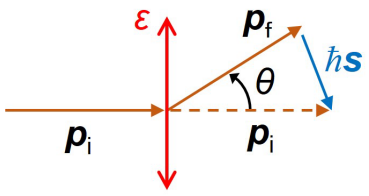

Figure 10: The relationship of the electron momenta and the laser polarization vector. $\boldsymbol{p}_\mathrm{i}$ and $\boldsymbol{p}_\mathrm{f}$ are the momenta of the electron before and after the scattering, respectively, $\boldsymbol{\epsilon}$ is the polarization vector of the laser field, θ is the scattering angle, and $\boldsymbol{s}$ is the scattering vector. All the vectors are in the same plane.

2.3.2 Femtosecond laser-assisted electron scattering experiments

In 2010, we succeeded in observing the LAES signals by femtosecond laser pulses for the first time [44]. The apparatus we developed is described in Section 3.5 of this thesis and in Ref. [69]. The high sensitivity of the apparatus allows us to measure the LAES signals with a count rate of 0.01 count/sec. Thanks to the high energy resolution of 0.7 eV, the intensity of the tail of the elastic background signals at $\Delta E = \pm h\nu$ are suppressed to the same extent as that of the LAES signals. In our experiment, the polarization direction of the femtosecond laser field was perpendicular to the direction of the incident electrons (Fig. 10). The kinetic energy of the incident electrons was 1000 eV. We measured the electrons scattered in a plane defined by the polarization vector of the laser field ($\boldsymbol{\epsilon}$) and the momentum of the incident electron ($\boldsymbol{p}_\mathrm{i}$). By using a toroidal energy analyzer and a two-dimensional imaging detector, we recorded a kinetic energy distribution and a scattering angle distribution simultaneously.

Figure 11(a) shows kinetic energy spectra of electrons scattered by Xe atoms. The red circles show the spectrum when the laser pulse and the electron pulse were temporally overlapped. The spectrum plotted as back squares is a background spectrum measured by delaying the arrival time of the electron pulse by 100 ps. The duration of the laser pulse was 200 fs, and the peak field intensity was 1.8×10^{12} W/cm^2. The data accumulation time was 83 hours for both spectra. We observed clear increases in signal intensity at $\Delta E = \pm 1.55$ eV which correspond to a photon energy ($\lambda = 800$ nm). The LAES signals became clearer when the background spectrum was subtracted (red circles in Fig. 12(b)). The observed signal intensities were compared with a numerical simulation in which KWA (Eq. (2.36)) was adopted. The result of the simulation shown in Fig. 11(b) as a blue curve reproduces the observed signal intensities. This agreement confirmed our observation of the LAES signals in the femtosecond laser field. The angular distributions of the one-photon ($n = \pm1$) LAES signals are shown in Figs. 12(a) and (b) as red circles. Blue lines in Figs. 12(a) and (b) are the result of the numerical simulation. The observed angular distributions were also reproduced by the numerical simulation.

In the next year, we reported the observation of the LAES signals by shorter (50 fs) laser pulses with a peak field intensity of 1.4×10^{12} W/cm^2. The background subtracted kinetic energy

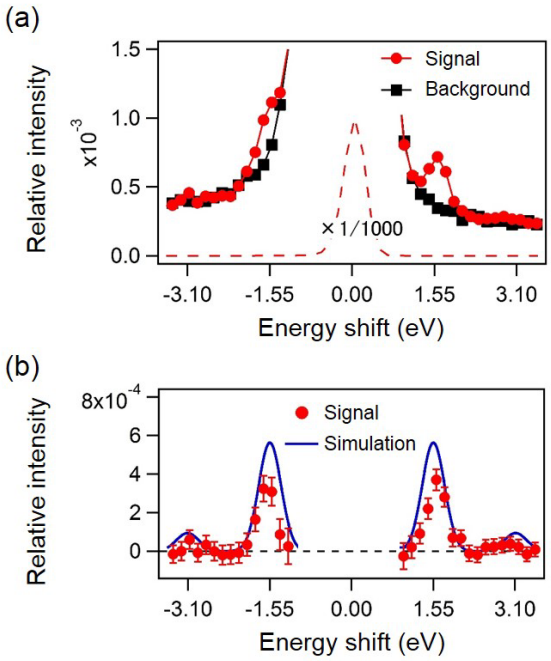

Figure 11: Kinetic energy spectra of scattered electrons. (a) The kinetic energy spectrum of electrons scattered in a laser field and the background energy spectrum. Red circles show energy spectrum of electrons scattered by Xe in a 200 fs laser field. Black squares show energy spectrum of electrons scattered by Xe outside the laser field. (b) Background subtracted kinetic energy spectrum. Red circles show the experimental spectrum. The error bars represent one standard deviation. Blue line shows the result of the numerical simulation. The signals in the energy range of $\Delta E < 1$ eV are not shown because of the large errors originating from the large background signals.

spectrum is shown in Fig. 13 as red circles. At $\Delta E = \pm 1.55$ eV, we observed unambiguous peaks which were assigned to the LAES processes with the energy shift of $\pm h\nu$ ($n = \pm 1$).

2.3.3 Application of femtosecond laser-assisted electron scattering

The LAES process induced by femtosecond laser pulses which we have observed for the first time can be applied to the ultrafast imaging of atomic and molecular processes. As discussed in Section 1.1, the electron scattering without laser fields can be used to determine the geometrical structures of gas-phase molecules and the electron density distributions of atoms and molecules. However, it has been challenging to investigate the ultrafast nuclear and electron dynamics of gas-phase samples by using the electron scattering. This is greatly related with the thickness of the gaseous samples. As discussed in Section 2.3.1, it takes 50 ps for 1 keV electrons to pass through a 1 mm gaseous sample. This means that the scattered electrons have the information of the sample over 50 ps, and difficult to be used for the investigation of ultrafast phenomena which

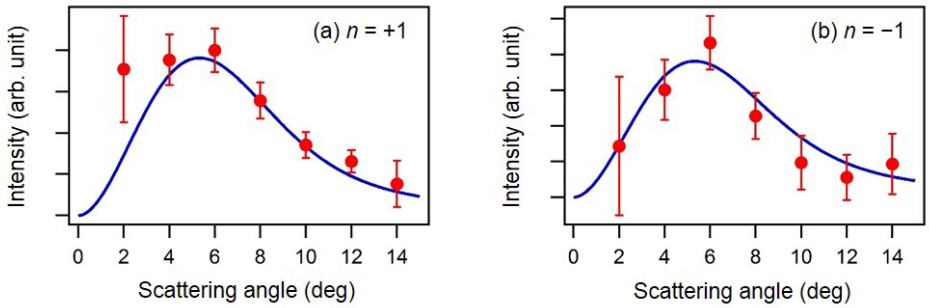

Figure 12: Angular distributions of the LAES signals by Xe in the 200 fs laser field. (a) The angular distribution of LAES $n = +1$ process. (b) The angular distribution of LAES $n = -1$ process. These angular distributions were obtained by integrating the electron signals over the range of 0.7 eV centered at the energy shifts of $\pm h\nu$. Red circles show the angular distribution obtained by the experiment. Blue curves are the simulated angular distributions calculated by using KWA. Blue curves in (a) and (b) are almost identical with each other (Eq. (2.34)).

proceed on the time scale of femtoseconds. The detailed discussion on the temporal resolution will be done in Section 3.2.2.

Because the LAES process is induced only in the presence of a laser field, it can be used to extract electrons scattered only inside an ultrashort and intense laser field by selecting scattered electrons according to their kinetic energies. These extracted electrons carry the information of atoms and molecules with an ultrashort duration of the laser field and in the intense laser field. Therefore, the LAES process can be used as (i) a probe of ultrafast atomic and molecular processes induced by ultrashort laser pulses, and (ii) a probe of atoms and molecules in intense laser fields. Details of the two applications are described below.

By using the LAES process as a probe of an ultrafast phenomenon induced by a pump laser pulse, the phenomenon can be investigated with a temporal resolution as short as laser pulse durations. This is because, as described above, the LAES process works as an ultrafast gating for extracting electrons scattered only within the duration of the laser pulse. In next chapter, an experiment is done in order to demonstrate that the LAES process can be used to determine the instantaneous geometrical structures of gas-phase molecules with femtosecond temporal resolution.

The LAES process can also be used to investigate atomic and molecular processes which are induced only in intense laser fields. For example, it has been known that the strong laser fields can induce the modifications of the electron density distributions of atoms and molecules [103] and the deformations of the geometrical structures of molecules [104–108]. Conventionally, these processes have been investigated by detecting ions and electrons produced as a result of the interaction between samples (atoms and molecules) and intense laser fields. On the other hand, by using the LAES process induced by intense laser pulses, it will be able to directly probe

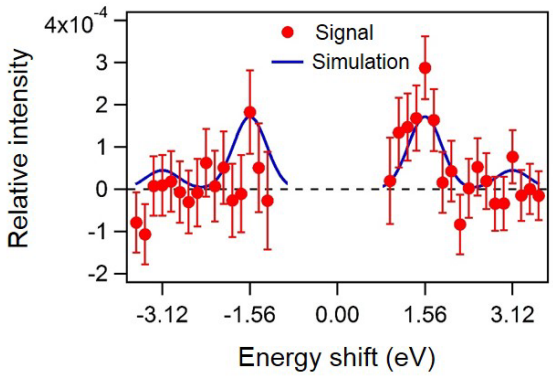

Figure 13: Kinetic energy spectra of scattered electrons in a 50 fs laser field. Red circles show the experimental spectrum. The error bars represent one standard deviation. Blue line shows the result of the numerical simulation based on KWA.

the electron density distributions of atoms and molecules and/or the geometrical structures of molecules which are interacting with intense laser fields. In this case, the intense laser pulses are used to induce both the intense-field induced processes and the LAES process. In Chapter 4, it is shown that the LAES signals carry the information of the electron density distributions of atoms and molecules in intense laser fields.

3 Laser-assisted electron diffraction

The gas-phase electron diffraction (GED) has been a powerful tool for determining geometrical structures of gas-phase molecules. The precise molecular structures determined by GED are compiled in a database [109–111], and have been used as an essential information in modern science. On the other hand, it is still challenging to determine instantaneous geometrical structure of molecules during dynamical processes such as chemical bond breaking and rearrangement.

In this chapter, I show experimentally that the instantaneous geometrical structure of gas-phase molecules can be determined by the laser-assisted electron diffraction (LAED) which uses the LAES process as an ultrafast gating of the GED measurement. In Section 3.1, I introduce the basic theory of GED. Section 3.2 is devoted to an introduction of recent works on time-resolved electron diffraction measurements. In Section 3.3, I explain the principles and advantages of the LAED method. In Section 3.4, the purpose of this study is described. The experimental apparatus used for the observation of LAED is described in Section 3.5. In Section 3.6, results of the experiment are presented with discussions on the them. Finally, a summary of this work and a discussion on the future prospects are given in Section 3.7.

3.1 Theory of gas-phase electron diffraction

In this section, I introduce basic formulae used in GED. The derivations of some formulae follow the textbooks [10, 11]. The discussion of this section is focused on the scattering of electrons by atoms and molecules without laser fields. First, the angular distribution of electrons elastically scattered by atoms is discussed. Then, a discussion on the angular distribution of electrons elastically scattered by gas-phase molecules is made. Finally, the procedures for the determination of the geometrical structure of molecules are introduced.

3.1.1 Angular distribution of electrons scattered by atoms

As introduced in Section 1.1, the scattering potential of an atom is given by

$$V_{\mathrm{atom}}(\boldsymbol{r}) = -\frac{1}{4\pi\epsilon_0}\frac{Ze^2}{|\boldsymbol{r}|} + \frac{e^2}{4\pi\epsilon_0}\int \frac{\rho_{\mathrm{atom}}(\boldsymbol{r}')}{|\boldsymbol{r}-\boldsymbol{r}'|}\mathrm{d}\boldsymbol{r}', \tag{3.1}$$

where Z is an atomic number, $\rho_{\mathrm{atom}}(\boldsymbol{r})$ is an electron density distribution of the atom, and $\boldsymbol{r}$ is a position vector of the incident electron. Because the electron density distribution of an atom is spherically symmetric, the electron density distribution can be written as $\rho_{\mathrm{atom}}(r)$, and the angular distribution of the scattered electrons becomes radially symmetric as shown in Fig. 2(a). Consequently, the angular distribution of the scattered electrons or the differential cross section

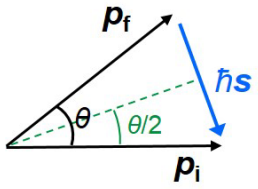

Figure 14: Relationship between the momenta of incoming ($\boldsymbol{p}_\mathrm{i}$) and scattered ($\boldsymbol{p}_\mathrm{f}$) electrons and the scattering vector ($\boldsymbol{s}$) . The scattering angle is represented by θ.

can be expressed by a function of the scattering angle θ,

$$\frac{\mathrm{d}\sigma_\mathrm{el}}{\mathrm{d}\Omega} = |f_\mathrm{atom}(\theta)|^2 \tag{3.2}$$

where $f_\mathrm{atom}(\theta)$ is an elastic scattering amplitude of an electron by an atom. The simplest method for the calculating the scattering amplitude is the first Born approximation (FBA), which is a lowest-order perturbation theory for calculating an amplitude of a potential scattering. The validity of FBA is discussed in the next subsection. In FBA, the scattering amplitude is given by

$$f_\mathrm{atom}(\theta) = -4\pi^2\hbar m_\mathrm{e} \int \phi^*_{\boldsymbol{p}_\mathrm{f}}(\boldsymbol{r}')V_\mathrm{atom}(\boldsymbol{r}')\phi_{\boldsymbol{p}_\mathrm{i}}(\boldsymbol{r}')\mathrm{d}\boldsymbol{r}', \tag{3.3}$$

where $\phi_{\boldsymbol{p}}(\boldsymbol{r})$ is a plane wave which is expressed as

$$\phi_{\boldsymbol{p}}(\boldsymbol{r}) = \frac{1}{(2\pi\hbar)^{3/2}} \exp(\frac{\mathrm{i}}{\hbar}\boldsymbol{r}\cdot\boldsymbol{p}), \tag{3.4}$$

and $\boldsymbol{p}_\mathrm{i}$ and $\boldsymbol{p}_\mathrm{f}$ are momenta of the incident and scattered electrons. By using the definition of the scattering vector $\boldsymbol{s}$ (Eq. 2.6, Fig. 14), the scattering amplitude in FBA is given by

$$\begin{aligned} f_\mathrm{atom}(\theta) &= -\frac{m_\mathrm{e}}{2\pi\hbar^2}\int V_\mathrm{atom}(\boldsymbol{r}')\mathrm{e}^{\mathrm{i}\boldsymbol{s}\cdot\boldsymbol{r}'}\mathrm{d}\boldsymbol{r}' \\ &= \frac{2m_\mathrm{e}e^2}{4\pi\epsilon_0\hbar^2}\Big(\frac{Z-A(\theta)}{s^2}\Big), \end{aligned} \tag{3.5}$$

where

$$A(\theta) = 4\pi\int_0^\infty \rho_\mathrm{atom}(r)\frac{\sin(sr)}{sr}r^2\mathrm{d}r, \tag{3.6}$$

is called (X-ray) atomic scattering factor [11], and s is the absolute value of $\boldsymbol{s}$. Equation (3.5) shows that the scattering amplitude in FBA is given by the Fourier transform of the scattering

potential. The absolute value of $\boldsymbol{s}$ can be written as a function of θ

$$\begin{aligned} s &= 2\frac{|\boldsymbol{p}_\mathrm{i}|}{\hbar}\sin(\frac{\theta}{2}) \\ &= \frac{4\pi}{\lambda_\mathrm{D}}\sin(\frac{\theta}{2}) \end{aligned} \tag{3.7}$$

where λ_D is the deBroglie wavelength of the electrons (Eq. (1.4)). By using the expression of the Bohr radius [112]

$$a_0 = \frac{4\pi\epsilon_0\hbar^2}{m_\mathrm{e}e^2}, \tag{3.8}$$

Eq. (3.5) can be re-written as

$$f_\mathrm{atom}(\theta) = \frac{2}{a_0}\Big(\frac{Z - A(\theta)}{s^2}\Big) \tag{3.9}$$

Because $f_\mathrm{atom}(\theta)$ has the dependence of s^{-2}, the differential cross section decreases with scattering angles. In FBA, the scattering amplitude is always real as long as the scattering potential is real.

Another useful method for obtaining the elastic scattering amplitudes is the partial wave analysis. The scattering amplitude obtained by the partial wave analysis is usually more accurate than that obtained by FBA. In the partial wave analysis, the scattering amplitude is expanded in partial waves which are characterized by the angular momentum l [113],

$$f_\mathrm{atom}(\theta) = \frac{1}{2\mathrm{i}k}\sum_{l=0}^{\infty}\Big\{(l+1)(\mathrm{e}^{2\mathrm{i}\delta_l^+} - 1) + l(\mathrm{e}^{2\mathrm{i}\delta_l^-} - 1)\Big\}P_l(\cos\theta), \tag{3.10}$$

where k is a wave number of the incoming electron which is defined by $k = |\boldsymbol{p}_\mathrm{i}|/\hbar$, $P_l(\cos\theta)$ is the Legendre polynomial, and δ_l^+ and δ_l^- are the phase shifts for the spin-up and spin-down scatterings, respectively. This equation states that the scattering amplitude can be calculated from the phase shifts (δ_l^+ and δ_l^-), which can be obtained by numerical methods [11, 113, 114]. The scattering amplitude obtained by the partial wave analysis is complex, and therefore, can be expressed as

$$f_\mathrm{atom}(\theta) = |f_\mathrm{atom}(\theta)|\exp(\mathrm{i}\eta_\mathrm{atom}(\theta)). \tag{3.11}$$

The magnitude ($|f_\mathrm{atom}(\theta)|$) and the phase ($\eta_\mathrm{atom}(\theta)$) of the scattering amplitude are available in databases [113–116].

3.1.2 Validity of first Born approximation

In this subsection, I discuss the validity of FBA. It has been known that FBA is valid when (i) the scattering potential is very weak and/or (ii) the kinetic energy of electron is so high that the electron can pass through the potential region before receiving significant effect from the

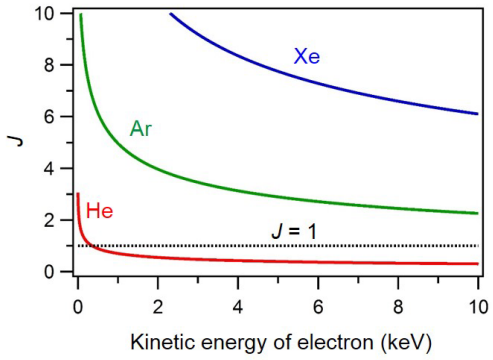

Figure 15: Validity of the first Born approximation for the electron scattering by He, Ar, and Xe. The parameter J (Eq. (3.15)) is potted for He (red curve), Ar (green curve), and Xe (blue curve) as a function of the kinetic energy of incident electrons. If the value of J is less than 1, the first Born approximation is valid.

potential [70]. By assuming that the strength and the range of the potential are $|V_0|$ and L, respectively, the condition (ii) can be expressed by the following formula,

$$\frac{\tau_1}{\tau_2} \ll 1, \tag{3.12}$$

with

$$\tau_1 = \frac{L}{v}, \tag{3.13}$$

$$\tau_2 = \frac{\hbar}{|V_0|}, \tag{3.14}$$

where v is a speed of the electron, τ_1 represents a time required for the electron to pass through the potential range, and τ_2 represents a time necessary for potential to have a significant effect on the electron [70]. By using the Yukawa potential (Eq. (2.8)), the validity of FBA is expressed by [117]

$$J \equiv \frac{m_e Z e^2}{4\pi\epsilon_0 \hbar^2 k} \sqrt{\{\ln(\sqrt{1+4a^2k^2})\}^2 + \{\arctan(2ak)\}^2} \ll 1, \tag{3.15}$$

where $a = a_0/Z^{1/3}$ (a_0 is the Bohr radius). In Fig. 15, J is plotted for He ($Z = 2$), Ar ($Z = 18$), and Xe ($Z = 54$) as a function of the kinetic energy of the incident electron. For 1 keV electrons which are used in this study, J is smaller than 1 for He, but much larger than 1 for Ar and Xe. Therefore, FBA is appropriate for He, but inadequate for Ar and Xe when the kinetic energy of the electron is 1 keV.

In order to confirm the conclusion reached above, I compared the differential cross sections calculated by FBA, and those by the partial wave analysis. Red lines in Fig. 16 show the differential cross sections for the scattering of 1 keV electrons which were adopted from Ref.

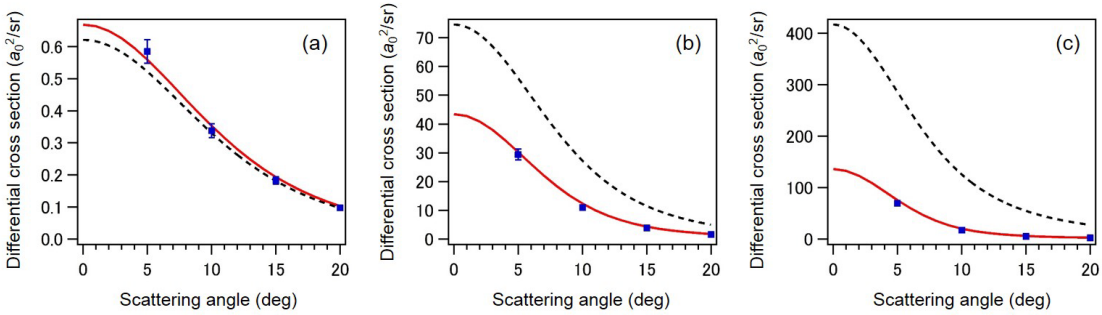

Figure 16: Differential cross section of elastic scattering of 1 keV electrons by He (a), Ar (b), and Xe (c). Red curves show the simulated differential cross sections obtained by the partial wave analysis [113]. Black curves show the differential cross sections obtained by the first Born approximation [118]. Blue squares show the experimental data. The experimental data of He and Ar are adopted from Ref. [119] and the data of Xe are adopted from Ref. [120]

[113]. The differential cross sections calculated by the FBA are shown by black broken lines. The differential cross sections in FBA were adopted from Ref. [118]. In the case of He (Fig. 16(a)), the two curves are almost identical and coincident with the experimental data shown by blue squares [119]. However, in the cases of Ar and Xe (Figs. 16(b) and (c)), the differential cross sections in FBA are much larger than those in partial wave analysis and experimental data [119, 120]. This clearly shows that FBA is not appropriate for the scattering of 1 keV electrons by Ar and Xe. In this study, CCl_4 (this chapter), Ar (this chapter), and Xe (Chapter 4) are used as samples. Because the value of J is larger than 1 even for the C atom ($Z = 6, J = 1.9$), the partial wave analysis is employed for obtaining the scattering amplitude.

I would like to note that even though the results of the partial wave analysis reproduces the experimental data as shown in Fig. 16, there are two effects which are not included in the partial wave analysis: the exchange effect and the polarization effect [121]. The exchange effect is originating from the exchange between the incoming electron and atomic electron. Because it has been known that the exchange rarely occurs when the kinetic energy of the electron is much higher than binding energies of atomic electrons, the exchange effect is not important in this study. The polarization effect is originating from the distortion of the electron cloud of the target atom induced by the incoming electron. It has been known that the polarization effect enhances the intensity of the scattered electrons at small scattering angles [122, 123]. Although the the results of the partial wave analysis agree well with the experimental data at $\theta = 5^\circ$ (Fig. 16), the polarization effect may cause significant effect at the scattering angle less than 5°.

3.1.3 Angular distribution of electrons scattered by gas-phase molecules

In this subsection, the elastic scattering of electrons by gas-phase molecules is considered. The scattering potential of a molecule is represented by

$$V_{\rm mol}(\boldsymbol{r}) = -\frac{1}{4\pi\epsilon_0}\sum_{j=1}^{N}\frac{Z_j e^2}{|\boldsymbol{r}-\boldsymbol{r}_j|} + \frac{e^2}{4\pi\epsilon_0}\int\frac{\rho_{\rm mol}(\boldsymbol{r}')}{|\boldsymbol{r}-\boldsymbol{r}'|}{\rm d}\boldsymbol{r}', \tag{3.16}$$

where N is a number of atoms in the molecule, Z_j is an atomic number of the j-th atom, $\boldsymbol{r}_j$ is a position vector of nucleus of the j-th atom, and $\rho_{\rm mol}(\boldsymbol{r})$ is an electron density distribution of the molecule. In order to derive a simple formula which provides the angular distributions of scattered electrons, I employ the assumption called independent atom model (IAM) [10]. In IAM, the electron density distribution of the molecule is assumed to be given by the sum of the electron density distributions of free atoms,

$$\rho_{\rm mol}(\boldsymbol{r}) = \sum_{j=1}^{N}\rho_{{\rm atom},j}(\boldsymbol{r}-\boldsymbol{r}_j). \tag{3.17}$$

Then, the scattering potential is given by the sum of the scattering potential of atoms which constitute the molecule,

$$V_{\rm mol}(\boldsymbol{r}) = \sum_{j=1}^{N}V_{{\rm atom},j}(\boldsymbol{r}-\boldsymbol{r}_j). \tag{3.18}$$

Therefore, under the assumption of IAM, the wavefunction of the electrons scattered by the molecule is given by the sum of the wavefunctions of electrons scattered by the atoms whose nucleus are located at $\boldsymbol{r}_j (j = 1, 2, \cdots N)$.

In order to derive the differential cross section in IAM, the wavefunction of electrons at a detector is considered. It has been known that the wavefunction of electrons far from the scattering point is given by the sum of a plane wave and a spherical wave [70],

$$A\Big(\exp({\rm i}\frac{\boldsymbol{p}_{\rm i}}{\hbar}\cdot\boldsymbol{r}) + f\frac{\exp({\rm i}\boldsymbol{p}_{\rm f}\cdot\boldsymbol{r}/\hbar)}{|\boldsymbol{r}|}\Big), \tag{3.19}$$

where A is a constant. When the origin of the scattering potential is shifted by $\boldsymbol{R}$, the wavefunction becomes

$$\begin{aligned} & A\Big(\exp({\rm i}\frac{\boldsymbol{p}_{\rm i}}{\hbar}\cdot(\boldsymbol{r}-\boldsymbol{R})) + f\frac{\exp({\rm i}\boldsymbol{p}_{\rm f}\cdot(\boldsymbol{r}-\boldsymbol{R})/\hbar)}{|\boldsymbol{r}-\boldsymbol{R}|}\Big) \\ \simeq\ & A\Big(\exp({\rm i}\frac{\boldsymbol{p}_{\rm i}}{\hbar}\cdot(\boldsymbol{r}-\boldsymbol{R})) + f\frac{\exp({\rm i}\boldsymbol{p}_{\rm f}\cdot(\boldsymbol{r}-\boldsymbol{R})/\hbar)}{|\boldsymbol{r}|}\Big). \end{aligned} \tag{3.20}$$

Because the phase of the plane wave at the detector should not be changed by the position of the

potential, this wavefunction should be re-written as

$$A'\Big(\exp(\mathrm{i}\frac{\boldsymbol{p}_\mathrm{i}}{\hbar}\cdot\boldsymbol{r})+f\exp(\mathrm{i}\boldsymbol{s}\cdot\boldsymbol{R})\frac{\exp(\mathrm{i}\boldsymbol{p}_\mathrm{f}\cdot\boldsymbol{r}/\hbar)}{|\boldsymbol{r}|}\Big). \tag{3.21}$$

This formula shows that the phase of the scattering amplitude is shifted by $\exp(\mathrm{i}\boldsymbol{s}\cdot\boldsymbol{R})$ when the origin of the scattering potential is shifted by $\boldsymbol{R}$ [124]. Consequently, the differential cross section of the electrons scattered by molecules is given by

$$\begin{aligned}\frac{\mathrm{d}\sigma_\mathrm{el}}{\mathrm{d}\Omega} &= \Big|\sum_{j=1}^{N} f_j(\theta)\mathrm{e}^{\mathrm{i}\boldsymbol{s}\cdot\boldsymbol{r}_j}\Big|^2 \\ &= \sum_{j=1}^{N}|f_j(\theta)|^2+\sum_{j=1}^{N}\sum_{k=1(k\neq j)}^{N} f_j(\theta)f_k^*(\theta)\mathrm{e}^{\mathrm{i}\boldsymbol{s}\cdot\boldsymbol{r}_{j,k}},\end{aligned} \tag{3.22}$$

where f_j and f_k are the elastic scattering amplitudes of an electron by j-th and k-th atoms, $\boldsymbol{r}_{j,k}$ is defined by $\boldsymbol{r}_{j,k}=\boldsymbol{r}_j-\boldsymbol{r}_k$. In deriving above equations, the molecules are assumed to be rigid, i.e., the internuclear distances are fixed. When molecules are oriented randomly, the differential cross section becomes [10, 11],

$$\frac{\mathrm{d}\sigma_\mathrm{el}}{\mathrm{d}\Omega}=\sum_{j=1}^{N}|f_j(\theta)|^2+\sum_{j=1}^{N}\sum_{k=1(k\neq j)}^{N} f_j(\theta)f_k^*(\theta)\frac{\sin(sr_{jk})}{sr_{jk}}. \tag{3.23}$$

By using the expression of the complex scattering amplitude (Eq. (3.11)), the differential cross section is given by [125]

$$\frac{\mathrm{d}\sigma_\mathrm{el}}{\mathrm{d}\Omega}=\sum_{j=1}^{N}|f_j(\theta)|^2+\sum_{j=1}^{N}\sum_{k=1(k\neq j)}^{N}|f_j(\theta)||f_k(\theta)|\cos[\eta_j(\theta)-\eta_k(\theta)]\frac{\sin(sr_{jk})}{sr_{jk}}. \tag{3.24}$$

Because $\sin(sr_{jk})/sr_{jk}$ is an oscillatory function (known as the zeroth order spherical bessel function), the differential cross section shows a diffraction patterns which depend on the internuclear distance r_{jk}. Therefore, by analyzing the gas-phase electron diffraction (GED) pattern, the internuclear distances between atoms can be determined. Because the first term on the right-hand side of Eq. (3.24) does not contain the oscillatory function, it is called background intensity. On the other hand, the second term is called molecular scattering intensity.

When the distribution of the internuclear distances due to vibrations is taken into account, the differential cross section is given by [10, 11]

$$\frac{\mathrm{d}\sigma_\mathrm{el}}{\mathrm{d}\Omega}=\sum_{j=1}^{N}|f_j(\theta)|^2+\sum_{j=1}^{N}\sum_{k=1(k\neq j)}^{N}|f_j(\theta)||f_k(\theta)|\cos[\eta_j(\theta)-\eta_k(\theta)]\int P_{j,k}(r)\frac{\sin(sr)}{sr}\mathrm{d}r, \tag{3.25}$$

where $P_{j,k}(r)$ represents the distribution function of the internuclear distance between the j-th and k-th atoms. If $P_{j,k}(r)$ has a Gaussian distribution centered at $r_{j,k}$,

$$P_{j,k}(r) = \frac{1}{\sqrt{2\pi l_{j,k}^2}} \exp\Big(-\frac{(r-r_{j,k})^2}{2l_{j,k}^2}\Big), \tag{3.26}$$

it follows that

$$\begin{aligned} \frac{\mathrm{d}\sigma_{\mathrm{el}}}{\mathrm{d}\Omega} &= \sum_{j=1}^{N} |f_j(\theta)|^2 + \sum_{j=1}^{N} \sum_{k=1(k\neq j)}^{N} |f_j(\theta)||f_k(\theta)| \\ &\times \cos[\eta_j(\theta) - \eta_k(\theta)] \exp\Big(-\frac{l_{j,k}^2}{2} s^2\Big) \frac{\sin[s(r_{j,k} - l_{j,k}^2/r_{j,k})]}{sr}, \end{aligned} \tag{3.27}$$

where $l_{j,k}$ denotes the width of the distribution, and is called mean amplitude. Because of the decay term $\exp[-l_{j,k}^2 s^2/2]$, the contribution of the interference term (second term in the right-hand side of Eq. (3.27)) becomes small at large scattering angles.

3.1.4 Determination of geometrical structure of molecules from GED patterns

In order to determine internuclear distances, the modified molecular intensity which is represented by $sM(s)$ are usually calculated from the observed angular distribution of the scattered electrons,

$$sM(s) = s\frac{I(\theta) - I_{\mathrm{B}}(\theta)}{I_{\mathrm{B}}(\theta)}, \tag{3.28}$$

where $I(\theta)$ is the angular distribution of the scattered electrons obtained by an experiment,

$$I(\theta) = N\frac{\mathrm{d}\sigma_{\mathrm{el}}}{\mathrm{d}\Omega}, \tag{3.29}$$

and I_{B} is the background intensity which is given by,

$$I_{\mathrm{B}}(\theta) = N\sum_{j=1}^{N} |f_j(\theta)|^2, \tag{3.30}$$

and N is a normalization constant. By substituting the first Born amplitude (Eq. (3.5)) into the definition of $sM(s)$, it follows that

$$sM(s) = \sum_{j=1}^{N} \sum_{k=1(k\neq j)}^{N} \mu_{j,k}(\theta) \int_0^\infty P_{j,k}(r) \frac{\sin(sr)}{r} \mathrm{d}r, \tag{3.31}$$

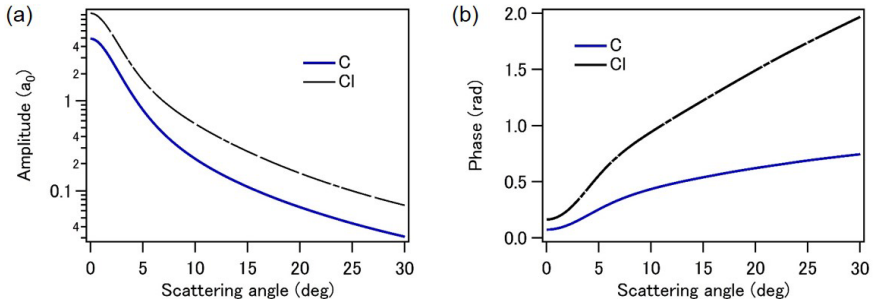

Figure 17: Atomic scattering amplitudes of C and Cl atoms. (a) The magnitudes of the scattering amplitudes. (b) The phases of the scattering amplitudes. The magnitudes and phases of the amplitudes are calculated at 20 keV electrons.

where

$$\mu_{j,k}(\theta) = \frac{(Z_j - A_j(\theta))(Z_k - A_k(\theta))}{\sum_m (Z_m - A_m(\theta))^2}. \tag{3.32}$$

If the dependence on θ (or s) in $\mu_{j,k}$ is neglected, $sM(s)$ simply becomes the Fourier transform of $P_{j,k}(r)/r$.

$$sM(s) = \sum_{j=1}^{N} \sum_{k=1(k\neq j)}^{N} \mu_{j,k} \int_0^\infty \frac{P_{j,k}(r)}{r} \sin(sr) \mathrm{d}r. \tag{3.33}$$

It is known that except small scattering angles, the θ dependence of $\mu_{j,k}$ can be neglected [126].

There are two methods to determine the geometrical structure of molecules from $sM(s)$: (i) least-square analysis and (ii) Fourier analysis. In the least-square analysis, parameters ($r_{j,k}$ and $l_{j,k}$) are determined through the least-square fitting of simulated $sM(s)$ to the experimental $sM(s)$. By this analysis, the parameters ($r_{j,k}$ and $l_{j,k}$) are determined with a resolution as high as 0.01 Å. The second method is the inverse Fourier transform of $sM(s)$. Because $sM(s)$ is given by the Fourier transform of $P_{jk}(r)/r$ (Eq. (3.33)), the inverse Fourier transform of $sM(s)$ gives

$$\begin{aligned} D(r) &= \int_0^\infty sM(s) \sin(sr) ds \\ &= \frac{\pi}{2} \sum_{j=1}^{N} \sum_{k=1(k\neq j)}^{N} \mu_{j,k} \frac{P_{j,k}(r)}{r}. \end{aligned} \tag{3.34}$$

The function $D(r)$ is called radial distribution function.

In order to show an example of the analysis introduced above, I conducted an analysis of the simulated GED pattern of CCl_4 by 20 keV electrons. The differential cross section of the elastic

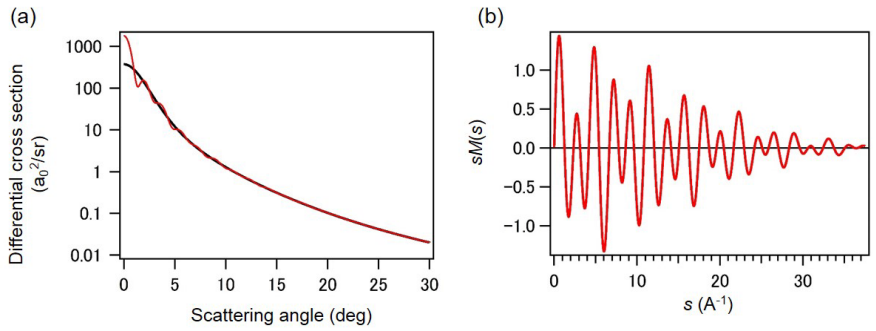

Figure 18: Simulated electron diffraction pattern of gas-phase CCl_4 by 20 keV electrons. (a) The angular distributions of the scattered electrons. Red curve shows the angular distribution calculated by Eq. (3.35). Black curve is the background intensity which was calculated by neglecting the interference terms. The scattering angle of 30° corresponds to $s = 37.5$ Å^{-1}. (b) The modified molecular intensity, $sM(s)$ of CCl_4 calculated by using the angular distributions in (a).

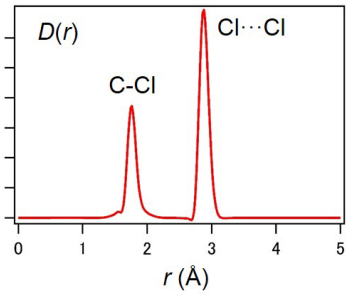

Figure 19: Radial distribution function of CCl_4 obtained by the inverse Fourier transformation of $sM(s)$ shown in Fig. 18(b).

scattering by CCl_4 is given by

$$\begin{aligned}\frac{d\sigma_{el}}{d\Omega} &= |f_C(\theta)|^2 + 4|f_{Cl}(\theta)|^2 \\ &+8|f_C(\theta)||f_{Cl}(\theta)|\cos(\eta_C(\theta)-\eta_{Cl}(\theta))\frac{\sin(sr_{C,Cl})}{sr_{C,Cl}}\exp\left(-\frac{l_{C,Cl}^2}{2}s^2\right) \\ &+12|f_{Cl}(\theta)|^2\frac{\sin(sr_{Cl,Cl})}{sr_{Cl,Cl}}\exp\left(-\frac{l_{Cl,Cl}^2}{2}s^2\right) \qquad (3.35)\end{aligned}$$

where f_C and f_{Cl} are the atomic scattering amplitudes of C and Cl atoms, η_C and η_{Cl} are the phases associated with the scattering amplitudes, $r_{C,Cl}$ is the internuclear distance between C and Cl atoms, $r_{Cl,Cl}$ is that between two Cl atoms, l_{C-Cl} and l_{Cl-Cl} are the mean amplitudes. The scattering amplitudes for 20 keV electrons are obtained by the ELSEPA code developed

Table 3: Structural parameters of CCl_4 at 295 K [127]. The numbers in parentheses are standard errors.

	C-Cl	Cl$\cdots$Cl
r_g	1.766(3)	2.888(3)
l_h	0.050(2)	0.070(1)

by Salvat *et al.* [128] in which the scattering amplitudes are calculated by the partial wave analysis. The magnitudes and phases of the scattering amplitudes are shown in Fig. 17. I adopted the structural parameters of CCl_4 reported by Morino *et al.* [127] (Table 3). By using these parameters, I obtained the GED pattern of 20 keV electrons shown in Fig. 18(a) by a red curve. Due to the background intensity ($|f_{\rm C}(\theta)|^2 + 4|f_{\rm Cl}(\theta)|^2$) shown by a black curve in Fig. 18(a), the interference pattern is rather unclear. By calculating the $sM(s)$, the interference pattern becomes much clearer than that in Fig. 18(a). The calculated $sM(s)$ is shown in Fig. 18(b). The amplitude of $sM(s)$ decays with an increase of s. This decay in oscillation amplitude is mainly due to the distribution of the internuclear distance represented by the term $\exp(-l^2s^2/2)$ in Eq. (3.35). By conducting an inverse Fourier transformation of $sM(s)$ according to Eq. (3.34), the radial distribution function of CCl_4 was obtained. The calculated radial distribution function shown in Fig. 19 shows two peaks which correspond to the internuclear distances between C and Cl atoms, and two Cl atoms. The width of each peak is determined by two factors: the mean amplitude l and the range of s used for the Fourier transformation. When the range of s is represented by Δs, the distribution should have a width of $2\pi/\Delta s$. Therefore, in order to determine the mean amplitudes from the Fourier analysis, the range of s should be large enough to make $2\pi/\Delta s$ smaller than the mean amplitudes.

3.2 Time-resolved electron diffraction

Recent development in technologies to generate ultrashort electron pulses made it possible to measure the laser-induced ultrafast structural changes induced in gas-phase molecules and solid samples though the diffraction of ultrashort electron pulses (Fig. 20). The progress of the ultrafast electron diffraction is summarized in review papers [40, 129–135] and books [136–138].

In this section, I briefly introduce the pioneering works and recent progress on the ultrafat electron diffraction. Then, I discuss the temporal resolution of the ultrafast electron diffraction.

3.2.1 Electron diffraction by ultrashort electron pulses

Since the first observation of the electron diffraction patten by crystals in 1927 [139] and gas-phase molecules in 1930 [140], the electron diffraction has been a standard method to determine the structure of crystals and isolated molecules. The studies on the time-dependent structural changes using electron diffraction began in 1980s. The first observation of the electron diffrac-

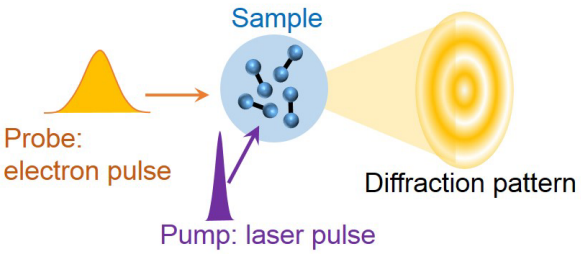

Figure 20: Schematic of the ultrafast electron diffraction method with ultrashort electron pulses. Molecules are excited by an ultrashort laser pulse. The changes in molecular structure are probed by the diffraction of an ultrashort electron pulse.

tion pattern by short electron pulses were reported by Mourou and Williamson in 1982 [39]. They observed the transmission electron diffraction pattern of an Al thin foil by 100 ps electron pulses. The short electron pulse was generated by illuminating a photocathode with a short UV laser pulse. In 1983, Ischenko *et al.* reported the construction of the pioneering experimental apparatus for measurement of time-resolved GED patterns [136, 141]. In their apparatus, the electron pulses were generated by chopping the continuous wave electron beam with an electromagnetic chopper. In the next year, Williamson and Mourou performed the time-resolved electron diffraction experiment with the short electron pulses generated from the photocathode-type electron gun [142]. They studied the laser-induced melting of an Al thin foil with 20 ps electron pulses.

In 2000s, the temporal resolution of the ultrafast electron diffraction for thin solid samples improved to hundreds of femtoseconds. With the femtosecond or picosecond temporal resolutions, the ultrafast electron diffraction had been used to investigate ultrafast phenomena induced in solid samples such as laser induced heating and melting [143–147], phase transitions [148–152], lattice oscillation [153], and photochemical reactions [154]. Recently, electron pulse compression technique has successfully been employed in the ultrafast electron diffraction experiments. By compressing a high density electron pulse, one can obtain a bright femtosecond electron pulse which can be used for recording a diffraction pattern in a single shot [155–157]. The single-shot measurement is useful for studying irreversible processes [133]. By compressing a single-electron pulse (≤ 1 electron/pulse), the duration of the electron pulse can be as short as attoseconds [158–161]. The attosecond electron pulses can be used for recoding electron motions with unprecedented spatiotemporal resolutions (attosecond and 0.01 Å) [38, 162].

The ultrafast electron diffraction method with ultrashort electron pulses has also provided valuable insights into the ultrafast dynamics of gas-phase molecules [40]. In 1992, Ewbank *et al.* and Williamson *et al.* reported the development of the time-resolved GED technique which uses the short electron pulses generated from the photocathode-type electron gun [163, 164]. The ultrafast GED had been used to determine the molecular structures in photochemical reactions

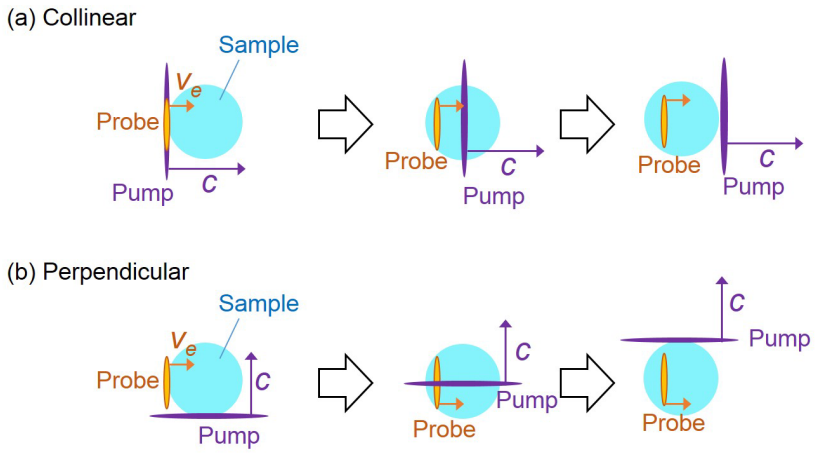

Figure 21: Illustration of the velocity mismatch effect. The pulses shown in purple are the pump laser pulses. The pulses shown in orange are the probe electron pulses. c and v_e represent the speed of light and electron, respectively. Because of the difference in velocity, the delay between the pump and probe pulses is blurred.

[165–167] and to probe the laser induced molecular alignment processes [168–170] with 0.01 Å spatial resolution. However, because of the velocity mismatch effect which is discussed in the next subsection, the temporal resolution in GED is limited to 1 ps, even though femtosecond electron pulses are employed. Therefore, the motion of atoms in a gas-phase molecule cannot be probed in real-time by the ultrafast GED method with ultrashort electron pulses.

3.2.2 Velocity mismatch effect

The temporal resolution of the laser-pump, electron-probe experiment is given as follows [171],

$$\tau = \sqrt{\tau_\mathrm{l}^2 + \tau_\mathrm{e}^2 + \tau_\mathrm{VM}^2}, \tag{3.36}$$

where τ is the overall temporal resolution, τ_l is a temporal duration of the pump laser pulse, τ_e is a temporal duration of the probe electron pulse, and τ_VM is the velocity mismatch effect between the laser and the electron pulses. The schematic of the velocity mismatch effect is shown in Fig. 21. Due to the difference in velocities, the delay time between the pump laser pulse and the probe electron pulse changes depending on the position on the sample. In both of the collinear (Fig. 21(a)) and perpendicular (Fig. 21(b)) arrangements, the molecules located on the left-hand side of the sample experience the almost zero delays. On the other hand, the molecules located on the right-hand side of the sample experience large delays. The velocity mismatch effect depends on the thickness of the sample. When the thin (≤ 100 nm) solid sample is used, the velocity mismatch effect is much shorter than 1 fs, and the temporal resolution is

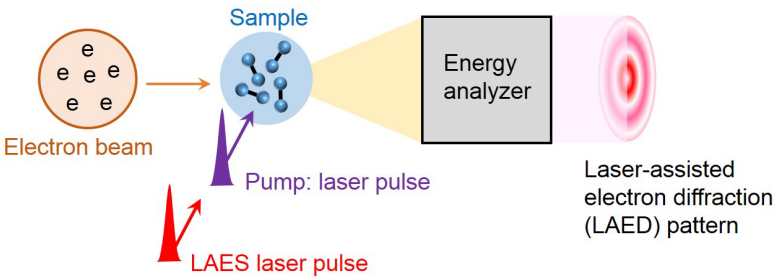

Figure 22: Schematic of the LAED method. A laser pulse (purple) is used to excite the molecular samples. The changes in molecular structure is probed by the LAES process. The LAES process is induced by the laser pulse shown in red. The kinetic energy of the scattered electrons are resolved by the energy analyzer. The electron diffraction pattern of the electrons whose energies are shifted by $nh\nu(n \neq 0)$ carries the information of molecular structure only in the presence of the laser pulse shown in red.

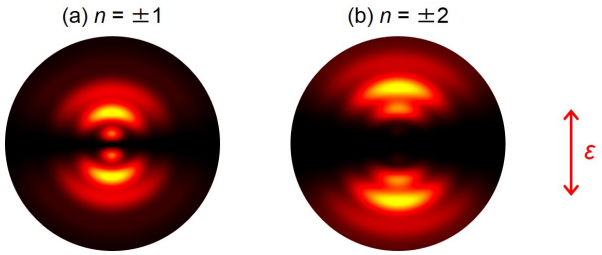

Figure 23: Simulated laser-assisted electron diffraction patterns of CCl_4 with the kinetic energy shift of $nh\nu$. The kinetic energy of the electron is 10 keV. The maximum scattering angle is 14°. The laser polarization direction is represented by $\boldsymbol{\epsilon}$. The Kroll-Watson approximation is adopted for the simulation. The parameters used for this simulation are same as the experimental conditions of this study.

mainly determined by the temporal durations of the laser pulse (τ_{l}) and the electron pulse (τ_{e}). However, in the case of the gas-phase samples, the velocity mismatch effect has a significant effect on the temporal resolution. According to the calculations by Williamson and Zewail [171], the resolution degradation caused by the velocity mismatch effect is larger than 1 ps under a typical experimental condition of the ultrafast GED method. Therefore, even though the ultimately short laser and electron pulses are employed, the temporal resolution of the ultrafast GED cannot be shorter than 1 ps. Even though it has been known that the velocity mismatch effect can be suppressed by using the relativistic electron pulses [172–176] or the pulse-front-tilted laser pulses [177, 178], the femtosecond temporal resolution has not been achieved yet.

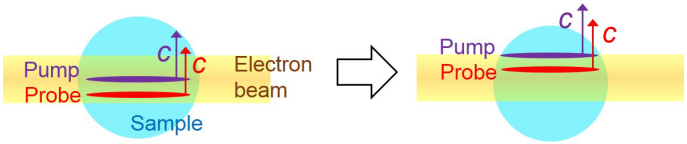

Figure 24: Velocity mismatch effect in LAED method. Because the LAES process occurs only in the presence of the probe laser pulse (shown in red), the velocity mismatch effect vanishes when the pump and probe laser pulses are introduced collinearly.

3.3 Laser-assisted electron diffraction

In order to achieve the femtosecond temporal resolution in GED, we proposed a method called laser-assisted electron diffraction (LAED) [44]. The schematic of the LAED method is shown in Fig. 22. As in the case of the ultrafast GED method with ultrashort electron pulses, the gas-phase molecules are excited by an ultrafast laser pulse (shown by purple in Fig. 22). However, the structural changes in molecules are probed by the LAES process induced by another ultrashort laser pulse (shown by red in Fig. 22). By using an electron energy analyzer, we record the LAED patterns, i.e., the GED patterns appearing in the angular distribution of the LAES signals whose kinetic energies are shifted by $nh\nu(n = \pm 1, \pm 2, \cdots)$ from the kinetic energy of incoming electrons. Simulated LAED patterns of CCl_4 are shown in Fig. 23. The intensity of the LAED pattern depends on the polarization direction of the laser field ($\boldsymbol{\epsilon}$). The advantages of the LAED method are (i) high temporal resolution as short as the laser pulse durations ($\leq$ 10 fs), (ii) ultrashort electron pulses are not prerequisite, and (iii) high spatial resolution ($\sim$0.01 Å).

Because the LAES process is induced only in the presence of the laser pulse (shown by red in Fig. 22), the velocity mismatch effect vanishes when we introduce the pump laser pulse and the laser pulse for LAED collinearly (Fig. 24). Therefore, the temporal resolution of the LAED method is given by

$$\tau = \sqrt{\tau_{\mathrm{l,pump}}^2 + \tau_{\mathrm{l,probe}}^2}, \tag{3.37}$$

where $\tau_{\mathrm{l,pump}}$ and $\tau_{\mathrm{l,probe}}$ are the temporal durations of the pump laser pulse and probe laser pulse for inducing the LAES process, respectively. The temporal resolution of the LAED method is the same as that of laser pulse pump/laser pulse probe experiments, and does not depend on the electron pulse duration. The LAED method does not require the ultrashort electron pulses, and in principle, can be performed by cw electron beams. Because the ultrashort laser pulses whose durations are less than 10 fs are currently avaivable [179–181], the temporal resolution of the LAED method can be as short as 10 fs.

The LAES process can also be induced by the pump laser pulse (purple pulse in Fig. 22). However, it has little effect on the measurement of the LAES signals induced by the probe laser pulse (red pulse in Fig. 22) when the wavelength of the pump laser pulse is shorter than that of the probe laser pulse. If the wavelength of the pump and probe laser pulses are different,

the LAES signals induced by the pump laser pulse can be distinguishable from those induced by the probe laser pulse according to the energy shift of the scattered electrons. Furthermore, because the signal intensity of the LAES n-photon process is proportional to the $4n$-th power of the wavelength (λ^{4n}, Eq. (2.24)), the intensity of the LAES signals induced by the pump laser pulse can be negligibly small. The condition that the wavelength of the pump laser pulse is shorter than that of the probe laser pulse is usually fulfilled in the laser pump/LAED probe experiment. This is because the visible or ultraviolet laser pulses are usually used for initiating chemical reactions, and the high power near-infrared laser pulses from the Ti:sapphire lasers ($\lambda \sim 0.8\mu$m) or the femtosecond fiber lasers ($\lambda \sim 1\mu$m) are appropriate for inducing LAES processes.

The spatial resolution of the LAES method is the same as that of the GED method with cw- and pulsed-electrons. According to KWA which has been known to provide quantitatively accurate differential cross section of the LAES process, LAED patterns are given by the product of the square of the Bessel function and the field-free elastic differential cross section (Eq. (2.36)). Because the Bessel function does not depend on molecular species, the Bessel function can be determined both numerically and experimentally without the information on the geometrical structure of molecules. Therefore, from the LAED pattern, one can obtain the field-free elastic differential cross section which is measured by the GED methods cw- and pulsed-electrons. The spatial resolution of the LAED method is independent of the laser pulse durations. In the LAED method, the kinetic energy and the scattering angle of the scattered electrons are recorded. If we use the ultrashort laser pulses for the measurement of the LAED patterns, the kinetic energy of the scattered electrons are blurred due to the uncertainty between the time and energy. However, the angular distribution is independent of the laser pulse duration, and is not blurred. Therefore, the spatial resolution is not affected by the laser pulse durations, and the LAED pattern observed at a kinetic energy provides the instantaneous geometrical structure of molecules with 0.01 Å resolution which has been achieved in the GED methods with cw- and pulsed-electron beams. Because geometrical structures of gas-phase molecules (and clusters) which contain more than 20 atoms have been determined by the GED method with cw-electron beams [182–184], the LAED method can be used to probe ultrafast nuclear motions in the large molecules.

3.4 Purpose and abstract of this work

As discussed in Section 2.2, most of the conventional LAES experiments were conducted using slow electrons ($\leq$ 76 eV) and rare gas atoms. Therefore, the LAED pattern has not been observed yet. In this study, the LAED pattern is observed for the first time by measuring the angular distribution of the LAES signals of 1 keV electrons scattered by gas-phase CCl_4 in a femtosecond laser field (τ = 520 fs, $I = 6 \times 10^{11}$ W/cm^2). The sample (CCl_4) and the duration of the laser pulse (τ = 520 fs) were chosen in order to observe unambiguous electron diffraction patterns in the angular distribution of the LAES $n = \pm 1$ processes. Through the analysis of the observed LAED pattern, I show that the instantaneous geometrical structure can be determined

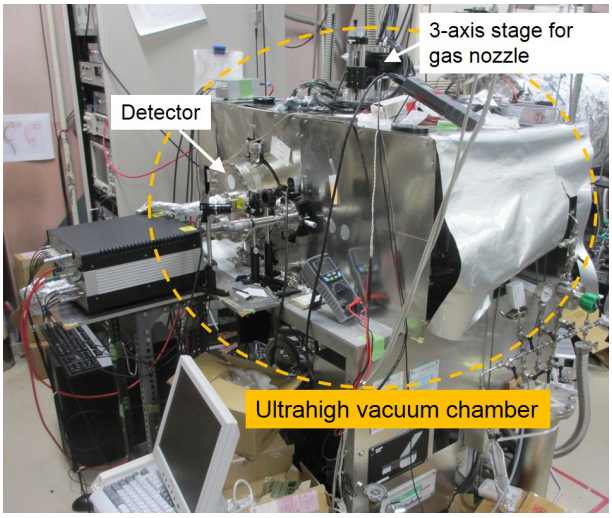

Figure 25: Photograph of the ultrahigh vacuum chamber developed for the first observation of LAED patterns.

by the LAED method.

3.5 Experimental set-up

In this section, the experimental apparatus used for the observation of the LAED patterns is introduced. The apparatus is composed of an ultrahigh vacuum chamber and a femtosecond laser system. The appearance of the ultrahigh vacuum chamber is shown in Fig. 25. The chamber is surrounded by μ-metal plates for shielding the chamber from the earth magnetic field. The inner surface of the chamber is also covered by μ-metal plates for the magnetic field shielding. The schematics of the apparatus is shown in Fig. 26. A electron gun, a gas-nozzle, a beam monitor, a toroidal energy analyzer, and a detector are placed inside the ultrahigh vacuum chamber. The photocathode-type electron gun generates a pulsed electron beam. The kinetic energy and the pulse duration of the electron beam are 1 keV and $\sim$15 ps, respectively. The electron beam monitor is used for measuring the spatial profile of the electron beam and for securing the spatio-temporal overlap for the electron beam and the laser beam. The electron beam crosses both a molecular beam and a laser beam. The molecular beam is introduced continuously through the nozzle. The electrons scattered by molecules are skimmed by a slit placed in front of the toroidal energy analyzer. The kinetic energy distribution and the angular distribution of the scattered electrons are resolved by the analyzer. All the components except the laser system and the detector are designed and made in our group. In what follows, the details of each components are described.

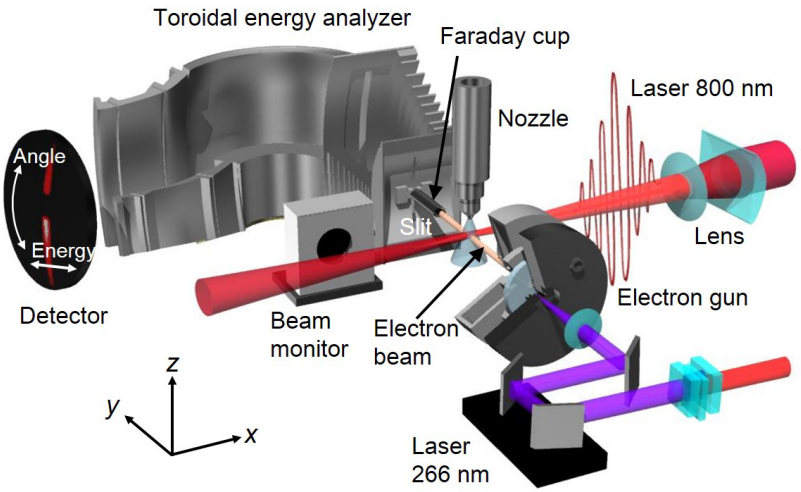

Figure 26: Schematic of the femtosecond-LAED apparatus

3.5.1 Laser system

In this study, we use the custom-made Ti:sapphire femtosecond laser system (Pulser 5000, Amplitude Technologies). This laser system adopts the chirped pulse amplification (CPA) scheme [185]. Figure 27 shows the schematic of the CPA laser system. The CPA laser system is composed of mainly four parts: oscillator, stretcher, amplifier, and compressor. In the CPA laser system, an ultrashort laser pulse is generated by a laser oscillator. Then, the duration of the laser pulse is elongated by a stretcher. After being stretched, the laser pulse is amplified by a series of amplifier. Finally, the amplified laser pulse is compressed to an ultrashort duration. The elongation of the laser pulse duration before the amplification reduces the peak intensity of the laser pulse, and prevents the laser crystals used for the amplification from being damaged.

Our laser system generates the $\geq$1 mJ laser pulses at a repetition rate of 5 kHz. The spectrum of the output pulses is shown in Fig. 28(a). The center wavelength is 800 nm ($h\nu$ = 1.55 eV), and the full-width of half maximum (FWHM) is 27 nm. The shortest laser pulse duration is $\sim$30 fs. In what follows, I explain the details of our laser system.

Oscillator

Figure 29 shows the schematics of the laser oscillator (Femtosource Scientific 20, Femtolasers Produktions GmbH). A cavity is composed of a mirror and an output coupler. Inside the cavity, a Ti:sapphire crystal is installed at a Brewster's angle. The chirped dispersive mirrors are used

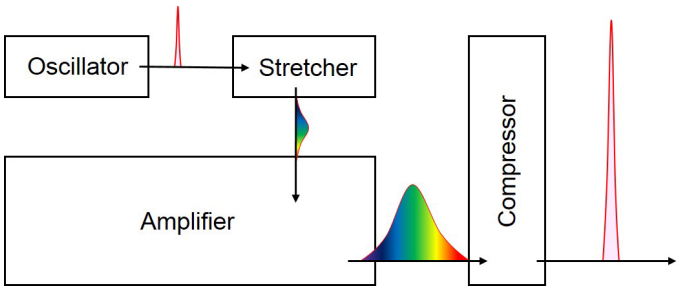

Figure 27: Schematic of the CPA laser system. An ultrashort laser pulse generated by an oscillator is stretched by a stretcher to prevent the damages to the laser crystals in the amplifier. The stretched pulse is amplified and then compressed to an ultrashort intense laser pulse.

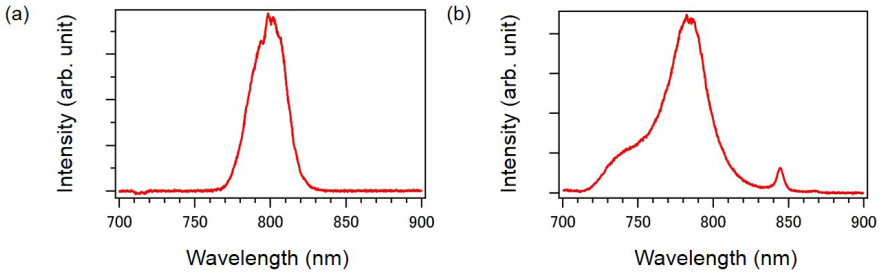

Figure 28: Spectra of laser pulses. (a) The spectrum of the laser pulses after the pulse compressor. (b) The spectrum of the output of the oscillator.

to compensate the dispersion generated in the cavity [186]. The 532 nm laser beam (4.2 W, continuous beam) from the Verdi V5 (Coherent Inc.) is used to pump the Ti:sapphire crystal. The optical Kerr effect induced in the Ti:sapphire crystal results in the generation of ultrashort laser pulses (Kerr lens mode locking) [187]. The output power of the oscillator is 350 mW at a repetition rate of 75 MHz. The spectrum is shown in Fig. 28(b). The center wavelength is 780 nm, and spectral width is 35 nm (FWHM).

Stretcher

The output of the oscillator is introduced into the pulse stretcher. The schematics of the pulse stretcher is shown in Fig. 30. This type of stretcher is called Öffner triplet which is composed only of reflective optics: a concave mirror, a convex mirror and a grating [188]. By using the equations in Ref. [189, 190], the group delay dispersion induced by the stretcher is calculated to be 3.7×10^6 fs^2. When the pulse duration of the output of the oscillator is 40 fs, the pulse duration is elongated to 260 ps by the stretcher. After passing the stretcher, the laser pulse is introduced into the Faraday isolator and acousto-optic programmable dispersive filter (AOPDF) [191]. The Faraday isolator is used to remove the laser pulses reflected by the optics in the amplifier. The

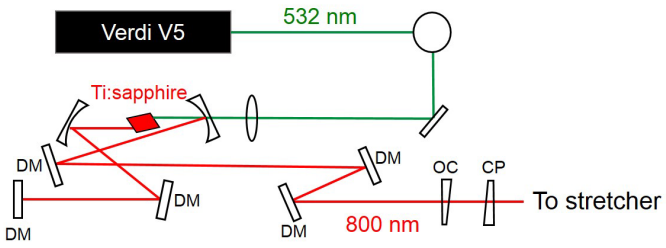

Figure 29: Schematic of the oscillator. A Ti:sapphire crystal is pumped by a cw laser beam. DM: dispersive chirped mirror. OC: output coupler, CP: wedge plate.

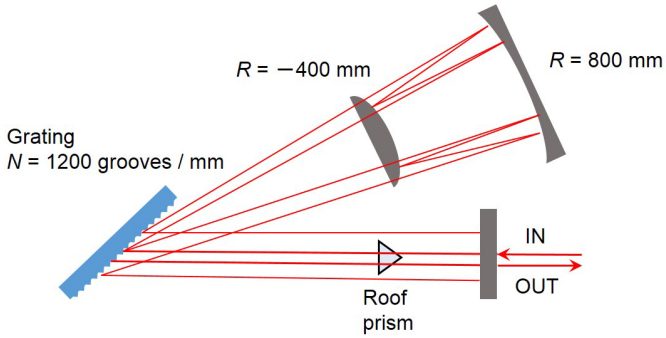

Figure 30: Schematic of the Öffner type pulse stretcher. The laser pulse diffracted by the grating is reflected by the concave and convex lens and returns back to the grating. Because the stretcher is composed of reflective optics, the chromatic aberration is not induced.

removal of the reflected laser light is necessary to keep the oscillator stable. AOPDF (Dazzler, Fastlite Inc.) is a tool for shaping the spectral phase and amplitude of the laser pulse. AOPDF takes advantages of the diffraction of a light by an acoustic wave in a uniaxial birefringent crystal [192]. The spectral phase and amplitude of the laser pulse is controlled by introducing a programmed acoustic wave into the crystal. In our experiment, AOPDF is used to cancel the higher order dispersions induced by the amplifier.

Amplifier

The amplification stage consists of a regenerative amplifier, a two-pass preamplifier, and a multipass amplifier (Fig. 31). A Ti:sapphire crystal in the regenerative amplifier is pumped by a part of the output from a Nd:YLF laser (λ =527 nm, 30 W, 5 kHz, DM20, Photonics Industries Inc.). The crystal is cooled by water (17 °C). By the combination of the Pockels cells and polarizers, laser pulses to be amplified are selected from the train of the laser pulses (75 MHz). The Pockels cell is a device which can rotate the polarization direction of the laser pulse depending on the voltage applied to it. The repetition rate of the output of the regenerative

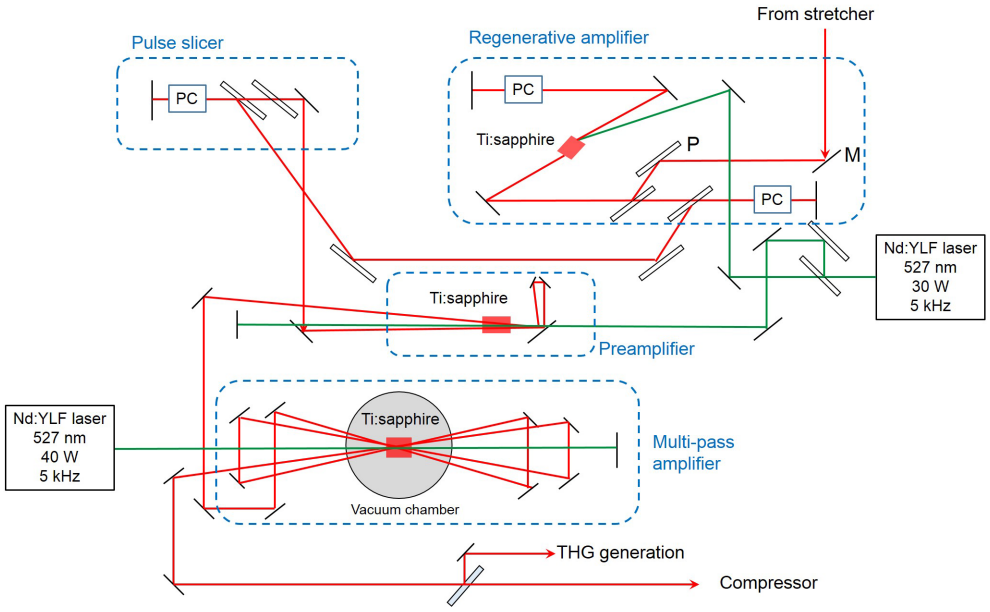

Figure 31: Schematic of the amplifier in the CPA laser system. The amplifier consists of the regenerative amplifier, the two-pass preamplifier, and the multipass amplifier. PC: pockels cell, P: polarizer, M: mirror.

amplifier is set to be 5 kHz. The output of the regenerative amplifier (0.3 mJ) is introduced into a pulse slicer. The pulse slicer transmits the laser pulse only when a transient voltage is applied to the pockels cell. Therefore, the contrast of the laser pulse, i.e., the intensity ratio between the the main laser pulse and the background laser light, is increased.

The laser pulse which transmits the pulse slicer is amplified by the two-pass preamplifier. The Ti:sapphire crystal is pumped by the Nd:YLF laser (DM20), and is cooled by water (17 °C). The energy of the laser pulse increases to 0.5 mJ. The laser pulse is further amplified by the 4-pass amplifier. A Ti:sapphire crystal is pumped by a Nd:YLF laser (λ =527 nm, 40 W, 5 kHz, DM30, Photonics Industries Inc.). The crystal is cryogenically cooled to -110°C. The energy of the laser pulse is increased to 2.2 mJ. After the amplification, a fraction of the laser pulse is split by a quartz plate. The split laser pulse is converted to the third order harmonics and used for the generation of electron pulses. The other part of the laser pulse enters the pulse compressor.

Compressor

As shown in Fig. 32, the pulse compressor is composed of a mirror and two gratings. The group delay dispersion (ϕ_2) induced by the compressor is given by [13, 193]

$$\phi_2 = -2 \times \frac{\lambda^3 l_g}{2\pi c^2 d^2}\left[1 - \left(\frac{\lambda}{d} - \sin\gamma\right)^2\right]^{-3/2}, \tag{3.38}$$

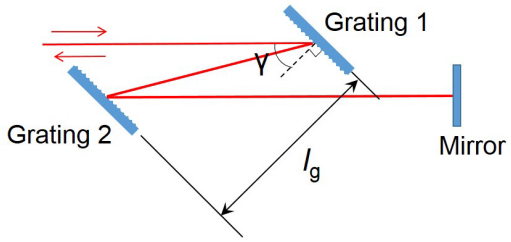

Figure 32: Schematic of the laser pulse compressor. γ: incident angle, l_g: distance between the gratings.

where l_g is a distance between the gratings, λ is a center wavelength of the laser pulse, d is a groove density of the gratings, c is the speed of light, and γ is a incident angle on the first grating. By substituting the values, l_g = 650 mm, λ = 800 nm, $d = 6.7 \times 10^4$ mm, γ = 45° into the above equation, the group delay dispersion of the compressor is determined to be -3.9×10^6 fs^2. This dispersion cancels the positive dispersion induced by the stretcher. Therefore, the amplified laser pulse is compressed to an ultrashort laser pulse. Because of the diffraction efficiency of the gratings, the pulse energy decreases to ∼1 mJ. One of the gratings (Grating 2 in Fig 32) is mounted on a high-precision motorized stage. The pulse duration of the laser pulse is adjusted by changing the distance between the gratings (l_g).

3.5.2 Layout of optics

The overall layout of optics used in this study is shown in Fig. 33. The output of the compressor (λ = 800 nm) is focused into a vacuum chamber by a combination of a cylindrical lens (f = 10000 mm) and a spherical lens (f = 400 mm). A method for the measurement of the focal diameter is described in Section 3.5.7. Between the two lenses, a half-waveplate is installed. The polarization direction of the laser beam can be controlled by rotating the half-waveplate.

An UV laser pulse used for producing the electron pulse is generated from the positively chirped laser pulse (τ ∼200 ps, λ = 800 nm) which is split before the pulse compressor. The advantage of using the chirped laser pulses is that the parameters of the generated UV laser pulses (pulse duration and intensity) does not change when the pulse duration of the compressed laser pulse is varied. The beam size of the chirped laser pulse is reduced by the combination of two lenses (f = 350 mm and f = −100 mm). The second order harmonic (λ = 400 nm) is generated by a BBO crystal (Type I, 8 mm (this chapter) and 500 μm (Chapter 4)). Then, the polarization of the 800 nm laser pulse is rotated by 90°. A 266 nm laser pulse is generated by the sum frequency generation at another BBO crystal (Type I, 200 μm thickness). The power of the 266 nm laser pulse is adjusted by rotating the half-waveplate for the 800 nm laser pulse. The intensity of the 266 nm laser pulse becomes maximum when the polarization direction of the 800 nm laser pulse is parallel to that of 400 nm, and minimum when the polarization directions of the two laser pulses are perpendicular with each other. The generated UV laser pulse passes

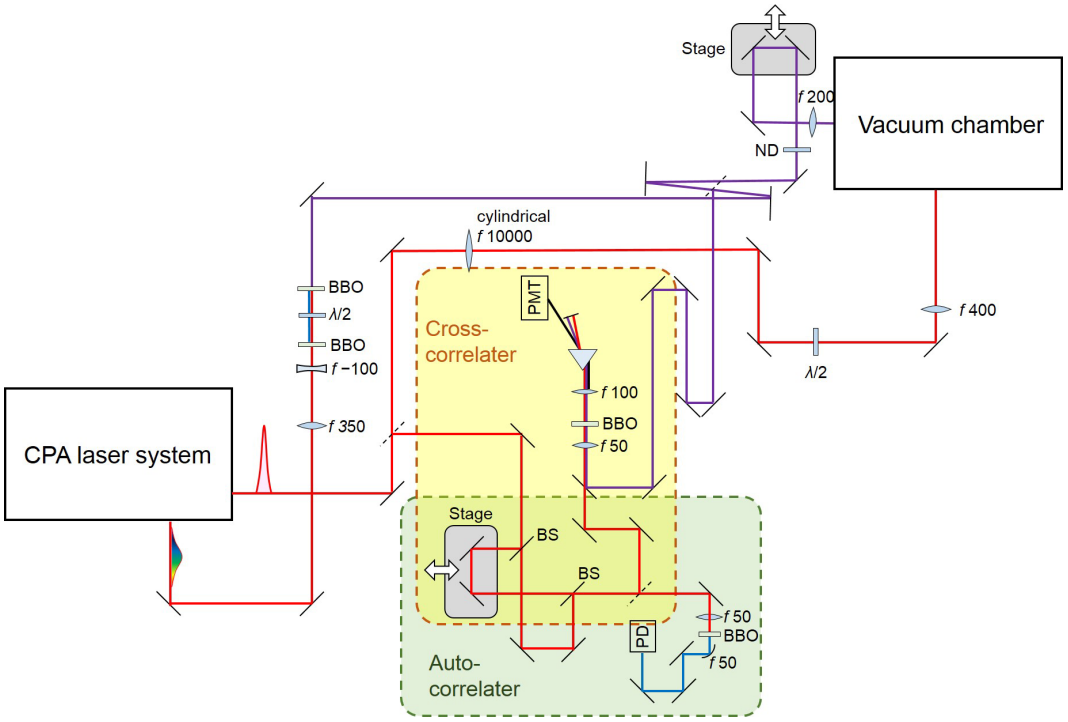

Figure 33: Overall layout of the optics. The compressed laser pulse is used to induce the LAES and LAED process. An un-compressed laser pulse is used to generate a third order harmonics which is used to generate the electron pulse. The auto-correlator (marked by the green box) is used to measure the duration of the 800 nm laser pulse. The cross-correlator (marked by the yellow box) is used to measure the duration of the third order harmonics. BS: beam splitter, PD: photodiode, $\lambda/2$: half-wave plate, ND: neutral density filter.

through an optical delay line. The delay time between the electron pulse and laser pulse at the scattering point is adjusted by this optical delay line. The UV laser pulse is focused onto the photocathode in an electron gun by a spherical lens (f = 200 mm).

3.5.3 Measurement of laser pulse duration

In this experiment, we use 800 nm laser pulse for inducing the LAES process and the 266 nm laser pulse for generating electron pulses. In this subsection, procedures for the measurement of the durations of 800 nm and 266 nm laser pulses are described.

Duration of the 800 nm laser pulse

The duration of the 800 nm laser pulse is measured by a scanning-type autocorrelator which I have constructed. In Fig. 34, a photograph of the autocorrelator is shown. An incoming laser pulse is split into two by a beam splitter. After reflected by two mirrors, the split laser pulses are

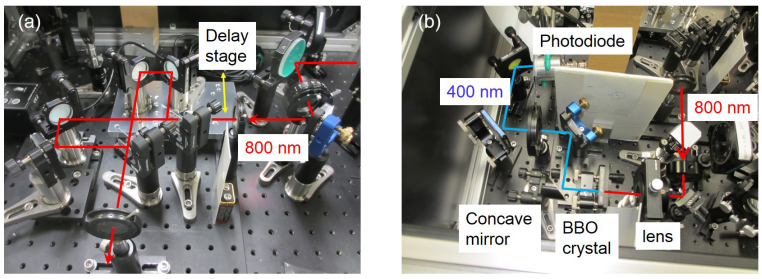

Figure 34: Pictures of the home-made autocorrelator for the pulse-duration measurement of the 800 nm laser pulse. (a) The picture of the interferometer. The laser pulse introduced into the interferometer is split into two by the beam splitter. The relative delay between the two laser pulses can be adjusted by the motorized optical delay stage. (b) The arrangement of optics for the second harmonic generation and its detection. The output of the interferometer is focused to the BBO crystal (10 μm thickness). The generated second order harmonics ($\lambda = 400$ nm) is detected by the photodiode.

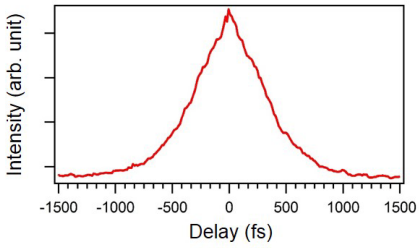

Figure 35: Autocorrelation trace of 800 nm laser pulse. The intensity of second harmonic is plotted as a function of the delay time between the two replicas of the 800 nm laser pulse.

re-combined by another beam splitter. Reflecting mirrors used in one of the two optical paths are mounted on a motorized stage. The delay time between the two pulses can be varied by the stage. The re-combined laser beam is focused onto a BBO crystal (10 μm thickness, Type I) by a spherical lens (f = 50 mm). The intensity of the generated second order harmonic (λ = 400 nm) is measured by a photodiode. The output signals of the photodiode are averaged by a boxcar integrator (SR250, Stanford Research Systems Inc.) and recorded by a PC through an AD converter. By measuring the pulse duration of the $\sim$ 40 fs laser pulses, I confirmed that the pulse duration measured by this autocorrelator is consistent with that measured by using a spectral phase interferometry for direct electric field reconstruction set-up (SPIDER [194], APE GmbH).

In Fig. 35, the measured intensity of the second order harmonic is plotted as a function of the delay time between the two pulses. The distribution width is 740 fs (FWHM). The intensity

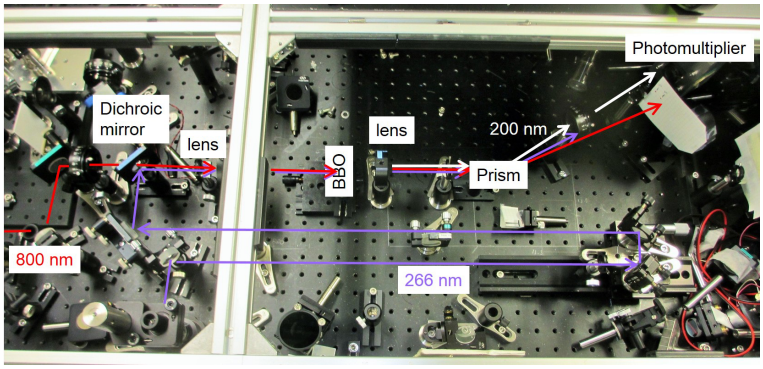

Figure 36: Picture of the home-made cross-correlator for the pulse-duration measurement of the 266 nm laser pulse. The 266 nm laser pulse and 800 nm laser pulse are combined by the dichroic mirror. Only when the 266 nm laser pulse and the 800 nm laser pulse is temporally overlapped, the 200 nm laser pulse is generated. The intensity of the 200 nm laser pulse is measured by the photomultiplier. The relative delay between the 266 nm laser pulse and the 800 nm laser pulse is scanned by using the delay stage shown in Fig. 34(a).

of the second order harmonic is given by [195]

$$I^{400}(\tau) \propto \int_{-\infty}^{\infty} I^{800}(t) I^{800}(t-\tau) \mathrm{d}t, \tag{3.39}$$

where τ is the delay time between two pulses and $I(t)$ represents the temporal profile of the laser pulse intensity. If the temporal profile of the laser pulse intensity is expressed by a Gaussian,

$$I^{800}(t) \propto \exp\Big(-4(\ln 2)\frac{t^2}{\tau_{800}^2}\Big), \tag{3.40}$$

then, the intensity of the second order harmonic is given by

$$I^{400}(\tau) \propto \exp\Big(-4(\ln 2)\frac{\tau^2}{(\sqrt{2}\tau_{800})^2}\Big). \tag{3.41}$$

Therefore, the pulse duration of the laser pulse can be determined by dividing the distribution width of $I^{400}(\tau)$ by $\sqrt{2}$. Because the distribution width of $I^{400}(\tau)$ is 740 fs (FWHM), the duration of the 800 nm laser pulse is 520 fs (FWHM). The uncertainty is estimated to be better than 50 fs for the 520 fs laser pulse.

Duration of the 266 nm laser pulse

The duration of the 266 nm laser pulse is measured by the cross-correlator which I have made (Fig. 36). The 266 nm and 800 nm laser pulses are collineary focused to the BBO crystal (40 μm thickness, Type I). When the two laser pulses are temporally overlapped on the BBO crystal, the

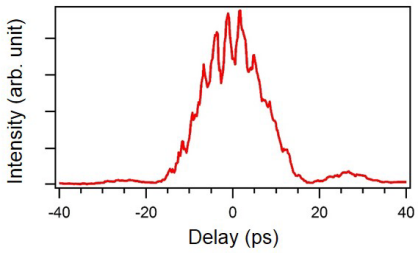

Figure 37: Cross correlation trace between 800 nm laser pulse and 266 nm laser pulse. The intensity of 200 nm laser pulse is plotted as a function of the delay time between the two pulses.

sum frequency generation process occurs, and a 200 nm laser pulse is emitted. The transmitted light is dispersed by the fused silica prism according to the wavelength. Only the 200 nm laser light is detected by the photomultiplier (R166UH, Hamamatsu Photonics). The output signals of the photomultiplier are averaged by the boxcar integrator. The delay time between the 800 nm laser pulse and the 266 nm laser pulse is varied by the a motorized optical stage installed in the autocorrelator discussed above.

In Fig. 37, the measured intensity of the 200 nm laser pulse is plotted as a function of the delay time between the two laser pulses. The distribution width is about 15 ps (FWHM). The intensity of the 200 nm laser pulse is given by

$$I^{200}(\tau) \propto \int_{-\infty}^{\infty} I^{266}(t) I^{800}(t-\tau) \mathrm{d}t, \tag{3.42}$$

where τ is the delay time between the two laser pulses, $I^{800}(t)$ and $I^{266}(t)$ are the temporal profile of the 800 nm and 266 nm laser pulse intensities, respectively. If these temporal profiles are expressed as

$$I^{800}(t) \propto \exp\Big(-4(\ln 2)\frac{t^2}{\tau_{800}^2}\Big), \tag{3.43}$$

$$I^{266}(t) \propto \exp\Big(-4(\ln 2)\frac{t^2}{\tau_{266}^2}\Big), \tag{3.44}$$

the intensity of the 200 nm laser pulse is given by

$$I^{200}(\tau) \propto \exp\Big(-4(\ln 2)\frac{\tau^2}{(\sqrt{\tau_{266}^2+\tau_{800}^2})^2}\Big). \tag{3.45}$$

Therefore, the distribution width of $I^{200}(\tau)$ is determined by $\sqrt{\tau_{266}^2+\tau_{800}^2}$. The pulse duration of the 800 nm laser pulse is $\tau_{800} = 520(50)$ fs (FWHM) which was determined above. Consequently, the duration of the 266 nm laser pulse is $\tau_{266} = 15$ ps (FWHM). The uncertainty is estimated to be better than 1 ps.

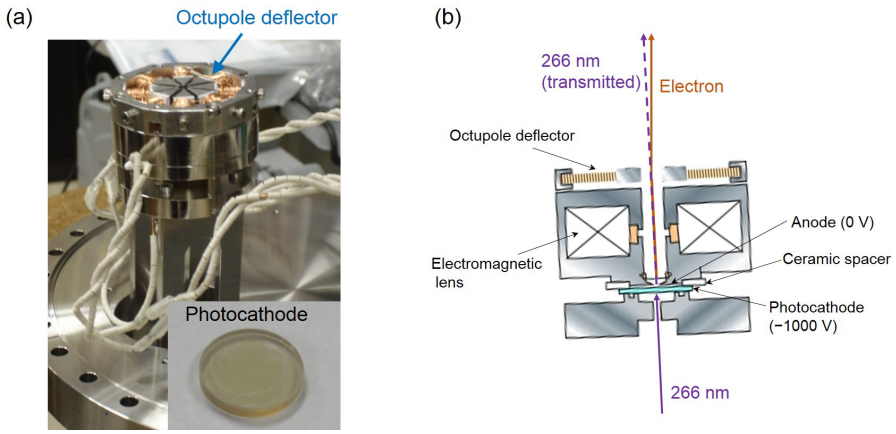

Figure 38: Photocathode-type electron gun. (a) The appearance of the electron gun. The electron gun is mounted on the vacuum flange. (b) The schematics of the electron gun. Electrons are generated by an irradiation of the 266 nm laser pulse on the surface of a photocathode. The electron gun is placed with a tilt angle of 3°. The traveling direction of the electron beam is controlled by the octupole deflector.

3.5.4 Electron gun and electron beam monitor

In this study, a photocathode-type electron gun is used to generate a pulsed electron beam. The kinetic energy of the electron beam is 1 keV. Even though tens of keV electrons are usually employed for recording GED patterns, the 1 keV electrons are used for the first observation of the LAED patterns. This is because discharges inside the electron gun and the analyzer are suppressed at lower voltages, and the detection efficiency of the detector for 1 keV electrons is higher than that for the tens of keV electrons. The duration of the pulsed electron beam is determined by the pulse duration of the UV laser pulse used for the generation of the laser pulse. As discussed in Section 3.3, ultrashort electron pulses are not prerequisite for the LAED experiment. The pulse durations of the electron beam are 15 ps (this chapter) and 19 ps (Chapter 4). The electron beam is monitored by an electron beam monitor.

Electron gun

Figures 38(a) and (b) show a photograph and a schematic of the cross section of the home-made photocathode-type electron gun, receptively. An electron pulse is generated through the photoelectric effect by an irradiation of the UV laser pulse on the surface of a photocathode. The photocathode was made by the evaporation of gold on a surface of a quartz plate. The thickness of the gold film is 10 nm. The energy width of the electrons generated by the gold photocathode is less than 0.4 eV, which is much narrower than that generated from a silver photocathode (0.7 eV) which we used in the previous studies [44, 69]. The number of electrons contained in an electron pulse is $\sim$100 which is small enough to neglect the energy and temporal broadening due to the space charge effect, i.e., the Coulomb repulsion between electrons. The generated elec-

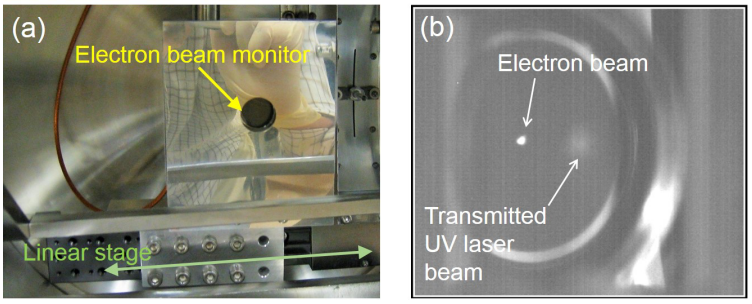

Figure 39: Electron beam monitor. (a) The picture of the electron beam monitor. The monitor is mounted on a linear stage. When the scattered electrons are measured by using the energy analyzer, the electron beam monitor is moved to the left side of the picture. (b) The image of the electron beam and transmitted ultraviolet laser beam measured by the electron beam monitor.

trons are accelerated to 1 keV by a static electric field applied between the cathode (-1000 V) and the anode (0 V). The distance between the cathode and the anode is 0.3 mm. The accelerated electron beam is skimmed by a pinhole ($\phi 0.5$ mm) and is focused by the electromagnetic lens. The focal point of the electron beam is located in the midway between the exit of the electron gun and the scattering point. This focusing condition was determined in order to achieve a high resolution of scattering angles on the detector [196].

A part of the UV light used for generating the electron pulse can transmit the photocathode. When the transmitted light enters the energy analyzer, electrons which become background signals are generated through the photoelectric effect on the surface of the analyzer. In order to prevent the transmitted UV light from entering the energy analyzer, the electron gun is placed with a tilt angle of 3° as shown in Fig. 38(b). The traveling direction of the electron beam is adjusted by an octupole electromagnetic deflector.

When the CCl_4 gas was introduced into the vacuum chamber, the number of electrons in the electron beam drastically decreased due to the adsorption of the CCl_4 on the surface of the photocathode. In order to suppress the adsorption, the electron gun was heated up by a resistive heater. Because the complete recovery of the number of generated electrons was observed at $\sim$ 360 K, the electron gun was kept at $\sim$ 370 K during the experiment.

Electron beam monitor

In order to measure the spatial profile of the electron beam, and to secure the spatio-temporal overlap between the electron, laser, and molecular beam, a home-made electron beam monitor was installed in the chamber. Figure 39 (a) shows a picture of the electron beam monitor. The monitor consists of the micro-channel plate (MCP) and a phosphor screen. The diameter of the MCP and the phosphor screen is 10 mm. The image of the electron beam on the phosphor screen is recorded by a CCD camera placed outside the vacuum chamber. An example of the image of the electron beam is shown in Fig. 39 (b).

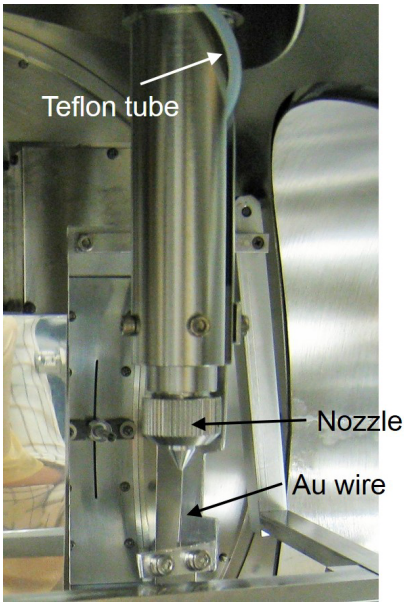

Figure 40: Appearance of the nozzle unit. The nozzle unit is mounted on a high-precision 3 axis stage (Fig. 25). A thin gold wire is mounted below the nozzle.

3.5.5 Nozzle

A picture of a home-made nozzle unit is shown in Fig. 40. The sample CCl_4 (purity $\geq$ 99.9 %, Kanto Chemical Co. Inc.) was degassed by the freeze-pump-thaw cycles. The sample gas is introduced continuously and effusively through the nozzle. The temperature of the sample is about 300 K. The diameter of the nozzle orifice is 0.5 mm. The electron beam and the laser beam cross 0.6 mm below the orifice of the nozzle. The density of the molecules at the scattering point can be determined by the equations [197],

$$\frac{n}{n_0} = \frac{1-\cos\theta}{2}, \tag{3.46}$$

$$\tan\theta = \frac{D}{2x}, \tag{3.47}$$

where n_0 is the density of molecules at the orifice, n is the density of molecules x mm below the orifice, D is the diameter of the orifice. Considering the backing pressure (about 1 Torr) of the sample gas, n_0 is estimated to be 4×10^{16} cm^{-3}. Then, by substituting the values, $n_0 = 4 \times 10^{16}$ cm^{-3}, $D = 0.5$ mm, $x = 0.6$ mm, into above equations, the density of molecules at the scattering point is obtained as $n = 1 \times 10^{15}$ cm^{-3}. Because the total cross section (including inelastic and ionizing scattering) of CCl_4 for 1 keV electron is 2.9×10^{-16} cm^2 [198], the scattering probability is 3 % when the distribution width of the sample is 1 mm. Therefore, the effect of the double scattering is negligibly small.

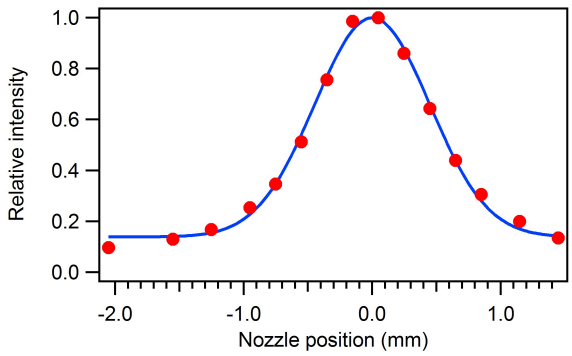

Figure 41: Measurement of the distribution width of the CCl_4 beam 0.6 mm below the nozzle orifice. The intensity of the elastically scattered electrons are plotted as a function of the position of the nozzle in the x direction. The vertical axis is normalized at the peak intensity. Red circles show the experimental data. Blue curve shows the result of the fitting using a Gaussian.

The nozzle unit is mounted on a 3-axis stage (Fig. 25). The distribution width of the sample gas is determined by measuring the signal intensity of the elastic scattering while scanning the position of the nozzle unit along the x-axis (Fig. 26). The result of the measurement is shown in Fig. 41 as red circles. The obtained distribution is well approximated by a Gaussian distribution (blue solid line) whose width is 1.05 mm (FWHM) with an offset of 14 %. The offset originates from the elastic scattering by a residual gas, i.e., the CCl_4 molecules outside the molecular beam. Because the LAES process occurs only where the laser and electron beams are overlapped, the residual gas does not contribute to the LAES signals.

A gold thin wire ($\phi 100$ μm) is mounted 24 mm below the nozzle orifice (Fig. 40). The wire is used for securing the spatio-temporal overlap between the laser and electron beams. Because the the wire is far below the nozzle (24 mm), the wire does not affect the measurement of the LAES process.

3.5.6 Spatio-temporal overlap of three beams: electron beam, laser beam, and molecular beam

In order to observe the LAES process, the spatio-temporal overlap between the laser beam, the electron beam, and the molecular beam should be achieved. Because the molecular beam is introduced continuously and the distribution width of the molecular beam is larger than the diameters of the electron beam and the laser beam, the overlap between the laser beam and the electron beam is important. In order to secure the spatio-temporal overlap between the laser beam and the electron beam, the thin gold wire ($\phi 100$ μm) is installed below the nozzle. The wire is mounted on the 3-axis stage and its position can be adjusted with a precision of 10 μm. By monitoring the shadow graphs of the wire and the apex of the nozzle appearing in the images of electron and laser beams, the spatio-temporal overlap is achieved. As shown in Fig. 42, the

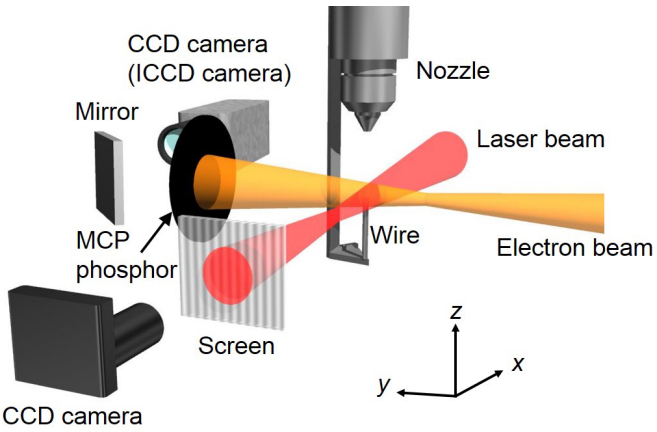

Figure 42: Experimental configuration for securing the spatio-temporal overlap between the laser beam and the electron beam. The shadow graphs of the gold thin wire (100 μm ϕ) in the laser and electron beam are monitored simultaneously.

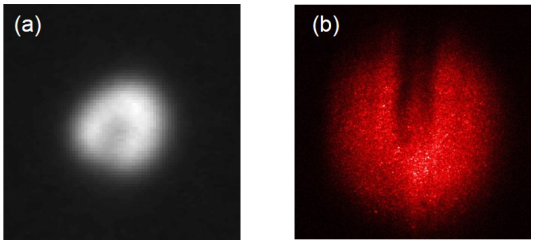

Figure 43: Shadow graphs of thin wire. (a) The shadow graph of the wire in the electron beam. (b) The shadow graph of the wire in the laser beam.

image of the laser beam is recorded by using a screen and a CCD camera. The electron beam is monitored by the electron beam monitor described in Section 3.5.4.

Spatial overlap

The spatial overlap between the laser, electron, and molecular beam is achieved by the following procedure. First, the nozzle is lifted down by 0.6 mm and the shadow graph of the apex of the nozzle in the laser beam is monitored. The position of the laser beam along the y-axis is adjusted so that the shadow of the apex is located in the center of the laser beam. The alignment along the y-axis does not have to be performed precisely. This is because the spatial overlap along the y-axis is equivalent to the temporal overlap between the laser and electron beams, and the temporal overlap is achieved with high precision by the method described below. Then, by monitoring the shadow graph of the wire in the electron beam (Fig. 43(a)), the position of the wire (along the x and z axes) is adjusted so that the tip of the wire is located in the center of the electron beam.

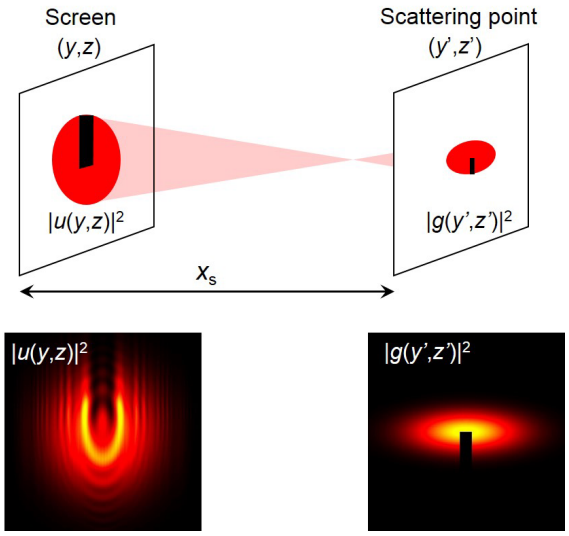

Figure 44: Simulation of the shadow graph of the thin wire appearing in the laser beam. The lower left image shows the result of the numerical simulation.

The position of the wire along the y-axis is adjusted by monitoring the shadow graph of the laser beam (Fig. 43(b)). Finally, the position of the laser beam along the z-axis is adjusted so that the tip of the wire is located in the center of the laser beam. Because the effect of the diffraction is significant in the shadow graph in the laser beam, the precise alignment of the laser beam along the z-axis is done by comparing the observed shadow graph and a simulated shadow graph. The method for simulating the shadow graph of the wire in the image of the laser beam is described in the next paragraph. The effect of the diffraction in the shadow graph of the electron beam is negligibly small because of the short deBroglie wavelength (0.39 Å) and low spatial coherence (≤ 1 nm). By this alignment procedure, the spatial overlap between the laser and electron beams along the z-axis are secured with a precision of 100 μm which is high enough to observe the LAES process.

Simulation of the shadow graph

The shadow graph of the thin wire appearing in the image of the laser beam is simulated by adopting the Frenel-Kirchhoff diffraction formula [199]. When the (complex) amplitude of the laser light at the position of the wire is expressed as $g(y', z')$, the amplitude of the light at the position of the screen is given by

$$u(y,z) = \frac{\mathrm{i}}{\lambda}\int_{-\infty}^{\infty}\int_{-\infty}^{\infty} g(y',z')L(y',z')\frac{\mathrm{e}^{-2\pi \mathrm{i} r/\lambda}}{r}\mathrm{d}y'\mathrm{d}z', \tag{3.48}$$

where λ is the wavelength of light, r is a distance between two points (y', z') and (y, z), and

$L(y', z')$ represents the phase variation due to the focusing of the laser light,

$$L(y', z') = \exp\Big[\frac{\pi \mathrm{i}}{\lambda}\Big(\frac{y'^2}{f_y} + \frac{z'^2}{f_z}\Big)\Big], \tag{3.49}$$

where f_y and f_z are distance between the wire and the focal points in y and z directions, respectively. In this experiment, the distance between the wire and the screen is much longer than the size of the laser beam. Therefore, r can be approximated as

$$\begin{aligned} r &= \sqrt{x_{\mathrm{s}}^2 + (y'-y)^2 + (z'-z)^2} \\ &\simeq x_{\mathrm{s}} + \frac{1}{2x_{\mathrm{s}}}\Big((y'-y)^2 + (z'-z)^2\Big), \end{aligned} \tag{3.50}$$

where x_{s} is the distance between the wire and the screen along the x-axis. By combining the above formulae, the shadow graph of the thin wire shown in Fig. 44 was obtained.

Temporal overlap

The direct way to secure the temporal overlap between the laser and electron beams is to measure the signal intensity of the LAES process while scanning the delay time (Δt) between the laser and electron beams. However, because the signal intensity of the LAES process is quite weak, it requires a long accumulation time. It has been known that the temporal overlap can also be achieved by taking advantage of the pondermotive scattering [200, 201], the Kapitza-Dirac scattering [202], the photoionization of molecules [203], and the photoelectron emission from a metal wire [204]. In this study, we adopted the method developed by Park *et al.* [204] which uses the photoelectron emission from a metal wire. This is because their method can be performed quickly by using the same set-up used for achieving the spatial overlap. It is true that the precise (sub-ps) zero delay time (Δt = 0) can be determined by their method, but under the conditions of this experiment, $\Delta t = 0$ cannot be obtained with the high precision. Therefore, their method is used to find $\Delta t = 0$ roughly, and the precise $\Delta t = 0$ is determined by measuring the LAES signals.

In the Park *et al.*'s method, a thin metallic wire is placed at a point where the laser and electron beams intersect with each other. By the irradiation of the laser pulse, an electron cloud is generated on the surface of the wire. The electron cloud deflects the incoming electron beam and changes the spatial profile of the electron beam. By measuring the changes of the spatial profile of the electron beam as a function of the delay time between the laser and electron beams, the zero delay time (Δt = 0) can be determined with sub-ps precision [204]. The advantage of the method is that the changes of the electron beam profile can easily be observed with low intensity laser intensity and low density electron beams.

Observed images of the electron beam are shown in upper panels of Fig. 45. Lower panels of Fig. 45 show the difference of the image at each delay time from the image at $\Delta t = -80$ ps. A pulse energy of the laser pulse (520 fs) is 30 μJ, and the peak field intensity is 3×10^{10}

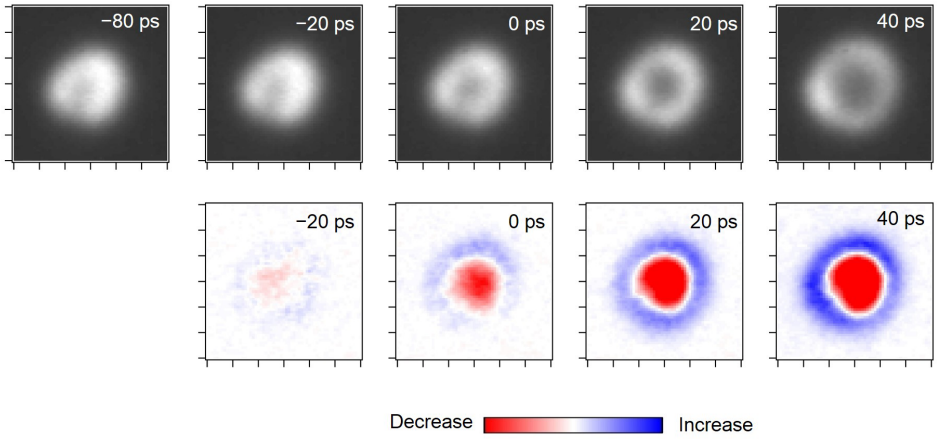

Figure 45: Changes in the electron shadow graphs of the wire. Upper panels show the images of the electron beam. The numbers written in each panels show the delay time between the laser and electron pulses. Lower panels show the changes of the images from the image measured at $\Delta t = -80$ ps.

W/cm^2. In order to measure the changes of the electron beam profile with short accumulation time, the size of the electron beam on the monitor is reduced by decreasing the current of the electromagnetic lens by 9 %. At this field intensity, any significant damages on the wire were not observed. The delay time between the laser and electron pulses is varied by the optical delay stage for the UV laser pulse (Fig. 33). As can be seen in the lower panels of Fig. 45, the density of electrons at the central part of the beam is decreased and the density in the surrounding part increases. The changes in these images show that the electron beam is expanded by the repulse force from the electron cloud on the wire. In order to evaluate the changes in the electron beam profile quantitatively, the amount of change, $D(\Delta t)$ is defined by

$$D(\Delta t) = \int r\Big(I(x,y,\Delta t) - I(x,y,\Delta t = -\infty)\Big)\mathrm{d}x\mathrm{d}y, \tag{3.51}$$

with

$$r = \sqrt{(x-x_0)^2 + (y-y_0)^2}, \tag{3.52}$$

where $I(x,y,t)$ is the image of the electron beam at the delay time of Δt, and (x_0, y_0) represents the center position of the electron beam. In order to make $D(\Delta t)$ sensitive to the change of the spatial profile of the electron beam rather than the changes of the intensity on each pixel, the radius (r) is multiplied.

In Fig. 46, $D(\Delta t)$ is plotted as a function of the delay time Δt by red circles. The image measured at $\Delta t = -80$ ps was adopted as the reference image ($I(x,y,\Delta t = -\infty)$). The measurement took about 15 minutes. The amount of the change increases for $\sim$70 ps, and approaches to a constant value at large delays. I found that the shape of $D(\Delta t)$ is little affected

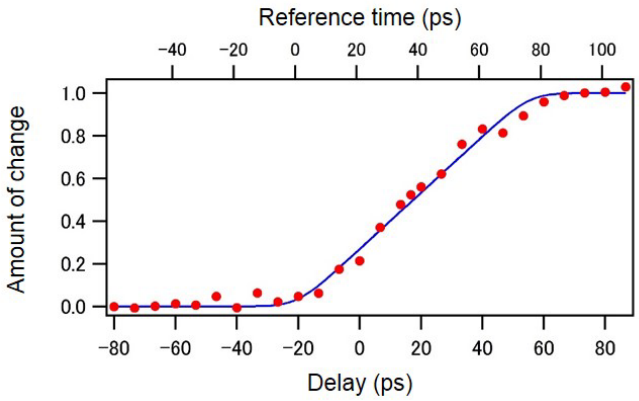

Figure 46: Changes of the electron shadow graph of the wire as a function of the delay time between the electron and laser pulses. The lower horizontal axis shows the delay time between the electron and laser pulses. The upper horizontal axis shows the reference time determined by the least square analysis. The red circles show the experimental data. The blue curve shows the result of the fitting.

by the the pulse duration of the laser pulse and the laser field intensity. Because the duration of the laser pulse (520 fs) is much shorter than the rising time of $D(\Delta t)$ ($\sim$70 ps), the rising time is determined by the pulse duration of the electron pulse and the time evolution of the electron cloud on the wire. Under two assumptions described below, the obtained $D(\Delta t)$ was reproduced numerically. The first assumption is that $D(\Delta t)$ is given by the convolution of the temporal shape of the electron beam and the time variation of the electron cloud,

$$D(\Delta t) = \int_{-\infty}^{\infty} \exp(-4(\ln 2)\frac{t'^2}{\tau_{\rm e}^2}) W(\Delta t - t')\mathrm{d}t' \tag{3.53}$$

where $\tau_{\rm e}$ is the pulse duration of the electron pulse, $W(t)$ is the time variation of the electron cloud on the wire. From the measurement of the pulse duration of the UV laser pulse, the pulse duration of the electron pulse ($\tau_{\rm e}$) is expected to be around 15 ps. The second assumption is that the time variation of the electron cloud is described by

$$W(t) \propto \begin{cases} 0 & (t \leq 0) \\ t/\tau_W & (0 \leq t < \tau_W) \\ 1 & (\tau_W \leq t) \end{cases} \tag{3.54}$$

Under these assumptions, $\Delta t = 0$ can be determined by comparing a simulated curve and the experimental curve. The simulated curve best matches the experimental curve when τ_W = 75 ps and the delay time shown in the upper horizontal axis in Fig. 46 is used. As discussed below, the delay time determined by this analysis needs to be corrected (should be shifted by $\sim$ 21 ps). This means that the assumptions (Eqs. (3.53) and (3.54)) are not so appropriate. However,

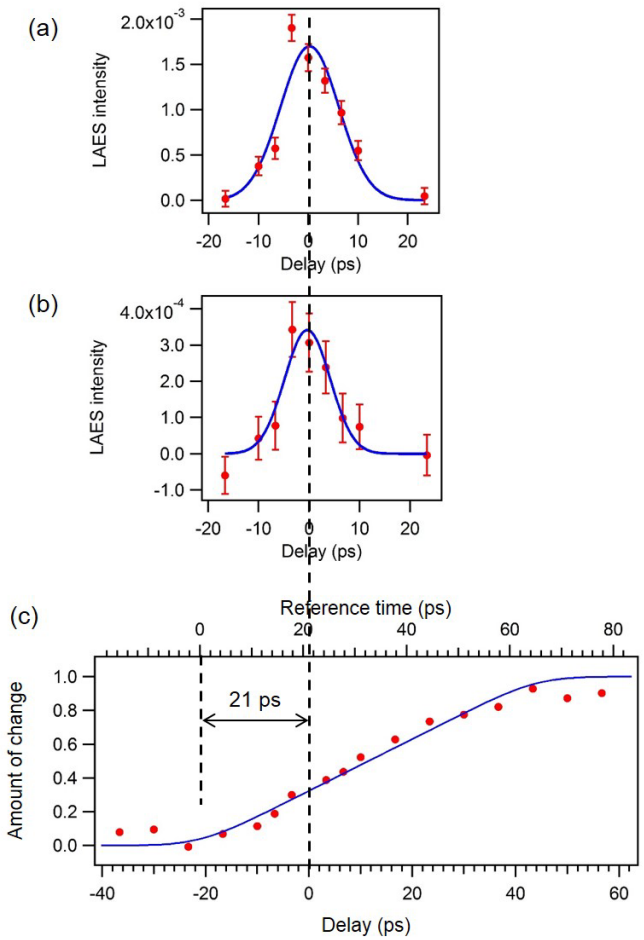

Figure 47: Determination of the zero delay time ($\Delta t = 0$). Panels (a) and (b) show the LAES signal intensities as a function of the delay time between the laser and electron pulses. Panel (a) shows the signal intensity of LAES $n = \pm 1$ processes, and panel (b) shows the signal intensity of LAES $n = \pm 2$ processes as a function of the delay time between the laser and electron pulses. Red circles show the experimental results. The error bars represent one standard deviation. The Blue curves show the results of the least-square fitting by Gauss functions. Panel (c) shows the changes of the electron shadow graphs of the wire measured under the same laser focusing condition as that used for the measurement of the LAES signals shown in panels (a) and (b). The red circles show the experimental results. The lower horizontal axis represent the delay time between the laser and electron pulses determined by the measurement of LAES signals in panels (a) and (b). The upper horizontal axis represents the reference time determined by the least-square fitting to the delay-dependent changes of electron shadow graphs. The blue circle shows the result of the fitting based on Eqs. (3.53) and (3.54).

this analysis can be used for finding a reference point ($\Delta t = -21$ ps) quickly with a several ps resolution.

In order to find the point of true $\Delta t = 0$ in $D(\Delta t)$, the LAES signal intensities were mea-

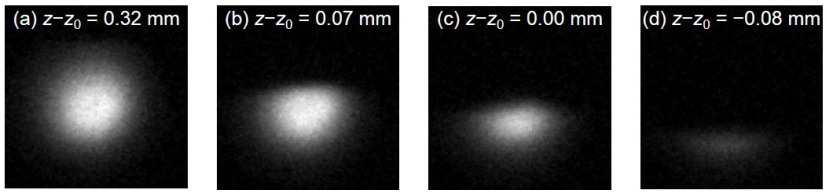

Figure 48: Images of the electron beam. Panel (a) shows the image of the electron beam which is not blocked by the nozzle. Panels (b)-(d) show the images of the electron beam which is partially blocked by the nozzle. The numbers written in the panels represent the position of the nozzle apex.

sured as a function of the delay time, Δt. Because the temporal overlap becomes more severe with decreasing the focal size of the laser beam along the y-axis, the laser beam is focused to a diameter of 100 μm by removing the cylindrical lens (f = 10000 mm) and changing the position of the spherical lens (f = 400 mm). Considering the speed of the 1 keV electrons (19 μm/ps), $\Delta t = 0$ can be determined with 5 ps precision by the measurement of LAES signals. Figures 47(a) and (b) show the LAES signal intensities with one- and two-photon energy shifts as a function of the delay time. The measurement of LAES signals takes one hour at a delay, and about ten hours in total. The horizontal axes in Figs. 47(a) and (b) are determined by fitting the observed LAES signals by Gaussians. The center positions of the fitting curves shown in Figs. 47(a) and (b) as blue curves are almost identical. The distribution width (FWHM) of these curves are 13(2) ps (Fig. 47((a), FWHM) and 12(3) ps (Fig. 47(b), FWHM), and are in consistent with the expected pulse duration of the electron beam (15 ps, FWHM). Figure 47(c) shows the $D(\Delta t)$ curve measured by the tightly focused laser beam. The upper horizontal axis in Fig. 47(c) represents the delay time determined by the analysis based on Eqs. (3.53) and (3.54). The lower horizontal axis shows the "true" delay time determined by the LAES signals. This graph shows that the "true" delay time can be obtained by subtracting 21 ps from the result of the simple analysis in $D(\Delta t)$.

Based on the above results, the following procedure is used for securing $\Delta t = 0$. First, by measuring the electron shadow graphs of the wire, $D(\Delta t)$ curve is obtained. By comparing the experimental $D(\Delta t)$ and simulated $D(\Delta t)$, a reference delay time ($\Delta t = -21$ ps) is determined. The optical delay stage is set to the point of $\Delta t = 0$. Finally, the precise $\Delta t = 0$ is determined by measuring the LAES signal intensity a few times around the $\Delta t = 0$ determined from $D(\Delta t)$. By this procedure, the temporal overlap can be secured with a precision of 5 ps, which corresponds to the 0.1 mm precision of the spatial overlap between the laser and electron beam along the y-axis.

3.5.7 Measurement of the size of the laser and electron beams at the scattering point

In this subsection, procedures for the measurement of the size of the electron beam and the laser beam at the scattering point are described.

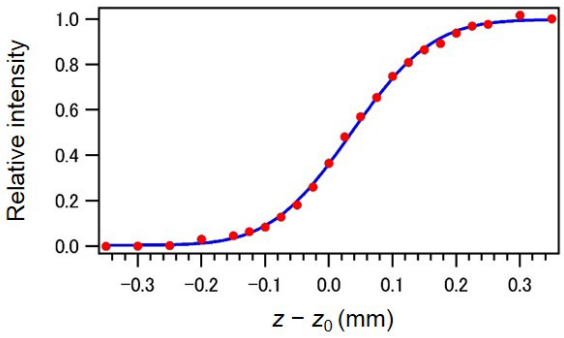

Figure 49: Intensity of the electron beam at the electron beam monitor. The intensity is plotted as a function of the position of the nozzle apex along the z-axis. The red circles represent the experimental data. The blue curve shows result of the least-square fitting.

Measurement of electron beam diameter

The diameter of the electron beam is measured by using the nozzle and the electron beam monitor. When a part of the electron beam is blocked by the nozzle, the integrated intensity of the electron beam on the electron beam monitor is decreased as shown in Fig. 48. The integrated intensity of the electron beam is expressed by

$$I(z) = \int_{-\infty}^{\infty}\int_{-\infty}^{z} I_{\mathrm{e}}(x', z')\mathrm{d}x'\mathrm{d}z', \tag{3.55}$$

where z is the position of the apex of the nozzle, $I_{\mathrm{e}}(x, z)$ is the two-dimensional profile of the electron beam at the scattering point. In deriving above equation, the apex of the nozzle is assumed to be flat in the xy plane. When the spatial profile of the electron beam is expressed by a Gaussian,

$$I_{\mathrm{e}}(x, z) = \exp\Big(-4(\ln 2)\frac{(x - x_0)^2 + (z - z_0)^2}{w_{\mathrm{e}}^2}\Big), \tag{3.56}$$

the integrated intensity of the electron beam is given by

$$I(z) = \frac{I_{\mathrm{e}}^{\mathrm{tot}}}{2}\Big(1 + \mathrm{erf}\Big(\frac{2\sqrt{\ln 2}}{w_{\mathrm{e}}}(z - z_0)\Big)\Big), \tag{3.57}$$

where x_0 and z_0 are the center position of the electron beam and w_{e} is the diameter of the electron (FWHM), $I_{\mathrm{e}}^{\mathrm{tot}}$ is the intensity of the electron beam when the beam is not blocked by the nozzle, and $\mathrm{erf}(z)$ is the error function which is defined by [75]

$$\mathrm{erf}(z) = \frac{2}{\pi}\int_{0}^{z} \exp(-z'^2). \tag{3.58}$$

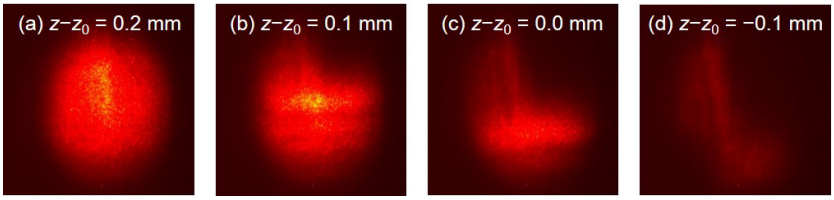

Figure 50: Images of the laser beam on the screen. Panel (a) shows an image of the laser beam which is not blocked by the nozzle. Panels (b)-(c) show images of the laser beam which is partially blocked by the nozzle. The number written in each panel represents the position of the nozzle along the z-axis. The weak vertical lines appearing in panels (b)-(d) are originating from the diffraction of the laser light by the nozzle.

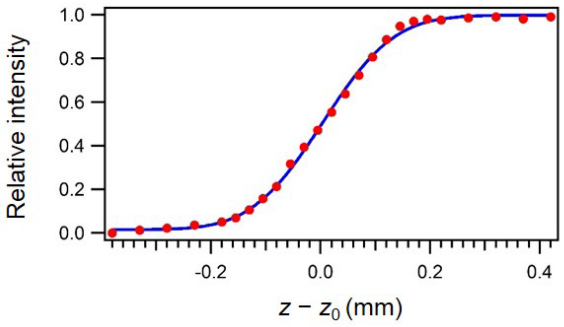

Figure 51: Intensity of laser beam on the screen as a function of the position of the nozzle apex. Red circles represent the experimental data. Blue curve represents the result of the fitting which uses Eq. (3.57).

In Fig. 49, the intensity of the electron beam is plotted as a function of the position of the nozzle. The red circles show the experimental data. A least-square fitting to the experimental data is conducted by using Eq. (3.57). The result of the fitting is shown by a blue curve in Fig. 49. The fitting curve reproduces the experimental data almost perfectly. From the least-square analysis, the diameter of the electron beam was determined to be $w_{\rm e}$ = 0.24(7) (FWHM).

Measurement of laser focal size

As described in Section 3.5.2, the laser beam is focused by the combination of the spherical lens (f = 400 mm) and the cylindrical lens (f = 10000 mm). The laser beam has an elliptical shape at the scattering point with a major axis along the y-aixs. Therefore, both of the diameter along the y-axis and that along the z-axis should be measured.

The laser beam diameter along the z-axis is determined by employing the same method as that used for the measurement of the electron beam diameter. Some of the shadow graphs of the nozzle apex appearing in the image of the laser beam are shown in Fig. 50. The images of the

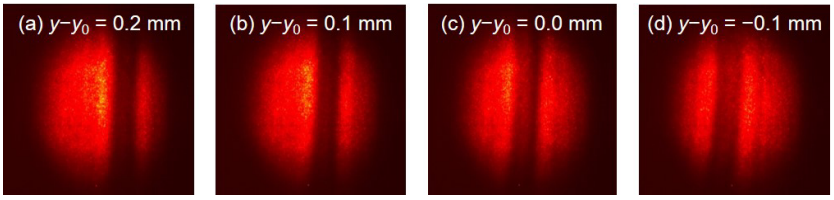

Figure 52: Images of the shadow graphs of the thin wire (100 μ m) appearing in the laser beam. The wire is lifted up by 0.4 mm from the position used for securing the spatio-temporal overlap (Section 3.5.6). The position of the thin wire along the y-axis is written in each panel. The position of the wire on the x-axis is the same as that used for securing the spatio-temporal overlap.

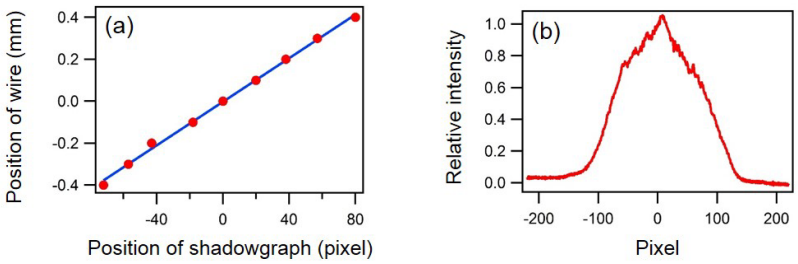

Figure 53: Measurement of laser beam diameter along the y-axis. (a) The relationship between the center position of the shadow graph of the thin wire appearing in the images of laser beam and the position of the thin wire at the scattering point. Red circles show the observed data. Blue line shows the result of the fitting in which a linear function was used. (b) The spatial profile of the laser beam along the horizontal direction on the screen (Fig. 50(a)).

laser beam are recorded by the setup shown in Fig. 42. Red circles in Fig. 51 show the observed laser beam intensity integrated over an image as a function of the position of the nozzle apex. By using Eq. (3.57), the experimental data was fitted. The result of the least-square fitting is shown by a blue curve. The diameter of the laser beam along the z-axis was determined to be 0.25(1) mm (FWHM) and 0.42(1) mm (1/e^2 full width).

In order to determine the laser beam diameter along the y-axis, the thin wire which was used for securing the spaito-temporal overlap is employed. As shown in Fig. 52, the shadow graphs of the thin wire are recorded at different positions along the y-axis. Then, the center position of the shadow graph of the wire appearing in the images of the laser beam and the the position of the wire at the scattering point are compared. The result of the comparison is shown in Fig. 53(a) as red circles. The results are well fitted by a linear function as shown by a blue line. From the fitting, it was found that one pixel in the image corresponds to 5.2 μm at the scattering point. Because the distribution width of the laser beam along the y aixs is 151(1) pixel (FWHM) and 231(2) pixel (1/e^2 full) in the image (Fig. 53(b)), the laser beam diameter along the y-axis at the scattering point was determined to be 0.785(5) mm (FWHM) and 1.2(1) mm (1/e^2 full width).

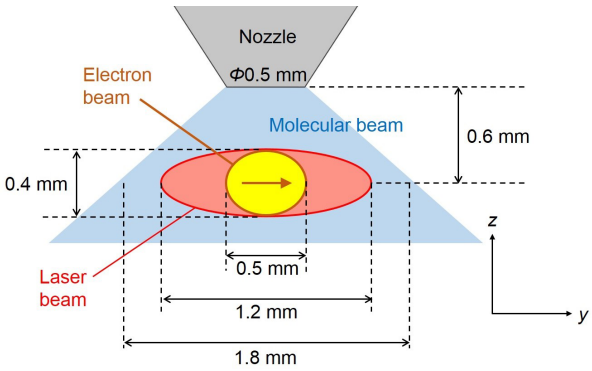

Figure 54: Overlap of the laser, electron, and molecular beams. The sizes of the beams represent the $1/e^2$ full width. The brown arrow written in the electron beam shows the propagation direction of the electron beam.

The results of the beam size measurements are summarized in Fig. 54. The size of the electron beam along the y-axis is determined by the pulse duration (15 ps, FWHM) and the speed of the electron (18.8 mm/ns). The size of the laser beam along the y-axis is larger than that of the electron beam. Therefore, a slight mismatch of the temporal overlap ($\leq$ 5 ps) between the electron and the laser beams has little influence on the LAES signals. The size of the laser beam along the z-axis is almost identical to that of the electron beam.

3.5.8 Toroidal analyzer

Overview of the analyzer

A picture of the toroidal analyzer is shown in Fig. 55. The toroidal analyzer consists of three components: input lens, toroidal electrodes, and output lens. Figure 56 shows the simulated trajectory of scattered electrons. The analyzer is symmetric with respect to the laser propagation axis shown in red. Therefore, the scattering angles of the scattered electrons are conserved until they are detected. The input lens consists of 11 plate electrodes which are arranged at irregular intervals. The first electrode is a 0.8 mm slit which is grounded (0 V). The scattered electrons are skimmed by the slit. The slit is parallel to the yz plane (Fig. 26). The skimmed electrons are decelerated and focused on a 0.5 mm slit by the electric field of the input lens. Because the voltage of -970 V is applied to the 0.5 mm slit (11th plate), the scattered electrons are decelerated to around 30 eV. Then, the decelerated electrons are dispersed according to their kinetic energies by the electric field between the toroidal electrodes. Finally, the electrons are accelerated to 1000 eV by the output lens and detected by the detector. The detectable range of the kinetic energy is from -4 eV to $+4$ eV. This energy range is determined by the deceleration voltage (-970 V) and the gap between the toroidal electrodes (30 mm). The maximum scattering angle is determined by the size of the detector. In this experiment, the maximum scattering angle

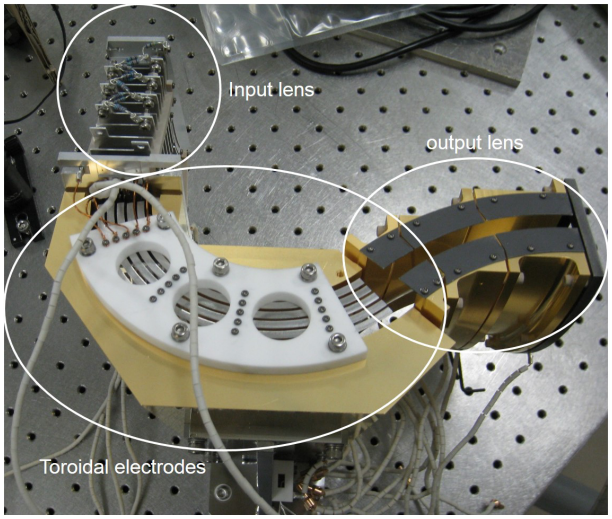

Figure 55: Picture of the toroidal energy analyzer. The toroidal analyzer is composed of the input lens, the toroidal deflecting electrodes, and the output lens.

is 12.5°. The minimum scattering angle is determined by the diameter of the Faraday cup which is placed in front of the analyzer (Fig. 26). The Faraday cup is used to collect the electrons which are not scattered by the sample molecules. The outer diameter of the Faraday cup used in this study is 7 mm, and the minimum detectable scattering angle is 2.5°.

Trajectory of scattered electrons

Figure 57 shows the simulated image of the scattered electrons with the energy shift of $nh\nu$ ($h\nu = 1.55$ eV, $n = 0, \pm1, \pm2$) on the detector. The scattered electrons with the same kinetic energy form an arc structure whose center is located on the symmetrical axis (red line in Fig. 56). The radius of the arc corresponds to the kinetic energy of the scattered electron. As mentioned above, the scattering angle is conserved inside the analyzer. Therefore, the kinetic energy and the scattering angle of the scattered electron can be determined from the two-dimensional position on the detector.

Calibration of the amount of kinetic energy shift

The calibration of the kinetic energy shift was conducted by measuring the angular distribution of elastically scattered electrons whose energies are shifted by $nh\nu$ $(n = 0, \pm1, \pm2)$ from 1000 eV. The kinetic energy of the electron beam was changed by shifting the acceleration voltage applied to the photocathode. The acceleration voltage can be adjusted with a precision of 0.01 V. Figure 58(a) shows the observed image of the electrons scattered by Xe. The arc structures appear at almost regular intervals. By comparing with this calibration image, the kinetic energy of scattered electrons can be determined.

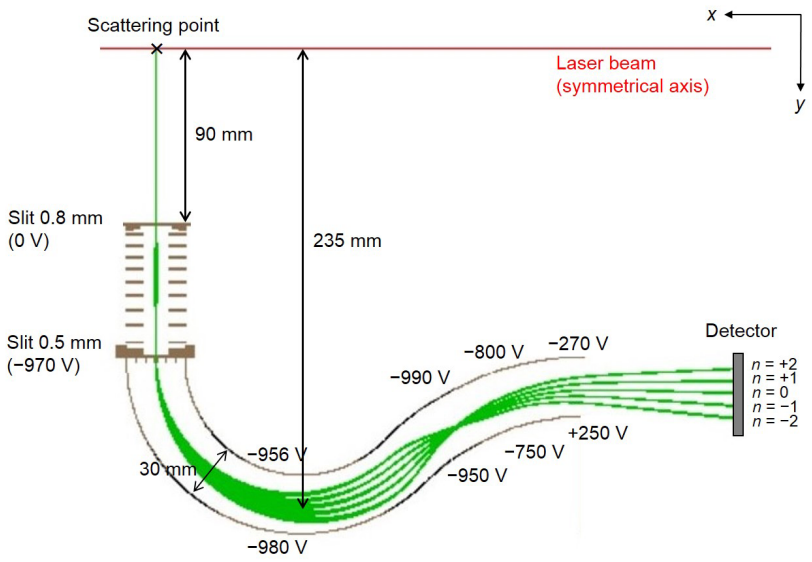

Figure 56: Simulated trajectory of the scattered electrons. The green lines show the trajectories of the scattered electrons whose kinetic energies are shifted by $nh\nu$ ($h\nu = 1.55$ eV, $n = 0, \pm 1, \pm 2$). The analyzer and the trajectories are symmetric to the laser propagation axis shown by the red line.

Resolution of the kinetic energy shift

The width of an arc shown in Fig. 58(b) corresponds to the overall energy resolution of the apparatus. The overall energy resolution of the apparatus is mainly determined by two factors: the energy resolution of the toroidal analyzer and the energy distribution of the electron beam. From the result of trajectory simulations, the energy resolution of the analyzer is estimated to be better than 0.4 eV. The energy distribution of the electron pulse is determined by the difference between the photon energy of the UV laser pulse used for generating the electron pulse and the work function of the photocathode material (Au). Figure 58(b) shows the kinetic energy spectrum of the electrons obtained by integrating the image shown in Fig. 58(a) over the entire scattering angle range. The width of the peak appearing at $n = 0$ ($\Delta E = 0$ eV) is $\sim$0.4 eV. Therefore the energy resolution is $\sim$0.4 eV.

Calibration of scattering angle

The calibration of the scattering angle was performed by measuring the angular distribution of the scattered electrons by installing the mask pattern shown in Fig. 59(a) just in front of the 0.8 mm slit of the analyzer. The mask pattern has horizontal slits through which electrons scattered at $\theta = 2^\circ, 4^\circ, 6^\circ, 8^\circ, 10^\circ, 12^\circ$ can enter the analyzer. In Fig. 59(b), the image of the scattered electrons whose kinetic energies are shifted by $nh\nu$ $(n = 0, \pm 1, \pm 2)$ are shown. By using this

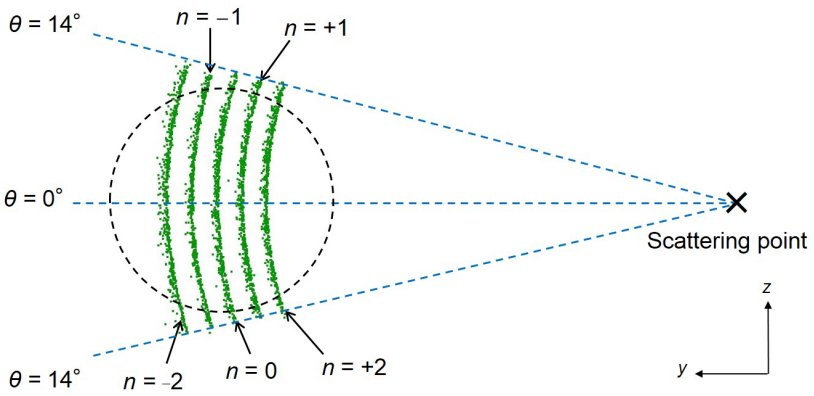

Figure 57: Simulated image of the scattered electrons on the detector. The green dots represent the simulated image of the scattered electrons. The circle represented by the black broken line shows the size of the detector.

image, the scattering angle of a scattered electron whose kinetic energies are shifted by $nh\nu$ $(n = 0, \pm 1, \pm 2)$ can be determined from the a position on the detector.

Resolution of the scattering angle

The angular resolution was estimated by measuring the electron diffraction pattern of a graphene (Graphene Laboratories Inc.) which is mounted on a copper mesh. The samples was fixed to a home-made sample folder and mounted on the nozzle system. The observed electron diffraction pattern of the graphene is shown in Fig. 60. The peak which can be assigned to (hkl) = (100) and (101) [205] was observed at $\theta = 10.5°$ ($s = 3.0$ Å^{-1}). Because the (100) and (101) peak appears at almost the same scattering angle [205], these peaks are completely overlapped. The width of the observed peak is about $0.9°$ (FWHM). Therefore, the angular resolution at the scattering angle of $\theta = 10.5°$ is found to be better than $1°$, which is high enough to observe the electron diffraction patterns of gas-phase molecules.

Calibration of detection efficiency

The detection efficiency of this apparatus is dominated by two factors: the transmission efficiency of the analyzer and the sensitivity of the detector. In order to evaluate the detection efficiency, the angular distributions of the elastic scattering by Xe were measured at the kinetic energy of $1000 + nh\nu$ eV $(n = 0, \pm 1, \pm 2)$. By comparing each of the observed angular distributions and a simulated angular distribution, the detection efficiencies for the $1000 + nh\nu$ eV $(n = 0, \pm 1, \pm 2)$ electrons were obtained. The simulated angular distribution was obtained by the ELSEPA code [128] in which the polarization effect is included.

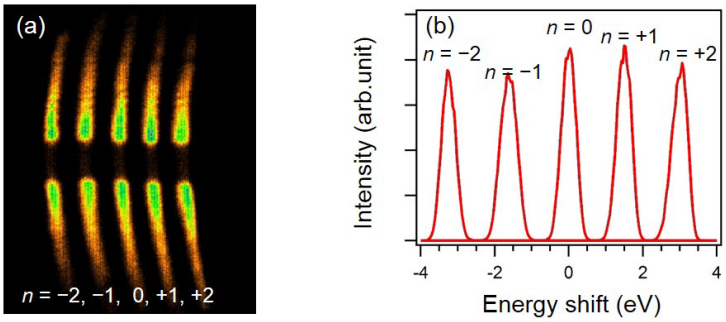

Figure 58: Calibration of kinetic energy shift and the measurement of kinetic energy resolution. (a) The observed image of the scattered electrons by Xe. Each of the observed arc-like structures corresponds to the signals measured at the kinetic energy of $1000 + nh\nu$ eV ($h\nu$ = 1.55 eV, $n = 0, \pm 1, \pm 2$). The electrons scattered less than 2° are blocked by the Faraday cup placed in front of the analyzer and are not detected. (b) The kinetic energy spectrum of the scattered electrons which is obtained by integrating the signals in panel (a) over the entire scattering angle range.

3.5.9 Detector

The scattered electrons are detected by the MCP detector with delay-line anodes [206] (HEX-80, RoentDek Handels GmbH). The photograph of the detector is shown in Fig. 61. When an electron hits the detector, the electron is multiplied by a pair of the MCPs (chevron assembly, 75 mmϕ, pore diameter 10 μm, aperture ratio 62%, thickness 0.61 mm, bias angle 19°). The position and the arrival time of the electron signal are measured by the delay-line anodes.

The working principle of the delay-line anode is shown in Fig. 62. When the electron signal amplified by the MCPs arrive at the delay-line anode, the signal propagates in directions towards the both ends of the delay-line. If the arrival time of the signal on each end of the line are written

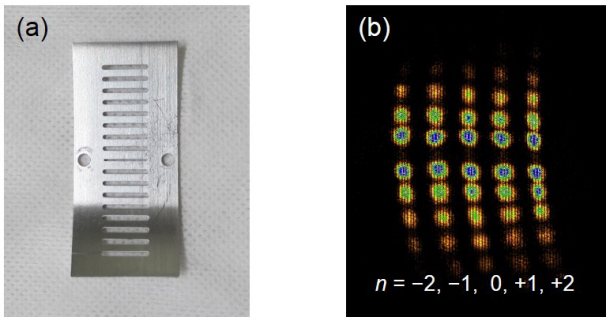

Figure 59: Calibration of the scattering angle. (a) The photograph of a mask pattern. The horizontal slits are arranged to transmit the electrons scattered at $\theta = 2^\circ, 4^\circ, 6^\circ, 8^\circ, 10^\circ, 12^\circ$. The width of the slit is 1 mm. (b) The observed image of the electrons scattered by Xe.

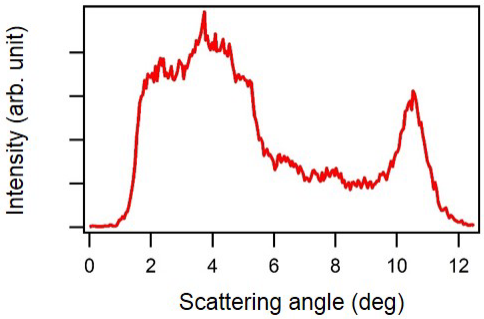

Figure 60: Observed electron diffraction pattern of the graphene. The electron signals were accumulated over 3h with a count rate of 7.4 count/sec.

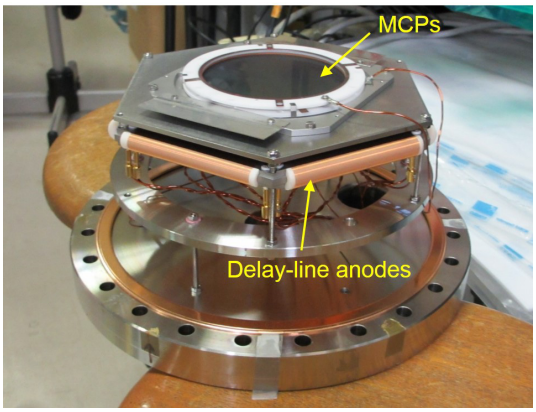

Figure 61: Appearance of the detector (HEX-80) mounted on the ICF253 flange. Signals are multiplied by the microchannel plates (MCPs), and detected by three layers of delay-line anodes (hexanode).

as t_1 and t_2, the difference between these arrival times gives the position where the electron signal hits the detector,

$$x = \frac{t_1 - t_2}{2} v_x, \tag{3.59}$$

where the x is the position along the direction perpendicular to the winding direction of the delay-line, v_x is the speed of the signal propagation along the x-axis. Considering the resolution for the arrival time measurement (500 ps) and the speed of the signal propagation (v_x = 0.7 mm/ns) of our detector, the spatial resolution is 0.35 mm. The arrival time of the signal is measured by using a circuit (constant fraction discriminator) attached to the delay-line detector and a time-to-digital converter (TDC) installed in a computer. In this experiment, TDC measures the time from when the signal of the delay-line arrives till when a trigger signal arrives. An output of a photodiode which receives the a fraction of a laser light is used as the trigger signal.

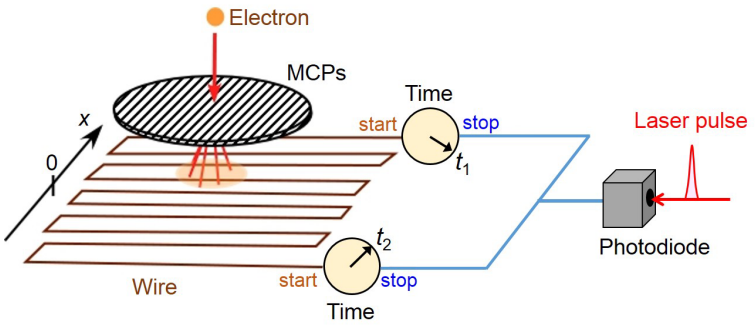

Figure 62: Working principle of the delay-line anode detector. When an electron hits the microchannel plates (MCPs), the electron signal is amplified. The amplified signal propagates toward the both ends of the delay-line. In this study, the arrival time of the signal at the end of the delay-line is measured as the time difference between the signal and a trigger signal from the output of the photodiode (common stop mode). The difference of the arrival times ($t_2 - t_1$) of the electron signal measured at the ends of the anodes depends on the position where the signal electrons hit the detector.

The sum of the arrival times, $t_1 + t_2$, does not depend on the position where the signal hits. Because t_1 and t_2 contains the information of the time difference between the signal of the wire and the trigger signal, it can be used as a probe of the time when the electron signal hits the detector. Therefore, from t_1 and t_2, we can determine the arrival position and the arrival time of the signal.

In order to determine the two-dimensional position of a signal, at least two delay-line anodes are required. As shown in Fig. 61, the detector used in this study has three delay-line anodes (named as u, v, and w) which are arranged at 60° intervals. Each delay-line anode consists of two wires: signal and reference. A positive voltage (20 V) is applied to the signal wires, and therefore, most of the electrons hit the signal wires. By taking the differential signals between the signal and reference wires, noises such as cross-talk can be removed. When the signals are detected by at least two delay-line anodes properly, the two-dimensional position can be determined. However, in this study, only the signals, which are detected by all the delay-line anodes and their positions determined by the (u, v) anodes are consistent with those determined by the (v,w) anodes, are used for the analysis in order to suppress noises.

In order to further suppress noises, only the signals arrived at the detector within a short duration are used for the analysis. Figure 63 shows measured arrival-time distributions of scattered electrons with kinetic energies of 1000 + $nh\nu$ eV ($h\nu = 1.55$ eV, $n = 0, \pm1, \pm2$). Because the arrival time represents the time from when a signal arrives at the detector till when the trigger signal arrives, smaller arrival time means that the signal hits the detector later. Since higher energy electrons travel through longer trajectories in the toroidal energy analyzer (Fig. 56), electrons with higher kinetic energies reach the detector later than those of smaller kinetic energies. The distributions plotted in Fig. 63 shows that most of the electrons with kinetic energies of

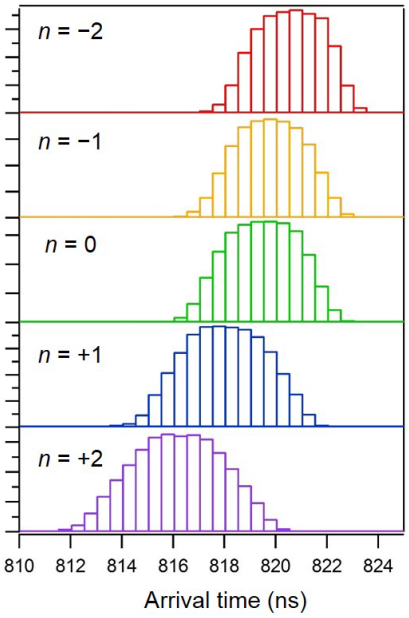

Figure 63: Arrival-time distributions of scattered electrons on the detector. These distributions were measured by the electrons with the kinetic energy of $1000 + nh\nu$ eV ($h\nu$ = 1.55 eV, $n = 0, \pm1, \pm2$). The sample was the Xe gas.

1000 + $nh\nu$ eV ($n = 0, \pm1, \pm2$) arrive at the detector within a duration of 11 ns (from 812 ns to 823 ns). Therefore, in this study, only the electron signals which hit the detector within a duration of 15 ns (from 810 ns to 825 ns) are used for the analysis.

As discussed in Ref. [69, 196], noises measured in the femtosecond-LAES experiments are mainly originating from metastable atoms and molecules generated through multiphoton excitation processes induced by intense laser pulses. When metastable atoms or molecules hit the surface of the toroidal energy analyzer, electrons can be generated. Some of the generated electrons are accelerated by the electric field of the analyzer and reach the detector. Because the generation of the electrons occurs continuously[196], the noise can be suppressed by analyzing only the electrons which arrive at the detector within a short temporal duration. The intensity of noise appearing in the signals obtained with the 15 ns temporal duration is much smaller than the signal intensities of the LAES process.

3.6 Results and Discussion

In this section, results of an experiment are presented. In the experiment, the LAES signals by CCl_4 were measured in order to observe the LAED patterns. The experimental results are compared with numerical simulations based on KWA.

Table 4: Summary of experimental conditions

Kinetic energy of electron	1 keV
Duration of electron pulse (FWHM)	15 ps
Number of electrons in a pulse	10^2
Sample	CCl_4
Temperature	300 K
Sample density	10^{15} cm^{-3}
Wavelength of laser light	800 nm
Pulse energy	0.6 mJ
Pulse duration (FWHM)	520 fs
Peak intensity	6×10^{11} Wcm^{-2}
Polarization	linear (along the z-axis)
Focal size (z-axis, 1/e^2 full)	0.4 mm
Focal size (y-axis, 1/e^2 full)	1.2 mm
Repetition rate	5 kHz
Signal count rate (including background)	90 count/sec
Count rate of LAES signals	0.2 count/sec
Accumulation time	24 h

3.6.1 Experimental results

The experimental conditions are summarized in Table 4 . The laser pulse duration is 520 fs, and the peak field intensity is 6×10^{11} W/cm^2. The laser polarization axis is along the z-axis. The background signals were measured at the delay times of $\Delta t = -70$ ps and $\Delta t = +70$ ps. The positive sign in the delay represents that the electron pulse arrives the scattering point after the laser pulse passes. The signals measured at $\Delta t = 0$ ps and background signals ($\Delta t = -70$ ps or Δt = +70 ps) were accumulated alternatively every 5 hours. At the time of the alternation (every 5 hours), experimental conditions were checked and slightly adjusted, if necessary. The data at $\Delta t = 0$ ps were accumulated for 24 hours. The background signals were accumulated for 12 hours for both $\Delta t = -70$ ps and $\Delta t = +70$ ps. At the delay time of $\Delta t = \pm 70$ ps, the overlap between the laser pulse and the electron pulse is negligible. Therefore, the LAES signals would not be observed at the delay time of $\Delta t = \pm 70$ ps.

The raw images of the observed electron signals are shown in Fig. 64. As shown in Fig. 57, the horizontal direction of the images represents the kinetic energy, and the vertical direction represents the scattering angle of a scattered electron. The detectable scattering angle and energy ranges are $2.5^\circ \leq \theta \leq 12.5^\circ$ and -4 eV $\leq \Delta E \leq +4$ eV, respectively. The electrons scattered at $\theta < 2.5^\circ$ were blocked by the Faraday cup. The intense signals appearing in these images are the elastic scattering ($\Delta E = 0$ eV). At the scale of Figs. 64 (a), (c), and (e), any difference could not be discerned between the image of $\Delta t = 0$ ps and the images $\Delta t = \pm 70$ ps. As discussed

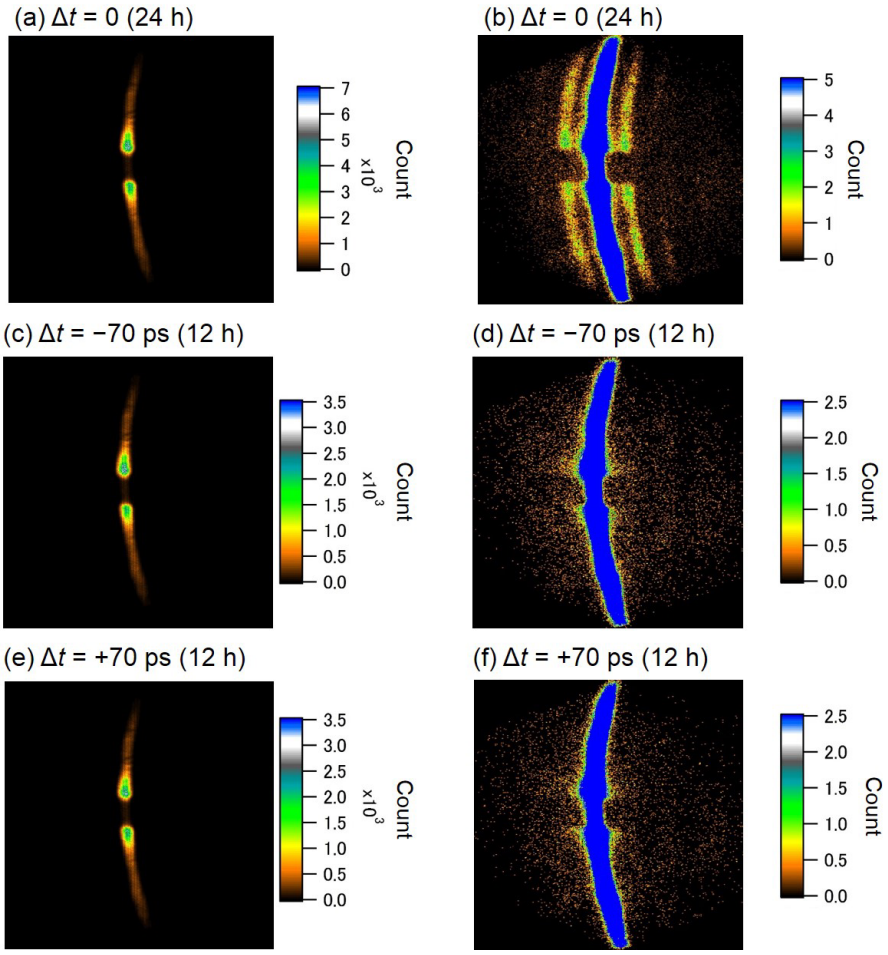

Figure 64: Raw images of electrons scattered by CCl_4 measured at the delay time of $\Delta t = 0$ ps ((a) and (b)), $\Delta t = -70$ ps ((c) and (d)), and $\Delta t = +70$ ps ((e) and (f)). Rescaled images of images (a), (c), and (e) are shown in (b), (d), and (f), respectively.

in Section 2.3.1, most of the elastic scattering signals are originating from the scattering events which occur outside the laser field. Therefore, the LAES signals ($\Delta E = nh\nu$) are much weaker than that of the elastic scattering ($\Delta E = 0$ eV). When the scale of the images are changed as shown in Figs. 64 (b), (d), and (f), significant differences were recognized. Only in the image of $\Delta t = 0$ ps, signals appear on both sides of the elastic scattering signals. The electron signals appearing on the right and left side of the elastic peak are the LAES $n = +1$ ($\Delta E = +h\nu$) and $n = -1$ ($\Delta E = -h\nu$) signals, respectively. The intensities of the observed LAES $n = +1$ and $n = -1$ signals are almost identical. The intensities of the LAES signals appearing on the upper half of the image is almost same as that appearing on the lower half of the image. This is because the duration of the laser pulses used in this work (520 fs, FWHM) is much longer than

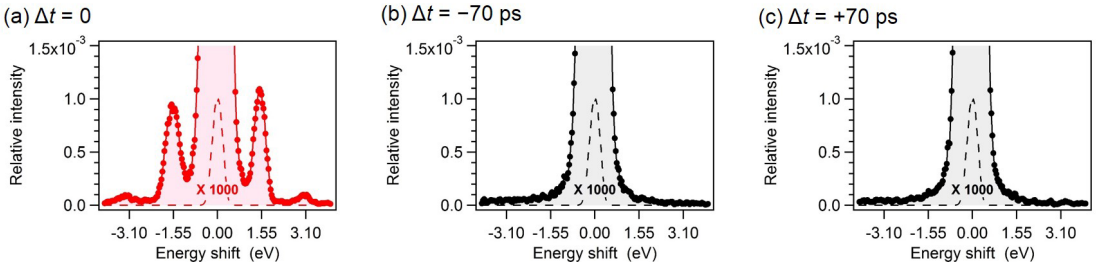

Figure 65: Kinetic energy spectra of electrons scattered by CCl_4 at the delay time of $\Delta t = 0$ ps (a), $\Delta t = -70$ ps (b), and $\Delta t = +70$ ps (c). The intensities of the spectra are normalized by the peak intensities of the elastic signals ($\Delta E = 0$ eV).

the oscillation cycle of the electric field of the laser light (2.7 fs), and therefore, the probability of the LAES process in the direction of $+z$ is almost same as that in the direction of $-z$.

Kinetic energy spectra of scattered electrons

By integrating the electron signals (Fig. 64) over the scattering angle in the entire ranges ($2.5° \leq \theta \leq 12.5°$), kinetic energy spectra of the scattered electron were obtained (Fig. 65). The intensity of the energy spectra are normalized by the peak intensity of the elastic scattering signals ($\Delta E = 0$ eV). The energy resolution of the kinetic energy shift is 0.4 eV (FWHM, Section 3.5.8). Signals of inelastic scatterings due to vibrational excitation of CCl_4 could appear at around $\Delta E = -0.1$ eV [207, 208]. However, the energy spectrum of the elastic scattering ($\Delta E = 0$ eV) is symmetric about $\Delta E = 0$ eV and any significant signals of the vibrational inelastic scattering were not measured.

In the energy spectrum of $\Delta t = 0$ ps (Fig. 65(a)), clear peaks are observed at $\Delta E = \pm 1.55$ eV and $\Delta E = \pm 3.10$ eV. The amount of the energy shifts corresponds to the energy of one- and two-photons ($h\nu$ = 1.55 eV). The signal intensities of the LAES signals are of the order of 10^{-3}, which reflect the ratio between the duration of the laser pulse (520 fs) and the time required for electrons to pass through the sample ($\sim$ 70 ps) (Section 2.3.1). The peak intensity of the LAES $n = -1$ process is slightly weaker than that of $n = +1$ process. This is because the energy resolution of the signals at $n = -1$ are slightly lower than that of $n = +1$ (Fig. 58).

Laser-assisted electron diffraction patterns

In Figs. 66(a) and (b), the angular distributions of the observed LAES $n = +1$ and $n = -1$ processes are plotted by red circles. These angular distributions were obtained by integrating the electron signals (Fig. 64(a)) over the 0.4 eV energy range centered at $\Delta E = \pm 1.55$ eV and subtracting the background. Because the LAES signals appearing in the upper-half of the image is, in principle, identical with that appearing in the lower-half of the image (Fig. 64(b)), the signals of the upper- and lower-half of the image were added for better statistics. The angular

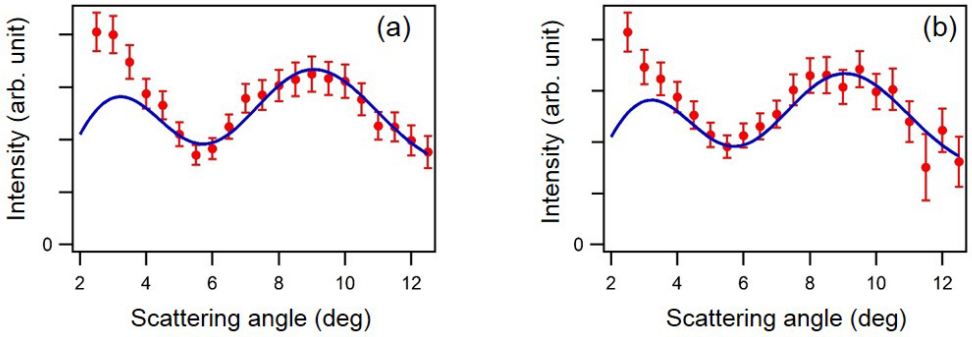

Figure 66: Angular distributions of the LAES $n = +1$ (a) and $n = -1$ (b) processes by CCl_4. Red circles represent the observed angular distributions. The error bars represent one standard deviation. Blue curves show the simulated angular distributions based on KWA.

distributions of the $n = +1$ and $n = -1$ processes are almost identical with each other with the experimental errors. In these angular distributions, we observed clear electron diffraction patterns which show minima at around 5.5° and maxima at around 9°. This shows that we succeeded in observing the LAED patterns for the first time.

Effect of ionization and dissociation

For analyses of the observed LAED patterns, it is important to evaluate the effect of ionization and dissociation of CCl_4 induced by the laser irradiation. It has been known that the ionization of molecules enhances the intensity at small angles due to the long range Coulombic scattering potential, and the dissociation of molecules changes the electron diffraction patterns. In order to investigate the effect of the ionization and/or the dissociation of CCl_4, the electron diffraction pattern appearing in the angular distribution of elastically scattered electrons ($\Delta E = 0$ eV) measured at $\Delta t = -70$ ps was compared with that measured at $\Delta t = +70$ ps. The observed electron diffraction patterns are shown in Fig. 67 (a) by red circles ($\Delta t = -70$ ps) and black squares ($\Delta t = +70$ ps). In order to clarify the difference between these diffraction patterns, the normalized difference $\Delta I/I(\theta)$ was calculated. The normalized difference $\Delta I/I(\theta)$ is defined as

$$\frac{\Delta I}{I}(\theta) = \frac{I(\theta, \Delta t = +70 \text{ ps}) - I(\theta, \Delta t = -70 \text{ ps})}{\frac{1}{2}\Big(I(\theta, \Delta t = +70 \text{ ps}) + I(\theta, \Delta t = -70 \text{ ps})\Big)} \tag{3.60}$$

where $I(\theta, \Delta t)$ is the elastic electron diffraction pattern observed at the delay time of Δt. In Fig. 67 (b), $\Delta I/I$ is plotted by black squares. No significant deviations from $\Delta I/I$ = 0 are not identified. Therefore, the effects of the ionization and the dissociation of CCl_4 are negligibly small.

Enhancement of the visibility of the electron diffraction pattern

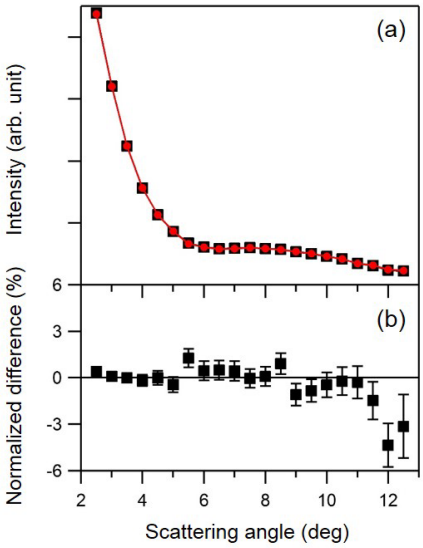

Figure 67: Effect of ionization and dissociation of CCl_4. (a) The electron diffraction patterns measured at $\Delta t = -70$ ps (red circles) and $\Delta t = +70$ ps (black squares). (b) The difference in the electron diffraction patterns shown in (a). The error bars represent one standard deviation.

When the observed LAED patterns (Fig. 66) and the elastic GED patterns (Fig. 67(a)) are compared, it is found that the visibility of the diffraction in LAED patterns is much higher than that of the GED patterns appearing in the angular distribution of elastic scatterings. This is because the cross section of the LAES process is suppressed at small θ (or s) (Eq. (2.29)). This higher visibility is an advantage of the LAED method in determining the molecular structures over the electron diffraction methods which measure the elastic GED patterns. In the conventional GED method with continuous electron beams, a rotating sector is usually used in order to suppress the signal intensity at small angles and to increase the visibility [10]. In the LAED method, electron diffraction patterns can be observed with high visibility without using the rotating sectors.

3.6.2 Numerical simulations

In order to confirm that the observed electron diffraction patterns reflect the geometrical structure of CCl_4, a numerical simulation was conducted by adopting KWA (Eq. (2.29)). KWA has commonly been used for calculating the differential cross section of the LAES process, and most of the experimental results reported so far are well reproduced by KWA. In KWA, the differential cross section or the angular distribution of the LAES process is given by the product of the square of the Bessel function and the field-free differential cross section (Eq. (2.36)). Because the field-free differential cross section does not depend on the parameters of the laser field, only the square of the Bessel function needs to be calculated by considering the spatio-

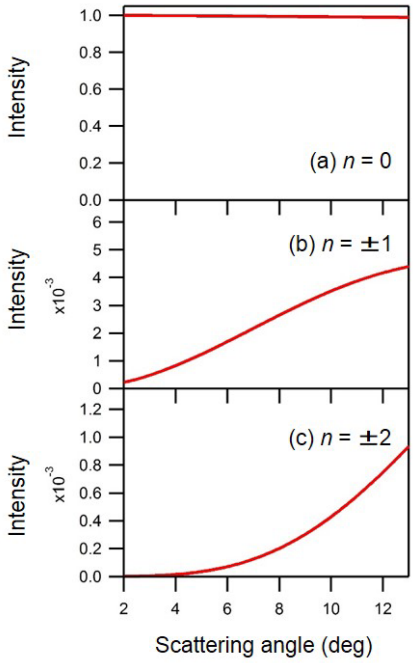

Figure 68: Spatio-temporally averaged squared Bessel functions obtained by the numerical simulation. The overlap between the laser, electron, and molecular beams are considered. Red curves show the squared bessel function for $n = 0$ (a), $n = \pm 1$ (b), and $n = \pm 2$ (c).

temporal overlap between the three beams: laser beam, electron beam, and molecular beam. Consequently, the experimental angular distribution of the LAES n-photon process is given by

$$I_n(\theta) = \langle J_n^2(\theta) \rangle \, I_{\rm el}(\theta), \tag{3.61}$$

with

$$\langle J_n^2(\theta) \rangle = \int \mathrm{d}\boldsymbol{x} \int \mathrm{d}t \rho_{\rm g}(\boldsymbol{x}) \rho_{\rm e}(\boldsymbol{x}, t) J_n^2(\boldsymbol{\alpha}_0(\boldsymbol{x}, t) \cdot \boldsymbol{s}). \tag{3.62}$$

where $I_{\rm el}(\theta)$ is an angular distribution of the elastic scattering, $\rho_{\rm g}(\boldsymbol{x})$ is the density of the molecules, and $\rho_{\rm e}(\boldsymbol{x}, t)$ is the time-dependent density of an electron beam. In what follows, the spatio-temporally averaged squared Bessel function $\langle J_n^2(\theta) \rangle$ and the angular distribution of elastically scattered electrons $I_{\rm el}(\theta)$ are calculated separately.

Simulation of squared Bessel functions

In Fig. 68, the spatio-temporally averaged Bessel functions ($n = 0, \pm 1, \pm 2$) are shown. Because of the relationship $J_{-n}(x) = (-1)^n J_n(x)$ [75], the squared Bessel function of the order n is almost identical with that of $-n$. The intensities are normalized by using the sum rule of

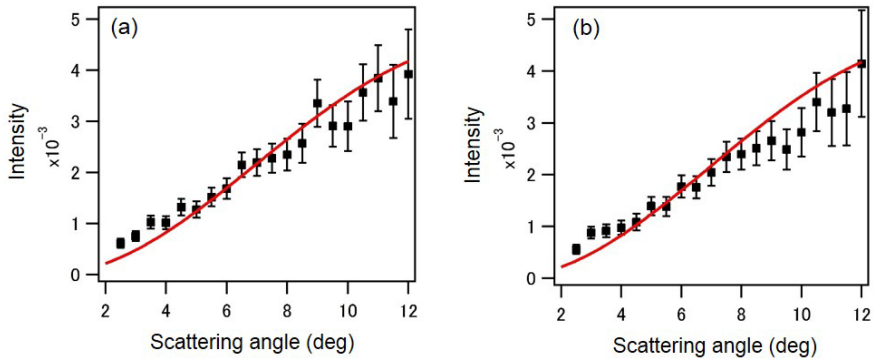

Figure 69: Spatio-temporally averaged Bessel functions for LAES $n = 1$ (a) and $n = -1$ (b) processes. Black squares show the squared Bessel functions obtained by the experiment in which Ar was used as a sample. The error bars represent one standard deviation. Red curves show the simulated squared Bessel functions. Red curves are same as that in Fig. 68 (b).

squared Bessel functions (Eq. (2.25)). As explained in Section 2.3.1, more than 99 % of the scattering events occur outside the laser field. The scattering events outside the laser field contribute only to the elastic scattering ($n = 0$). Therefore, $\langle J_0^2(\theta)\rangle$ has a value of almost 1, and $\langle J_1^2(\theta)\rangle$ and $\langle J_2^2(\theta)\rangle$ are of the order of 10^{-3}. The simulated $\langle J_n^2(\theta)\rangle$ $(n = \pm 1, \pm 2)$ is a monotonically increasing function within the detectable angular range. On the other hand, $\langle J_0^2(\theta)\rangle$ is a monotonically decreasing function. This is because the absolute value of the scattering vector (s) and the argument of the Bessel function ($\boldsymbol{s}\cdot\boldsymbol{\alpha}_0$ in Eq. (2.36)) becomes large with the increase of the scattering angle.

In order to confirm the validity of the numerical simulation of $\langle J_n^2(\theta)\rangle$, the simulated $\langle J_n^2(\theta)\rangle$ $(n = \pm 1)$ were compared with those obtained by an experiment. The experiment was done by using Ar as a sample under the same experimental condition used for the experiment of CCl_4. According to Eq. (3.61), the spatio-temporally averaged squared Bessel function can be obtained by dividing the observed angular distributions of the LAES signals by the angular distribution of the elastic scattering. Black circles in Fig. 69 show the squared Bessel function which was obtained from the experimental LAES signals of Ar. These plots agree well with the simulated squared Bessel functions shown by red lines. This agreement shows that the computational method used here can correctly evaluate the spatio-temporal averaging effect.

Simulation of angular distribution of elastically scattered electrons

The angular distribution of elastically scattered electrons in the absence of laser fields ($I_{\rm el}(\theta)$) was calculated by adopting IAM (Eq. (3.35)) and the structural parameters shown in Table 3). The scattering amplitudes, $f_{\rm C}(\theta)$ and $f_{\rm Cl}(\theta)$, for 1 keV electrons were obtained by using the ELSEPA code [128]. Because the effect of the phase shift ($\cos(\eta_{\rm C} - \eta_{\rm Cl})$ in Eq. (3.61)) is considerably small at the scattering angle region in this experiment ($2.5^\circ \leq \theta \leq 12.5^\circ$,

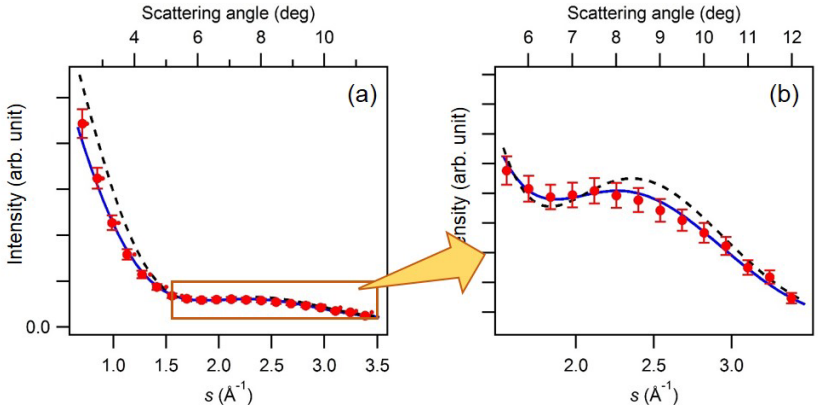

Figure 70: Angular distribution of the elastic scattering of 1 keV electrons by CCl_4. The enlarged view of the area indicated by the orange square in panel (a) is shown in panel (b). Red circles show the experimental result. Blue solid line and black broken line show the simulated results with and without the corrections to the independent atom model, respectively. The error bars represent one standard deviation.

0.7 Å^{-1} $\leq s \leq$ 3.5 Å^{-1}), it was neglected. The simulated angular distribution of elastically scattered electrons is shown by a black broken line in Fig. 70. For comparison, the angular distribution observed at $\Delta t = \pm 70$ ps is shown by red circles. Each of the simulated and experimental distributions is normalized by using the reported values at $s = 3$ Å^{-1} in Ref. [209]. The agreement between the simulated and experimental distributions is not satisfactory. The disagreement may be attributed to two effects which are not included in IAM: polarization of target molecules by incident electrons [70] and chemical bonding effect [210–212]. It has been known that due to these effects, IAM could not provide quantitatively accurate result at small scattering angles ($s < 10$ Å^{-1}). The polarization of molecules induced by the incident electrons gives rise to the long range potential and modifies the intensity at small scattering angles. The polarization effect is frequently considered by using the Buckingham potential [213],

$$V_{\rm pol}(\boldsymbol{r}) = -\frac{1}{4\pi\epsilon_0}\frac{ae^2}{2(|\boldsymbol{r}|^2+d^2)^2}, \tag{3.63}$$

where a is the dipole polarizability of the molecule, and d is the cutoff parameter. We adopted $a = 10.0$ Å^3 from Ref [214]. Formulae which give the cutoff parameter were reported by Mittleman and Watson [215], Salvat [216], and Adibzadeh and Theodosiou [217]. Here, the value of $d = 1.77$ Å (= $r_{\rm C-Cl}$) is adopted from Ref. [218]. The origin of the polarization potential is assumed to be located at the C atom. The corresponding scattering amplitude in the first Born approximation is given by [219, 220],

$$f_{\rm pol}(\theta) = \frac{2m_{\rm e}e^2}{4\pi\epsilon_0\hbar^2}\frac{\pi a}{8d}{\rm e}^{-sd}. \tag{3.64}$$

In IAM, the electron density distribution of molecules ($\rho_{\rm mol}(\boldsymbol{r})$) is assumed to be given by the sum of the free atoms (Eq. (3.17)). However, $\rho_{\rm mol}(\boldsymbol{r})$ can be modified by the creation of chemical bondings. When the change in the electron density distribution by the chemical bonding is written by $\Delta\rho(\boldsymbol{r})$, the scattering potential originating from the chemical bonding effect is given by

$$V_{\rm CBE}(\boldsymbol{r}) = \frac{e^2}{4\pi\epsilon_0}\int\frac{\Delta\rho(\boldsymbol{r}')}{|\boldsymbol{r}-\boldsymbol{r}'|}{\rm d}\boldsymbol{r}' \tag{3.65}$$

On the basis of the result of the GED experiment of CCl_4 with 50 keV electrons [10, 209], a model for $\Delta\rho(\boldsymbol{r})$ is considered. According to Ref. [10, 209], the chemical bonding effect increases the electron density distribution at the distance of 2.9 Å from a Cl atom, and decreases the electron density distribution at the distance of 3.4 Å from a Cl atom. Therefore, $\Delta\rho(\boldsymbol{r})$ is modeled as follows,

$$\Delta\rho(\boldsymbol{r}) = \sum_{j=1}^{4}\Big\{\Delta\rho_1(\boldsymbol{r}-\boldsymbol{R}_{{\rm Cl}j}) - \Delta\rho_2(\boldsymbol{r}-\boldsymbol{R}_{{\rm Cl}j}-\delta\boldsymbol{R}_j)\Big\}, \tag{3.66}$$

where

$$\Delta\rho_1(\boldsymbol{r}) = A_1\exp\Big(-\frac{|\boldsymbol{r}'|}{2w_1^2}\Big), \tag{3.67}$$

$$\Delta\rho_2(\boldsymbol{r}) = A_2\exp\Big(-\frac{|\boldsymbol{r}'|}{2w_2^2}\Big), \tag{3.68}$$

$$\delta\boldsymbol{R}_j = 0.6({\rm Å})\frac{\boldsymbol{R}_{{\rm Cl}j}-\boldsymbol{R}_{\rm C}}{|\boldsymbol{R}_{{\rm Cl}j}-\boldsymbol{R}_{\rm C}|}, \tag{3.69}$$

$\boldsymbol{R}_{{\rm Cl}j}$ is the position vector of the j-th Cl atom, and $\boldsymbol{R}_{\rm C}$ is the position vector of the C atom. A_1, A_2, w_1, and w_2 are positive parameters which are determined by the analysis below. The functions $\Delta\rho_1(\boldsymbol{r})$ and $\Delta\rho_2(\boldsymbol{r})$ represent the increase and decrease of the electron density distribution, respectively. The schematic of $\Delta\rho(\boldsymbol{r})$ is shown in Fig. 71. In order for the total charge in a molecule to be conserved, the increase in electron density ($\Delta\rho_1$) should be balanced with the decrease in electron density ($-\Delta\rho_2$),

$$\int\Delta\rho(\boldsymbol{r}){\rm d}\boldsymbol{r} = 0. \tag{3.70}$$

When the scattering amplitude from the potential in Eq. (3.65) is evaluated by first Born approximation, the scattering amplitude becomes

$$f_{\rm CBE} = \sum_{j=1}^{4}\Big\{f_{\rm CBE1}(\theta) + f_{\rm CBE2}(\theta){\rm e}^{i\boldsymbol{s}\cdot\delta\boldsymbol{R}_j}\Big\}{\rm e}^{i\boldsymbol{s}\cdot\boldsymbol{R}_{{\rm Cl}j}}, \tag{3.71}$$

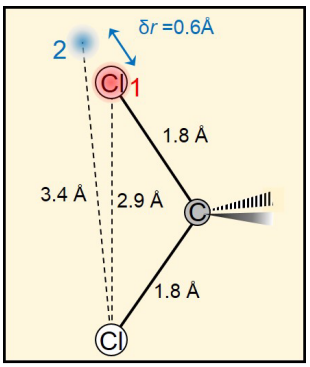

Figure 71: Schematic of $\Delta\rho(\boldsymbol{r})$ in CCl_4 induced by the chemical bonding effect. The red distribution shows the increase in the electron density, while the blue distribution shows the decrease in the electron density.

where

$$f_{\mathrm{CBE1}}(\theta) = \frac{2m_{\mathrm{e}}e^2}{4\pi\epsilon_0\hbar^2}\frac{Q}{s^2}\exp(-\frac{s^2w_1^2}{2}), \tag{3.72}$$

$$f_{\mathrm{CBE2}}(\theta) = \frac{2m_{\mathrm{e}}e^2}{4\pi\epsilon_0\hbar^2}\frac{Q}{s^2}\exp(-\frac{s^2w_2^2}{2}), \tag{3.73}$$

and

$$\begin{aligned} Q &= 4\pi\int_0^\infty r^2\Delta\rho_1(r)\mathrm{d}r \\ &= 4\pi\int_0^\infty r^2\Delta\rho_2(r)\mathrm{d}r. \end{aligned} \tag{3.74}$$

Then, the angular distribution which includes both of the polarization effect and the chemical bonding effect can be described by

$$\begin{aligned} I_{\mathrm{el}}(\theta) &= N\Big\langle\Big|\{f_{\mathrm{C}}(\theta)+f_{\mathrm{pol}}(\theta)\}\mathrm{e}^{i\boldsymbol{s}\cdot\boldsymbol{R}_{\mathrm{C}}} \\ &\quad+\sum_{j=1}^{4}\{f_{\mathrm{Cl}}(\theta)+f_{\mathrm{CBE1}}(\theta)+f_{\mathrm{CBE2}}(\theta)\mathrm{e}^{i\boldsymbol{s}\cdot\delta\boldsymbol{R}_j}\}\mathrm{e}^{i\boldsymbol{s}\cdot\boldsymbol{R}_{\mathrm{Cl}j}}\Big|^2\Big\rangle_T, \end{aligned} \tag{3.75}$$

where N is a normalization parameter, the braket ($\langle\rangle_T$) represents the averaging over the distribution of the internuclear distance ($P_{j,k}$) at the temperature of T = 300 K and the orientation of molecules. The parameters N, Q, A_1, A_2, w_1, and w_2 are determined by the least-square fitting of Eq. (3.75) to the experimental angular distribution of the elastic scattering (red circles in Fig.

70). Because A_1 and A_2 can be expressed as

$$A_1 = \sqrt{\frac{2}{\pi}} \frac{Q}{4\pi w_1^3}, \tag{3.76}$$

$$A_2 = \sqrt{\frac{2}{\pi}} \frac{Q}{4\pi w_2^3}, \tag{3.77}$$

the free parameters are N, Q, w_1 and w_2. The result of the fitting is shown in Fig. 70 as a blue curve. This curve reproduces the experimental angular distribution very well. The optimized parameters are $Q = 1.1(8)$, $w_1 = 0.4(2)$ Å, $w_2 = 0.6(1)$ Å, and $N = 1.0(1)$. From these parameters, A_1 and A_2 were determined as $A_1 = 1(2)$ Å^{-3} and $A_2 = 0.4(2)$ Å^{-3}.

Comparison with experimental results

By combining the simulated squared Bessel function ($\langle J_n^2(\theta)\rangle$) and the angular distribution of elastically scattered electrons ($I_{\mathrm{el}}(\theta)$), the angular distributions of the LAES process were calculated. The simulated angular distributions of the LAES $n = +1$ and $n = -1$ processes are shown in Figs. 66(a) and (b) as blue curves. These simulated distributions quantitatively agree with the experimental angular distributions shown by red circles. This agreement shows that the observed diffraction patterns reflect the geometrical structure of CCl_4.

A slight disagreement between the experimental and theoretical angular distributions can be seen at small scattering angles ($\theta \leq 3.5°$). The origin of the disagreement were investigated. As demonstrated in the previous subsection, the effects of the ionization and dissociation of CCl_4 are negligibly small under the experimental condition of this study. The laser-induced coupling to electronically excited states can change the geometrical structure of molecules. However, the data of photoabsorption [221] and electron energy loss spectroscopy [222] suggest that there are no electronically excited states with which the electronically ground state of the CCl_4 can strongly couple in the 800 nm laser field. Furthermore, by conducting numerical simulations, I confirmed that the observed disagreement could not be explained by the distortions of molecular structure induced by the laser field. The simulation which assumes the alignment of CCl_4 were also conducted, however, it could not reproduce the disagreement. The possible origin for causing the disagreement is the oscillation of the electron density distribution of molecules induced by the laser field. This effect is known as the light-dressing effect of target molecules (atoms), and is the main topic of the next chapter. Because KWA neglects the laser-molecule interaction, the light-dressing effect of molecules are not included. Even though it is very difficult to perform a simulation which includes the light-dressing effect of CCl_4 properly, it has been known that the light-dressing effect of atoms and molecules appears only at the small scattering angles. As will be discussed in the next subsection, the disagreement due to the light-dressing effect appearing at small scattering angles does not affect the precision of the structural determination when the higher energy (tens of keV) electrons are employed for the measurement of the LAED patterns.

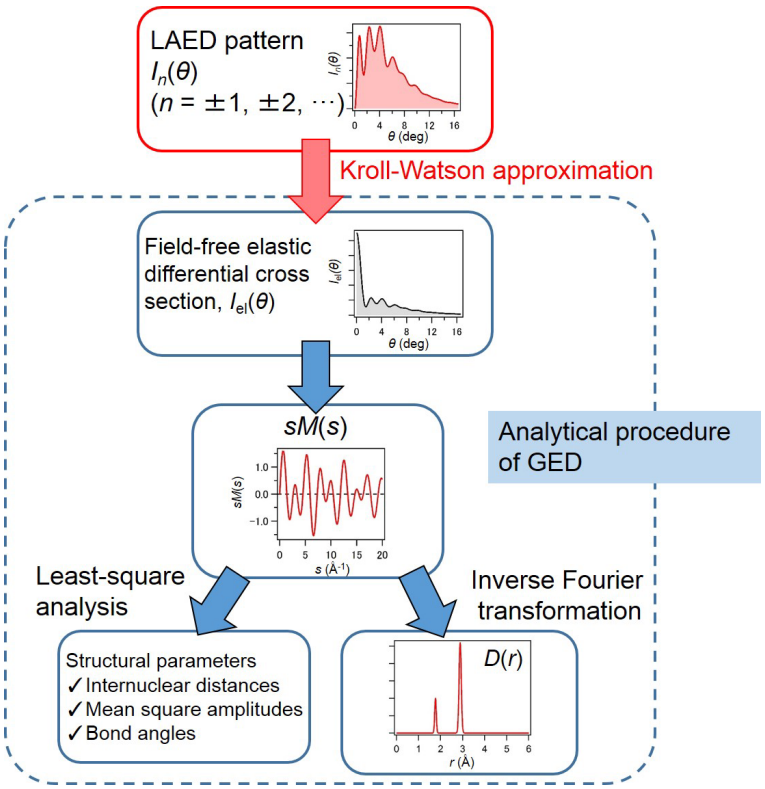

Figure 72: Analytical procedure for the determination of the geometrical structure of gas-phase molecules from the LAED patterns. By combining KWA and the established analytical procedure of GED, the instantaneous structure of gas-phase molecules can be determined with 0.01 Å spatial resolution.

3.6.3 Analytical procedures for structural determination

In this subsection, analytical procedures for the determination of the molecular structure from the LAED patterns are discussed. In Fig. 72, the analytical procedures of the LAED method are summarized. According to KWA (Eqs. (2.29) and (2.36)), a field-free GED pattern can be obtained by dividing a LAED pattern by a spatio-temporally averaged squared Bessel function. Once the field-free GED pattern is obtained, the established analytical procedures used in GED can be adopted. The analytical procedure used in the GED method with cw- and pulsed electrons were discussed in Section 3.1. The first step of the analysis is calculation of $sM(s)$ from the field-free GED pattern. Then, the geometrical structure of molecules is determined by the least square fitting or the inverse Fourier transformation of $sM(s)$. In what follows, as an example of the analysis, the observed LAED patterns of CCl_4 are analyzed and show that the geometrical structure of molecules can be determined from the LAED patterns.

By using the spatio-temporally averaged Bessel function shown in Fig. 68(b) and the scatter-

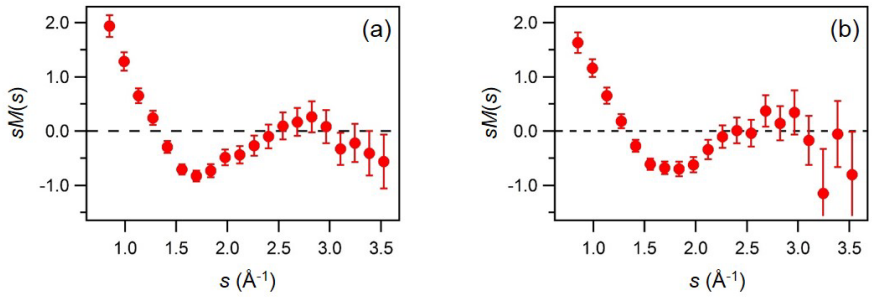

Figure 73: Modified molecular scattering intensity ($sM(s)$) calculated from the observed LAED patterns of $n = +1$ (a) and $n = -1$ (b). The error bars represent one standard deviation.

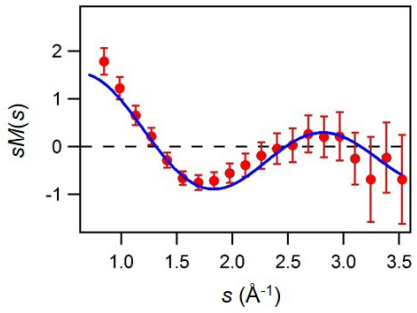

Figure 74: Least square fitting to $sM(s)$. Red circles show experimental $sM(s)$ which is an average of the two curves in Fig. 73. The error bars represent one standard deviation. Blue curve is the fitting curve.

ing amplitudes ($f_{\mathrm{C}}(\theta)$ and $f_{\mathrm{Cl}}(\theta)$) obtained by the ELSEPA code, $sM(s)$ was calculated from the observed LAED patterns ($n = \pm 1$). Figures 73(a) and (b) show the $sM(s)$ calculated from the LAED patterns of $n = +1$ and $n = -1$ processes, respectively. Because $sM(s)$ is usually discussed in the framework of IAM, the corrections to IAM, i.e., the polarization effect and the chemical bonding effect, were applied. In the following analysis, the geometrical structure of CCl_4 is determined by the two methods: the least-square fitting and the inverse Fourier transform. Because $sM(s)$ calculated from the LAED $n = +1$ (Fig. 73(a)) and $n = -1$ (Fig. 73(b)) processes are nearly identical, the average of these curves was used for the analysis.

First, the least-square fitting to the experimental $sM(s)$ was conducted. For simplicity, CCl_4 is assumed to have T_d symmetry. The distribution of the internuclear distances (the mean amplitudes, $l_{j,k}$ in Eq. (3.35)) are neglected, because they have little effect on $sM(s)$ at the small s ($s \leq 3.5$ Å) measured in this study. Consequently, only the distance between C and Cl atoms ($r_{\mathrm{C-Cl}}$) is a fitting parameter. The best fit curve is shown in Fig. 74 by a blue line. The optimized distance is $r_{\mathrm{C-Cl}}$ = 1.72 (3) Å, which is very close to the literature value (1.77 Å, Table 3). The slight disagreement may be due to the light-dressing effect of molecules which

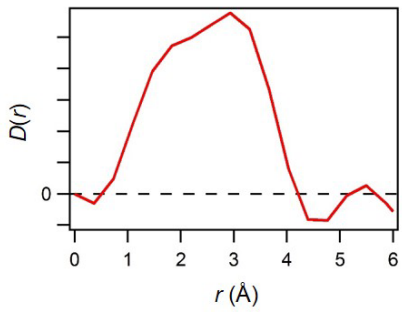

Figure 75: Radial distribution function ($D(r)$) of CCl_4 obtained by the inverse Fourier transform of $sM(s)$ which was calculated from the observed LAED patterns. The width of the distribution is determined by the observation range of s ($\Delta s \sim 3$ Å^{-1}).

was discussed in the previous subsection.

Then, the inverse Fourier transformation of $sM(s)$ was conduced to obtain the radial distribution function, $D(r)$ (Eq. (3.34)). The obtained $D(r)$ is shown in Fig. 75. Even tough the distribution is broad due to the small observation range of s ($\Delta s \sim 3$ Å^{-1}), the distribution takes a maximum value at around ~ 3 Å which corresponds to the distance between two Cl atoms. The signals appearing as a shoulder at around 1.8 Å corresponds to the between C and Cl atoms.

The results of the analyses show that the geometrical structure of molecules can be determined from the observed LAED patterns. By using higher energy electrons, the spatial resolution becomes higher. When tens of keV electrons are employed, the spatial resolution can be as high as 0.01 Å which has been achieved in the GED method with the cw- or the pulsed-electrons. This is because the deBroglie wavelength of the electrons (Eq. (1.4)) becomes shorter, and the observable range of s becomes larger with an increase of the kinetic energy. Since the $D(r)$ is given by the inverse Fourier transform of $sM(s)$, the spatial resolution improves with an increase of the observable range of s. Moreover, at large s, the deviations from the theoretical models of IAM and KWA, i.e., the charge cloud polarization, the chemical bonding effect, and the light-dressing effect of molecules, are negligibly small. Therefore, the analysis based on IAM and KWA can provide precise molecular structures. Indeed, in the GED method with cw-electron beam, the diffraction patterns at small range of s (< 5 Å^{-1}) are not usually measured or are excluded from the analysis.

3.7 Summary and future prospects

In this chapter, the first observation of the LAED patterns was reported. By measuring the LAES signals by CCl_4, clear electron diffraction patterns were observed in the angular distributions of the LAES processes with one-photon energy shifts. The observed LAED patterns were well reproduced by the numerical simulation which uses KWA and the field-free geometrical structure

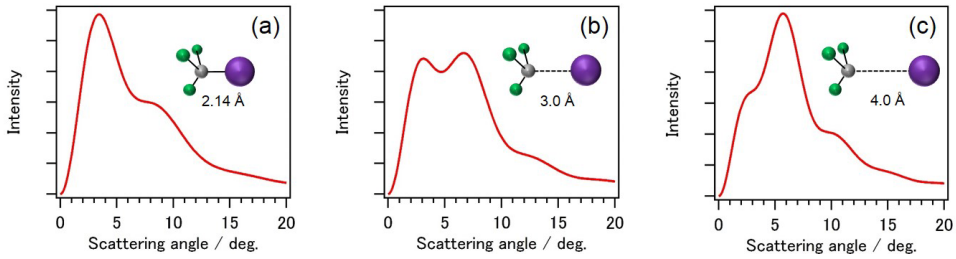

Figure 76: Simulated LAED patterns of CF_3I for different internuclear distances between C and I atoms, 2.14 Å (a), 3.0 Å (b), and 4.0 Å (c). The simulations were conducted by adopting the Kroll-Watson approximation and the independent atom model. The simulated squared Bessel function shown in Fig. 68 (b) was used for the simulation.

of CCl_4. Through the analysis of the observed LAED patterns, it was demonstrated that the geometrical structure of molecules at the moment of the laser irradiation can be determined from the LAED patterns. It has been discussed that the geometrical structure of gas-phase molecules can be determined with femtosecond temporal resolution by the ultrafast X-ray diffraction method using the X-ray free electron lasers [223, 224] and the photoelectron diffraction method using intense (near) IR laser pulses [225–227] and the ultrashort X-ray pulses [228, 229]. This study shows that the LAED method is also a promising technique for the determination of instantaneous geometrical structure of gaseous molecules. When a chemical reaction of gas-phase molecules is induced by an untrashort laser pulses and is probed by the LAED method, the temporal evolution of the geometrical structure can be determined as a series of snapshots with 0.01 Å spatial resolution. The temporal resolution of the pump-probe experiment is determined only by the laser pulse durations (Eq. (3.37)), and the temporal resolution as short as 10 fs can in principle be achieved.

Figure 76 shows the simulated LAED patterns ($n = \pm 1$) of CF_3I molecules with different C-I distances. For the simulation, IAM and KWA are adopted. The kinetic energy of the electron is 1 keV. The CF_3I molecules are assumed to be oriented randomly. The scattering amplitude are calculated by the ELSEPA code [128], and the structural parameters of CF_3I (C-I: 2.1 Å) are adopted from Ref. [230]. The structure of CF_3 moiety is assumed to be the same as that in the equilibrium state (C-I: 2.1 Å). Because the scattering intensity is higher for heavier atoms (Eq. (3.5)), the elimination of the I atom strongly modifies the LAED pattern. With the elongation of the distance between C and I atoms, peaks in the LAED pattern shifts to smaller angles. For example, the peak appearing at 3.4° (C-I: 2.1 Å) is shifted to 3.1° (C-I: 3.0 Å) and 2.4° (C-I: 4.0 Å). The peak at 9.0° is also shifted to and 6.6° (C-I: 3.0 Å), and 5.7° (C-I: 4.0 Å). This is because the oscillation period of the interference term $\sin(sr)/sr$ (Eq. 3.23) is inversely proportional to the internuclear distance r. The elimination reaction of the I atom from a CF_3I can be induced by the irradiation the third order harmonics of the Ti:sapphire laser ($\lambda \sim 266$ nm) [164]. From the ultrafast spectroscopic studies, it was found that the reaction completes within

350 fs [231, 232]. Therefore, this reaction cannot be probed by the ultrafast electron diffraction method with ultrashort electron pulses, but can be followed in real-time by the LAED method.

In this work, the accumulation of the signals for 24 hours was required to record the LAED patterns. In order to perform the pump-probe experiment, the accumulation time should be shortened by at least one order of magnitude. Moreover, in order to observe the LAES patterns with tens of keV electrons, the sensitivity should be further increased by one order of magnitude. This is because the cross section of the elastic scattering becomes one order of magnitude smaller than that of 1 keV. Therefore, the improvement of the sensitivity by two orders of magnitude should be achieved in order to perform the pump-probe experiment with tens of keV electrons. The increase in sensitivity by two order of magnitude will be attainable by improving the analyzer, laser system, and molecular beam. The collection efficiency of the toroidal analyzer (~ 1 %) is determined by the transmission efficiency of the slit placed in front of the analyzer. By using an analyzer which does not have thin slits [233], the collection efficiency and the sensitivity will be improved a hundredfold. The repetition rate of the laser system limits the signal count rate. The use of the state-of-the-art high power and high repetition rate ultrashort laser sources [234–237] will increase the signal count rate. In this study, the molecular beam is introduced continuously into the chamber. By introducing the molecular beam as a pulse [238], the density of molecules at the moment when the electron and laser pulses reach the scattering point will be increased by about ten times without an increase of the background pressure.

The LAED method can also be used for solid-state samples. The solid samples which satisfy the following two conditions are suitable for the LAED method, (i) thin (≤ 100 nm) enough for observing transmission electron diffraction patterns and (ii) almost transparent to NIR or IR laser light in order for preventing a damage from laser pulses used for inducing the LAES process. The temporal resolution of the ultrafast electron diffraction method with ultrashort electron pulses is mainly determined by the duration of the electron pulse in the case of the thin solid samples (Section 3.2.2). However, it is highly difficult to generate the ultrashort electron pulses whose durations are less than tens of femtosecond. By using the LAED method, it will be possible to achieve 10 fs or shorter temporal resolution without using ultrashort electron pulses.

By taking advantage of the LAED method, the deformation of molecular structure in intense laser fields [104–108] can also be investigated. From the LAED patterns measured with more intense ($\sim 10^{14}$ W/cm^2) laser fields, we can determine the structure of gas-phase molecules in intense laser fields, which is useful in understanding of strong field induced molecular processes. Because the LAED patterns carry the information of the geometrical structure of molecules only in the presence of laser fields, the LAED method is an ideal technique to study the deformation of geometrical structure in intense laser fields.

4 Light-dressing effect of target atoms in laser-assisted electron scattering

In the laser-assisted electron scattering (LAES) process, three kinds of interactions take place simultaneously (Fig. 7): laser-electron, laser-atom and electron-atom interactions. As discussed in Section 2.1, the laser-atom interaction is not prerequisite for electrons to change their kinetic energies in the LAES process. In the Kroll-Watson approximation (KWA) [67] which has been most commonly employed for simulating the LAES signals, the laser-atom interaction is neglected. In KWA, laser fields interact only with incident electrons, and the LAES process is considered as a scattering of light-dressed electrons by un-dressed atoms. The terms "light-dressing" and "light-dressed" represent the states which are strongly disturbed by the laser fields. Because the intensities and frequencies of the laser fields used in the conventional LAES experiments were relatively low ($\leq 10^9$ W/cm^2) and far below the resonance frequency of the optical transition of atoms, most of the experimental results reported so far were quantitatively reproduced by numerical simulations based on KWA.

When the intensity of the laser field is strong or the frequency of the laser field is near the resonance frequency of the electronic transition of atoms, the laser-atom interaction cannot be neglected. In such a laser field, atoms are in the light-dressed states and their electron density distributions are distorted through the interaction with the laser field. Consequently, the LAES process which occurs in such a laser field is described as the scattering of light-dressed electrons by light-dressed atoms. In Figs. 77 (a) and (b), simulated electron density distributions of H atom and Xe atom in a strong static electric field (3×10^9 V/m, which corresponds to a peak field amplitude of a laser field with a peak field intensity of $I \sim 10^{12}$ W/cm^2) are shown. Even though the modifications of the electron density distributions by the electric field are very weak and can be recognized only after the subtraction of the electron density distributions in the absence of the field (Figs. 77 (c) and (d)), the deformations of the electron density distributions play an important role in the atomic and molecular processes induced by intense laser fields [239]. Because the electrons scattered by atoms carry the information of the electron density distribution of the atoms (Section 1.1), the LAES signals can be modified reflecting the electron density distribution of the light-dressed atoms. The light-dressing effect of target atoms, i.e., the modification of the LAES signals originating from the formation of the light-dressed atoms, will be useful for investigating the electron density distribution of atoms and molecules deformed by the laser fields. However, the light-dressing effect of target atoms appearing in the LAES signals has not been observed yet, even though it has been studied theoretically for more than 30 years. In this study, the observation of the light-dressing effect of target atoms appearing in the LAES signals is reported for the first time.

In Section 4.1, I discuss the information of the electron density distribution which can be

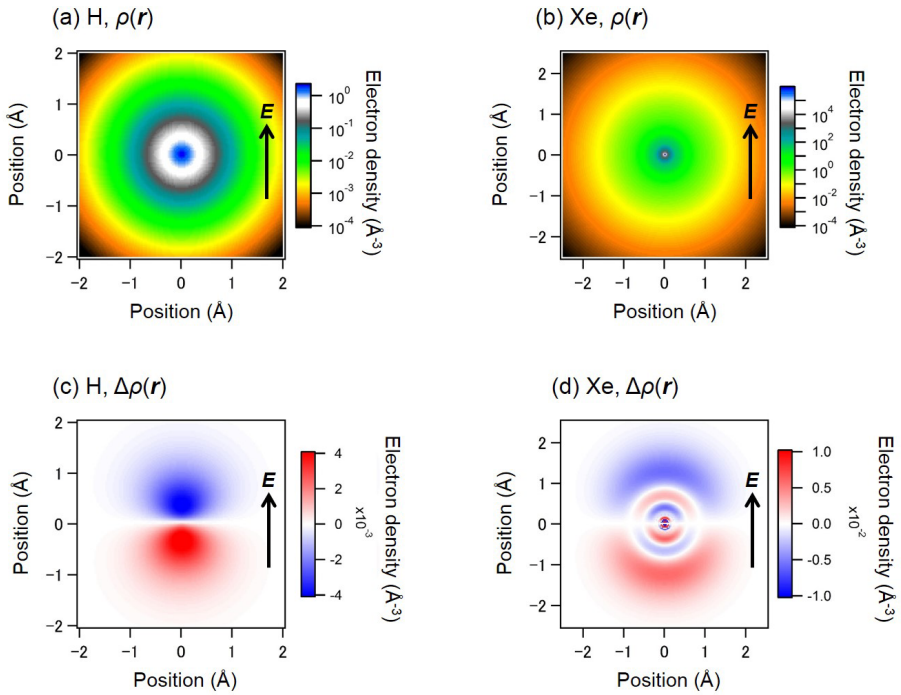

Figure 77: Deformation of the electron density distributions induced by an intense electric field. The cross sections of simulated electron density distributions of H atom and Xe atom in a DC electric field (3×10^9 V/m) are shown in panels (a) and (b), respectively. Panels (c) and (d) show the changes in the electron density distributions of H and Xe induced by the electric field. The arrows shown in the panels represent the direction of the electric field. The calculation of the electron density distributions were conducted by using the Gaussian 09 program [240] at the levels of B3LYP/aug-cc-pVQZ for H atom and B3YLP/AQZP [241] for Xe atom. The spatial distribution of the modified electron density distribution of Xe (panel (d)) shows the internal structure.

obtained from the electrons elastically scattered by atoms and molecules without laser fields. In Section 4.2, the theoretical and experimental studies on the light-dressing effect of target atoms appearing in the LAES signals are described. The purpose and the abstract of this study are described in Section 4.3. Then, in Section 4.4, I describe the improvements of the apparatus done for the observation of the light-dressing effect of target atoms. The experimental data and a result of a numerical simulation are presented in Section 4.5. Finally, in Section 4.6, I describe a summary of this study and discuss a possibility for determining the electron density distribution deformed by laser fields.

4.1 Investigation of electron density distributions by electron scattering

In this section, I give an introduction to experimental and theoretical studies on the electron density distribution of atoms and molecules by the electron scattering. The discussion of this

section is focused on the elastic scattering by atoms and molecules without laser fields.

4.1.1 Determination of electron density distribution of atoms

When the kinetic energy of the incoming electron is so high that the first-Born approximation (FBA, Section 3.1) becomes applicable, the electron density distribution of an atom can be determined from the angular distribution of scattered electrons. The angular distribution of the scattered electrons in FBA are given by using Eq. (3.9),

$$\frac{\mathrm{d}\sigma_{\mathrm{el}}}{\mathrm{d}\Omega} = \left|\frac{2}{a_0}\left(\frac{Z - A(\theta)}{s^2}\right)\right|^2, \tag{4.1}$$

where Z is the atomic number, a_0 is the Bohr radius, and $A(\theta)$ is the atomic scattering factor. By rearranging this equation, the atomic scattering factor is given by

$$\begin{aligned} A(\theta) &= Z - \frac{a_0}{2}\sqrt{s^4\frac{\mathrm{d}\sigma_{\mathrm{el}}}{\mathrm{d}\Omega}} && (4.2)\\ &\equiv F(s), && (4.3) \end{aligned}$$

Because the differential cross section ($\mathrm{d}\sigma_{\mathrm{el}}/\mathrm{d}\Omega$) can be determined experimentally, $F(s)$ can be obtained from an experiment. By using the definition of the atomic scattering factor (Eq. (3.6)), this equation becomes

$$\int_0^\infty 4\pi r^2 \rho_{\mathrm{atom}}(r)\frac{\sin(sr)}{r}\mathrm{d}r = sF(s), \tag{4.4}$$

where $\rho_{\mathrm{atom}}(r)$ is the electron density distribution of the atom. By conducting the inverse Fourier transformation of this equation, the following formula can be obtained,

$$4\pi r^2 \rho_{\mathrm{atom}}(r) = \frac{2r}{\pi}\int_0^\infty sF(s)\sin(sr)\mathrm{d}s. \tag{4.5}$$

This equation states the radial distribution function of atomic electrons ($D(r) \equiv 4\pi r^2\rho_{\mathrm{atom}}(r)$) can be determined by analyzing the angular distribution of the scattered electrons. The first experimental study on the electron density distribution of an atom by the electron scattering was reported by Bartell and Brockway in 1953 [4]. They measured the angular distribution of 40 keV electrons scattered by Ar. They fit the experimental $F(s)$ by a polynomial, and obtained the radial distribution function of an electron density distribution of Ar by conducting the inverse Fourier transform of the fitting curve.

In Fig. 78, schematics of the radial distribution functions ($D(r)$) and corresponding atomic scattering factors ($F(s)$) are shown. Because $D(r)$ and $F(s)$ are related by the Fourier transformation, the atomic scattering factor of electrons distributed near a nucleus (marked as A) has a broad distribution. On the other hand, the atomic scattering factor of electrons which are broadly distributed (marked as C) has a narrow distribution around $s = 0$. This means that in or-

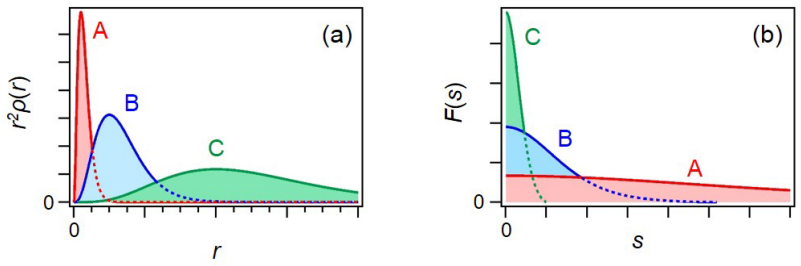

Figure 78: Schematic of the radial distribution function of atomic electrons (a) and corresponding atomic scattering factors (b) [4]. The length from an atomic nucleus is represented by r. The absolute value of the scattering vector is represented by s.

der to investigate electron density distributions near the nucleus, the angular distribution should be measured over a large scattering angle range.

4.1.2 Investigation of electron density distribution of gas-phase molecules

From observed angular distributions of electrons scattered by gas-phase molecules, electron density distributions of the molecules can be investigated. As discussed in the previous subsection, the electron density distribution of atoms can be determined by the Fourier analysis. However, it was demonstrated mathematically that the electron density distribution of molecules cannot be determined uniquely from the angular distributions of scattered electrons [7]. The investigation of the electron density distribution of molecules requires a comparison with simulated angular distributions which are calculated by using theoretically obtained electron density distributions. By the comparison, one can judge the validity of the theoretical electron density distributions [121].

The experimental studies on the electron density distributions of molecules by the electron scattering began in the mid-1960s. Most of the experimental studies focused on the observation of a deviation between the experimental angular distribution and theoretical angular distribution calculated by using the independent atom model (IAM, Section 3.1). Because an electron density distribution of a molecule used in IAM is assumed to be given by the sum of the spherical electron density distributions of atoms (Eq. (3.17)), the deviation reflects the modification of the electron density distribution due to the formation of chemical bonds, and therefore, is called chemical bonding effect. The first observation of the chemical bonding effect was reported by Geiger in 1964 [210] and Bonham and Iijima in 1965 [211] independently. Since then, the chemical bonding effect has been investigated for a wide variety of gas-phase molecules [121, 242]. In general, the chemical bonding effect mainly appears at small scattering angles. This can be understood from the classical relationship between the scattering angle and the impact parameter of an incident electron. When an electron comes close to an atomic nucleus

(small impact parameter), the electron is deflected at a large angle by the strong Coulombic field near the nucleus. On the other hand, when an electron passes far from the nucleus, the electron is deflected at a small angle by the weak Coulombic field which is shielded by the molecular electrons [10]. Therefore, the electrons scattered at small scattering angles strongly reflect the electron density distribution of molecules.

4.2 Theoretical and experimental studies on light-dressing effect of target atoms

As discussed in the previous section, the angular distribution of the scattered electrons carries the information of the electron density distribution of atoms and molecules. When atoms and molecules are exposed to intense laser fields, the electron density distributions of atoms and molecules are deformed through the laser-atom and laser-molecule interactions. Accordingly, the angular distributions of the electrons scattered by atoms and molecules inside the laser fields can also be modified. If we can detect this light-dressing effect, the modification of the electron density distributions induced by intense laser fields can be investigated. In this section, I give an introduction to theoretical and experimental studies on the light-dressing effect of atoms appearing in the angular distribution of the LAES process.

Theoretical studies on the light-dressing effect

The theoretical studies on the light-dressing effect of target atoms in the LAES process has been reported since the mid-1970s. The early theoretical works were reported by Gersten and Mittleman [243], and Mittleman [244–247], Zon [248], Deguchi, Taylor, and Yaris [249], Lami and Rahman [250, 251], and Beilin and Zon [252]. The detailed calculation of the light-dressing effect appearing in the angular distribution of the LAES process was reported by Byron and Joachain in 1984 [48]. They calculated the angular distributions of the LAES $n = 0, \pm 1$ processes in a non-resonant intense laser field ($I = 1.3 \times 10^{13}$ W/cm^2, $\lambda = 620$ nm). The target atom is a hydrogen atom, and the kinetic energy of an incident electron is 100 eV. They adopted the first-order perturbation theory and FBA to the laser-atom interaction and the electron-atom interaction, respectively. They compared the angular distributions of the LAES processes calculated with and without the light-dressing effect of target atoms. They found that only when the light-dressing effect is taken into account, an intense peak appears at the small scattering angle range ($\theta \leq 4^\circ$) in the angular distribution of the LAES $n = \pm 1$ processes. Similar small-angle peak profiles can also be found in the angular distribution calculated by Dubois, Maquet, and Jetzke [253]. They also used the first-order perturbation theory for treating the laser-atom interaction.

The theories which can treat the laser-atom interaction non-perturbatively were also developed. The Born-Floquet theory developed by Faisal [60] and the non-Hermitian Born-Floquet theory developed by Dörr *et al.* [254] are the theories which can evaluate the light-dressing effect in the LAES process of high energy (≤ 100 eV) electrons. Dörr *et al.* compared the light-dressing effect of target atoms evaluated by the non-perturbative theory and that evaluated

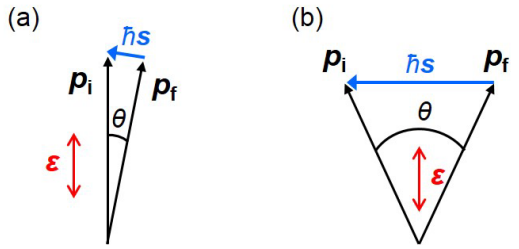

Figure 79: Critical geometries where the differential cross section of the LAES process ($n \neq 0$) in the Kroll-Watson approximation vanishes. (a) The direction of the incoming electron is parallel to the laser polarization direction. The electrons are scattered at small angles. (b) The scattering angle is bisected by the laser polarization vector. $\boldsymbol{p}_\mathrm{i}$ and $\boldsymbol{p}_\mathrm{f}$: momenta of the incoming and scattered electron. θ: scattering angle. $\boldsymbol{s}$: scattering vector. $\boldsymbol{\epsilon}$: polarization vector of the laser field.

by the first-order perturbation theory. They found that when the frequency of the laser field is far off the resonance frequency of the optical transition of target atoms, the simulated result of the first-order perturbation theory shows a good agreement with that calculated by the non-perturbative theory at the the laser field intensity of 1.3×10^{13} W/cm^2 and 5×10^{13} W/cm^2. Their study shows that the first-order perturbation theory is evaluate to analyze the light-dressing effect of target atoms induced by non-resonant and not so strong ($< 10^{14}$ W/cm^2) laser fields. For the LAES process of slow electrons, the R-matrix Floquet theory [255, 256] can be used for evaluating the laser-atom interaction non-perturbatively.

Experimental studies on the light-dressing effect

As described in Section 2.2, the conventional LAES experiments were conducted by cw- or pulsed-CO_2 lasers ($\lambda = 10.6$ μm) with the field intensity less than 10^9 W/cm^2. Because the laser-atom interaction is negligibly small at the relatively moderate intensity and the long wavelength, most of the experimental results were well reproduced by KWA. The exceptions which cannot be reproduced by KWA were reported by Wallbank and Holmes in 1993 and 1994 [93–95]. They measured the LAES signals in the two special geometrical arrangements that are called as critical geometries (Fig. 79). At the first critical geometry (Fig. 79(a)), the direction of the incident electron ($\boldsymbol{p}_i$) is parallel to the electric field vector ($\boldsymbol{\epsilon}$), and the electron is scattered at a small angle. At the second critical geometry (Fig. 79(b)), the electric field vector $\boldsymbol{\epsilon}$ bisects the scattering angle (θ). At these geometries, the scattering vector $\boldsymbol{s}$ is nearly perpendicular to the electric field vector $\boldsymbol{\epsilon}$, and the argument of the Bessel function (Eq. (2.29)) becomes almost zero. Therefore, at the critical geometries, the differential cross section of the LAES process ($n \neq 0$) given by KWA (Eq. (2.29)) almost vanishes. However, the differential cross sections measured by Wallbank and Holmes are several orders of magnitude higher than that given by KWA. They suggested that the observed discrepancies may be due to the light-dressing effect of target atoms. Their experimental results stimulated a number of theoretical works.

The light-dressing effect of target atoms under the experimental condition of Wallbank and Holmes (I = 10^8 W/cm^2, $\lambda = 10.6$ μm) was theoretically evaluated by Rabadán, Méndez, and Dickinson [257], Geltman [258], and Varró and Ehlotzky [259]. They found that the light-dressing effect under the experimental condition is too small to account for the observed discrepancies. Even though the theoretical efforts to understand the origin of the observed discrepancies were extensively made [260–269], the exact origin is still under debate. Several theoretical works suggested that the discrepancy might be the experimental error due to the double scattering [264, 269, 270].

Very recently, Musa *et al.* reported the experimental result which also shows a significant discrepancy from the prediction of KWA at the second critical geometry (Fig. 79(b)) [99]. They measured the differential cross section of the LAES process by CO_2 molecules in a microsecond CO_2 molecules laser field. They suggested that the light-dressing effect of CO_2 may be an origin of the observed discrepancy. However, because there are no theoretical studies on their experimental results, the origin of the observed deviation is obscure. On the other hand, the experimental result reported by deHarak *et al.* agrees well with the prediction of KWA at the second critical geometry. They investigated the LAES process by He in a nanosecond intense laser field ($\lambda = 1.06$ μm, $I = 5 \times 10^9$ W/cm^2). Even though the intensity and the wavelength of the laser field is higher and shorter than those of the conventional LAES experiments with the CO_2 lasers, the LAES signal intensity observed by deHarak *et al.* is consistent with the signal intensity calculated by using KWA. Accordingly, it could be stated that the light-dressing effect of target atoms appearing in the LAES signals has not been observed yet.

4.2.1 Theoretical model

This subsection is devoted to the introduction of the theoretical model given by Zon in 1977 [248]. His model includes the light-dressing effect of target atoms in the simplest way.

In general, the scattering potential of an atom whose electron density distribution is modified by a laser field is given by

$$V_{\mathrm{TE}}(\boldsymbol{r},t) = -\frac{1}{4\pi\epsilon_0}\frac{Ze^2}{|\boldsymbol{r}|} + \frac{e^2}{4\pi\epsilon_0}\int \frac{\rho_{\mathrm{atom}}(\boldsymbol{r}',t)}{|\boldsymbol{r}-\boldsymbol{r}'|}\mathrm{d}\boldsymbol{r}', \tag{4.6}$$

where $\rho_{\mathrm{atom}}(\boldsymbol{r},t)$ is the time-dependent electron density distribution. When the electron density distribution is expressed as

$$\rho_{\mathrm{atom}}(\boldsymbol{r},t) = \rho^{(0)}(\boldsymbol{r}) + \Delta\rho(\boldsymbol{r},t), \tag{4.7}$$

the scattering potential is divided into two parts,

$$V_{\mathrm{TE}}(\boldsymbol{r},t) = V_{\mathrm{atom}}(\boldsymbol{r}) + V_{\mathrm{dress}}(\boldsymbol{r},t), \tag{4.8}$$

with

$$V_{\rm atom}(\boldsymbol{r}) = -\frac{1}{4\pi\epsilon_0}\frac{Ze^2}{|\boldsymbol{r}|} + \frac{e^2}{4\pi\epsilon_0}\int \frac{\rho^{(0)}(\boldsymbol{r}')}{|\boldsymbol{r}-\boldsymbol{r}'|}{\rm d}\boldsymbol{r}', \tag{4.9}$$

and

$$V_{\rm dress}(\boldsymbol{r},t) = \frac{e^2}{4\pi\epsilon_0}\int \frac{\Delta\rho(\boldsymbol{r}',t)}{|\boldsymbol{r}-\boldsymbol{r}'|}{\rm d}\boldsymbol{r}', \tag{4.10}$$

where $\rho^{(0)}(\boldsymbol{r})$ is the electron density distribution of the atom in the absence of the laser field, $\Delta\rho(\boldsymbol{r},t)$ represents the modification of the electron density distribution induced by the laser field, $V_{\rm atom}(\boldsymbol{r})$ is the scattering potential of the atom without laser fields, and $V_{\rm dress}(\boldsymbol{r},t)$ is the scattering potential which gives rise to the light-dressing effect of the target atom.

Zon's model

It has been known that the term $1/|\boldsymbol{r}-\boldsymbol{r}'|$ appearing in Eq. (4.10) can be expanded as follows [271].

$$\frac{1}{|\boldsymbol{r}-\boldsymbol{r}'|} = \frac{1}{|\boldsymbol{r}|}\sum_{l=0}^{\infty}\Big(\frac{|\boldsymbol{r}'|}{|\boldsymbol{r}|}\Big)^l P_l(\cos\theta'), \tag{4.11}$$

where $P_l(\cos\theta')$ is the Legendre polynomial and θ' is the angle between the two vectors $\boldsymbol{r}$ and $\boldsymbol{r}'$. By using the law of cosines, $\cos\theta'$ is given by

$$\cos\theta' = \frac{\boldsymbol{r}\cdot\boldsymbol{r}'}{|\boldsymbol{r}||\boldsymbol{r}'|}. \tag{4.12}$$

By substituting Eq. (4.11) into Eq. (4.10), the scattering potential of the light-dressing effect becomes

$$V_{\rm dress}(\boldsymbol{r},t) = \frac{e^2}{4\pi\epsilon_0}\sum_{l=0}^{\infty}\frac{1}{|\boldsymbol{r}|^{l+1}}\int \Delta\rho(\boldsymbol{r}',t)|\boldsymbol{r}'|^l P_l(\cos\theta'){\rm d}\boldsymbol{r}'. \tag{4.13}$$

By using the relationship $P_0(x)=1$, the leading term ($l=0$) of $V_{\rm dress}(\boldsymbol{r},t)$ is given by

$$V_{\rm dress}^{(l=0)}(\boldsymbol{r},t) = \frac{e^2}{4\pi\epsilon_0}\frac{1}{|\boldsymbol{r}|}\int \Delta\rho(\boldsymbol{r}',t){\rm d}\boldsymbol{r}'. \tag{4.14}$$

Because of the conservation of the charge,

$$\int \Delta\rho(\boldsymbol{r}',t){\rm d}\boldsymbol{r}' = 0, \tag{4.15}$$

the leading term $V_{\rm dress}^{(l=0)}(\boldsymbol{r},t)$ vanishes. Then, by using the the relationship $P_1(x)=x$, the second term $(l=1)$ is given by

$$V_{\rm dress}^{(l=1)}(\boldsymbol{r},t) = \frac{e}{4\pi\epsilon_0}\frac{\boldsymbol{r}}{|\boldsymbol{r}|^3}\cdot\int \boldsymbol{r}' e\Delta\rho(\boldsymbol{r}',t){\rm d}\boldsymbol{r}'. \tag{4.16}$$

The term $\int \boldsymbol{r}' e\Delta\rho(\boldsymbol{r}', t)\mathrm{d}\boldsymbol{r}'$ represents a dipole induced in the target atom. In the Zon's model, non-linear effects in the induced dipole are neglected. Then, the induced dipole is given by

$$\int \boldsymbol{r}' e\Delta\rho(\boldsymbol{r}', t)\mathrm{d}\boldsymbol{r}' = a(\omega)\boldsymbol{F}(t), \tag{4.17}$$

where $a(\omega)$ is the dipole polarizability of the atom at the frequency of ω and $\boldsymbol{F}(t)$ is the electric field vector of the laser light (Eq. (2.16)). This potential $V_{\mathrm{dress}}^{(l=1)}(\boldsymbol{r}, t)$ represents the interaction between the incoming electron and an induced dipole in the atom. In the Zon's model, $V_{\mathrm{dress}}^{(l=1)}(\boldsymbol{r}, t)$ is adopted for representing the light-dressing effect of target atoms. By using Eq. (2.16), $V_{\mathrm{dress}}(\boldsymbol{r}, t)$ in the Zon's model can be expressed as

$$V_{\mathrm{dress}}(\boldsymbol{r}, t) = -\frac{e}{4\pi\epsilon_0}\frac{a(\omega)F_0}{r^3}(\boldsymbol{\epsilon}\cdot\boldsymbol{r})\sin\omega t, \tag{4.18}$$

where F_0 is the amplitude of the electric field of the laser light, $\boldsymbol{\epsilon}$ is the unit vector which represents the laser polarization direction.

In the Zon's model, the scattering amplitude of the LAES process is evaluated by using FBA. By substituting the scattering potential (Eq. (4.8)) into Eq. (2.20), the differential cross section of the LAES process with an energy shift of n-photon is given by

$$\frac{\mathrm{d}\sigma_n^{\mathrm{B1}}}{\mathrm{d}\Omega} = \frac{|\boldsymbol{p}_{\mathrm{f},n}|}{|\boldsymbol{p}_{\mathrm{i}}|}\Big|f_{\mathrm{atom}}(\theta)J_n(\xi) - f_{\mathrm{dress}}(\theta)\Big(J_{n-1}(\xi) - J_{n+1}(\xi)\Big)/2\Big|^2, \tag{4.19}$$

with

$$f_{\mathrm{atom}}(\theta) = \frac{2}{a_0}\Big(\frac{Z - A(\theta)}{s^2}\Big), \tag{4.20}$$

$$f_{\mathrm{dress}}(\theta) = \frac{2a(\omega)}{a_0 e}\frac{F_0}{s^2}(\boldsymbol{\epsilon}\cdot\boldsymbol{s}), \tag{4.21}$$

and

$$\xi = \boldsymbol{\alpha}_0\cdot\boldsymbol{s} \tag{4.22}$$

$$= \frac{eF_0}{m_{\mathrm{e}}\omega^2}(\boldsymbol{\epsilon}\cdot\boldsymbol{s}), \tag{4.23}$$

where $f_{\mathrm{atom}}(\theta)$ is the amplitude of the elastic scattering without the laser field (Eq. (3.5)), $f_{\mathrm{dress}}(\theta)$ is the scattering amplitude by the potential of V_{dress}, and a_0 is the Bohr radius. By using the definition of ξ (Eq. (4.23)), $f_{\mathrm{dress}}(\theta)$ can be re-written as

$$f_{\mathrm{dress}}(\theta) = \frac{2m_{\mathrm{e}}\omega^2 a(\omega)}{a_0 e}\frac{\xi}{s^2}. \tag{4.24}$$

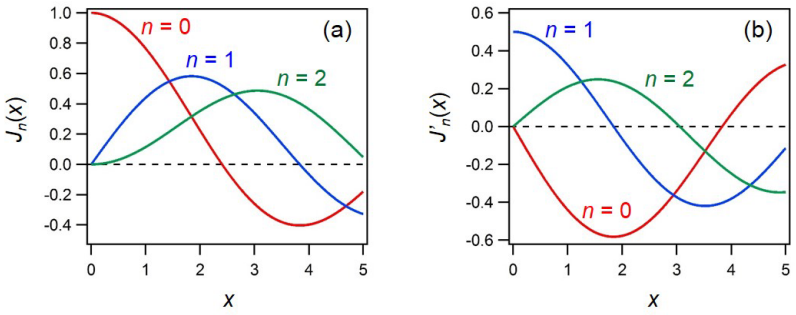

Figure 80: Bessel functions and the derivatives of the Bessel function. Panel (a) shows the Bessel functions of the first kind ($J_n(x)$) for $n = 0$ (red), $n = 1$ (blue), and $n = 2$ (green). Panel (b) shows the derivative of the Bessel functions of the first kind ($J'_n(x)$) for $n = 0$ (red), $n = 1$ (blue), and $n = 2$ (green).

Moreover, by using the relationship [75],

$$2J'_n(x) = J_{n-1}(x) - J_{n+1}(x), \tag{4.25}$$

Equation (4.19) can also be expressed as

$$\frac{\mathrm{d}\sigma_n^{\mathrm{Zon}}}{\mathrm{d}\Omega} = \frac{|\boldsymbol{p}_{\mathrm{f},n}|}{|\boldsymbol{p}_{\mathrm{i}}|}\left|f_{\mathrm{atom}}(\theta)J_n(\xi) - f_{\mathrm{dress}}(\theta)J'_n(\xi)\right|^2, \tag{4.26}$$

where $J'_n(x)$ is the derivative of the n-th order Bessel function of the first kind. Because of the relationships, $J_{-n}(x) = (-1)^n J_n(x)$ and $J'_{-n}(x) = (-1)^n J'_n(x)$, the light-dressing effect of target atoms appearing in the angular distribution of the LAES process with a n-photon energy shift is nearly identical to that appearing in the angular distribution of the LAES process with a $-n$-photon energy shift within the Zon's model.

Light-dressing effect in Zon's model

By using Eqs. (4.20), (4.21) and (4.26), the dependence of the light-dressing effect on θ (or s) and n is discussed. Equation (4.21) shows that $f_{\mathrm{dress}}(\theta)$ has the dependence of s^{-1}. On the other hand, as demonstrated below, $f_{\mathrm{atom}}(\theta)$ has the dependence of s^0 at small scattering angles. Therefore, the light-dressing effect becomes significant at small scattering angles.

The asymptotic form of $f_{\mathrm{atom}}(\theta)$ at $\theta \sim 0$ can be obtained by using the relation of the

spherical Bessel function [75],

$$\begin{aligned}\frac{\sin x}{x} &= \sum_{k=0}^{\infty}\frac{(-1)^k}{(2k+1)!}x^{2k} \\ &= 1-\frac{1}{6}x^2+\cdots . \end{aligned} \tag{4.27}$$

By using the definition of the atomic scattering factor ($A(\theta)$, Eq. (3.6)), $A(\theta)$ can be expanded as

$$\begin{aligned}A(\theta) &= 4\pi\int_0^{\infty}\rho_{\rm atom}(r)r^2{\rm d}r-\frac{s^2}{6}4\pi\int_0^{\infty}\rho_{\rm atom}(r)r^4{\rm d}r+\cdots \\ &= Z-\frac{s^2}{6}4\pi\int_0^{\infty}\rho_{\rm atom}(r)r^4{\rm d}r+\cdots . \end{aligned} \tag{4.28}$$

Therefore, $f_{\rm atom}(\theta)$ becomes

$$f_{\rm atom}(\theta)=\frac{2}{a_0}\frac{4\pi}{6}\int_0^{\infty}\rho_{\rm atom}(r)r^4{\rm d}r+\cdots , \tag{4.29}$$

and has the dependence of s^0.

The Bessel function and its derivative in Eq. (4.26) give the n-dependence of the light-dressing effect of target atoms. In Fig. 80, the Bessel function ($J_n(x)$) and the derivative of the Bessel function ($J_n'(x)$) are plotted for $n=0,1,2$. For $n=+1$, the Bessel function ($J_1(x)$) becomes zero at $x=0$. On the other hand, the derivative of the Bessel function ($J_1'(x)$) takes a maximum value (0.5) at $x=0$. This means that the second term in the square modulus of the right-hand side of Eq. (4.26), which represents the light-dressing effect, dominates the differential cross section of the LAES $n=+1$ process at the scattering angles near 0°. Because the derivative of the Bessel function ($J_n'(x)$) for $n=0$ and $n=+2$ becomes zero at $x=0$, the light-dressing effects of target atoms appearing in the differential cross section of the LAES $n=0$ and $n=+2$ processes are much smaller than that of the LAES $n=+1$ process.

Laser parameter dependence of the light-dressing effect of atoms

By using Eq. (4.26), the the laser parameter dependence of the light-dressing effect is considered. When the frequency ω is far below the resonance frequency of the target atom, the polarizability $a(\omega)$ is approximated by the static polarizability ($a_{\rm s}$) and its frequency dependence can be neglected. Then, the laser parameter dependence can be obtained by expanding the Bessel function using Eq. (2.23). The laser parameter dependences of the first and second terms in the square modulus of the right-hand side of Eq. (4.26) are given by

$$f_{\rm atom}(\theta)J_n(\xi)\propto(\sqrt{I}\lambda^2)^{|n|}, \tag{4.30}$$

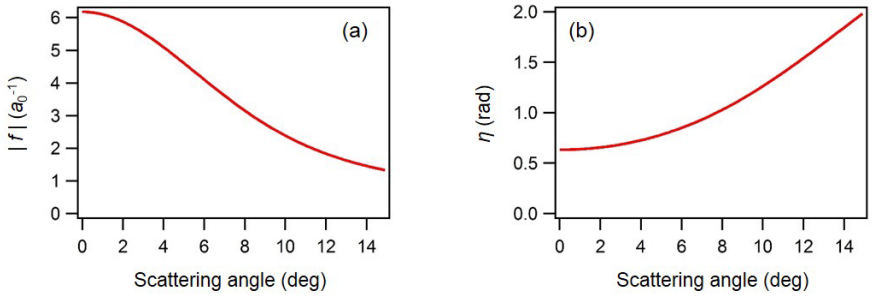

Figure 81: Simulated scattering amplitude of the 1 keV electron by Xe. The simulation was conducted by the ELSEPA code [128]. Panel (a) shows the magnitude of the scattering amplitude. Panel (b) shows the phase of the scattering amplitude.

$$f_{\mathrm{dress}}(\theta)J'_n(\xi) \propto (\sqrt{I})^{|n|}\lambda^{2|n|-2}, \tag{4.31}$$

where I and λ are the intensity and the wavelength of the laser field, respectively. Both of the scattering amplitudes become large with an increase of the laser intensity (I) and the wavelength (λ). When Eq. (4.31) is divided by Eq. (4.30), one obtains

$$f_{\mathrm{dress}}(\theta)J'_n(\xi)/f_{\mathrm{atom}}(\theta)J_n(\xi) \propto \lambda^{-2}. \tag{4.32}$$

This formula states that the relative amplitude of the second term (light-dressing effect) to the amplitude of the first term becomes smaller with an increase of the wavelength of the laser field. Because the differential cross section is given by the square of the scattering amplitude, the relative intensity of the light-dressing effect is in proportion of λ^{-4}. Consequently, in order to observe the light-dressing effect in the LAES signals, the wavelength should be short, otherwise, the light-dressing effect is buried in the LAES signals originating from the first term. This wavelength dependence may be a major reason why the light-dressing effect of target atoms was not observed in the previous LAES experiments in which CO_2 lasers ($\lambda = 10.6$ μm) are employed.

Numerical simulation

In order to examine whether it is possible to observe the light-dressing effect of target atoms by using our experimental apparatus, a numerical simulation was performed by using Eq. (4.26). The simulation was conducted by using the experimental conditions of this study (summarized in Table 5 in Section 4.5). The laser polarization direction ($\boldsymbol{\epsilon}$) is perpendicular to the propagation direction of the incoming electron. The spatio-temporal overlap between the laser, electron, and atomic beams was taken into account. The target atom is Xe, and the electron kinetic energy is 1 keV. In this simulation, the scattering amplitude $f_{\mathrm{atom}}(\theta)$ appearing in the formula of the Zon's model (Eq. (4.26)) is substituted by the complex scattering amplitude calculated by the

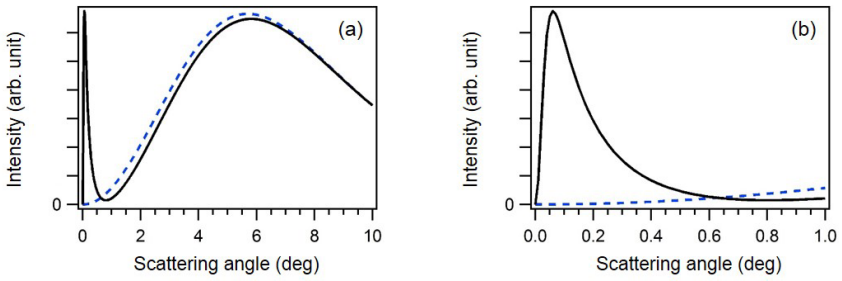

Figure 82: Simulated angular distribution of the LAES signals by Xe atoms. The kinetic energy of the electrons is 1 keV. The peak intensity of the laser field is 1.5×10^{12} W/cm^2. Black solid lines show the angular distributions calculated based on Eq. (4.26). Blue broken lines show the angular distributions in which the light-dressing effect of target atoms is not included. Panel (b) is the enlarged view of the small-angle region in the panel (a). The angular resolution of the apparatus is not considered.

partial-wave analysis [128]. This is because, as shown in Section 3.1.2 and in Fig. 15, FBA is not good enough for evaluating the amplitude of the elastic scattering of 1 keV electrons by Xe. Then, the differential cross section of the LAES process with n-photon energy shift is given by

$$\frac{\mathrm{d}\sigma_n}{\mathrm{d}\Omega} = \frac{|\boldsymbol{p}_{\mathrm{f},n}|}{|\boldsymbol{p}_{\mathrm{i}}|}\left||f_{\mathrm{el}}(\theta)|\mathrm{e}^{i\eta(\theta)}J_n(\xi) - \frac{2m_{\mathrm{e}}\omega^2 a(\omega)}{a_0 e}\frac{\xi}{s^2}J_n'(\xi)\right|^2, \tag{4.33}$$

where $|f_{\mathrm{el}}(\theta)|$ and $\eta(\theta)$ are the magnitude and the phase of the scattering amplitude, respectively. The simulated $|f_{\mathrm{el}}(\theta)|$ and $\eta(\theta)$ are shown in Fig. 81.

In Fig. 82(a), a simulated LAES angular distribution of the LAES $n = +1$ process is shown by a black solid line. The static dipole polarizability of Xe (a_{s} = 4.044 Å) was adopted from Ref. [272]. For comparison, an angular distribution which was obtained by neglecting the second term in the square modulus of the right-hand side of Eq. (4.33) is shown by a blue broken line. Figure 82(b) is an enlarged view of the small angle region ($\theta \leq 1.0^\circ$) in Fig. 82(a). In the angular distribution which was calculated with the light-dressing effect (black curves), a peak structure appears at a scattering angle range of $\theta \leq 0.7^\circ$. The peak takes a maximum value at $\theta = 0.06^\circ$. The intensity of the peak is almost same as the intensity of the LAES signals at larger scattering angles ($\theta \sim 6^\circ$). This means that it is possible to observe the peak structure originating from the light-dressing effect of target atoms by using the femtosecond intense laser pulses. At the scattering angle of $\theta = 0^\circ$, the intensity of the LAES signal becomes zero. This is because, at $\theta = 0^\circ$, the scattering vector ($\boldsymbol{s}$) is perpendicular to the polarization direction of the laser field ($\boldsymbol{\epsilon}$).

4.3 Purpose and abstract of this work

As described in Section 4.2, the light-dressing effect of target atoms in the LAES signals has not been observed yet, even though 30 years have passed since the theoretical work by Byron and Joachain was published. In this study, I report the first observation of the light-dressing effect in the LAES signals. The apparatus was improved in order to detect the small-angle LAES signals. In the angular distribution of the LAES $n = \pm 1$ processes induced by intense ultrashort laser pulses (I_{peak} = 1.5×10^{12} W/cm^2), sharp peak structures were observed at small scattering angle range of $\theta \leq 0.5^{\circ}$. Through a comparison with numerical simulations, I confirmed that the observed peaks are attributed to the light-dressing effect of target atoms.

4.4 Experimental set-up

The experimental set-up is the same as that used in the LAED experiment (Chapter 3) except some improvements described below. The kinetic energy of the incident electron is 1000 eV. The wavelength of the laser field is 800 nm. Xe gas is used as a sample.

In what follows, I first describe the improvements of the apparatus conducted for the measurement of small-angle signals. Then, methods for estimating the angular resolution and for calibrating the detection efficiency are described. Finally, the experimental conditions of this study are summarized.

4.4.1 Improvements of apparatus for the observation of small-angle scattering signals

According to the numerical simulation (Fig. 82), the peak structure originating from the light-dressing effect of target atoms appears at the small scattering angle less than 0.7° under the experimental conditions of this study. On the other hand, the minimum scattering angle that can be detected in the LAED experiment (Chapter 3) was 2.5°. Therefore, in order to observe the light-dressing effect of target atoms, the apparatus needs to be improved.

The minimum detectable scattering angle (2.5°) was determined by the outer diameter of the Faraday cup (7.0 mm) placed in front of the toroidal analyzer. The Faraday was used to collect electrons which are not scattered by sample gases. When the un-scattered electrons are not blocked by the Faraday cup, they cause huge background signals. Considering the scattering probability of electrons by sample gases ($\sim$ 1%) and the collection efficiency of the toroidal analyzer ($\sim$ 1%), the number of the un-scattered electrons that can arrive at the detector is four orders of magnitude larger than that of elastic scattering signals, and seven orders of magnitude larger than that of LAES signals $(n \neq 0)$. Therefore, in order to measure the weak LAES signals, the un-scattered electrons should be blocked before they reach the detector.

In this study, two approaches were tested for the measurement of electrons scattered at small angles. By the first approach, the minimum detectable scattering angle was decreased to zero ($\theta = 0^{\circ}$). However, it was found that the approach was not suited for the measurement of the LAES signals under the experimental conditions of this study. Therefore, the second approach

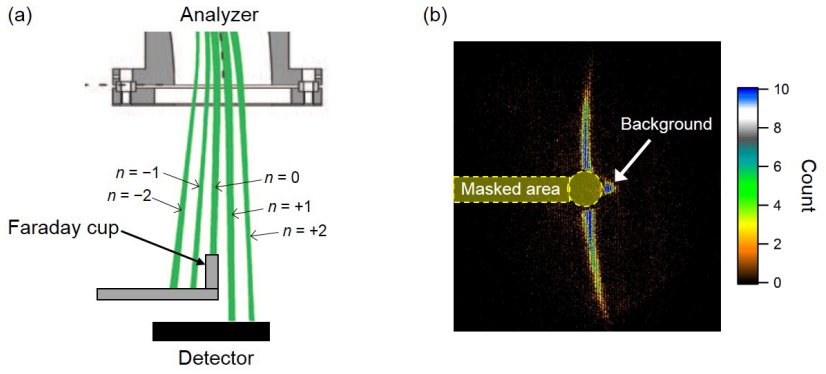

Figure 83: Installation of the Faraday cup in front of the detector. (a) Schematics of the experimental configuration. The un-scattered electrons and the electrons elastically scattered at small-angles are collected by the Faraday cup. The small-angle LAES $n = -1, -2$ signals are blocked by the bar used to mount the Faraday cup. (b) Image of electron signals. The arc-like signals are the elastically scattered electrons. The background signals appear on the right-hand side of the shadow graph of the Faraday cup.

was pursued. The second approach made it possible to detect the electrons whose scattering angles are larger than 0.1°. The minimum angle of 0.1° is small enough to observe the peak structure originating from the light-dressing effect of target atoms. The details of these approaches are described in the followings.

Trial 1. Faraday cup in front of a detector

In the first approach, the Faraday cup placed in front of the analyzer was removed and another Faraday cup was installed just in front of the detector. The diameter of the installed Faraday cup is 6 mm. The Faraday cup is grounded and is mounted on a bar which is attached to a 3-axis stage. Because electrons are spatially dispersed by the toroidal analyzer depending on their kinetic energies (Fig. 56), the newly installed Faraday cup collects the un-scattered electrons and small-angle elastic scattering signals. Though the small-angle LAES $n = -1, -2$ signals are blocked by the bar used for mounting the Faraday cup, the small-angle LAES $n = +1, +2$ signals are not blocked by the Faraday cup (Fig. 83(a)).

Figure 83(b) shows an image of the electron signals on the detector. The image was obtained by using the Xe gas without a laser field. In the image, background signals appear on the right-hand side of the shadow graph of the Faraday cup (indicated by a white arrow in Fig. 83(b)). When the number of incoming electrons was doubled, the intensity of the background signals increased fourfold. The origin of the background may be the Coulomb repulsion between the un-scattered electrons inside the analyzer. Because large number of electrons (~ 100 e/pulse) are contained in an electron pulse, the Coulomb repulsion between un-scattered electrons can cause significant effect. In the analyzer, electrons are decelerated from 1000 eV to ∼30 eV, and therefore, the Coulomb repulsion between electrons are pronounced. The broadening in

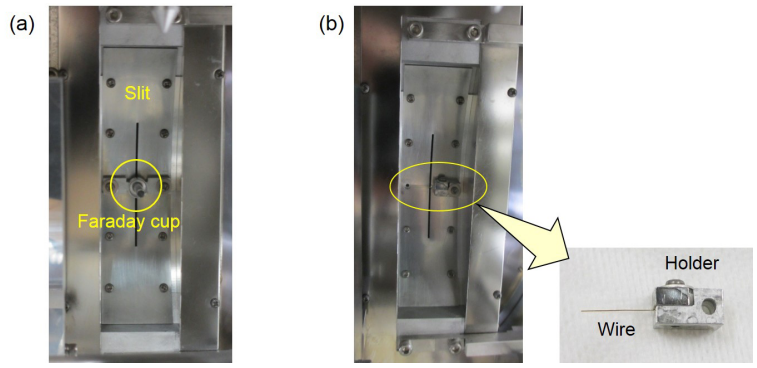

Figure 84: Pictures of the Faraday cup and the thin wire placed in front of the energy analyzer. In order to observe small-angle LAES signals, the Faraday cup shown in (a) is replaced by the thin wire shown in (b).

kinetic energy and the deflection of trajectory due to the Coulomb repulsion can make the spatial distribution of the un-scattered electrons on the detector broad and cause the background signals.

This Coulomb repulsion can be suppressed by reducing the number of electrons in an electron pulse. By employing high-repetition laser sources ($\geq$MHz), the LAES signals can be observed with the low density ($\leq$ 1 e/pulse) electron beams. However, with the current low repetition rate laser source (5 kHz), the observation of the LAES signals with the low density electron beam is all but impossible, because it will take exceedingly long accumulation time ($\sim$1000 hours).

Trial 2. Thin wire in front of the analyzer

The result of the first approach shows that the un-scattered electrons should be blocked before they enter the energy analyzer. In the second approach, the Faraday cup placed in front of the analyzer was replaced by a thin wire (Fig. 84). Because the detectable minimum angle is determined by the outer diameter of the Faraday cup, the minimum angle can be reduced by using the thin wire instead of the Faraday cup. In order to block most of the un-scattered electrons with the thin wire, the size of the electron beam at the wire should be smaller than the diameter of the wire. In order for achieving a thinner electron beam, three improvements were done. The improvements are summarized in Fig. 85. First, a pinhole installed in the electron gun was changed to the smaller one: from 0.5 mmϕ to 0.1 mmϕ. Second, another pinhole with a diameter of 0.3 mm was installed at the exit of the electron gun. Third, the electron beam was focused on the wire by adjusting the current flowing into the electromagnetic coil of the electron gun. In order to minimize the number of the un-scattered electrons to reach the detector, the pointing of the electron beam along the z-axis is adjusted by the octupole deflector (Fig. 38). The x, y,and z axes are defined in Fig. 26. By using the method introduced in Section 3.5.7, the electron beam diameter at the position of the nozzle was measured to be 0.24(1) mm (1/e^2

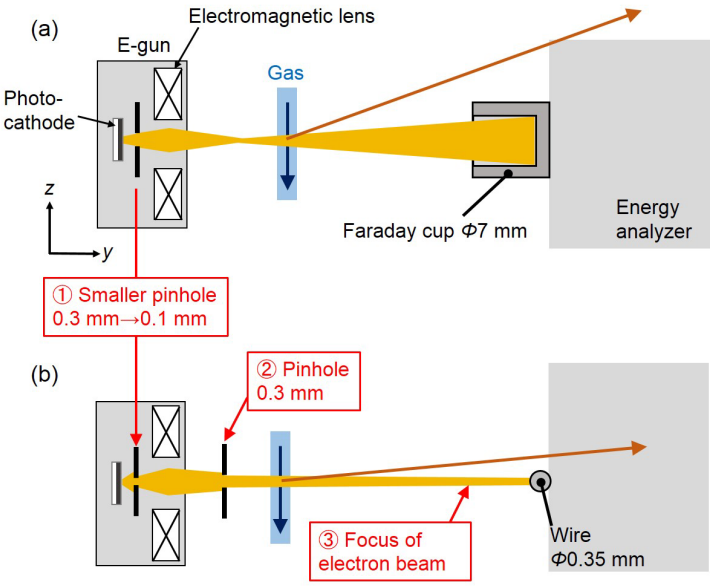

Figure 85: Improvements of the apparatus for the observation of small-angle LAES signals. (a) Schematic of the apparatus used in the LAED experiment (Chapter 3). (b) Schematic of the apparatus used in this experiment. The orange beams represent the electron beam. In order to observe electron signals scattered at small angles, three improvements were made: (i) installation of smaller pinhole ($\phi 0.1$ mm) in the electron gun, (ii) installation of another pinhole ($\phi 0.3$ mm) at the exit of the electron gun, and (iii) focusing of the electron beam at the wire.

full width). Even though the number of electrons in a pulse was dropped by 70 % by the use of the small pinholes, the electron beam diameter at the wire becomes less than 0.3 mm as shown below.

A photograph of the thin wire is shown in Fig. 84(b). When a 0.2 mmϕ wire (Au) was employed, 5% of the un-scattered electrons were not block by the wire. This indicates that the diameter of the electron beam on the wire is $\sim$0.2 mm ($1/e^2$ full width). Considering the scattering probability ($\sim 1\%$) and the collection efficiency of the analyzer ($\sim 1\%$), more than 99.99% of the un-scattered electrons should be blocked by the wire in order to observe the LAES signals. This was achieved when a 0.35 mmϕ wire (Mo) was used. The intensity of the un-scattered electrons on the detector was of the order of 10^{-6} of the incident electrons, which corresponds to 1% of the elastically scattered electrons. The detectable minimum scattering angle with the 0.35 mmϕ wire is 0.11°, which is small enough to observe the peak structure originating from the light-dressing effect of target atoms. No significant effects originating from the scattering by the thin wire were observed as shown in the next paragraph.

Figure 86(a) shows a measured angular distribution of the electrons scattered elastically by Xe (red curve) and an angular distribution of the un-scattered electrons (blue curve). The angular distribution of the un-scattered electrons was measured without introducing sample gases. The

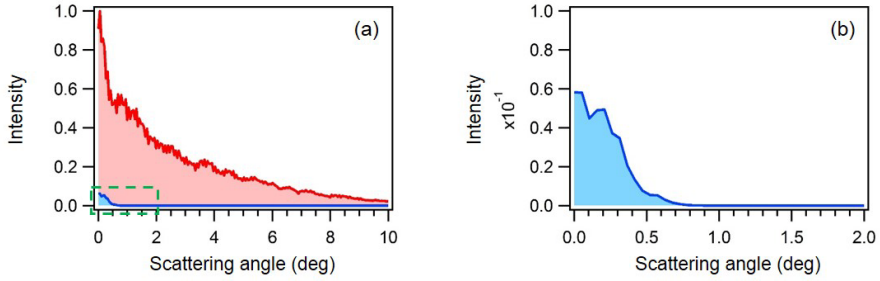

Figure 86: Comparison between the angular distribution of electrons scattered by Xe and the angular distribution of un-scattered electrons. The set-up shown in Fig. 85(b) was adopted for the measurement of these angular distributions. Red curve in (a) shows the angular distribution of 1 keV electrons elastically scattered by Xe outside laser fields. Blue curve in (a) shows the angular distribution of electrons which are not scattered by sample gas and are not blocked by the thin wire placed in front of the analyzer. Because most of the un-scattered electrons are blocked by the wire, the blue curve represents the angular distribution of a fraction (10^{-6}) of the un-scattered electrons. Panel (b) shows the enlarged view of the area indicated by the green broken box in panel (a).

intensity of the un-scattered electrons was much weaker than that of the elastically scattered electrons. Figure 86(b) is the enlarged view of the angular distributions of the un-scattered electrons at small scattering angles ($\theta \leq 2.0^\circ$), which is indicated by the green box shown in Fig. 86(a). Because of a limited angular distribution, the distribution of the un-scattered electrons has a width of 0.7° (FWHM). In the angular distribution of the un-scattered electrons, any significant signals were not detected at the angular range of $\theta \geq 1.0^\circ$. This means that the effect of the scattering by the wire is negligibly small because electrons scattered by the wire would appear at the large scattering angles.

4.4.2 Estimation of angular resolution

The estimation of the resolution in scattering angle is crucial for analyzing experimental results. The angular resolution depends on the size of the scattering region. When the volume of the scattering region is smaller, the angular resolution becomes higher. In the previous chapter, the angular resolution was estimated by measuring the electron diffraction pattern of graphene.

In this chapter, the angular resolution of the scattered electrons was estimated by measuring the angular distributions of the un-scattered electrons on the detector. This is because the focus of this study is on the observation of the peaks appearing at around $\theta = 0^\circ$, and the un-scattered electrons can be considered as the electrons scattered at $\theta = 0^\circ$. In order to measure the angular distribution of the un-scattered electrons without the influence of the wire, the electron beam was deflected upward ($+z$ direction) by using the octupole deflector (Fig. 38). I experimentally confirmed that the deflection angle of the electron beam has little effect on the distribution width by comparing the distribution widths measured at different deflection angles. In order to sup-

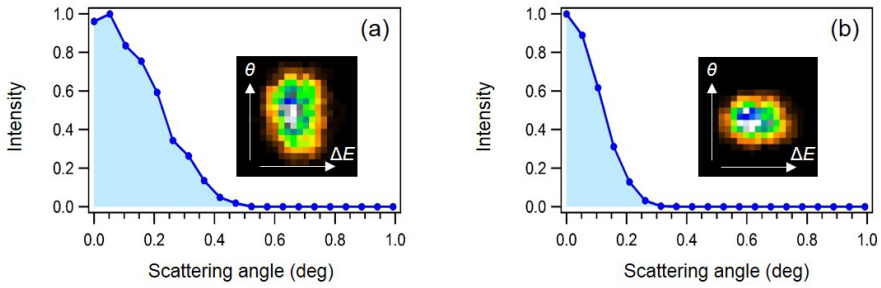

Figure 87: Angular distributions of the un-scattered electrons on the detector measured with 0.3 mmϕ (a) and 0.1 mmϕ (b) pinholes installed on a course of the electron beam between the scattering point and the exit of the electron gun. The image in each figure shows the raw data of electron signals on the detector.

press the Coulomb repulsion between electrons inside the analyzer, the number of the electrons was reduced to the order of 0.01 e/pulse by decreasing the pulse energy of the UV laser light ($\lambda = 266$ nm) used for generating electron pulses.

Figure 87 shows angular distributions of the un-scattered electrons on the detector. The distribution shown in Fig. 87(a) was measured by the set-up shown in Fig. 85(b). The distribution shown in Fig. 87(b) was observed by replacing the $\phi 0.3$ mm pinhole shown in Fig. 85(b) to a $\phi 0.1$ mm pinhole. The sample gas was not introduced in these measurements. The widths of the distributions in Fig. 87(a) and (b) are 0.44° (FWHM) and 0.24° (FWHM), respectively. The diameters of the electron beam below the nozzle were measured to be 0.24(1) mm ($1/e^2$ full width) and 0.12(1) mm ($1/e^2$ full width) for the case of Fig. 87(a) and (b), respectively. The reason why the angular distributions of the un-scattered electrons were measured under the two conditions is that the effective electron beam diameter which can contribute to the LAES signals can be decreased depending on the diameter of the laser beam along the z-axis. This is because the LAES process occurs only where the laser and electron beams are overlapped. As described in Section 4.4.4, the diameter of the laser beam along the z-axis is 0.12 mm, which is smaller than the diameter of the electron beam diameter (0.24 mm). Therefore, the effective electron beam diameter for the LAES process can be considered as 0.12 mm. This means that the width of the distribution shown in Fig. 87(b) (0.24°, FWHM) can be considered as the angular resolution of the LAES signals. On the other hand, the width of the distribution shown in Fig. 87(a) (0.44°, FWHM) corresponds to the angular resolution of the elastically scattered electrons outside laser fields.

4.4.3 Calibration of detection efficiency

The detection efficiency can be determined by comparing the observed and simulated angular distributions of the elastic scattering. The observed angular distribution of the scattered electrons

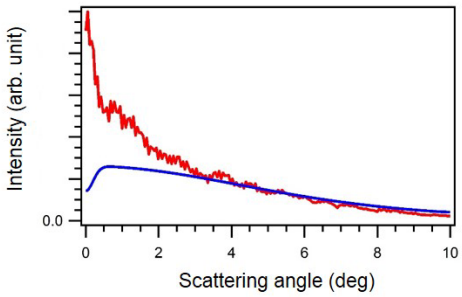

Figure 88: Angular distribution of electrons elastically scattered by Xe. Red curve represents the observed angular distribution. Blue curves shows the simulated angular distribution obtained by the partial-wave analysis. The transmission efficiency of the thin wire placed in front of the analyzer was considered in the simulation. The discrepancy at the small scattering angles ($\theta \leq 3.0^\circ$) may be due to the charge-cloud polarization effect induced by an incident electron. The small discrepancy at large scattering angles ($\theta \geq 7^\circ$) is due to the degradation of the detection efficiency originating from the slight misalignment of the entrance slit (0.8 mm width) of the toroidal analyzer.

by Xe is shown by a red line in Fig. 88. The blue curve in Fig. 88 shows the simulated angular distribution which was obtained by the partial-wave analysis [128]. In the simulation, the transmission efficiency of the wire and the resolution in scattering angle (0.44°, FWHM) were taken into account. The intensity of the observed and simulated angular distributions were normalized at the scattering angle of $\theta = 5.0^\circ$. Because the absolute value of the signal intensity is not discussed in this study, the angle used for the normalization has no effect on results and analyses. As shown in Fig. 16, the result of the partial-wave analysis agrees well with the experimental data reported by Jansen *et al.* [120] at the scattering angle range of $\theta \geq 5.0^\circ$. Therefore, the detection efficiency at the scattering angle range of $\theta \geq 5.0^\circ$ was determined by comparing the experimental angular distribution (red line in Fig. 88) and the simulated angular distribution (blue curve in Fig. 88).

However, the validity of the simulation based on the partial-wave analysis at the scattering angle range of $\theta < 5.0^\circ$ has not been confirmed. To the best of my knowledge, the experimental angular distribution less than 5.0° has not been reported for the elastic scattering of 1 keV electrons by Xe. The angular distribution observed in this study plotted in Fig. 88 shows a significant disagreement with the simulated angular distribution at the scattering angle range of $\theta \leq 3.0^\circ$. This may be due to the charge-cloud polarization effect which is not included in the simulation based on the partial-wave analysis. It has been known that the polarization effect enhances the intensity at small scattering angles [122, 123]. The polarization effect has been frequently evaluated by considering the Buckingham potential (Eq. (3.63)). If the Buckingham potential was adequate for estimating the polarization effect appearing at the scattering angle range ($0.1^\circ \leq \theta < 5.0^\circ$) of 1 keV electrons, the detection efficiency at the scattering angle range of $\theta < 5.0^\circ$ could be obtained by comparing the experimental angular distribution and a

simulated angular distribution which includes the polarization effect. However, as I show in the next paragraph, the Buckingham potential is not appropriate for assessing the polarization effect under the experimental conditions of this study. Consequently, it is difficult to determine the detection efficiency at $\theta < 5.0^\circ$. In this study, instead of determining the detection efficiency, I added an error of $\pm$20%, which was estimated based on the un-uniformity of the sensitivity of our detector, to the experimental signals observed at $\theta < 5.0^\circ$.

Validity of Buckingham potential

I discuss the validity of the Buckingham potential and consider whether the Buckingham potential is appropriate for estimating the polarization effect appearing at small scattering angles ($0.1^\circ \leq \theta \leq 5.0^\circ$) of 1 keV electrons. The Buckingham potential is derived under the adiabatic approximation [70] in which the electron-atom collision is assumed to proceed so slowly that the electron cloud of the atom can follow the motion of the incident electron. The validity of the adiabatic approximation can be expressed as [273]

$$\frac{\hbar}{\tau_{\rm col}} \ll \langle W_n - W_0 \rangle \,, \tag{4.34}$$

where $\tau_{\rm col}$ represents the collision time and $\langle W_n - W_0 \rangle$ is the averaged energy difference between excited states and a ground state of the target atom. The collision time ($\tau_{\rm col}$) is defined as the time originating from the uncertainty in energy of the incident electron during the collision [273]. The collision time can be estimated from the following formula,

$$\tau_{\rm col} \sim \frac{L}{v_{\rm e}}, \tag{4.35}$$

where L is the collision length and $v_{\rm e}$ is the speed of the incident electron. The collision length (L) is of the order of

$$L \sim \frac{1}{s}. \tag{4.36}$$

The calculated values of the left-hand side of Eq. (4.34) are 3.5 eV and 35 eV for $\theta = 0.1^\circ$ and 1.0°, respectively. Because the excitation energy of Xe is about 10 eV [274], the adiabatic approximation (Eq. (4.34)) does not hold. Therefore, the Buckingham potential is not appropriate for considering the polarization effect under the experimental conditions of this study.

4.4.4 Summary of experimental conditions

The experimental conditions of this study are summarized in Table 5. In order to improve the angular resolution of the LAES signals, the laser beam is tightly focused (0.12(3) mm, 1/e^2 full width) along the z-axis. The laser focal size along the y-axis (0.81(5) mm, 1/e^2 full width) is larger than that along z-axis in order to achieve high degree of spatial overlap with the electron beam. The methods for the measurement of the laser beam diameter were described in Section

Table 5: Summary of experimental conditions

Kinetic energy of electron	1 keV
Duration of electron pulse (FWHM)	19 ps
Number of electrons in a pulse	10^2
Sample	Xe
Sample density	10^{15} cm^{-3}
Wavelength of laser light	800 nm
Pulse energy	0.6 mJ
Pulse duration (FWHM)	970 fs
Peak intensity	1.5×10^{12} Wcm^{-2}
Polarization	linear (z-axis)
Focal size (z-axis, 1/e^2 full width)	0.1 mm
Focal size (y-axis, 1/e^2 full width)	0.8 mm
Repetition rate	5 kHz
Signal count rate (including background)	90 count/sec
Count rate of LAES signals	0.3 count/sec
Accumulation time	30 h

3.5.7. The laser pulse was elongated to 970(50) fs in order to suppress the ionization of atoms. This is because the LAES process by ions can enhance the LAES signal intensity at small scattering angles due to the long range Coulombic interaction between the incoming electron and the ion. The duration of the laser pulse was measured by using the home-made autocorrelator (Section 3.5.3). The sample is Xe. The scattering point where the laser, electron, and atomic beams cross is located 0.4 mm below the nozzle tip. The distribution width of the Xe gas 0.4 mm below the nozzle was measured to be 0.70(1) mm (FWHM). In Fig. 89, the schematic of the overlapping beams is shown. The distribution width of the electron beam along the y-axis (0.60 mm, 1/e^2 full width) is smaller that of the laser beam (0.81 mm, 1/e^2 full width). Therefore, a small deviation of the temporal overlap (several ps) between the laser and electron beams has little effect on the LAES signals.

4.5 Results and Discussion

The LAES signals at the delay time of $\Delta t = 0$ ps were accumulated for 30 hours. The background signals were measured at the delay time of $\Delta t = +100$ ps. The positive sign in the delay represents that the electron pulse arrives at the scattering point after the arrival of the laser pulse. At the delay time of $\Delta t = +100$ ps, the temporal overlap between the laser and electron pulses is negligibly small. The background signals were also accumulated for 30 hours. Every 4 hours, the experimental condition were checked and slightly adjusted. Especially, the position of the electron beam along the z-axis was adjusted by the octupole deflector to minimize the number

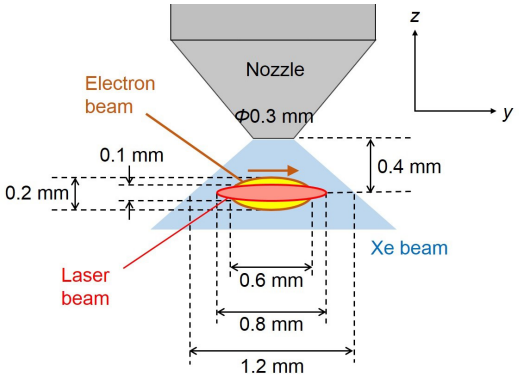

Figure 89: Overlap of the laser, electron, and atomic beams at the scattering point. The sizes of the beams written in this figure are represented in the $1/e^2$ full width. The brown arrow written above the electron beam shows the propagation direction of the electron beam.

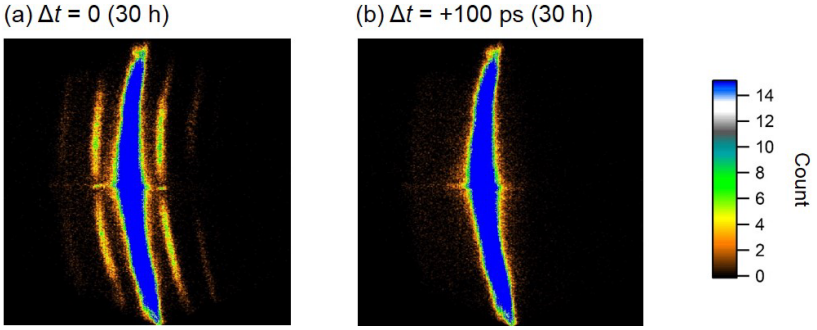

Figure 90: Raw images of the scattered electrons. (a) The images of the scattered electrons measured at the zero delay time ($\Delta t = 0$ ps). (b) The images of the scattered electrons at the delay time of $\Delta t = +100$ ps.

of the un-scattered electrons which reach the detector. The detectable minimum and maximum scattering angles are 0.1° and 10.0°, respectively.

4.5.1 Raw images and energy spectra

In Figs. 90(a) and (b), raw images of the electron signals at $\Delta t = 0$ ps and $\Delta t = +100$ ps are shown. Only when the electron and laser beams are temporally overlapped ($\Delta t = 0$ ps), the LAES signals ($\Delta E = nh\nu$, $n = \pm 1, \pm 2$) appear on both sides of the elastically scattered electrons ($\Delta E = 0$ eV). Figures 91(a) and (b) show the kinetic energy spectra of the scattered electrons at $\Delta t = 0$ ps and $\Delta t = +100$ ps, respectively. These spectra were obtained by integrating the electron signals shown in Figs. 90(a) and (b) over the entire scattering angle range ($\theta \leq 10.0°$). The spectral intensities are normalized by the peak intensities of the elastic

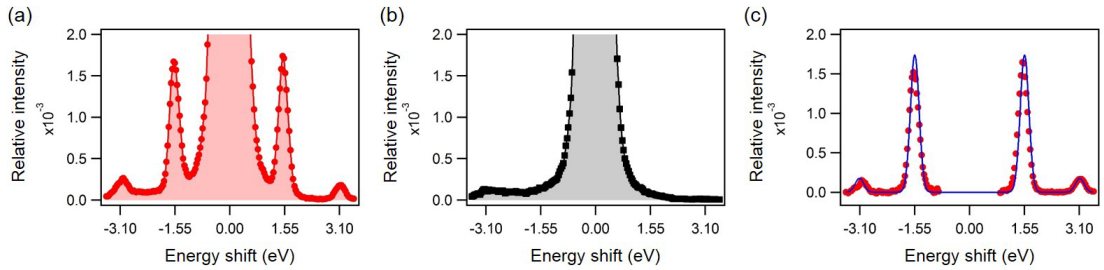

Figure 91: Kinetic energy spectra of scattered electrons. The spectra were obtained by integrating the electron signals over the scattering angle range of less than 10°. (a) The energy spectrum of the scattered electrons measured at $\Delta t = 0$ ps. (b) The energy spectrum measured at $\Delta t = +100$ ps. (c) The background-subtracted energy spectrum obtained by subtracting the spectrum in (b) from the spectrum in (a). Red circles show the experimental result. Blue line shows a result of a numerical simulation based on KWA.

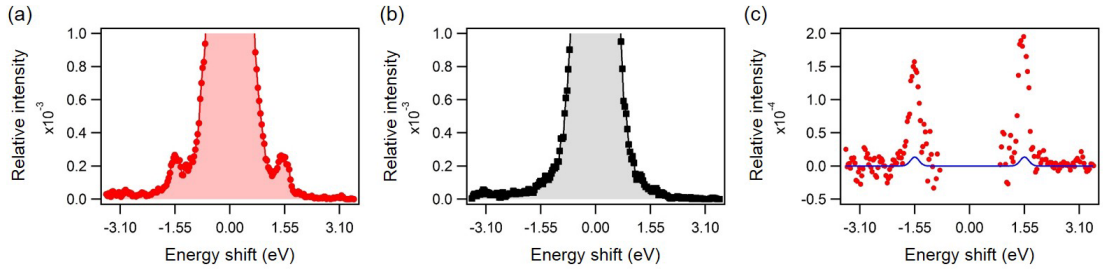

Figure 92: Kinetic energy spectra of scattered electrons observed at the small angle range ($\theta \leq 0.5°$). (a) The energy spectrum of the scattered electrons observed at $\Delta t = 0$ ps. (b) The energy spectrum observed at $\Delta t = +100$ ps. (c) The background-subtracted kinetic energy spectrum. Even though the signal intensities are one order of magnitude smaller than that in Fig. 91(c), clear LAES signals were observed. Blue line represents the simulated energy spectrum based on KWA.

scattering appearing at $\Delta E = 0$ eV. In order to compare the experimental data with a numerical simulation, the background intensity (Fig. 91(b)) was subtracted from the energy spectrum of $\Delta t = 0$ ps (Fig. 91(a)). The background-subtracted energy spectrum is plotted in Fig. 91(c) as red circles. The blue line shown in Fig. 91(c) is a result of the numerical simulation based on KWA (Eq. (2.36)). In KWA, the light-dressing effect of target atoms is not included. In the simulation, the angular distribution of the observed elastic scattering at $\Delta t = +100$ ps was adopted for the field-free elastic DCS ($\mathrm{d}\sigma_{\mathrm{el}}/\mathrm{d}\Omega$) appearing in the formula of KWA (Eq. (2.36)). The result of the simulation based on KWA (blue line) well reproduces the observed energy spectrum (red circles).

Then, the energy spectra of the electrons detected only at small scattering angles ($\theta \leq 0.5°$) are plotted in Figs. 92(a) and (b). The LAES signals ($\Delta E = \pm h\nu$) can be found in the energy

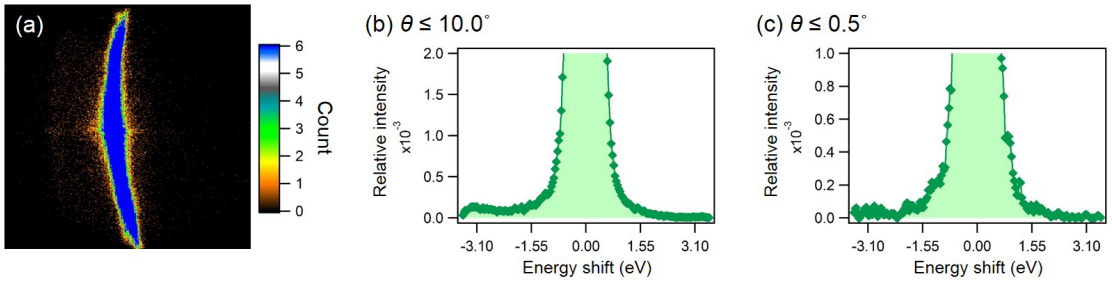

Figure 93: Electron signals measured with the horizontal polarization at $\Delta t = 0$ ps. The data were accumulated for 12 h. (a) The raw image of the electron signals. (b) The kinetic energy spectrum of the electrons scattered over the entire detectable scattering angles ($\theta \leq 10°$). (c) The kinetic energy spectrum of the electrons scattered at the small angles ($\theta \leq 0.5°$).

spectrum at $\Delta t = 0$ ps (Fig. 92(a)). The LAES signals became clearer when the background spectrum (Fig. 92(b)) was subtracted as shown in Fig. 92(c) by red circles. The blue curve in Fig. 92(c) shows the result of a numerical simulation based on KWA. The observed signal intensities of the LAES $n = \pm 1$ process are not reproduced by the numerical simulation based on KWA.

In order to confirm that the observed signals at the small angle range of $\theta \leq 0.5°$ (Fig. 92(c)) are the LAES signals, a measurement of the electron signals was conducted by changing the polarization direction from the vertical direction (along the z-axis) to the horizontal direction (along the y-axis). In the case of the horizontal polarization, the scattering vector $\boldsymbol{s}$ is nearly perpendicular to the polarization direction of the laser field (Fig. 79(a)), and therefore, the cross section of the LAES ($n \neq 0$) process is suppressed [44]. Figure 93(a) shows the raw image of the electron signals measured with the horizontal polarization at the zero delay time ($\Delta t = 0$ ps). The electron signals were accumulated for 12 h. The kinetic energy spectra of the entire angular range ($\theta \leq 10°$) and of the small angle range ($\theta \leq 0.5°$) are shown in Figs. 93 (b) and (c), respectively. In these energy spectra, any significant LAES signals are not identified. This polarization dependence confirms that the signals observed in Figs. 92(a) and (c) are the LAES signals.

4.5.2 Angular distribution of LAES signals

The angular distributions of the observed LAES $n = +1$ and $n = -1$ signals are shown in Figs. 94(a) and (b), respectively. These angular distributions are almost identical with each other within the experimental errors. Figure 94(c) and (d) are the magnified views of the small angle range ($\theta \leq 2.0°$) in Figs. 94(a) and (b), respectively. In both of the angular distributions, clear peak structures which may be originating from the light-dressing effect of target atoms are observed at the small scattering angles ($\theta \leq 0.5°$).

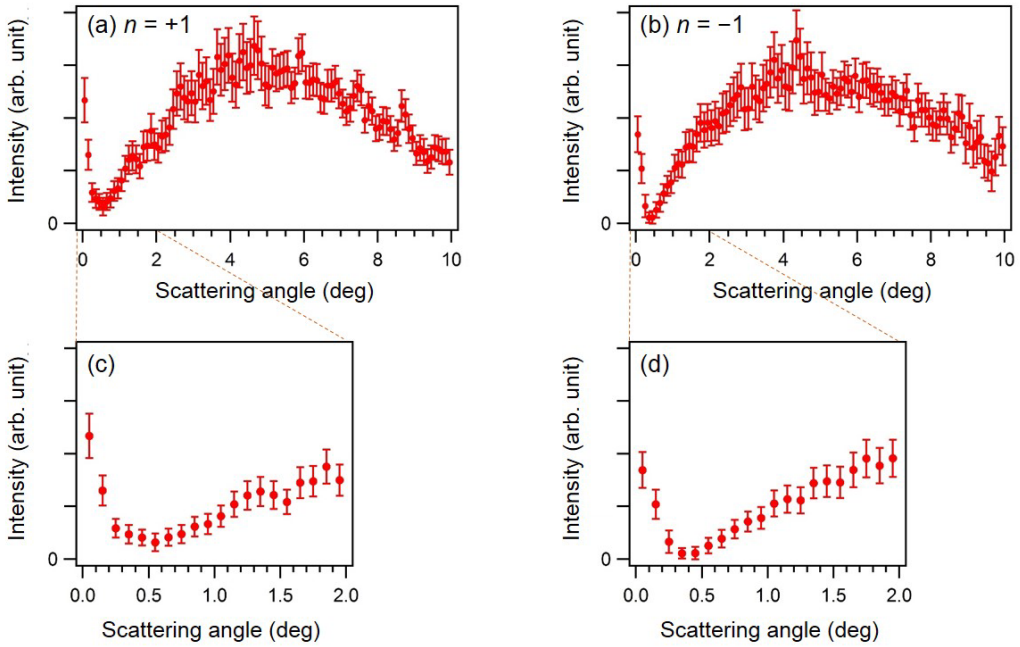

Figure 94: Observed angular distributions of LAES $n = \pm 1$ processes by Xe in intense laser fields. Panels (a) and (c) show the angular distribution of the LAES $n = +1$ process. Panel (b) and (d) show the angular distribution of the LAES $n = -1$ process. These angular distributions were obtained by integrating the electron signals shown in Fig. 90 over the 0.3 eV energy range centered at $\Delta E = \pm 1.55$ eV. The error bars represent one standard deviation.

In order to confirm that the observed peak structures at the small scattering angles are ascribed to the light-dressing effect of target atoms, the observed distributions are compared with simulated distributions. For a better comparison with numerical simulations, the observed angular distributions of the LAES $n = +1$ and $n = -1$ processes (Figs. 95(a) and (b)) were averaged. Red circles shown in Fig. 95 show the averaged experimental angular distribution. The angular distributions shown by blue broken lines in Fig. 95 are a result of a simulation based on KWA. In the simulated angular distributions, any peak structures were not identified at the small angle range of $\theta \leq 0.5°$. Therefore, the origin of the deviation observed in the energy spectrum in Fig. 92(c) is attributed to the peak structures at the small scattering angles. Then, a numerical simulation which includes the light-dressing effect of target atoms was conducted by using Eq. (4.33). The result of the simulation is shown in Fig. 95 by black lines. Details of the simulation were described in Section 4.2.1 and Appendix 2. The resolution in scattering angle ($0.24°$, FWHM) and the decrease in signal intensity at $\theta < 0.1°$ due to the wire placed in front of the analyzer were considered in the simulation. In the simulated distributions, peak structures are identified at the small angle range. This is in consistent with the experimental result. There-

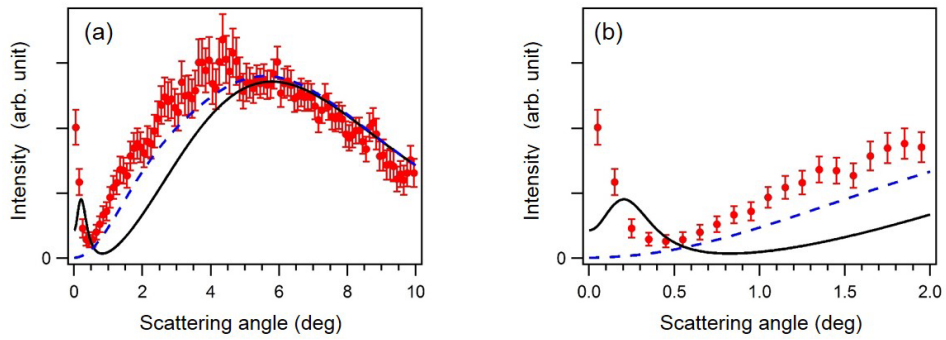

Figure 95: Experimental and numerical angular distributions of the LAES $n = \pm 1$ process. Red circles represent the experimental angular distribution which was obtained by averaging the angular distributions of LAES $n = +1$ and $n = -1$ processes shown in Fig. 94. The error bars represent one standard deviation. Blue broken lines show the angular distributions calculated by KWA. Black solid lines show the angular distributions calculated by the Zon's model (Eq. (4.33)). Panel (b) is a magnified view of the small-angle range in panel (a).

fore, it is confirmed that the observed peak structures are ascribed to the light-dressing effect of target atoms induced by intense laser fields.

When the observed angular distributions (red circles in Fig. 95) and the simulated angular distributions based on the Zon's model (black line in Fig. 95) are compared in detail, it can be seen that the intensity and the shape of the observed peak structure are not reproduced well by the numerical simulation. This disagreement may be due to the slight misalignment and/or the pointing fluctuation of the laser and electron beams along the z axis during the long accumulation time (72 h, in total). For example, a numerical simulation based on Eq. (4.33) was conducted by assuming that the focal position of the laser beam along the z-axis oscillates with an amplitude of 50 μm. The result of this simulation is shown in Fig. 96 by green curves. When the green curves are compared to the simulated angular distributions without considering the fluctuation of the laser focal point (black curves in Fig. 96), it is apparent that the shape and intensity of the peak are modified by the fluctuation of the laser focal point. The modifications of the peak structure are resulting from the the displacement of the scattering region of the LAES process according to the fluctuation of the laser focal point. This displacement of the scattering region along the z-axis changes the scattering angle range where the scattered electrons are blocked by the thin wire, and therefore, modifies the angular distribution of the LAES signals. Even though there are still quantitative differences between the experimental result and the result of the simulation conducted here, more elaborate simulations would provide a better agreement with the experimental data.

Another disagreement between the experimental and simulated angular distributions of the LAES $n = \pm 1$ process can be recognized at the larger scattering angle range of $0.5^\circ \leq \theta \leq 5.0^\circ$ in Fig. 95. At the angular range, the intensity of the experimental signals are higher than that

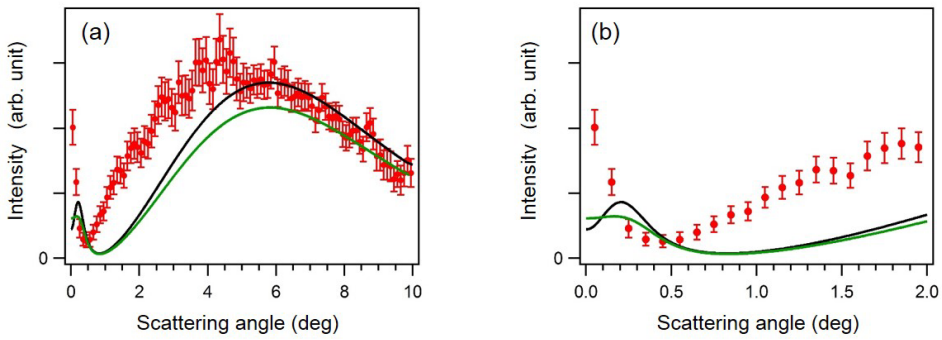

Figure 96: Effect of the laser focal point fluctuation. Green lines represent a result of a numerical simulation conducted by assuming that the focal point of the laser beam periodically oscillates along the z-axis with an amplitude of 50 μm. Black lines and red circles are identical with those in Fig. 95. The overall intensity of the green curves is weaker than that of the black curves. This is because the degree of spatial overlap between the laser and electron beams decreases by the oscillation of the laser focal point.

of the simulated signals. The charge-cloud polarization effect induced by incident electrons would be an origin of this disagreement. As described in the previous section, the polarization effect increases the signal intensity. Inaccuracies originating from the approximations used in the Zon's model might also be the origin of the disagreement. As discussed in Section 4.2.1, in the Zon's model, the interaction between an incoming electron and oscillating atomic electrons is approximated by the charge-dipole interaction (Eq. (4.18)) and the internal structure of the oscillating electrons are neglected. This assumption may not be appropriate for evaluating the light-dressing effect appearing in the relatively large scattering angles considered here ($\theta \geq 0.5^\circ$). As discussed in Section 4.1.1, the angular distribution at large scattering angles strongly reflects the electron density distribution near the atomic nucleus (Fig. 78). Because it has been known that $\Delta\rho(\boldsymbol{r}, t)$ can have internal structures near nucleus [103, 275] as shown in Fig. 77, the internal structures of $\Delta\rho(\boldsymbol{r}, t)$ might have a significant effect on the light-dressing effect appearing in the angular range of $0.5^\circ \leq \theta \leq 5.0^\circ$. Furthermore, in the Zon's model, FBA is adopted for calculating scattering amplitudes. The contribution of higher-order Born may also be the origin of the disagreement. Equations which can be used for considering the effect of the internal structure of the oscillating electrons and higher-order Born effect are introduced in Appendix 3 and 4. Consequently, a better agreement with the experimental result will be achieved by considering the polarization effect, internal structure of oscillating electrons, and higher-order Born terms.

Finally, observed angular distributions of the LAES $n = +2$ and $n = -2$ processes are shown by red circles in Figs. 97(a) and (b), respectively. No peak structures are identified in the angular distributions of LAES $n = \pm 2$ processes. This is because a dipole which oscillates with a frequency of $2q\omega (q = 1, 2, 3, \cdots)$ cannot be induced in atoms [45]. It has been known theoretically that when a dipole which oscillates with a frequency of $|n|\omega$ is induced by laser

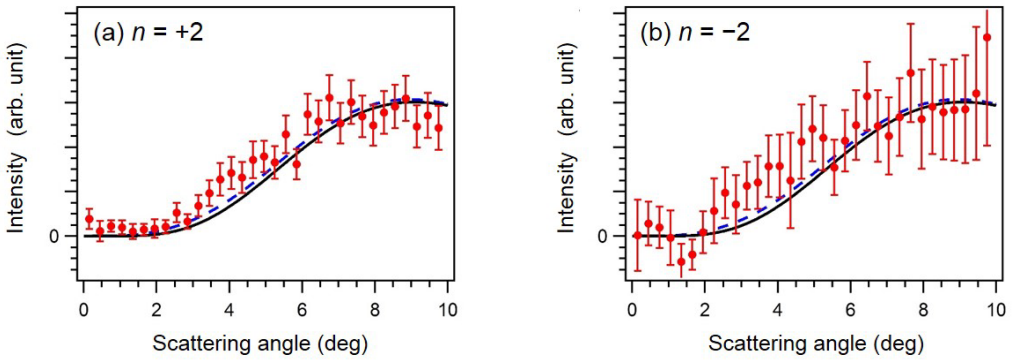

Figure 97: Angular distributions of LAES $n = \pm 2$ processes by Xe in the intense laser field. (a) The angular distribution of the LAES $n = +2$ process. (b) The angular distribution of the LAES $n = -2$ process. These angular distributions were obtained by integrating the electron signals shown in Fig. 90 over the 0.3 eV energy range centered at $\Delta E = \pm 3.10$ eV. Red circles show the experimental result. The error bars represent one standard deviation. Blue broken lines show the angular distributions simulated by KWA. Black solid lines show the angular distributions simulated by using the Zon's model Eq. (4.33).

fields, a peak structure appears in the angular distribution of the LAES process with a n-photon energy shift [252]. Because the dipole which oscillates with 2ω frequency cannot be induced in target atoms which have an isotropic electron density distribution, peak structures should not appear in the angular distributions of LAES $n = \pm 2$ processes. The detailed discussion on the light-dressing effect of target atoms appearing in the angular distribution of the LAES process with the energy shift of n-photon ($|n| > 1$) is given in Section 4.6. The observed angular distributions are compared with numerical simulations. The blue broken lines shown in Fig. 97 are the result of a numerical simulation based on KWA. Because the light-dressing effect appearing in the LAES $n = \pm 2$ processes are small, the simulated distributions based on KWA reproduce the experimental angular distributions very well. The black solid lines shown in Fig. 97 are the result of a numerical simulation based on the Zon's model (Eq. (4.33)). Because the dipole considered in the Zon's model oscillates only at the frequency of ω (Eq. (4.18)), the light-dressing effect appearing in the simulated angular distribution of the LAES $n = \pm 2$ processes is very weak. Therefore, the simulated angular distributions based on the Zon's model also agree with the experimental angular distributions.

4.5.3 Effect of ionization

In order to further confirm that the observed peak structures in the angular distributions of the LAES $n = \pm 1$ processes are ascribed to the light-dressing effect of target atoms, the effect of the ionization of target atoms induced by the laser field was investigated. This is because the LAES process by ions can enhance the signal intensity of the LAES process at small scattering angles by the long-range Coulmobic interaction between incoming electrons and the ions. In order to

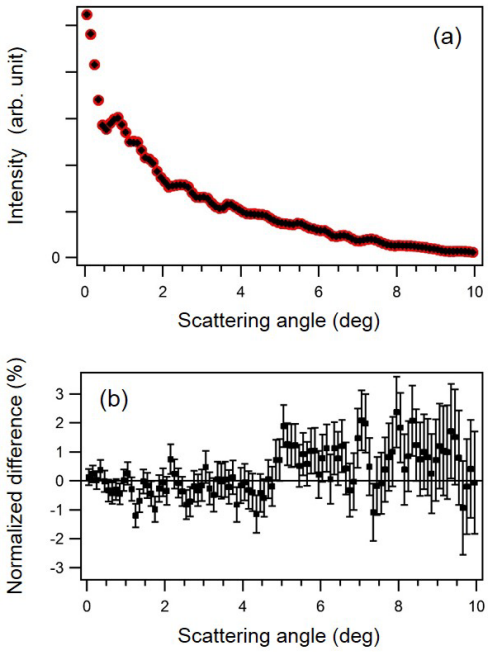

Figure 98: Effect of laser-induced ionization of target Xe atoms. (a) Angular distributions of elastic scattering at the delay time of $\Delta t = 0$ ps (red circles) and $\Delta t = +100$ ps (black squares). There distributions are normalized by their integrated intensities. (b) The normalized difference between two distributions shown in panel (a). The normalized difference is defined by Eq. (4.37). The error bars represent one standard deviation.

evaluate the effect of the ionization of Xe, angular distributions of the elastic scattering ($\Delta E = 0$ eV) measured at $\Delta t = 0$ ps and $\Delta t = +100$ ps were compared. Because the elastic scattering by an ion enhances the signal intensity of the elastic scattering at small scattering angles, the effect of the ionization can be evaluated by the comparison of the angular distributions. Even though the signals measured at $\Delta t = 0$ ps contain the electrons scattered inside the laser field, the influence of the scattering events in the presence of the laser field can be neglected. This is because more than 98% of the signals measured at $\Delta t = 0$ ps are originating from the scattering events outside the laser field (Section 2.3.1). In Fig. 98(a), the angular distributions of the elastic scattering ($\Delta E = 0$ eV) at $\Delta t = 0$ ps and $\Delta t = +100$ ps are shown by red circles and black squares, respectively. No significant differences between two distributions are recognized in Fig. 98(a). In order to make the differences between two distributions clearer, I calculated the normalized difference defined by the following formula,

$$\frac{\Delta I}{I}(\theta) = \frac{I_{\rm el}(\theta, \Delta t = +100 \text{ ps}) - I_{\rm el}(\theta, \Delta t = 0 \text{ ps})}{\frac{1}{2}\Big(I_{\rm el}(\theta, \Delta t = +100 \text{ ps}) + I_{\rm el}(\theta, \Delta t = 0 \text{ ps})\Big)}, \tag{4.37}$$

where $I_{\rm el}(\theta, \Delta t = +100\ {\rm ps})$ and $I_{\rm el}(\theta, \Delta t = 0\ {\rm ps})$ represent the angular distributions of elastic scattering at $\Delta t = 0$ ps and $\Delta t = +100$ ps, respectively. In Fig. 98(b), the calculated $\Delta I/I(\theta)$ is plotted by black squares. The enhancement of the signal intensity at small angles is not identified. Therefore, it was confirmed that the effect of the ionization was negligibly small. This further supports our observation of the light-dressing effect of target atoms.

4.6 Summary and future prospects

In this chapter, the first observation of the light-dressing effect of the target atoms appearing in the LAES signals was reported. The observation was made possible by improving the apparatus in order to detect the scattering signals at small angles ($\theta \geq 0.1^\circ$). This study opened a new field in collision experiments: the scattering of light-dressed electrons by light-dressed atoms. Moreover, this study paves the way for the investigation of the electron density distribution of the light-dressed atoms and molecules.

As described in Section 4.1, the electron density distribution of atoms and molecules can be investigated by analyzing the angular distribution of the elastically scattered electrons without laser fields [4, 212]. Here, a discussion is made on whether the spatial distribution of the oscillating electrons in light-dressed atoms can be determined from the angular distributions of the LAES process. In the Zon's model which was used for the comparison with the experimental data, the interaction between the incoming electron and the oscillating electrons in target atoms are approximated by the charge-dipole interaction and the internal structure of the oscillating electrons is neglected. In what follows, I present equations which gives the light-dressing effect without the approximations used in the Zon's model (Eq. (4.11)).

If atomic electrons follow the electric field of the laser light adiabatically, $\Delta\rho(\boldsymbol{r}, t)$ in Eq. (4.10) can be written as

$$\Delta\rho(\boldsymbol{r}, t) = \rho^{(1)}(\boldsymbol{r}) \sin(\omega t), \tag{4.38}$$

where $\rho^{(1)}(\boldsymbol{r})$ is the electron density distribution which oscillates with the angular frequency of ω. By substituting $\Delta\rho(\boldsymbol{r}, t)$ into Eq. (4.10), the scattering potential representing the light-dressing effect is given by

$$V_{\rm dress}(\boldsymbol{r}, t) = \frac{e^2}{4\pi\epsilon_0} \sin(\omega t) \int \frac{\rho^{(1)}(\boldsymbol{r}')}{|\boldsymbol{r} - \boldsymbol{r}'|} {\rm d}\boldsymbol{r}'. \tag{4.39}$$

By adopting FBA, the scattering amplitude by this potential is given by

$$f_{\rm dress}(\theta) = \frac{2m_{\rm e}e^2}{4\pi\epsilon_0\hbar^2 s^2} {\rm i} \int {\rm d}\boldsymbol{r} \rho^{(1)}(\boldsymbol{r}) e^{{\rm i}\boldsymbol{s}\cdot\boldsymbol{r}}. \tag{4.40}$$

This formula states that the scattering amplitude which leads to the light-dressing effect is proportional to the Fourier transform of the spatial distribution of the oscillating atomic electrons ($\rho^{(1)}(\boldsymbol{r})$). Therefore, by analyzing the observed angular distribution of the LAES process, the

spatial distribution of the oscillating electrons can be determined.

In general, electrons in an atom or a molecule exposed to an intense laser field oscillate not only with the frequency of ω but also with frequencies of of $l\omega$ ($l = 2, 3, 4 \cdots$). Then the evolution of the electron density distribution is given by

$$\Delta\rho(\boldsymbol{r}, t) = \sum_{l=1}^{+\infty} \rho^{(l)}(\boldsymbol{r}) \sin(l\omega t + \phi_l), \tag{4.41}$$

where ϕ_l represents the phase of the oscillation. The motion of electrons with the frequency of $l\omega$ has been known to be responsible for the high-order harmonic generation [45] which plays an important role in attosecond science. In this case, the differential cross section of the LAES process with the energy shift of n-photon is given by

$$\frac{\mathrm{d}\sigma_n^{\mathrm{B1}}}{\mathrm{d}\Omega} = \frac{|\boldsymbol{p}_{\mathrm{f},n}|}{|\boldsymbol{p}_{\mathrm{i}}|} \Big| f_{\mathrm{atom}}(\theta) J_n(\xi) - \sum_{l=1}^{+\infty} f_{\mathrm{dress},l}(\theta) \Big(\mathrm{e}^{-\mathrm{i}\phi_l} J_{n-l}(\xi) - \mathrm{e}^{\mathrm{i}\phi_l} J_{n+l}(\xi) \Big) / 2 \Big|^2, \tag{4.42}$$

$$f_{\mathrm{dress},l}(\theta) = \frac{2m_{\mathrm{e}}e^2}{4\pi\epsilon_0\hbar^2 s^2} \mathrm{i} \int \mathrm{d}\boldsymbol{r} \rho^{(l)}(\boldsymbol{r}) e^{\mathrm{i}\boldsymbol{s}\cdot\boldsymbol{r}}, \tag{4.43}$$

where FBA is adopted for calculating the scattering amplitudes. The derivation of the formulae is given in Appendix 3. Because the light-dressing effect usually becomes prominent at small scattering angles, the light-dressing effect appearing at $s \sim 0$ and $\xi \sim 0$ is considered. Because of the relationship of the Bessel function [75],

$$J_m(0) = \begin{cases} 1 & (m = 0) \\ 0 & (m \neq 0), \end{cases} \tag{4.44}$$

the contribution of the term $l = n$ dominates the differential cross section of the LAES process with a n-photon energy shift. Therefore, the light-dressing effect appearing in the LAES n-photon processes strongly reflects the density distribution of the electrons which oscillates with the frequency of $|n|\omega$ ($\rho^{(|n|)}(\boldsymbol{r})$) and the phase of the oscillation ($\phi_{|n|}$). This means that the spatial distribution of electrons which oscillates $|n|\omega$ and the phase ($\phi_{|n|}$) can be determined by analyzing the angular distributions of the LAES signals with the n-photon energy shift. If $\rho^{(l)}(\boldsymbol{r})$ and ϕ_l (for $l = 1, 2, 3, \cdots$) are obtained, the evolution of the electron density distribution in atoms or molecules ($\Delta\rho(\boldsymbol{r}, t)$) can be reconstructed by using Eq. (4.41). Towards the observation of the light-dressing effect in the LAES n-photon ($|n| \geq 2$) processes, we recently succeeded in observing the LAES $n = +1, \cdots, +6$ processes by using a tightly focused laser beam [276].

By the above discussion, it was confirmed that the spatial distribution of the oscillating electrons is indeed reflected in the angular distribution of the LAES signals. Future development in experimental techniques and theoretical methods will make it possible to determine the spatial

distribution of the electrons oscillated by intense laser fields. In order to measure the spatial distribution of the oscillating electrons by the scattering of ultrashort X-ray or electron pulses, the following two conditions should be satisfied: (i) the duration of the pulses and the velocity mismatch effect are shorter and less than the period of the oscillation, and (ii) the signal to noise ratio is so high that the changes of diffraction patterns originating from the deformation of electron density distribution, which are usually quite small compared with the electron density distribution in the absence of the laser fields (Fig. 77), can be recorded. The advantage of using the LAES process for the measurement of the oscillating electrons is that the information of the oscillation frequency and the spatial distribution of the oscillating electrons in the target atoms can be obtained from the energy and angular distributions of the LAES signals without using ultrashort electron pulses. Furthermore, as discussed above, the small-angle LAES signals with n-photon energy shift depend mainly on $\rho^{(|n|)}(\boldsymbol{r})$ not $\rho_{\rm atom}(\boldsymbol{r})$ (Eq. (4.7)), and consequently, the LAES signals are highly sensitive to the changes of the electron density distribution.

5 Apparatus for laser-assisted (e,2e)

In the preceding chapters, the laser-assisted electron (elastic) scattering (LAES) process was investigated. In the LAES process, the kinetic energy of a scattered electron is given by $E_0 + nh\nu$, where E_0 is the kinetic energy of an incident electron, n is integer ($n = 0, \pm1, \pm2, \cdots$), h is the Planck constant, and ν is the frequency of a laser field. In addition to the LAES process, the laser-assisted electron impact excitation process and the laser-assisted electron impact ionization process can also occur through the collision between an electron and an atom (or a molecule) in the presence of a laser field. Figures 99(a) and (b) show schematics of the laser-assisted electron impact excitation process and the laser-assisted electron impact (single) ionization process, respectively.

In the laser-assisted electron impact excitation process (Fig. 99(a)), the kinetic energy of the scattered electron is given by $E_0 - \Delta W + nh\nu$, where ΔW is an energy difference between electronic states of the target atom before and after the scattering. This scattering process is also called simultaneous electron-photon excitation process ($\Delta W > 0$) or simultaneous electron-photon de-excitation process ($\Delta W < 0$). The laser-assisted inelastic scattering process was first observed by Mason and Newell in 1987 [277]. Subsequently, a number of experimental studies were reported [278–285].

In the laser-assisted electron impact ionization process (Fig. 99(b)), more than one electrons are ejected from the target atom. Here, I focus on the single ionization process expressed as (e,2e) in which an electron is ejected from the target atom. Strictly speaking, the scattered electron and the ejected electron cannot be distinguished. However, for convenience, a faster electron is called scattered electron, and a slower electron is called ejected electron in this study. When the kinetic energies of the scattered and the ejected electrons are expressed as E_{A} and E_{B}

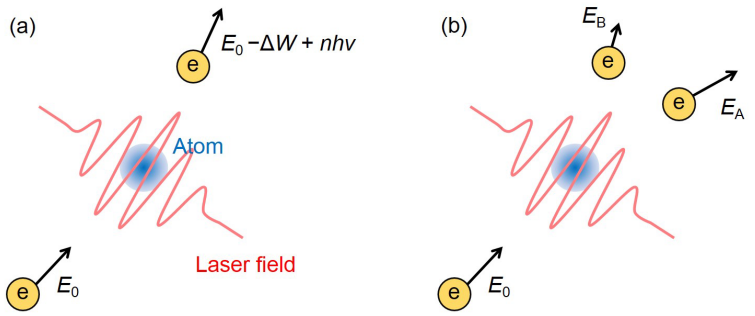

Figure 99: Schematics of the laser-assisted electron impact excitation process (a) and the laser-assisted (e,2e) process (b). E_0: kinetic energy of incident electron. ΔW: excitation energy of the target atom. ν: frequency of the laser field. h: Planck constant.

($E_{\mathrm{A}} \geq E_{\mathrm{B}}$), respectively, a sum of these kinetic energies is given by [286]

$$E_{\mathrm{A}} + E_{\mathrm{B}} = E_0 - E_{\mathrm{IP}} - U_{\mathrm{p}} + nh\nu, \tag{5.1}$$

where E_{IP} represents the Stark-shifted ionization potential of the target atom and U_{p} is the ponderomotive potential which is given by

$$U_{\mathrm{p}} = \frac{e^2 F_0^2}{4 m_{\mathrm{e}} \omega^2}, \tag{5.2}$$

where e is unit charge, m_{e} is the rest mass of electron, F_0 is the amplitude of the laser electric field (Eq. (2.16)), and ω is the angular frequency of the laser field. The ponderomotive potential corresponds to the cycle-averaged quiver energy of a free electron in a laser field [45]. The magnitude of the ponderomotive potential at the wavelength of 800 nm is given by $U_{\mathrm{p}} \simeq 6 \times 10^{-14} I$ (eV), where I is the intensity of the laser field in the unit of W/cm^2 [200]. As will be described in Section 5.2, the experimental study on the laser-assisted (e,2e) process was reported only by Höhr *et al.* [52]. This may be due to an experimental difficulty in detecting a scattered electron and an ejected in coincidence. The requirement of the coincidence detection makes the observation of the laser-assisted (e,2e) process much harder than the observations of the LAES process and the laser-assisted electron impact excitation process.

In this chapter, I report a construction of an apparatus for the observation of the laser-assisted (e,2e) process induced by femtosecond intense laser pulses. As will be discussed in Section 5.1, the (e,2e) process without laser fields can be used to determine the momentum distribution of atomic and molecular orbitals. Therefore, the signals of the laser-assisted (e,2e) process can be used to investigate the momentum distribution of atomic and molecular orbitals in the presence of intense laser fields, which are complementary information to the electron density distribution of atoms and molecules which can be probed by the LAES process (Chapter 4).

The structure of this chapter is as follows. In Section 5.1, I briefly introduce a theory for the (e,2e) process without laser fields. Then, in Section 5.2, I introduce previous theoretical and experimental studies of the laser-assisted (e,2e) process. The details of the apparatus developed in this study are presented in Section 5.3. Section 5.4 is devoted to a numerical simulation of the laser-assisted (e,2e) signals and an estimation of a count rate of the laser-assisted (e,2e) signals measured with the apparatus. Section 5.5 describes a summary of this study and discussions on the applications of the laser-assisted (e,2e) process and on other experimental studies which can be conducted with the apparatus.

5.1 Theory of (e,2e) process without laser fields

In this section, a basic theory of an (e,2e) process without laser fields is introduced. The discussion of this section partially follows a textbook of Weigold and McCarthy [49] and review papers of Ehrhardt *et al.* [287] and Takahashi [50]. In a discussion of the (e,2e) process, the

triple differential cross section is usually employed,

$$\frac{\mathrm{d}^3\sigma}{\mathrm{d}\Omega_\mathrm{A}\mathrm{d}\Omega_\mathrm{B}\mathrm{d}E_\mathrm{B}} = \frac{|\boldsymbol{p}_\mathrm{A}||\boldsymbol{p}_\mathrm{B}|}{\hbar|\boldsymbol{p}_0|}|f(\boldsymbol{p}_\mathrm{A},\boldsymbol{p}_\mathrm{B};\boldsymbol{p}_0)|^2, \tag{5.3}$$

where $\hbar$ is the reduced Planck constant, $f(\boldsymbol{p}_\mathrm{A},\boldsymbol{p}_\mathrm{B};\boldsymbol{p}_0)$ is a scattering amplitude, and $\boldsymbol{p}_\mathrm{A}$, $\boldsymbol{p}_\mathrm{B}$, and $\boldsymbol{p}_0$ are momenta of the scattered, ejected, and incident electrons, respectively. The triple differential cross section can be determined by measuring momenta of a scattered electron and an ejected electron in coincidence. Here I consider a case in which the incoming and the scattered electrons are fast ($\geq$100 eV) and their wavefunctions are represented by plane waves. The target is an atom whose atomic number is represented by Z. By using the first Born approximation (FBA), the scattering amplitude is given by

$$\begin{aligned} f(\boldsymbol{p}_\mathrm{A},\boldsymbol{p}_\mathrm{B};\boldsymbol{p}_0) \quad \propto \quad & -4\pi^2\hbar m_\mathrm{e}\int\int\cdots\int \phi^*_{\boldsymbol{p}_\mathrm{A}}(\boldsymbol{r}_0)\psi^*_{\boldsymbol{p}_\mathrm{B}}(\boldsymbol{r}_Z)\psi^*_\mathrm{f}(\boldsymbol{r}_1,\boldsymbol{r}_2,\cdots,\boldsymbol{r}_{Z-1}) \\ & \times V(\boldsymbol{r}_0,\boldsymbol{r}_1,\cdots,\boldsymbol{r}_Z)\psi_\mathrm{i}(\boldsymbol{r}_1,\boldsymbol{r}_2,\cdots,\boldsymbol{r}_Z)\phi_{\boldsymbol{p}_0}(\boldsymbol{r}_0)\mathrm{d}\boldsymbol{r}_0\mathrm{d}\boldsymbol{r}_1\cdots\mathrm{d}\boldsymbol{r}_Z, \end{aligned} \tag{5.4}$$

with

$$V(\boldsymbol{r}_0,\boldsymbol{r}_1,\cdots,\boldsymbol{r}_Z) = -\frac{e^2}{4\pi\epsilon_0}\frac{Z}{|\boldsymbol{r}_0|} + \frac{e^2}{4\pi\epsilon_0}\sum_{j=1}^{Z}\frac{1}{|\boldsymbol{r}_0-\boldsymbol{r}_j|}, \tag{5.5}$$

where ϵ_0 is the permittivity of vacuum, $\phi_{\boldsymbol{p}_0}(\boldsymbol{r}_0)$ and $\phi_{\boldsymbol{p}_\mathrm{A}}(\boldsymbol{r}_0)$ are wavefunctions of the incident electron and the scattered electron which are represented by the plane waves defined by Eq. (3.4), $\psi_\mathrm{i}(\boldsymbol{r}_0,\boldsymbol{r}_1,\cdots,\boldsymbol{r}_Z)$ is a wavefuntion of the target atom before the scattering, $\psi_{\boldsymbol{p}_\mathrm{B}}(\boldsymbol{r}_Z)$ is a wavefunction of the ejected electron, and $\psi_\mathrm{f}(\boldsymbol{r}_0,\boldsymbol{r}_1,\cdots,\boldsymbol{r}_{Z-1})$ is a wavefunction of an ion generated by the scattering. The exchange between the incident electron and the atomic electron is neglected. By using the definition of the plane wave (Eq. (3.4)), the scattering amplitude becomes

$$\begin{aligned} f(\boldsymbol{p}_\mathrm{A},\boldsymbol{p}_\mathrm{B};\boldsymbol{p}_0) \quad \propto \quad & -\frac{2m_\mathrm{e}e^2}{4\pi\epsilon_0\hbar^2}\frac{1}{s^2}\int\int\cdots\int \psi^*_{\boldsymbol{p}_\mathrm{B}}(\boldsymbol{r}_Z)\psi^*_\mathrm{f}(\boldsymbol{r}_1,\boldsymbol{r}_2,\cdots,\boldsymbol{r}_{Z-1}) \\ & \times\Big(\sum_{j=1}^{Z}\mathrm{e}^{\mathrm{i}\boldsymbol{s}\cdot\boldsymbol{r}_j} - Z\Big)\psi_\mathrm{i}(\boldsymbol{r}_1,\boldsymbol{r}_2,\cdots,\boldsymbol{r}_Z)\mathrm{d}\boldsymbol{r}_1\mathrm{d}\boldsymbol{r}_2\cdots\mathrm{d}\boldsymbol{r}_Z, \end{aligned} \tag{5.6}$$

where s is the absolute value of the scattering vector $\boldsymbol{s} = (\boldsymbol{p}_0-\boldsymbol{p}_\mathrm{A})/\hbar$. When the wavefunctions of the target atom before (ψ_i) and after the scattering ($\psi_{\boldsymbol{p}_\mathrm{B}}\psi_\mathrm{f}$) are orthogonal, this equation can

be written as

$$f(\boldsymbol{p}_{\rm A},\boldsymbol{p}_{\rm B};\boldsymbol{p}_0) \propto -\frac{2m_{\rm e}e^2}{4\pi\epsilon_0\hbar^2}\frac{1}{s^2}\int\int\cdots\int\psi^*_{\boldsymbol{p}_{\rm B}}(\boldsymbol{r}_Z)\psi^*_{\rm f}(\boldsymbol{r}_1,\boldsymbol{r}_2,\cdots,\boldsymbol{r}_{Z-1}) \times\sum_{j=1}^{Z}{\rm e}^{{\rm i}\boldsymbol{s}\cdot\boldsymbol{r}_j}\psi_{\rm i}(\boldsymbol{r}_1,\boldsymbol{r}_2,\cdots,\boldsymbol{r}_Z){\rm d}\boldsymbol{r}_1{\rm d}\boldsymbol{r}_2\cdots{\rm d}\boldsymbol{r}_Z. \quad (5.7)$$

In order to consider the information which the scattering amplitude carries, I make two assumptions: (i) the repulsive interaction between the incoming electron and the electrons in the target atom (second term in the right-hand side of Eq. (5.5)) is dominated by the term $j = Z$ and (ii) the ejected electron is so fast and its wavefunction is given by the plane wave (Eq. (3.4)). Under these assumptions, the scattering amplitude is given by

$$f(\boldsymbol{p}_{\rm A},\boldsymbol{p}_{\rm B};\boldsymbol{p}_0) \propto -\frac{2m_{\rm e}e^2}{4\pi\epsilon_0\hbar^2}\frac{1}{s^2}\int\psi_{\rm D}(\boldsymbol{r}_Z){\rm e}^{{\rm i}\boldsymbol{Q}\cdot\boldsymbol{r}_Z}{\rm d}\boldsymbol{r}_Z, \quad (5.8)$$

with

$$\psi_{\rm D}(\boldsymbol{r}_Z) = \int\int\cdots\int\psi^*_{\rm f}(\boldsymbol{r}_1,\boldsymbol{r}_2,\cdots,\boldsymbol{r}_{Z-1})\psi_{\rm i}(\boldsymbol{r}_1,\boldsymbol{r}_2,\cdots,\boldsymbol{r}_Z){\rm d}\boldsymbol{r}_1{\rm d}\boldsymbol{r}_2\cdots{\rm d}\boldsymbol{r}_{Z-1}, \quad (5.9)$$

and

$$\boldsymbol{Q} = \frac{\boldsymbol{p}_0-\boldsymbol{p}_{\rm A}-\boldsymbol{p}_{\rm B}}{\hbar}. \quad (5.10)$$

The one-electron wavefunction $\psi_{\rm D}(\boldsymbol{r}_Z)$ is known as the Dyson orbital. Equation (5.8) states that the scattering amplitude is proportional to the Fourier transform of the Dyson orbital. Therefore, the scattering amplitude carries the information of the momentum distribution of the Dyson orbital. By using Eq. (5.3), the following relationship is obtained.

$$\frac{{\rm d}^3\sigma}{{\rm d}\Omega_{\rm A}{\rm d}\Omega_{\rm B}{\rm d}E_{\rm B}} \propto \left|\int\psi_{\rm D}(\boldsymbol{r}_Z){\rm e}^{{\rm i}\boldsymbol{Q}\cdot\boldsymbol{r}_Z}{\rm d}\boldsymbol{r}_Z\right|^2. \quad (5.11)$$

Because the triple differential cross section can be determined by an experiment, this equation states that the square of the momentum distribution of the Dyson orbital can be determined experimentally.

The method which has been used to determine the momentum distribution of the Dyson orbitals taking advantage of the (e,2e) process is called electron momentum spectroscopy (EMS) [49, 288]. In EMS, only the scattering events, which involve large scattering vectors and fast ejected electrons whose kinetic energies are similar to those of the scattered electrons ($E_{\rm B} \sim E_{\rm A}$), are measured. Such a scattering process is called electron Compton scattering and can be considered as a billiard-like collision between an incoming electron and an electron in a target atom (or a molecules) [50]. Consequently, the scattering potential is dominated by the repulsive interaction between the incoming electron and an atomic electron to be ejected. Furthermore,

the wavefunction of the ejected electron can be represented by the plane wave. Therefore, the assumptions described above can be satisfied. A detailed theoretical description on the triple differential cross section of the (e,2e) process measured in EMS is given in a review paper [53]. It is true that EMS is a powerful method to directly measure the momentum distributions of atomic and molecular orbitals, it requires long accumulation of signals because of the small cross section of the electron Compton scattering.

On the other hand, it is relatively easy to detect signals from (e,2e) processes in which the kinetic energies of the scattered electron and the ejected electron are asymmetric ($E_{\rm A} \gg E_{\rm B}$). The cross section of the asymmetric (e,2e) process is several orders of magnitude larger than that of the electron Compton scattering. Even though it is impossible to directly measure the momentum distributions of the Dyson orbitals, measured triple differential cross sections carry the information of orbitals [287]. Therefore, by a comparison with an elaborate theoretical calculation, it is possible to investigate the momentum distribution of orbitals.

5.2 Theoretical and experimental studies of laser-assisted (e,2e)

In this section, I give a brief introduction to theoretical and experimental studies on the laser-assisted (e,2e) process by an atom. The earliest theoretical study on the laser-assisted (e,2e) process was reported by Mohan and Chand in 1978 [289]. The Bunkin-Fedorov (Eq. (2.21)) type formula was derived by Cavaliere, Ferrante, and Leone in 1980 [290]. By adopting FBA and neglecting the laser-atom interaction (light-dressing of target atoms), they obtained the triple differential cross section of the laser-assisted (e,2e) process with a n-photon energy shift, which is expressed as

$$\frac{{\rm d}^3\sigma_{n,{\rm B1}}}{{\rm d}\Omega_{\rm A}{\rm d}\Omega_{\rm B}{\rm d}E_{\rm B}}(\boldsymbol{p}_{\rm A},\boldsymbol{p}_{\rm B};\boldsymbol{p}_0) = J_n^2(\boldsymbol{\alpha}_0\cdot\boldsymbol{Q})\frac{{\rm d}^3\sigma_{\rm ff,B1}}{{\rm d}\Omega_{\rm A}{\rm d}\Omega_{\rm B}{\rm d}E_{\rm B}}(\boldsymbol{p}_{\rm A},\boldsymbol{p}_{\rm B};\boldsymbol{p}_0), \tag{5.12}$$

where J_n is n-th order Bessel function of the first kind, ${\rm d}\sigma^3_{\rm ff,B1}/{\rm d}\Omega_{\rm A}{\rm d}\Omega_{\rm B}{\rm d}E_{\rm B}$ is the triple differential cross section for the (e,2e) process outside laser fields obtained by FBA, and $\boldsymbol{\alpha}_0$ is defined by Eq. (2.18). The Kroll-Watson (Eq. (2.29)) type formula was obtained by Banerji and Mittleman in the next year [291]. They also neglected the laser-atom interaction. By adopting the low-frequency approximation which was used in the Kroll-Watson approximation (Section 2.1.2), they derived the following formula,

$$\begin{aligned}\frac{{\rm d}^3\sigma_n}{{\rm d}\Omega_{\rm A}{\rm d}\Omega_{\rm B}{\rm d}E_{\rm B}}(\boldsymbol{p}_{\rm A},\boldsymbol{p}_{\rm B};\boldsymbol{p}_0) &= J_n^2(\boldsymbol{\alpha}_0\cdot\boldsymbol{Q})\frac{|\boldsymbol{p}_{\rm A}|}{|\boldsymbol{p}_{\rm A}-\boldsymbol{\gamma}|}\frac{|\boldsymbol{p}_{\rm B}|}{|\boldsymbol{p}_{\rm B}-\boldsymbol{\gamma}|}\frac{|\boldsymbol{p}_0-\boldsymbol{\gamma}|}{|\boldsymbol{p}_0|}\\ &\quad\times\frac{{\rm d}^3\sigma_{\rm ff}}{{\rm d}\Omega_{\rm A}{\rm d}\Omega_{\rm B}{\rm d}E_{\rm B}}(\boldsymbol{p}_{\rm A}-\boldsymbol{\gamma},\boldsymbol{p}_{\rm B}-\boldsymbol{\gamma};\boldsymbol{p}_0-\boldsymbol{\gamma}),\end{aligned} \tag{5.13}$$

with

$$\boldsymbol{\gamma} = \frac{m_{\rm e}n\omega}{\boldsymbol{\alpha}_0\cdot\boldsymbol{Q}}\boldsymbol{\alpha}_0. \tag{5.14}$$

Equations (5.12) and (5.13) show that the triple differential cross section of the laser-assisted (e,2e) process is proportional to the triple differential cross section of the (e,2e) process without laser fields when the light-dressing effect of target atoms can be neglected. Therefore, the information that can be obtained on the target atom from the triple differential cross section of the laser-assisted (e,2e) process is the same as that from the triple differential cross section of a (e,2e) process measured without laser fields.

The light-dressing effect of target atoms in the laser-assisted (e,2e) process was discussed by Joachain *et al.* [292–296]. By adopting the first-order perturbation theory to the laser-atom (H [292, 293] and He [294–296]) interaction, they simulated the triple differential cross section of the laser-assisted (e,2e) process. They found that the triple differential cross sections are strongly modified due to the light-dressing effect of target atoms in strong ($\geq 10^{12}$ W/cm^2) laser fields. Furthermore, they show that the light-dressing effect strongly depends on n. As far as I know, theories which treat the laser-atom interaction non-perturbatively have not been reported. Moreover, the information we can obtain from the light-dressing effect appearing in the laser-assisted (e,2e) process is still under debate [297].

The only experimental study on the laser-assisted (e,2e) process was reported by Höhr *et al.* in 2005 [52, 286]. They investigated the laser-assisted (e,2e) process of He atoms by 1 keV electrons in an intense nanosecond laser field (τ = 7 ns, λ = 1064 nm, $h\nu$ = 1.17 eV, I = 4×10^{12} W/cm^2, 10 Hz). They measured (e,2e) signals by using the multiparticle imaging device called reaction microscope [298]. The pulse duration of incident electrons is 1 ns. Instead of the coincidence detection of a scattered electron and an ejected electron, they detected an ejected electron (E_{B} = 3-15 eV) and a He ion, which are generated by the (e,2e) process, in coincidence. A kinetic energy or a momentum of the scattered electron was deduced from the momenta of the ejected electron and the ion by using the momentum conservation rule. The overall energy resolution ($\sim$ 30 eV) was not high enough to discriminate the energy shift by one-photon (=1.17 eV). However, they observed significant differences in triple differential cross sections measured with and without the laser fields. The differences they observed were not reproduced by a numerical simulation in which the light-dressing effect of target He atoms is neglected. According to a subsequent theoretical work [299], their experimental result was qualitatively reproduced by a numerical simulation which treats the light-dressing effect of the target He atoms perturbatively.

5.3 Apparatus for the observation of laser-assisted (e,2e) process

In this section, details of the apparatus developed in this study are described. Most of the components of this apparatus are home-made devices which I designed and constructed. As described in Section 2.3.1, in order to observe laser-assisted processes induced by femtosecond laser pulses, a sensitivity of the apparatus should be high enough to detect weak signals and an energy resolution should be high enough to distinguish laser-assisted (e,2e) signals ($n \neq 0$) from intense background signals originating from (e,2e) events outside laser fields. With specially de-

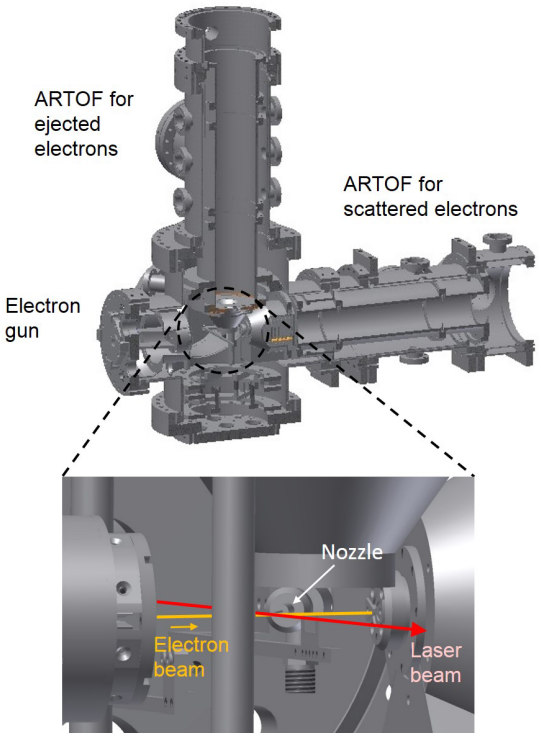

Figure 100: Schematic of an apparatus developed for the observation of the laser-assisted (e,2e) process. An electron gun and two angle-resolved time-of-flight (ARTOF) analyzers are installed in the ultrahigh vacuum chamber.

signed analyzers, the apparatus provides the high sensitivity to detect signals of the laser-assisted (e,2e) process with a count rate of 0.01 count/sec, and an energy resolution better than 0.7 eV. The procedure for the estimation of the signal count rate is described in Section 5.4.

A schematic of the apparatus is shown in Fig. 100. Inside an ultrahigh vacuum chamber, an electron gun and two angle-resolved time-of-flight (ARTOF) analyzers are installed. The photocathode-type electron gun generates a 1 keV electron beam. The ARTOF analyzers were designed in order to detect signals of the asymmetric ($E_{\rm A} \gg E_{\rm B}$) (e,2e) processes with high sensitivity. This is because, as described in Section 5.1, the triple differential cross section of the laser-assisted (e,2e) process in the asymmetric case is much higher than that in the symmetric case ($E_{\rm A} \sim E_{\rm B}$). The scattered and the ejected electrons are detected in coincidence by detectors placed at the end of the each analyzer. In what follows, I describe details of the vacuum chamber, the electron gun, the ARTOF analyzers, and the detectors.

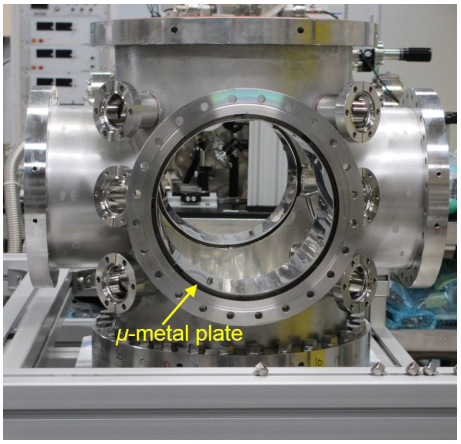

Figure 101: Photograph of an ultrahigh vacuum chamber. The chamber is made of stainless 316 steel. The inner surface of the chamber is covered by μ-metal plates.

5.3.1 Ultrahigh vacuum chamber

A photograph of an ultrahigh vacuum chamber is shown in Fig. 101. The inner surface of the chamber is covered by 1mm thick μ-metal plates for magnetic field shielding. The outside of the vacuum chamber will be covered by the magnetic shielding sheets (Hitachi Metals, Ltd.). A residual pressure in the chamber is of the order of 10^{-9} Torr without a bake-out.

5.3.2 Electron gun

The kinetic energy of the incident electron is 1 keV, which is the same as that of the LAES apparatus used in Chapters 3 and 4 (details on the LAES apparatus is provided in Section 3.5). This is because plenty of data taken with the LAES apparatus can be utilized for a designing and a calibration of the apparatus. A photograph of the electron gun is shown in Fig. 102. The overall structure of the electron gun is almost same as that used for the studies of the femtosecond-LAES process (Fig. 38, Section 3.5.4). An electron pulse is generated through the photoelectric effect on a surface of a gold photo-cathode (10 nm thickness) induced by an irradiation of a 266 nm laser pulse. The generated electron pulse is accelerated by a DC electric field applied between the photocahode (-1000 V) and an anode (0 V). The acceleration voltage can be adjusted within the range from -950 V to -1010 V with a resolution of 0.01 V. The gap between the photocathode and the anode is 0.3 mm. The diameter of the anode is 0.3 mm. The accelerated electron beam is skimmed by a 0.3 mmϕ pinhole placed 3 mm downstream of the anode. Then, the electron beam is collimated by an electromagnetic lens. An octupole deflector is used to adjust the propagation direction of the electron beam. The measured image of the electron beam is shown in Fig. 103.

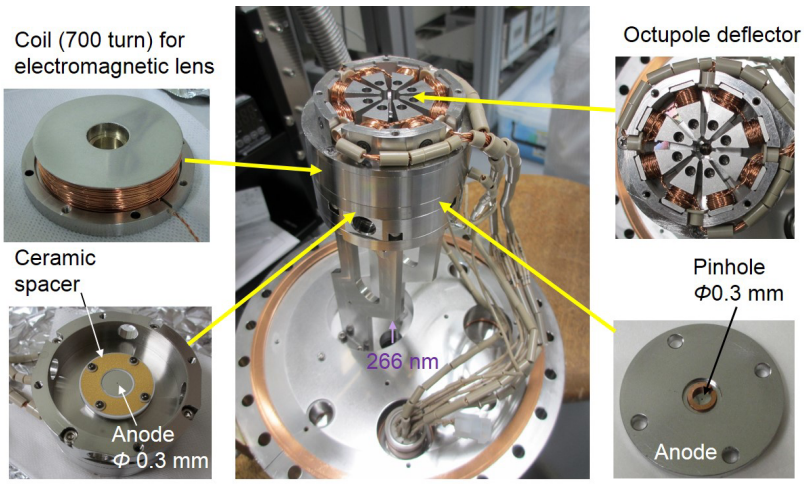

Figure 102: Photograph of a photocathode-type electron gun installed in the (e,2e) apparatus. The structure is almost same as that shown in Fig. 38.

5.3.3 Angle-resolved time-of-flight analyzers

In order to detect (e,2e) signals with high sensitivity, angle-resolved time-of-flight (ARTOF) analyzers [233, 300, 301] were designed and constructed. Because slits and tiny pinholes, which are usually used in conventional electrostatic analyzers, are not used in the ARTOF analyzers, the collection efficiency of the ARTOF analyzer is a few orders of magnitude higher than that can be achieved by the conventional analyzers. In an ARTOF analyzer, a flight time (T) and a two-dimensional position (X, Y) of a signal electron are measured by a detector placed at the end of the analyzer. From the information of T and (X, Y), a three-dimensional momentum (p_x, p_y, p_z) or the kinetic energies and angles (E, θ, ϕ) of the electron signal at the scattering point can be determined. In this study, two ARTOF analyzers were employed in order to detect a scattered electron and an ejected electron in coincidence.

The use of the two ARTOF analyzers for a study of (e,2e) processes was reported very recently by Huth *et al.* [302]. By employing two commercial ARTOF analyzers, they studied the (e,2e) process on solid targets. Their study demonstrates the usefulness of the ARTOF analyzers for the coincidence measurement of two electrons generated by an (e,2e) process. As far as I know, there are no reports about (e,2e) processes of gas-phase samples measured by two ARTOF analyzers.

The ARTOF analyzers developed in this study were deigned in order to detect the (e,2e) signals in the asymmetric energy sharing ($E_{\rm A} \gg E_{\rm B}$) with high sensitivity. One analyzer was designed in order to measure fast ($E_{\rm A}$ =965-975 eV) scattered electrons. The other analyzer was designed to measure slow ($E_{\rm B}$ = 3-14 eV) ejected electrons. These analyzers were designed by using the ion optics simulation software (SIMION 8.0, Scientific Instrument Services Inc.).

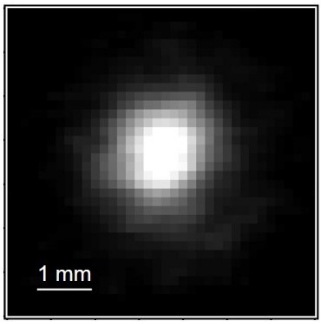

Figure 103: Measured image of the electron beam. The image was measured by a MCP/phosphor coupled with a CCD camera. The MCP/phosphor was installed 300 mm downstream of the electron gun. The diameter of the electron beam is 1.5 mm (FWHM).

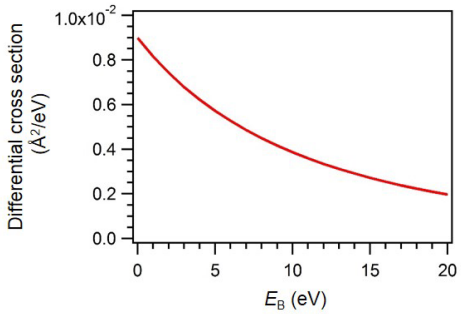

Figure 104: Single differential cross section ($\mathrm{d}\sigma/\mathrm{d}E$) of the (e,2e) process of 1 keV electron by He without laser fields. The data are adopted from Ref. [303]

The optimal geometries of electrodes and appropriate voltages applied to the electrodes were found by hand through trial and error. Detailed descriptions of the two ARTOF analyzers are given in the followings.

Angle-resolved time-of-flight analyzer for slow ejected electrons

In order to determine the kinetic energy range of the ejected electrons to be measured, a single differential cross section ($\mathrm{d}\sigma/\mathrm{d}E$) of a (e,2e) process is considered. In Fig. 104, a single differential cross section of the (e,2e) process of 1 keV electrons by He without laser fields is plotted as a function of a kinetic energy of the ejected electron. It is apparent that the differential cross section becomes small with an increase in the kinetic energy of the ejected electron (E_{B}). On the other hand, according to the experimental study of Höhr *et al.* [52, 286], large background signals appear at the kinetic energy range of less than 3 eV. The background signals are ascribed to the laser-induced ionizations of He atoms excited through the electron impact excitation pro-

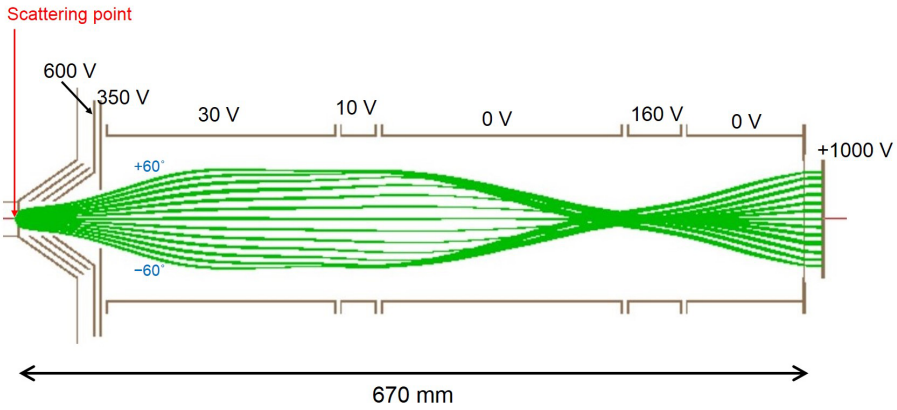

Figure 105: Angle-resolved time-of-flight analyzer for the slow (3-14 eV) ejected electrons. The green lines represent the simulated trajectories of 8 eV electrons.

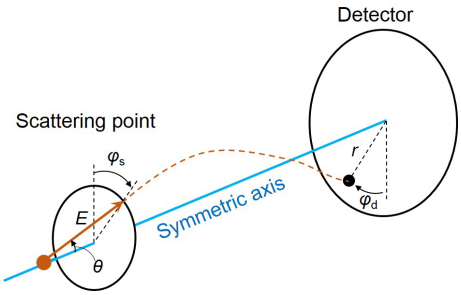

Figure 106: Working principle of the angle-resolved time-of-flight analyzer. The detector measures the two dimensional position ((X, Y) or (r, ϕ_{d})) and the time-of-flight (T). From (r, T), the kinetic energy (E) and the polar angle (θ) of the electron at the scattering point can be determined. From the azimuthal angle of the detector (ϕ_{d}), the azimuthal angle at the scattering point (ϕ_{s}) can be obtained.

cess [52, 286]. Therefore, the analyzer developed in this study was deigned for accepting ejected electrons whose kinetic energies are within the range from 3 eV to 14 eV. The ejected electrons whose kinetic energies are less than 3 eV or larger than 14 eV can be detected, however, three dimensional momenta of these electrons cannot be determined uniquely from the flight-time (T) and the two-dimensional position (X, Y) on the detector. As will be shown in Section 5.4, the slow ejected electrons have a large angular distribution. In order to detect the ejected electrons with high efficiency, the analyzer was deigned to accept electrons emitted into a solid angle of π rad.

Figure 105 shows a cross section of the ARTOF analyzer for the ejected electrons. The analyzer has a cylindrical symmetry. The entrance of the analyzer is grounded (0 V) and covered with a mesh in order to suppress stray electric fields. This is because the stray electric fields

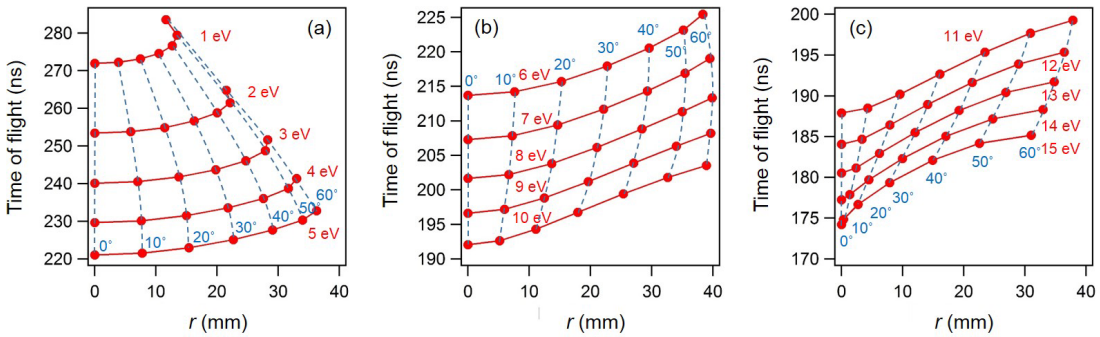

Figure 107: Simulated relationship between (r, T) and (E, θ) in the ARTOF analyzer of the ejected electrons. The kinetic energy of the electron (E) is (a) 1-5 eV, (b) 6-10 eV, and (c) 11-15 eV. The numbers denoted by blue represent the angle (θ, Fig. 106).

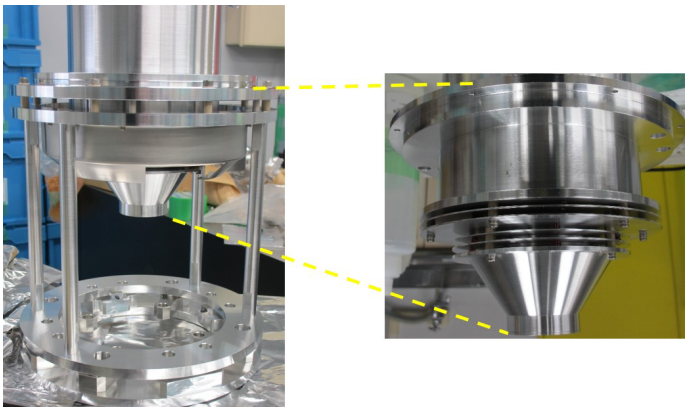

Figure 108: Photographs of the ARTOF analyzer for ejected electrons.

can distort trajectories of scattered electrons and can influence a resolution in kinetic energies of the scattered electrons. The distance between the scattering point and the grounded mesh is 3 mm. The electrons introduced into the analyzer are first accelerated to about 600 eV by three electrodes, and then decelerated to their initial kinetic energies. The trajectories of ejected electrons are shown in Fig. 105. The green lines show simulated trajectories of 8 eV electrons emitted with an angle of 0°, ±10°, $\cdots$, ±60°. Because of the cylindrical symmetry, a pair of the kinetic energy (E) and the polar angle (θ, defined in Fig. 106) of the ejected electron can be determined by the distance from the center of the detector ($r = \sqrt{X^2 + Y^2}$) and the flight-time (T). The relationship between (E, θ) and (r, T) is plotted in Fig. 107. The azimuthal angle ($\phi_{\rm s}$, defined in Fig. 106) can be determined by the azimuthal angle on the detector ($\phi_{\rm d}$ in Fig. 106). By conducting simulations in which the spatial distribution of the scattering point is taken into account, a resolution in kinetic energy was estimated to be better than 0.4 eV (FWHM) when the

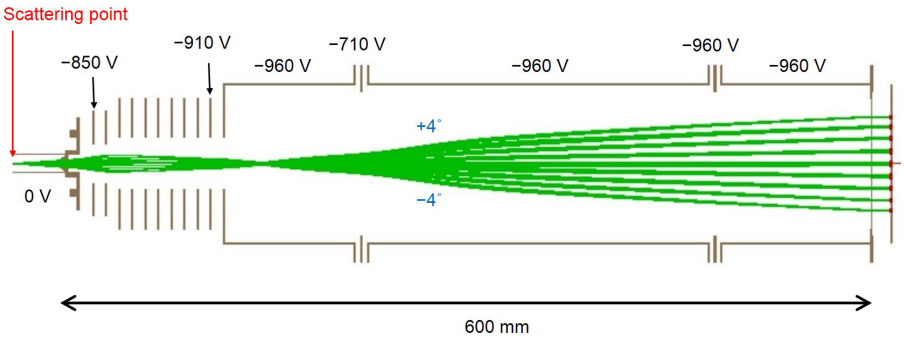

Figure 109: Angle-resolved time-of-flight analyzer for the fast scattered (965-975 eV) electrons. The green lines represent the simulated trajectories of 970 eV electrons.

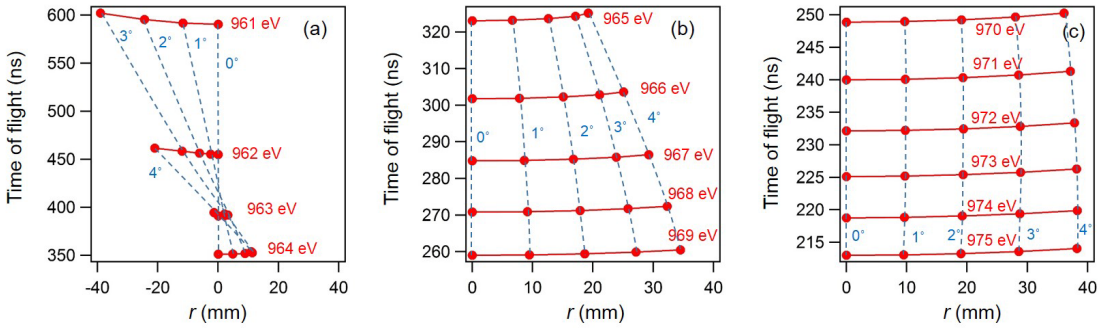

Figure 110: Simulated relationship between (r, T) and (E, θ) in the ARTOF analyzer of the scattered electrons. The kinetic energy of the electron (E) is (a) 961-964 eV, (b) 965-969 eV, and (c) 970-975 eV. The numbers denoted by blue represent the scattering angle. The negative value of r in panel (a) represents that the azimuthal angle on the detector ($\phi_{\rm d}$, Fig. 106) is shifted by π. The time-of-flight (T) for the elastically scattered electrons (1000 eV) is 144 ns.

detector introduced in Section 5.3.4 is used. A resolution in emission angle (θ) was estimated to be better than 3° (FWHM). Photographs of the analyzer are shown in Fig. 108. The analyzer is mounted on a 3-axis stage.

Angle-resolved time-of-flight analyzer for fast scattered electrons

The ARTOF analyzer for the fast scattered electrons was designed for electrons whose kinetic energies are in the range from 965 eV to 975 eV. This energy range was determined by considering the ionization potentials of He ($E_{\rm IP}$ = 24.6 eV), Ne ($E_{\rm IP}$ = 21.6 eV), and Ar ($E_{\rm IP}$ = 15.8 eV). By using Eq. (5.1), the kinetic energy of a scattered electron is given by

$$E_{\rm A} = E_0(\sim 1000\ {\rm eV}) - E_{\rm A}(3{-}14\ {\rm eV}) - E_{\rm IP} - U_{\rm p} + nh\nu. \tag{5.15}$$

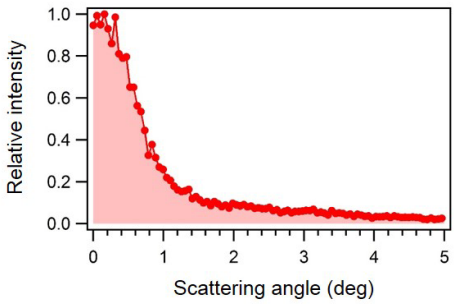

Figure 111: Measured angular distribution of scattered electrons originating from the (e,2e) process by Xe outside laser fields. The kinetic energies of the incident and the scattered electrons are 1000 eV and 985 eV, respectively. This angular distribution was measured by the LAES apparatus (Fig. 83).

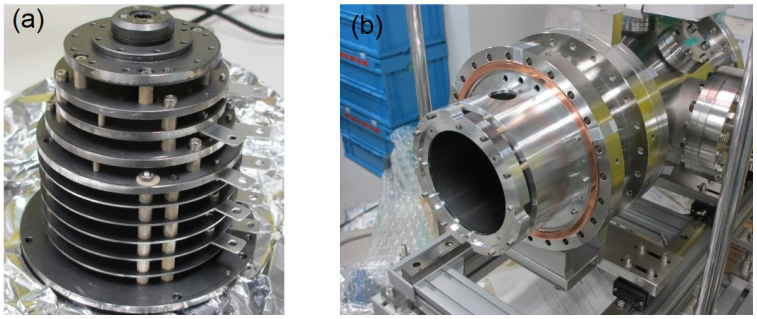

Figure 112: Photographs of the ARTOF analyzer for fast scattered electrons. (a) A photograph of the decelerating electrodes. (b) A photograph of the flight tube.

When ponderomotive potential ($U_{\rm p}$) is neglected, the range of $E_{\rm A}$ corresponding to $E_{\rm IP}$ = 21 eV is from 965 eV to 976 eV for $n = 0$. I note that this energy range does not restrict sample species to be investigated. In practice, depending on the ionization potential of sample species, the kinetic energy of the incident electron E_0, which can be varied from 950 eV to 1010 eV, is adjusted in order to achieve higher collection efficiency.

The analyzer was designed to accept electrons scattered less than 4°. This acceptance angle was determined by considering an angular distribution of scattered electrons measured by the LAES apparatus (Section 4.4.1, Fig. 83). Figure 111 shows the angular distribution of the scattered electrons originating from the (e,2e) process ($E_{\rm A} \sim$ 985 eV, $E_{\rm B} \sim$ 3 eV) of Xe atoms ($E_{\rm IP}$ = 12.1 eV) without laser fields. Most of the scattered electrons appear at the scattering angle range of less than 1°. This shows that the acceptance angle of 4° is large enough to detect most of the scattered electrons.

A cross section of the ARTOF analyzer for the fast electrons is shown in Fig. 109. The analyzer has a cylindrical symmetry. Scattered electrons introduced into the analyzer are decel-

erated by 11 electrodes. Because a voltage of -960 V is applied to a flight tube, the scattered electrons are decelerated to about 10 eV in the analyzer. The apex of the analyzer is located 35 mm downstream of the scattering point. The stray electric field at the scattering point is so small that it has little effect on the ejected electrons. The green lines in Fig. 109 are the simulated trajectories of 970 eV electrons scattered at 0°, ±1°, ±2°, ±3°, ±4°. As with the ARTOF analyzer of the ejected electrons, the kinetic energy (E) and the scattering angle (θ) of the scattered electrons are determined from (r, T). The relationship between (E, θ) and (r, T) is plotted in Fig. 110. By using the detector introduced in Section 5.3.4, an energy resolution better than 0.3 eV (FWHM) can be achieved. Because the energy resolution of the ARTOF analyzer for the ejected electrons is better than 0.4 eV, the overall energy resolution of this apparatus is estimated to be better than 0.7 eV, which is smaller than the photon energy of a 800 nm laser field ($h\nu$ = 1.55 eV). A resolution in scattering angle is estimated to be 0.3° (FWHM). Photographs of the analyzer are shown in Fig. 112.

Collection efficiency of analyzers

Collection efficiencies of the (e,2e) signals with the ARTOF analyzers are discussed. The acceptance angle and energy ranges of the analyzers determine the collection efficiency. As described above, fast scattered electrons originating from the asymmetric (e,2e) process predominantly appear at small scattering angles, and most of them can be accepted by the ARTOF analyzer of scattered electrons. On the other hand, slow ejected electrons are emitted into a large angular range. Because the ARTOF analyzer for ejected electrons can accept electrons emitted into a solid angle of π rad., the collection efficiency is 25% if the angular distribution of the ejected electrons is uniform. From the data of the singly differential cross section shown in Fig. 104, the probability that the kinetic energies of the scattered (E_{A}) and ejected electrons (E_{B}) are within the acceptance range of the analyzers are 40%. Therefore, the overall collection efficiency of the apparatus developed in this study is estimated to be about 25%$\times$40% $=$ 10%.

This collection efficiency is compared with that of a conventional (e,2e) analyzer. In conventional (e,2e) experiments, two electrostatic analyzers which have thin slits or tiny pinholes are usually employed [304]. Angular distributions of the scattered and ejected electrons have to be measured by scanning positions of the analyzers. Furthermore, in order to measure kinetic energy distributions, voltages applied to the analyzer should also be scanned. The advantage of using the ARTOF analyzers is that the scans of the angle and the kinetic energy are not required. Considering the acceptance angle of the conventional analyzer (of the order of milliradian), it can be stated that the collection efficiency of our apparatus is at least three orders of magnitude higher than that of the conventional (e,2e) analyzer.

5.3.4 Detector

In order to detect a scattered electron and an ejected electron in coincidence by using two ARTOF analyzers, two detectors are required. In addition to the delay-line anode detector

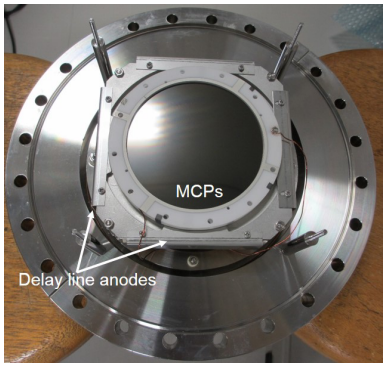

Figure 113: Photograph of a delay-line anode detector (DLD-80).

(HEX-80) described in Section 3.5.9, another delay-line anode detector (DLD-80, RoentDek Handels GmbH) is used. Figure 113 shows a photograph of the DLD-80 detector. Unlike the HEX-80 detector which consists of three delay-line anodes, the DLD-80 detector is composed of two delay-line anodes. The working principle of DLD-80 is the same as that of HEX-80 (Section 3.5.9). From a difference in the arrival times of a signal measured at the ends of anodes, a position and an arrival time of the electron signal on the detector can be determined. The temporal resolution of this analyzer is 500 ps. The spatial resolution is better than 0.5 mm.

5.3.5 Power supplies

I constructed stable power supplies for the electron gun and the ARTOF analyzers. Figure 114 shows photographs of a power supply for the electron gun and for the ARTOF analyzer of scattered electrons. I confirmed that the fluctuation of the voltages applied to the photocathode and electrodes of the analyzer is less than 0.1 V. Furthermore, in order to suppress a degradation of a resolution in kinetic energy originating from a fluctuation of the voltages, voltages applied to the photocathode (~ -1000 V) and the flight-tubes of the analyzer (~ -960 V) are floated on a common high voltage of -960 V. Figure 115 shows photographs of another power supply for the ARTOF analyzer of ejected electrons. It was confirmed that the fluctuation of voltages applied to electrodes of the ARTOF analyzer of ejected electrons is less than 0.1 V.

5.4 Numerical simulation of signal intensity

In this section, I present a result of a numerical simulation of the laser-assisted (e,2e) signals, and discuss an expected count rate of the laser-assisted (e,2e) signals detected by the apparatus developed in this study. The numerical simulation was conducted by adopting Eq. (5.12). Kinetic energies of the incident and the ejected electrons are assumed to be 1000 eV and 5 eV, respectively. Therefore, the kinetic energy of the scattered electron is much larger than the ejected electron ($E_{\mathrm{A}} \gg E_{\mathrm{B}}$). As shown in Fig. 116, momenta of the incident, scattered,

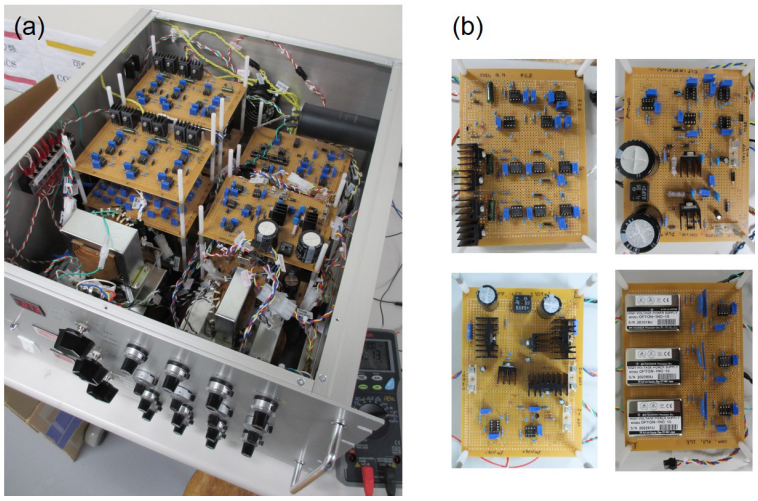

Figure 114: Photographs of the power supply for the electron gun and the ARTOF analyzer of scattered electrons. (a) The overall view of the power supply. (b) Photographs of some components.

and ejected electrons are assumed to lie in the same plane. This arrangement is known as the Ehrhardt asymmetric coplanar geometry [287]. The scattering angle is 1°. The target is H atom. The polarization direction of the laser field is perpendicular to the propagation direction of the incident electron. The averaging effect due to the spatio-temporal overlap of the laser, electron, and atomic beams was taken into account by using the experimental conditions of Chapter 4 (Table 5). The wavelength, the pulse duration, and the peak field intensity of the laser field are 800 nm, 970 fs, and 1.5×10^{12} W/cm^2, respectively.

In order to simulate the triple differential cross section of the laser-assisted (e,2e) process, the triple differential cross section of the (e,2e) process without laser fields is required (Eq. (5.12)). Within the first Born approximation, the triple differential cross section of the (e,2e) process of H atom outside laser fields is given by the following equations [48],

$$\frac{\mathrm{d}^3\sigma_{\mathrm{ff,B1}}}{\mathrm{d}\Omega_\mathrm{A}\mathrm{d}\Omega_\mathrm{B}\mathrm{d}E_\mathrm{B}} = \frac{|\boldsymbol{p}_\mathrm{A}||\boldsymbol{p}_\mathrm{B}|}{\hbar|\boldsymbol{p}_0|}|f_{\mathrm{ff,B1}}|^2, \tag{5.16}$$

$$\begin{aligned} f_{\mathrm{ff,B1}} \propto & -\frac{2}{a_0^4}\frac{1}{s^2}\frac{4\sqrt{2}}{\pi}\exp\Big(\frac{\pi\hbar}{2a_0|\boldsymbol{p}_\mathrm{B}|}\Big)\Gamma\Big(1-\frac{\mathrm{i}\hbar}{a_0|\boldsymbol{p}_\mathrm{B}|}\Big) \\ & \times\frac{\boldsymbol{s}\cdot[\boldsymbol{s}-\boldsymbol{p}_\mathrm{B}/\hbar(1+\mathrm{i}\hbar/a_0|\boldsymbol{p}_\mathrm{B}|)]}{[s^2-(|\boldsymbol{p}_\mathrm{B}|/\hbar+\mathrm{i}/a_0)^2]^{1+\mathrm{i}\hbar/a_0|\boldsymbol{p}_\mathrm{B}|}[(\boldsymbol{s}-\boldsymbol{p}_\mathrm{B}/\hbar)^2+1/a_0^2]^{2-\mathrm{i}\hbar/a_0|\boldsymbol{p}_\mathrm{B}|}}, \end{aligned} \tag{5.17}$$

where a_0 is the Bohr radius, Γ is the Gamma function.

Figures 117(a) and (b) show simulated triple differential cross sections of the laser-assisted (e,2e) $n=0$ and $n=+1$ processes, respectively. The azimuthal angles in Fig. 117(a) and

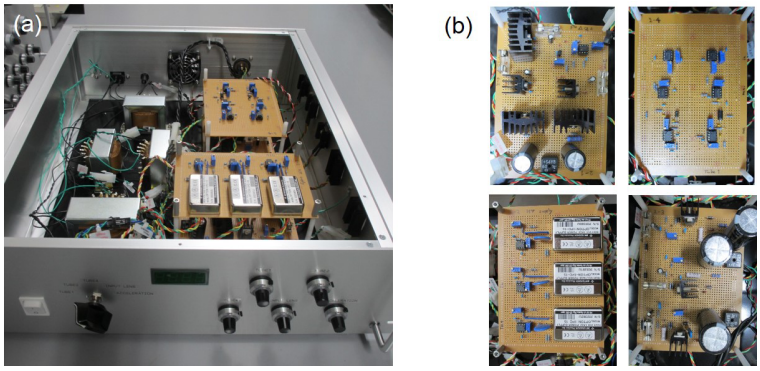

Figure 115: Photographs of the power supply for the ARTOF analyzer of ejected electrons. (a) The overall view of the power supply. (b) Photographs of some components.

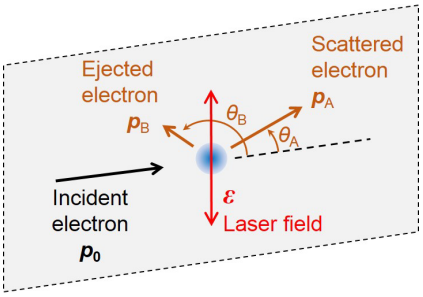

Figure 116: Schematic of a scattering geometry considered in the simulation. All the vectors lie in the same plane. The momenta of the incident, the scattered, and the ejected electrons are represented by $\boldsymbol{p}_0, \boldsymbol{p}_\mathrm{A}$, and $\boldsymbol{p}_\mathrm{B}$, respectively. The laser polarization direction is represented by $\boldsymbol{\epsilon}$.

(b) represent the emission angle of the ejected electron (θ_B) defined in Fig. 116. The triple differential cross section of the laser-assisted (e,2e) $n = 0$ process (Fig. 117(a)) shows two peaks. The peak along the direction of the scattering vector ($\boldsymbol{s}$) is called binary peak [287]. When the binary collision between an incoming electron and an electron in the target atom occurs, the electron is emitted to the direction of the binary peak. The peak in the opposite direction of $\boldsymbol{s}$ is called recoil peak. The the recoil peak is attributed to the backward scattering of the ejected electron by the atom from which the electron is ejected [305]. Within the first Born approximation, the triple differential cross section is symmetric with respect to the scattering vector ($\boldsymbol{s}$) [287].

In the triple differential cross section of the laser-assisted (e,2e) $n = +1$ process (Fig. 117(b)), the intensity of the recoil peak is enhanced compared to that of the $n = 0$ process (Fig. 117(a)). This is because the absolute value of the argument of the Bessel function $|\boldsymbol{\alpha}_0 \cdot \boldsymbol{Q}|$ (Eq. (5.12)) and the absolute value of the Bessel function ($|J_{n=1}(\boldsymbol{\alpha}_0 \cdot \boldsymbol{Q})|$) become large when the ejected electron is emitted to the direction of the recoil peak. A ratio of an integrated in-

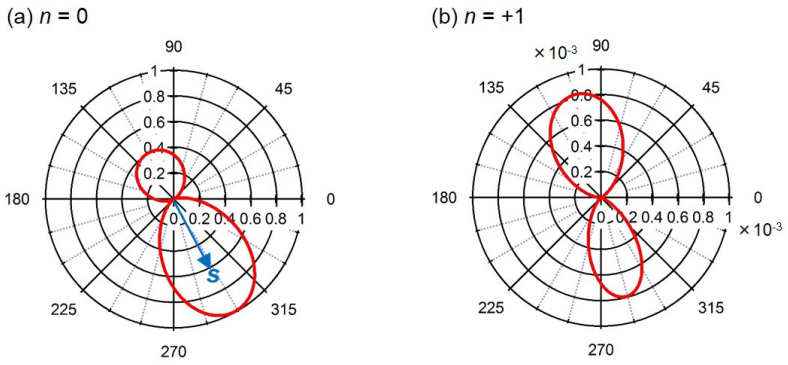

Figure 117: Simulated triple differential cross sections of the laser-assisted (e,2e) process. (a) The triple differential cross section of the laser-assisted (e,2e) $n = 0$ process. (b) The triple differential cross section of the laser-assisted (e,2e) $n = +1$ process. These triple differential cross sections are plotted as a function of the emission angle of the ejected electron ($\theta_{\rm B}$). These intensities are normalized by the peak intensity of the laser-assisted (e,2e) $n = 0$ process. The target is H atom. The direction of the scattering vector $\boldsymbol{s} = (\boldsymbol{p}_0 - \boldsymbol{p}_{\rm A})/\hbar$ is shown by the blue arrow in panel (a). The kinetic energy of the incident electron is $E_0 = 1000$ eV. The kinetic energy of the ejected electron is $E_{\rm B} = 5$ eV. The scattering angle is $\theta_{\rm A} = 1^\circ$. The experimental conditions shown in Table 5 (Chapter 4) are adopted.

tensity of the laser-assisted (e,2e) $n = +1$ process to that of $n = 0$ process is 9.0×10^{-4}. By conducting simulations with different values of $E_{\rm B}$ and $\theta_{\rm A}$, I confirmed that the ratio is not so influenced by these parameters.

By using the result of the simulation, a signal count rate of the laser-assisted (e,2e) $n = +1$ process that will be measured with the apparatus developed in this study was estimated. Even though the above simulation was conducted by considering the geometry in which the vectors of the electrons ($\boldsymbol{p}_0, \boldsymbol{p}_{\rm A}$, and $\boldsymbol{p}_{\rm B}$) and the electric field vector ($F_0\boldsymbol{\epsilon}$) lie in the same plane, the contribution from other geometries should be considered in order to estimate the signal count rate properly. When the electric field vector ($\boldsymbol{\epsilon}$) is out of the plane in which $\boldsymbol{p}_0, \boldsymbol{p}_{\rm A}$, and $\boldsymbol{p}_{\rm B}$ lie, the intensity of the laser-assisted (e,2e) signals ($n \neq 0$) becomes weak because the absolute value of the argument of the Bessel function ($|\boldsymbol{\alpha}_0 \cdot \boldsymbol{Q}|$) decreases. Here, by assuming that the ratio of the intensity of the laser-assisted (e,2e) $n = +1$ process to that of $n = 0$ process averaged over all geometries is 4.5×10^{-4}, which corresponds to 50% of the result of the simulation above, I estimate the signal count rate. Table 6 summarizes factors which mainly determine the signal count rate in the experiment of the LAES process (Chapter 4) and that in the experiment of the laser-assisted (e,2e) process. The signal count rate of the laser-assisted (e,2e) process was calculated by assuming that parameters which are not listed in the table are identical with those of the LAES experiment. By this calculation, it was confirmed that signals of the laser-assisted (e,2e) process will be detected with a count rate of 0.01 count/sec. Considering the signal count rate of the LAES signals ($\sim$0.01 count/sec) in our previous study [44], this result

Table 6: Comparison of signal cont rate in the LAES experiment and that in the laser-assisted (e,2e) experiment. The parameters of the LAES experiment are adopted from the experiment in Chapter 4. The relative intensity represents the ratio of the signal intensity of the $n = +1$ process to that of the $n = 0$ process. The signal count rate of the laser-assisted (e,2e) process was calculated by assuming that the experimental conditions (such as density of sample gases, parameters of the electron and laser beams) are identical with those of the LAES experiment. The detection efficiency of a detector is assumed to be 50%.

	LAES process	laser-assisted (e,2e)
Field-free cross section	Xe, elastic 2.8 Å^2 [113]	H, (e,2e) 0.12 Å^2 [303]
Collection efficiency of analyzer(s)	1%	10%
Detection efficiency of detector(s)	50%	25% (=50%×50%)
Relative intensity	1.7×10^{-3}	4.5×10^{-4}
Signal count rate of $n = +1$ process	0.15 count/sec (measured)	0.01 count/sec (calculated)

of the calculation shows that the collection efficiency of the apparatus developed in this study is so high that the laser-assisted (e,2e) $n = +1$ process induced by femtosecond laser pulses can be observed. As discussed in Section 3.7, by introducing the sample gas as a pulse, the signal count rate will be increased tenfold.

5.5 Summary and future prospects

In this study, the novel apparatus was developed for the observation of the laser-assisted (e,2e) process induced by femtosecond intense laser pulses. The apparatus was designed to detect signals of the asymmetric ($E_{\mathrm{A}} \gg E_{\mathrm{B}}$) (e,2e) process with high sensitivity. The estimated energy resolution of the apparatus is better than 0.7 eV, which is high enough to observe the kinetic energy shift of $h\nu$ ($h\nu$ = 1.55 eV). The signal count rate of the laser-assisted (e,2e) $n = +1$ process is estimated to be 0.01 count/sec, which is almost same as that of our previous LAES experiment described in Section 2.3.2. As discussed in Section 5.2, by using this apparatus, we can investigate momentum distributions of atomic and molecular orbitals in the presence of intense laser fields. Furthermore, we can measure the n-resolved triple differential cross sections of the laser-assisted (e,2e) process, which have not been obtained experimentally. Because the theoretical calculations show that the light-dressing effect of target atoms strongly depend on n (Section 5.2), the n-resolved triple differential cross sections will be useful for investigating the light-dressing effect.

By taking advantage of the high collection efficiency of this apparatus, experiments other than that concerning the laser-assisted (e,2e) process can be performed. In what follows, I propose four experimental studies that can be conducted with this apparatus.

(i) Laser-pump (e,2e)-probe experiment

Very recently, (e,2e) processes without laser fields began to be used as a probe of transient molecular orbitals [306]. When molecules are excited by an ultrashort laser pulse and are probed by the (e,2e) process induced by an ultrashort electron pulse, evolutions of molecular orbitals during chemical reactions can be investigated. Because of an experimental difficulty to measure (e,2e) signals by pulsed electrons with high sensitivity, this pump-probe experiment has been challenging. By taking advantage of the high sensitivity of our apparatus, we can conduct the pump-probe experiment.

Furthermore, by using the laser-assisted (e,2e) process as a probe instead of the (e,2e) process without laser fields, the temporal resolution of the pump-probe experiment can be improved. As discussed in Section 3.2.2, the temporal resolution of the pump-probe experiment in which a reaction of gas-phase molecules is initiated by a laser pulse and is probed by an electron pulse cannot be shorter than 1 ps due to the velocity mismatch effect. Because the laser-assisted (e,2e) process occurs only in the presence of a laser field, the temporal resolution of the pump-probe experiment, in which molecules are excited by an ultrashort laser pulse and probed by the laser-assisted (e,2e) process induced by another ultrashort laser pulse, can be as short as durations of the ultrashort laser pulses ($\leq$10 fs).

(ii) (e,2e) process by laser aligned molecules

Determination of molecular frame (e,2e) cross sections has been an important research topic in collision physics [307–309]. Because gas-phase molecules are oriented randomly, the molecular frame (e,2e) cross sections cannot be obtained by the coincidence detection of scattered and ejected electrons. Currently, in order to determine the molecular frame (e,2e) cross sections, dissociations of target molecules induced by the (e,2e) process has been used [307–309]. The dissociation of a target molecule which is ionized by an (e,2e) process results in an fragment ion. By measuring an emission direction of the fragment ion, the direction of the molecular axis at the moment of the (e,2e) process can be deduced if the dissociation proceeds much faster than the time scale of molecular rotation ($\sim$picoseconds). Therefore, by detecting a fragment ion in coincidence with a scattered electron and an ejected electron, the molecular frame (e,2e) cross sections can be determined.

An alternative method to determine the molecular frame (e,2e) cross sections is the use of the laser-induced molecular alignment technique. It has been known that gas-phase molecules can be aligned when they interact with a linearly polarized intense ultrashort laser pulse [310]. This means that by irradiating gas-phase molecules with ultrashort laser pulses, the molecular axis can be fixed in space. By measuring signals of an (e,2e) process of the aligned molecules, the molecular frame (e,2e) cross section can be determined. As far as I know, there are no experimental reports about the (e,2e) process by the laser-aligned molecules. By using our high-sensitive (e,2e) apparatus, the measurement of the (e,2e) process by the laser-aligned molecules can be performed. The advantage of using the laser-alignment technique is that it can be used to

measure the molecular frame (e,2e) cross sections of molecules which do not dissociate immediately after the (e,2e) process.

(iii) Light-dressing effect of target atoms and molecules in the LAES process

In Chapters 3 and 4 of this thesis, I presented angular distributions of the LAES $n = +1$ process by CCl_4 and Xe. I found that intensities of the observed angular distributions are higher than those of the simulated angular distributions at the scattering angle range less than $\sim 4^\circ$. In Chapter 4, I proposed that this disagreement may be attributed to the light-dressing effect of target atoms (molecules) originating from a deformation of an electron density distribution near an atomic nucleus. In order to confirm the hypothesis and to further examine the origin of the deviations, LAES signals should be detected with a higher signal-to-noise ratio and the deviations from simulation should be measured by changing experimental conditions. Because the ARTOF analyzer of scattered electrons developed in this study does not have a thin slit which is used in the toroidal energy analyzer (Chapters 3 and 4), the LAES signals can be observed with a sensitivity about two orders of magnitude higher than that of the toroidal energy analyzer. By measuring the LAES signals with the higher signal-to-noise ratio and by comparing the magnitude of the deviations measured by changing laser field intensities and sample species, a detailed discussion on the origin of the deviations will be done.

(iv) Light-dressing effect of target atoms and molecules in the laser-assisted electron impact excitation

As described in the introduction of this Chapter, the laser-assisted electron impact excitation process can also be induced by the collision between an electron and an atom in the presence of a laser field. According to a theoretical study [311], as in the case of the LAES process, a peak structure originating from the light-dressing of target atoms appears in an angular distribution of the laser-assisted electron impact excitation process. As discussed in Chapter 3, the peak structure appearing in the angular distribution of the LAES process reflects the interaction between a laser field and an atom which is in the ground state. On the other hand, the peak appearing in the angular distribution of the laser-assisted electron impact excitation process contains the information about the interaction between a laser field and an excited atom. Because there are few experimental reports about the laser-assisted electron impact excitation process in intense laser fields [284], the theoretical prediction has not been confirmed yet. By using the ARTOF analyzer of scattered electrons developed in this study, the light-dressing effect appearing in the laser-assisted electron impact excitation process induced by femtosecond intense laser pulses can be investigated. Thanks to the large acceptance energy range ($\sim$10 eV) of the analyzer, the measurement of the laser-assisted electron impact excitation process can be conducted simultaneously with the measurement of the laser-assisted (e,2e) process when the excitation energy (ΔW, Fig. 99) is several eV lower than the ionization potential.

6 Conclusion

This thesis has been concerned with three topics: (i) the development of the laser-assisted electron diffraction (LAED) method, (ii) the first observation of the light-dressing effect of target atoms in the laser-assisted electron scattering (LAES) process, and (iii) the development of a high-sensitive apparatus for the observation of the laser-assisted (e,2e) process induced by ultrashort laser pulses.

In the first topic, by measuring the angular distributions of the LAES signals of CCl_4 induced by femtosecond laser pulses, the LAED patterns were observed for the first time. I demonstrated that the geometrical structure of CCl_4 at the moment of the laser irradiation can be determined from the observed LAED patterns by using established analytical methods used in the conventional gas-phase electron diffraction. This means that LAED can be used to determine instantaneous geometrical structures of gas-phase molecules with 10 fs temporal resolution and 0.01 Å spatial resolution. By employing LAED, structural changes in gas-phase molecules such as chemical-bond breaking and rearrangement induced by ultrashort laser pulses can be probed as a series of snapshots.

In the second topic, the light-dressing effect of target atoms, i.e., the effect originating from the laser-induced deformation of the electron density distribution of atoms, was observed for the first time in the LAES signals. The light-dressing effect appearing in the LAES signals was predicted more than 30 years ago, however, it had not been detected. In this study, by improving the home-made femtosecond-LAES apparatus, I succeeded in observing sharp peak profiles which are attributed to the light-dressing effect of target Xe atoms at the small scattering angle range less than 0.5° in the angular distributions of the LAES $n = \pm 1$ processes. I demonstrated that the evolution of the electron density distribution of atoms and molecules can be probed by measuring the light-dressing effect appearing in the LAES signals. Combined with the LAED technique which uses electron diffraction patterns appearing at large scattering angles, the ultrafast evolution of the geometrical structure and the electron density distribution will be measured simultaneously. Furthermore, this study opened a new experimental research field in collision physics: the collision between light-dressed electrons and the light-dressed atoms, which have been only of theoretical interest so far.

In the third topic, a novel (e,2e) apparatus was developed for the observation of the laser-assisted (e,2e) process. In order to detect (e,2e) signals with high sensitivity, angle-resolved time-of-flight analyzers were originally designed. By conducting a numerical simulation, I showed that the laser-assisted (e,2e) process induced by femtosecond laser pulses can be measured by using this apparatus. The ultrafast laser-assisted (e,2e) process will be a unique tool to investigate momentum distributions of atomic and molecular orbitals in the presence of intense laser fields.

Appendix 1: Processes related to LAES

It has been known that a free electron cannot absorb or emit photons through the interaction with a laser field. This can be explained that the conservation of the kinetic energy and the conservation of momentum do not hold simultaneously [41]. On the other hand, when an electron and a laser field interact with a matter simultaneously, the electron can absorb or emit photons. This is because the matter can accept momentum which is required to satisfy the energy-momentum conservation. In the laser-assisted electron scattering (LAES) process, atoms accept momentum through the collision with electrons [41]. In this section, I introduce two processes similar to the LAES process by which the kinetic energy of electrons can be shifted. The first process has been used to measure the duration of ultrashort laser and electron pulses. The second process has been used for the ultrafast imaging of evanescent fields on nanostructures.

When a free electron abruptly enters or exits a laser field, the kinetic energy of the electron can be shifted. It has been known that the amount of the energy shift depends on the vector potential of the laser field at the moment of the abrupt entering or the abrupt exit [312, 313]. The abrupt entering into the laser field occurs when an electron is emitted through the ionization of an atom induced by an attosecond laser pulse in the presence of a VIS/NIR laser field [314]. The abrupt exit of the laser field can be induced by intersecting an electron beam and a laser beam at a thin foil mirror that reflects the laser beam [313]. The method called laser streaking uses the kinetic energy shift originating from the abrupt entering into or exit of the laser field in order to measure the durations of the laser and electron pulses with high temporal resolution. By taking advantage of the ultrafast oscillation of the vector potential (oscillation period = 2.7 fs when the wavelength is 800 nm), the durations of laser and electron pulses can be measured with attosecond temporal resolution by the method of laser streaking [313, 315].

The kinetic energy shift of electrons can also be induced when electrons interact with an evanescent optical field generated by an irradiation of a laser pulse on a nanostructured material [316]. Because evanescent optical fields generated on nanostructures are spatially confined, they have a broad momentum distribution. The broad distribution of momentum satisfy the energy-momentum conservation [317]. Consequently, electrons can absorb or emit photons through the interaction with the evanescent optical fields. This process has been used in the electron microscopy in order to investigate evanescent optical fields with nanometer spatial resolution [316, 318]. Because only the electrons which pass through evanescent fields can absorb or emit photons, the electron microscope images of the energy shifted electrons show the spatial distribution of the evanescent fields [316].

Appendix 2: Method for simulating LAES signals

In this section, I describe a procedure for simulating the angular distribution of the LAES process by considering the spatiotemporal overlap between the laser, electron, and atomic (molecular) beams. The simulation is performed in five steps. In the first step, a distribution of the laser field intensity at the moment of the scattering ($P(I)$), where I represents the laser field intensity, is calculated by considering the spatiotemporal overlap between the three beams. In Fig. 118, I show the calculated $P(I)$. The experimental conditions in Chapter 4 (Table 5) are used for the simulation in this section.

In the second step, a two-dimensional intensity distribution of the LAES signals on the slit of the analyzer (Section 3.5.8) is calculated by using $P(I)$. When the Kroll-Watson approximation (Section 2.1.2, Eq. (2.29)) is employed for the simulation, the intensity of the LAES signals with n-photon energy shift on the slit is given by the following equation,

$$I_n^{\mathrm{slit}}(\theta, x) = \int P(I) \frac{|\boldsymbol{p}_{\mathrm{f},n}|}{|\boldsymbol{p}_{\mathrm{i}}|} J_n^2(\xi) \frac{\mathrm{d}\sigma_{\mathrm{el}}}{\mathrm{d}\Omega} \mathrm{d}I, \tag{A2.1}$$

$$\xi = \frac{e}{m_{\mathrm{e}}\hbar\omega^2} (\boldsymbol{p}_{\mathrm{i}} - \boldsymbol{p}_{\mathrm{f},n}) \cdot \boldsymbol{F}, \tag{A2.2}$$

where θ is the scattering angle, x represents the position on the slit along the x axis (x, y, and z axes are defined in Fig. 26), $\boldsymbol{p}_{\mathrm{i}}$ and $\boldsymbol{p}_{\mathrm{f},n}$ are the momenta of the electron before and after the scattering, J_n is the n-th order Bessel function of the first kind, $\mathrm{d}\sigma_{\mathrm{el}}/\mathrm{d}\Omega$ is the differential cross section of the elastic scattering without laser fields, e is the unit charge, m_{e} is the mass of electron, ω is an angular frequency of the laser field, and $\boldsymbol{F}$ is the the amplitude vector of the electric field which depends on I. In Figs. 119(a) and (b), I show the simulated intensity distributions on the slit calculated by using the Kroll-Watson approximation and the Zon's model

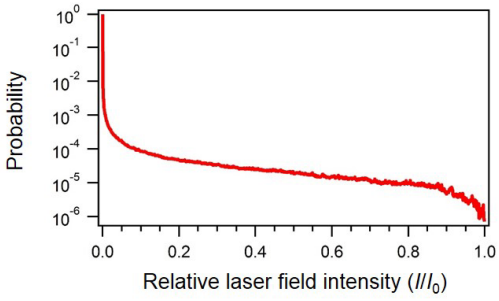

Figure 118: Distribution of the laser field intensity at the moment of the electron scattering. The intensity of the distribution is normalized so that the sum of the intensities is equal to unity. The spatio-temporal overlap between the laser beam, the electron beam, and the atomic beam is taken into account. The peak field intensity (I_0) is 1.5×10^{12} W/cm^2.

used in Section 4.2.1, respectively. Because the diameter of the electron beam (0.24 mm) at the scattering point is smaller than the width of the slit (0.8) mm, the spatial distribution of the scattering point was neglected in the simulation.

In the third step, the two-dimensional intensity distribution of the LAES signals on slit is integrated along the direction of the x axis,

$$I_n^{\mathrm{slit,int}}(\theta) = \int I_n^{\mathrm{slit}}(\theta, x)\mathrm{d}x. \tag{A2.3}$$

Figures 120(a) and (b) show the obtained angular distributions of the LAES signals simulated based on the Kroll-Watson approximation and the Zon's model, respectively.

In the fourth step, the experimental angular resolution (0.24° for $n = \pm 1$, FWHM) and the effect of the wire which blocks the electrons scattered at small angle range of $\theta < 0.11°$ are considered by using the following equation,

$$I_n^{\mathrm{Det}}(\theta) = \int_{-\infty}^{+\infty} W(|\theta'|) I_n^{\mathrm{slit,int}}(|\theta'|) \exp\Big(-4\ln(2)\frac{(\theta-\theta')^2}{A_\theta^2}\Big)\mathrm{d}\theta', \tag{A2.4}$$

$$W(\theta) = \begin{cases} 0 & (\theta < 0.11°) \\ 1 & (\theta \geq 0.11°), \end{cases} \tag{A2.5}$$

where $W(\theta)$ represents the effect of the wire and A_θ =0.24°.

In the final step, a normalization is performed. The normalization constant (N) is obtained by

$$N = \frac{\int_{\theta=0°}^{10°} I_{n=0}^{\mathrm{exp}}(\theta)\mathrm{d}\theta}{\int_{\theta=0°}^{10°} I_{n=0}^{\mathrm{Det}}(\theta)\mathrm{d}\theta}, \tag{A2.6}$$

where $I_{n=0}^{\mathrm{exp}}(\theta)$ is the observed angular distribution of the elastic scattering. As described in Section 3.5.5, about 10% of the elastic scattering signals is originating from the scattering by the residual gas, i.e., the Xe atoms outside the atomic beam. Because the LAES process occurs only where the laser, electron, and atomic beams are overlapped, the residual gas does not contribute to the LAES signals. Consequently, the correction of the normalization constant is required. When the correction factor is denoted by N_c and the normalized LAES angular distributions ($n \neq 0$) are represented by $N_c N I_n^{\mathrm{Det}}(\theta)$, the correction factor is $N_c = 0.9$ if the contribution of the residual gas to the elastic scattering is 10%.

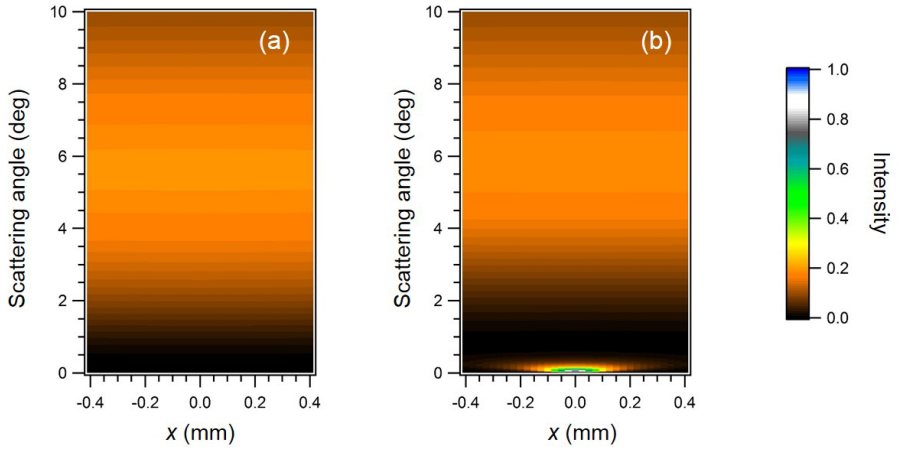

Figure 119: Signal intensity of the LAES $n = +1$ process on the slit (0.8 mm width) of the toroidal energy analyzer. (a) Result of the simulation based on the Kroll-Watson approximation in which the light-dressing effect of the target atoms is neglected. (b) Result of the simulation based on the Zon's model in which the light-dressing effect is approximately taken into account. The distribution of the laser field intensity shown in Fig. 118 was used for the simulations.

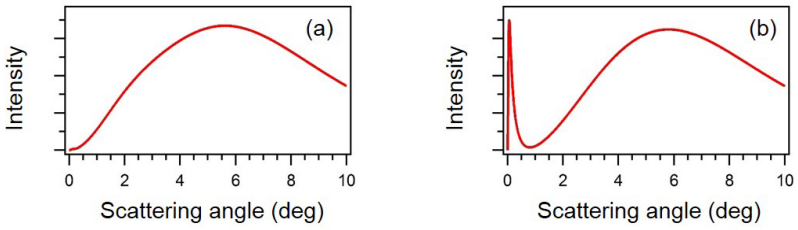

Figure 120: The angular distributions of the LAES process with one photon energy shift. (a) Angular distribution calculated using the Kroll-Watson approximation. (b) Angular distribution calculated using the Zon's model. These distributions were obtained by integrating the two-dimensional signal intensities shown in Fig. 119 along the x axis.

Appendix 3: Formulas for the light-dressing effect of target atoms in the LAES process

In this section, I discuss the kinetic energy distribution and the angular distribution of the LAES process by an atom whose electron density distribution changes with time, and provide a derivation of the formula presented in Section 4.6. First, I write the electron density distribution of the target atom as

$$\rho(\boldsymbol{r},t) = \rho^{(0)}(\boldsymbol{r}) + \Delta\rho(\boldsymbol{r},t), \tag{A3.1}$$

$$\Delta\rho(\boldsymbol{r},t) = \sum_{j=1}^{\infty} \Delta\rho_j(\boldsymbol{r})\sin(\omega_j t + \phi_j), \tag{A3.2}$$

where $\rho^{(0)}(\boldsymbol{r})$ represents the electron density distribution of the target atom which does not vary with time, $\Delta\rho_j(\boldsymbol{r})$ is the spatial distribution of the electrons in the target atom which oscillate with an angular frequency of ω_j, and ϕ_j represents the phase of the oscillation. Within the first Born approximation, the S-matrix for the LAES process is given by [45]

$$S_{\boldsymbol{p}_\mathrm{f},\boldsymbol{p}_\mathrm{i}} = \delta(\boldsymbol{p}_\mathrm{f} - \boldsymbol{p}_\mathrm{i}) - \frac{\mathrm{i}}{\hbar}\int\int \chi^*_{\boldsymbol{p}_\mathrm{f}}(\boldsymbol{r},t)V(\boldsymbol{r},t)\chi_{\boldsymbol{p}_\mathrm{i}}(\boldsymbol{r},t)\mathrm{d}\boldsymbol{r}\mathrm{d}t, \tag{A3.3}$$

where δ represents the delta function, $\chi_{\boldsymbol{p}}(\boldsymbol{r},t)$ is the Gordon-Volkov wavefunction defined by Eq. (2.13), and $V(\boldsymbol{r},t)$ is the scattering potential defined by Eq. (4.6). The value of $|S_{\boldsymbol{p}_\mathrm{f},\boldsymbol{p}_\mathrm{i}} - \delta(\boldsymbol{p}_\mathrm{f} - \boldsymbol{p}_\mathrm{i})|^2$ represents the probability that an incident electron with the momentum of $\boldsymbol{p}_\mathrm{i}$ is scattered to the state which is characterized by $\boldsymbol{p}_\mathrm{f}$. By using Eq. (4.8), I obtain

$$S_{\boldsymbol{p}_\mathrm{f},\boldsymbol{p}_\mathrm{i}} - \delta(\boldsymbol{p}_\mathrm{f} - \boldsymbol{p}_\mathrm{i}) = S^{(1)}_{\boldsymbol{p}_\mathrm{f},\boldsymbol{p}_\mathrm{i}} + S^{(2)}_{\boldsymbol{p}_\mathrm{f},\boldsymbol{p}_\mathrm{i}}, \tag{A3.4}$$

with

$$S^{(1)}_{\boldsymbol{p}_\mathrm{f},\boldsymbol{p}_\mathrm{i}} = -\frac{\mathrm{i}}{\hbar}\int\int \chi^*_{\boldsymbol{p}_\mathrm{f}}(\boldsymbol{r},t)V_\mathrm{atom}(\boldsymbol{r})\chi_{\boldsymbol{p}_\mathrm{i}}(\boldsymbol{r},t)\mathrm{d}\boldsymbol{r}\mathrm{d}t, \tag{A3.5}$$

$$S^{(2)}_{\boldsymbol{p}_\mathrm{f},\boldsymbol{p}_\mathrm{i}} = -\frac{\mathrm{i}}{\hbar}\int\int \chi^*_{\boldsymbol{p}_\mathrm{f}}(\boldsymbol{r},t)V_\mathrm{dress}(\boldsymbol{r},t)\chi_{\boldsymbol{p}_\mathrm{i}}(\boldsymbol{r},t)\mathrm{d}\boldsymbol{r}\mathrm{d}t, \tag{A3.6}$$

$$V_\mathrm{atom}(\boldsymbol{r}) = -\frac{Ze^2}{4\pi\epsilon_0|\boldsymbol{r}|} + \int \frac{e^2\rho^{(0)}(\boldsymbol{r}')}{4\pi\epsilon_0|\boldsymbol{r}-\boldsymbol{r}'|}\mathrm{d}\boldsymbol{r}', \tag{A3.7}$$

and

$$V_\mathrm{dress}(\boldsymbol{r},t) = \int \frac{e^2\Delta\rho(\boldsymbol{r}',t)}{4\pi\epsilon_0|\boldsymbol{r}-\boldsymbol{r}'|}\mathrm{d}\boldsymbol{r}' \tag{A3.8}$$

$$= \sum_{j=1}^{\infty}\sin(\omega_j t + \phi_j)\int \frac{e^2\Delta\rho_j(\boldsymbol{r}')}{4\pi\epsilon_0|\boldsymbol{r}-\boldsymbol{r}'|}\mathrm{d}\boldsymbol{r}' \tag{A3.9}$$

By using the definition of the Gordon-Volkov wavefunction (Eq. (2.13)), It follows that

$$\begin{aligned} S^{(1)}_{\boldsymbol{p}_\mathrm{f},\boldsymbol{p}_\mathrm{i}} &= -\frac{\mathrm{i}}{\hbar}\frac{1}{(2\pi\hbar)^3}\int\int\Big(-\frac{Ze^2}{4\pi\epsilon_0|\boldsymbol{r}|}+\int\frac{e^2\rho^{(0)}(\boldsymbol{r}')}{4\pi\epsilon_0|\boldsymbol{r}-\boldsymbol{r}'|}\mathrm{d}\boldsymbol{r}'\Big) \\ &\quad\times\exp\Big[\frac{\mathrm{i}}{\hbar}\Big\{(E_{\boldsymbol{p}_\mathrm{f}}-E_{\boldsymbol{p}_\mathrm{i}})t-(\boldsymbol{p}_\mathrm{f}-\boldsymbol{p}_\mathrm{i})\cdot(\boldsymbol{r}-\boldsymbol{\alpha}_0\sin\omega t)\Big\}\Big]\mathrm{d}\boldsymbol{r}\mathrm{d}t \\ &= -\frac{\mathrm{i}}{\hbar}\frac{1}{(2\pi\hbar)^3}f_\mathrm{atom}(\theta)\sum_{n=-\infty}^{\infty}J_n(\xi) \\ &\quad\times\int\exp\Big[\frac{\mathrm{i}}{\hbar}(E_{\boldsymbol{p}_\mathrm{f}}-E_{\boldsymbol{p}_\mathrm{i}}-n\hbar\omega)t\Big]\mathrm{d}t \\ &= -2\pi\mathrm{i}\frac{1}{(2\pi\hbar)^3}\sum_{n=-\infty}^{\infty}\delta(E_{\boldsymbol{p}_\mathrm{f}}-E_{\boldsymbol{p}_\mathrm{i}}-n\hbar\omega)J_n(\xi)f_\mathrm{atom}(\theta), \end{aligned} \tag{A3.10}$$

where $\boldsymbol{\alpha}_0$ is defined by Eq. (2.18), ω is the angular frequency of the laser field, $J_n(\xi)$ is the n-th order Bessel function of the first kind, ξ is defined by Eq. (4.23), and $f_\mathrm{atom}(\theta)$ is defined by Eq. (3.5). In deriving the above equation, the relation of the Bessel function shown by the following formula [75] was adopted.

$$\exp(\mathrm{i}z\sin\omega t)=\sum_{n=-\infty}^{\infty}\exp(\mathrm{i}n\omega t)J_n(z). \tag{A3.11}$$

The delta function in Eq. (A3.10) shows that the kinetic energy of the scattered electron can be changed by $n\hbar\omega(=nh\nu)$ by the LAES process.

Similarly, I obtain

$$\begin{aligned} S^{(2)}_{\boldsymbol{p}_\mathrm{f},\boldsymbol{p}_\mathrm{i}} &= -\frac{\mathrm{i}}{\hbar}\frac{1}{(2\pi\hbar)^3}\int\int\Big(\sum_{j=1}^{\infty}\sin(\omega_j t+\phi_j)\int\frac{e^2\Delta\rho_j(\boldsymbol{r}')}{4\pi\epsilon_0|\boldsymbol{r}-\boldsymbol{r}'|}\mathrm{d}\boldsymbol{r}'\Big) \\ &\quad\times\exp\Big[\frac{\mathrm{i}}{\hbar}\Big\{(E_{\boldsymbol{p}_\mathrm{f}}-E_{\boldsymbol{p}_\mathrm{i}})t-(\boldsymbol{p}_\mathrm{f}-\boldsymbol{p}_\mathrm{i})\cdot(\boldsymbol{r}-\boldsymbol{\alpha}_0\sin\omega t)\Big\}\Big]\mathrm{d}\boldsymbol{r}\mathrm{d}t \\ &= -\frac{\mathrm{i}}{\hbar}\frac{1}{(2\pi\hbar)^3}\sum_{j=1}^{\infty}\frac{e^2}{4\pi\epsilon_0}\Big(\int\int\frac{\Delta\rho_j(\boldsymbol{r}')}{|\boldsymbol{r}-\boldsymbol{r}'|}\exp(\mathrm{i}\boldsymbol{s}\cdot\boldsymbol{r})\mathrm{d}\boldsymbol{r}\mathrm{d}\boldsymbol{r}'\Big) \\ &\quad\times\int\sin(\omega_j t+\phi_j)\exp\Big[\frac{\mathrm{i}}{\hbar}(E_{\boldsymbol{p}_\mathrm{f}}-E_{\boldsymbol{p}_\mathrm{i}})t\Big]\exp(-\mathrm{i}\boldsymbol{s}\cdot\boldsymbol{\alpha}_0\sin\omega t)\mathrm{d}t \\ &= -\frac{\mathrm{i}}{\hbar}\frac{1}{(2\pi\hbar)^3}\sum_{j=1}^{\infty}\frac{e^2}{\epsilon_0 s^2}\Big(\int\Delta\rho_j(\boldsymbol{r})\exp(\mathrm{i}\boldsymbol{s}\cdot\boldsymbol{r})\mathrm{d}\boldsymbol{r}\Big) \\ &\quad\sum_{n=-\infty}^{\infty}\times\int J_n(\xi)\exp\Big[\frac{\mathrm{i}}{\hbar}(E_{\boldsymbol{p}_\mathrm{f}}-E_{\boldsymbol{p}_\mathrm{i}}-n\hbar\omega)t\Big] \\ &\quad\times\frac{\exp(\mathrm{i}\omega_j t+\mathrm{i}\phi_j)-\exp(-\mathrm{i}\omega_j t-\mathrm{i}\phi_j)}{2\mathrm{i}}\mathrm{d}t, \end{aligned} \tag{A3.12}$$

where $\boldsymbol{s}$ is the scattering vector which is defined by Eq. (2.6). By performing an integration on time (t), it follows that

$$\begin{aligned} S^{(2)}_{\boldsymbol{p}_\mathrm{f},\boldsymbol{p}_\mathrm{i}} &= -2\pi\mathrm{i}\frac{1}{(2\pi\hbar)^3}\frac{e^2}{\epsilon_0 s^2}\frac{1}{2\mathrm{i}}\sum_{j=1}^{\infty}\sum_{n=-\infty}^{\infty}\Big(\int \Delta\rho_j(\boldsymbol{r})\exp(\mathrm{i}\boldsymbol{s}\cdot\boldsymbol{r})\mathrm{d}\boldsymbol{r}\Big) \\ &\quad \times J_n(\xi)\Big\{\mathrm{e}^{\mathrm{i}\phi_j}\delta(E_{\boldsymbol{p}_\mathrm{f}}-E_{\boldsymbol{p}_\mathrm{i}}-n\hbar\omega+\hbar\omega_j) \\ &\quad -\mathrm{e}^{-\mathrm{i}\phi_j}\delta(E_{\boldsymbol{p}_\mathrm{f}}-E_{\boldsymbol{p}_\mathrm{i}}-n\hbar\omega-\hbar\omega_j)\Big\}. \end{aligned} \tag{A3.13}$$

This equation states that when electrons in the target atom oscillates with an angular frequency of ω_j, the kinetic energy of the scattered electrons can be shifted by $\pm\hbar\omega_j + n\hbar\omega$ by the LAES process. When $\omega_j \neq n\omega$ (for all n), the differential cross section for the scattering with the energy shift of $\hbar\omega_j$ ($n = 0$) is given by

$$\frac{\mathrm{d}\sigma}{\mathrm{d}\Omega} = \frac{|\boldsymbol{p}_\mathrm{f}|}{|\boldsymbol{p}_\mathrm{i}|}\Big|\frac{1}{a_0}J_0(\xi)\frac{\mathrm{i}}{s^2}\int \Delta\rho_j(\boldsymbol{r})\exp(\mathrm{i}\boldsymbol{s}\cdot\boldsymbol{r})\mathrm{d}\boldsymbol{r}\Big|^2. \tag{A3.14}$$

Because the differential cross section is proportional to the squared the Fourier transform of $\Delta\rho_j(\boldsymbol{r})$, $\Delta\rho_j(\boldsymbol{r})$ could be determined by analyzing the angular distribution of scattered electrons whose kinetic energies are shifted by $\hbar\omega_j$.

Then, I consider a case of $\omega_j = j\omega$. In this case, $\Delta\rho(\boldsymbol{r}, t)$ represents deformation of the electron density distribution induced by intense laser fields used for inducing the LAES process. In this case, $S^{(2)}$ is given by

$$\begin{aligned} S^{(2)}_{\boldsymbol{p}_\mathrm{f},\boldsymbol{p}_\mathrm{i}} &= -2\pi\mathrm{i}\frac{1}{(2\pi\hbar)^3}\frac{e^2}{\epsilon_0 s^2}\frac{1}{2\mathrm{i}}\sum_{j=1}^{\infty}\sum_{n=-\infty}^{\infty}\Big(\int \Delta\rho_j(\boldsymbol{r})\exp(\mathrm{i}\boldsymbol{s}\cdot\boldsymbol{r})\mathrm{d}\boldsymbol{r}\Big) \\ &\quad \times J_n(\xi)\Big\{\mathrm{e}^{\mathrm{i}\phi_j}\delta(E_{\boldsymbol{p}_\mathrm{f}}-E_{\boldsymbol{p}_\mathrm{i}}-n\hbar\omega+j\hbar\omega) \\ &\quad +\mathrm{e}^{-\mathrm{i}\phi_j}\delta(E_{\boldsymbol{p}_\mathrm{f}}-E_{\boldsymbol{p}_\mathrm{i}}-n\hbar\omega-j\hbar\omega)\Big\} \\ &= -2\pi\mathrm{i}\frac{1}{(2\pi\hbar)^3}\frac{e^2}{\epsilon_0 s^2}\frac{1}{2\mathrm{i}}\sum_{j=1}^{\infty}\sum_{n=-\infty}^{\infty}\Big(\int \Delta\rho_j(\boldsymbol{r})\exp(\mathrm{i}\boldsymbol{s}\cdot\boldsymbol{r})\mathrm{d}\boldsymbol{r}\Big) \\ &\quad \delta(E_{\boldsymbol{p}_\mathrm{f}}-E_{\boldsymbol{p}_\mathrm{i}}-n\hbar\omega)\Big\{\mathrm{e}^{\mathrm{i}\phi_j}J_{n+j}(\boldsymbol{s}\cdot\boldsymbol{\alpha}_0)-\mathrm{e}^{-\mathrm{i}\phi_j}J_{n-j}(\boldsymbol{s}\cdot\boldsymbol{\alpha}_0)\Big\}. \end{aligned} \tag{A3.15}$$

Consequently, the differential cross section of the LAES process with n-photon energy shift is given by

$$\frac{\mathrm{d}\sigma_n}{\mathrm{d}\Omega} = \frac{|\boldsymbol{p}_{\mathrm{f},n}|}{|\boldsymbol{p}_\mathrm{i}|}\Big|f_\mathrm{atom}(\theta)J_n(\xi) - \sum_{j=1}^{\infty}f_{\mathrm{dress},j}(\theta)\Big(\mathrm{e}^{-\mathrm{i}\phi_j}J_{n-j}(\xi)-\mathrm{e}^{\mathrm{i}\phi_j}J_{n+j}(\xi)\Big)/2\Big|^2 \tag{A3.16}$$

with

$$f_{\mathrm{dress},j}(\theta) = \frac{2}{a_0}\frac{\mathrm{i}}{s^2}\int \Delta\rho_j(\boldsymbol{r})\exp(\mathrm{i}\boldsymbol{s}\cdot\boldsymbol{r})\mathrm{d}\boldsymbol{r} \tag{A3.17}$$

Finally, by using Eq. (A3.16), I discuss the difference between the differential cross section of the LAES processes with n photon energy shift and that of the LAES process with $-n$ photon energy shift. The differential cross section of the LAES process with $-n$ photon shift can be obtained by replacing n with $-n$ in Eq. (A3.16),

$$\frac{\mathrm{d}\sigma_{-n}}{\mathrm{d}\Omega} = \frac{|\boldsymbol{p}_{\mathrm{f},-n}|}{|\boldsymbol{p}_{\mathrm{i}}|}\Big|f_{\mathrm{atom}}(\theta)J_{-n}(\xi) - \sum_{j=1}^{\infty} f_{\mathrm{dress},j}(\theta)\Big(\mathrm{e}^{-\mathrm{i}\phi_j}J_{-n-j}(\xi) - \mathrm{e}^{\mathrm{i}\phi_j}J_{-n+j}(\xi)\Big)/2\Big|^2. \tag{A3.18}$$

By using the relationship of the Bessel function (Eq. (2.27)), I have

$$\begin{aligned}
\frac{\mathrm{d}\sigma_{-n}}{\mathrm{d}\Omega} &= \frac{|\boldsymbol{p}_{\mathrm{f},-n}|}{|\boldsymbol{p}_{\mathrm{i}}|}\Big|f_{\mathrm{atom}}(\theta)(-1)^n J_n(\xi) \\
&\quad - \sum_{j=1}^{\infty} f_{\mathrm{dress},j}(\theta)\Big(\mathrm{e}^{-\mathrm{i}\phi_j}(-1)^{n+j}J_{n+j}(\xi) - \mathrm{e}^{\mathrm{i}\phi_j}(-1)^{n-j}J_{n-j}(\xi)\Big)/2\Big|^2 \\
&= \frac{|\boldsymbol{p}_{\mathrm{f},-n}|}{|\boldsymbol{p}_{\mathrm{i}}|}\Big|f_{\mathrm{atom}}(\theta)J_n(\xi) \\
&\quad - \sum_{j=1}^{\infty} f_{\mathrm{dress},j}(\theta)\Big(\mathrm{e}^{\mathrm{i}\phi_j}(-1)^{-j+1}J_{n-j}(\xi) - \mathrm{e}^{-\mathrm{i}\phi_j}(-1)^{j+1}J_{n+j}(\xi)\Big)/2\Big|^2 \\
&= \frac{|\boldsymbol{p}_{\mathrm{f},-n}|}{|\boldsymbol{p}_{\mathrm{i}}|}\Big|f_{\mathrm{atom}}(\theta)J_n(\xi) \\
&\quad - \sum_{k=1}^{\infty} f_{\mathrm{dress},(2k-1)}(\theta)\Big(\mathrm{e}^{\mathrm{i}\phi_{2k-1}}J_{n-(2k-1)}(\xi) - \mathrm{e}^{-\mathrm{i}\phi_{2k-1}}J_{n+(2k-1)}(\xi)\Big)/2 \\
&\quad + \sum_{k=1}^{\infty} f_{\mathrm{dress},2k}(\theta)\Big(\mathrm{e}^{\mathrm{i}\phi_{2k}}J_{n-2k}(\xi) - \mathrm{e}^{-\mathrm{i}\phi_{2k}}J_{n+2k}(\xi)\Big)/2\Big|^2.
\end{aligned} \tag{A3.19}$$

By comparing this equation with Eq. (A3.16), it is found that the sign appearing in the terms originating from the phase of the oscillation (ϕ_j), $\mathrm{e}^{-\mathrm{i}\phi_j}$ and $\mathrm{e}^{\mathrm{i}\phi_j}$, is reversed in $\mathrm{d}\sigma_{-n}/\mathrm{d}\Omega$. Moreover, the sign associated with $f_{\mathrm{dress},j}(\theta)$ is also reversed for $j = 2k$ ($k = 1, 2, \cdots$).

Appendix 4: Higher-order Born terms for the LAES process with the light-dressing effect of target atoms

In Chapter 4, I adopted the Zon's model [248] for calculating angular distributions of the LAES process by taking into account the light-dressing effect. In the Zon's model, the first Born approximation is used for evaluating the scattering amplitude (Eqs. (4.20) and (4.21)). However, in the simulation done in Section 4.2.1, I substituted the first Born amplitude for the elastic scattering ($f_{\rm atom}$) appearing in the formula of the Zon's model (Eq. (4.26)) by the scattering amplitude calculated by the partial-wave analysis (Eq. (4.33)). This is because the first Born approximation does not provide quantitatively accurate differential cross section for the elastic scattering of 1 keV electrons by Xe (Section 3.1.2). In this section, I present the higher-order Born terms for the LAES process with the consideration of light-dressing effect, and discuss the meaning of the substitution conducted in the simulation in Section 4.2.1.

Within the Born approximation, the S-matrix for the LAES process can be written as

$$S_{\boldsymbol{p}_{\rm f},\boldsymbol{p}_{\rm i}} = \delta(\boldsymbol{p}_{\rm f}-\boldsymbol{p}_{\rm i}) + S^{\rm B1}_{\boldsymbol{p}_{\rm f},\boldsymbol{p}_{\rm i}} + S^{\rm B2}_{\boldsymbol{p}_{\rm f},\boldsymbol{p}_{\rm i}} + S^{\rm B3}_{\boldsymbol{p}_{\rm f},\boldsymbol{p}_{\rm i}} + \cdots , \tag{A4.1}$$

with

$$\begin{aligned} S^{\rm B1}_{\boldsymbol{p}_{\rm f},\boldsymbol{p}_{\rm i}} &= -\frac{\mathrm{i}}{\hbar}\int \mathrm{d}\boldsymbol{r}\int \mathrm{d}t \chi^{*}_{\boldsymbol{p}_{\rm f}}(\boldsymbol{r},t)V(\boldsymbol{r},t)\chi_{\boldsymbol{p}_{\rm i}}(\boldsymbol{r},t) \\ &\equiv < \chi_{\rm f}|V|\chi_{\rm i} >, \end{aligned} \tag{A4.2}$$

$$\begin{aligned} S^{\rm B2}_{\boldsymbol{p}_{\rm f},\boldsymbol{p}_{\rm i}} &= -\frac{\mathrm{i}}{\hbar}\int \mathrm{d}\boldsymbol{r}\int \mathrm{d}t\int \mathrm{d}\boldsymbol{r}'\int \mathrm{d}t' \chi^{*}_{\boldsymbol{p}_{\rm f}}(\boldsymbol{r},t)V(\boldsymbol{r},t)G(\boldsymbol{r},t;\boldsymbol{r}',t')V(\boldsymbol{r}',t')\chi_{\boldsymbol{p}_{\rm i}}(\boldsymbol{r}',t') \\ &\equiv < \chi_{\rm f}|VGV|\chi_{\rm i} >, \end{aligned} \tag{A4.3}$$

and

$$\begin{aligned} S^{\rm B3}_{\boldsymbol{p}_{\rm f},\boldsymbol{p}_{\rm i}} &= -\frac{\mathrm{i}}{\hbar}\int \mathrm{d}\boldsymbol{r}\int \mathrm{d}t\int \mathrm{d}\boldsymbol{r}'\int \mathrm{d}t'\int \mathrm{d}\boldsymbol{r}''\int \mathrm{d}t'' \chi^{*}_{\boldsymbol{p}_{\rm f}}(\boldsymbol{r},t)V(\boldsymbol{r},t) \\ &\quad \times G(\boldsymbol{r},t;\boldsymbol{r}',t')V(\boldsymbol{r}',t')G(\boldsymbol{r}',t';\boldsymbol{r}'',t'')V(\boldsymbol{r}'',t'')\chi_{\boldsymbol{p}_{\rm i}}(\boldsymbol{r}'',t'') \\ &\equiv < \chi_{\rm f}|VGVGV|\chi_{\rm i} >, \end{aligned} \tag{A4.4}$$

where $\boldsymbol{p}_{\rm f}$ and $\boldsymbol{p}_{\rm i}$ are the momenta of the electron before and after the scattering, $S^{\rm B1}$, $S^{\rm B2}$, and $S^{\rm B3}$ represent the first, second, and third order contributions to the S-matrix, respectively, $\chi_{\boldsymbol{p}_{\rm i}}(\boldsymbol{r},t)$ is the Gordon-Volkov wavefunction (Eq. (2.13)), $V(\boldsymbol{r},t)$ (Eq. (4.8)) is the scattering potential, and $G(\boldsymbol{r},t;\boldsymbol{r}',t')$ is the Green function which is defined by [319]

$$G(\boldsymbol{r},t;\boldsymbol{r}',t') = \frac{1}{\mathrm{i}\hbar}\Theta(t-t')\int \mathrm{d}\boldsymbol{p}\chi_{\boldsymbol{p}}(\boldsymbol{r},t)\chi^{*}_{\boldsymbol{p}}(\boldsymbol{r}',t'), \tag{A4.5}$$

where $\Theta(t-t')$ is the Theta function which is given by [319]

$$\Theta(t) = \lim_{\epsilon\to+0}\frac{1}{2\pi\mathrm{i}}\int_{-\infty}^{\infty}\frac{\exp(\mathrm{i}tz)}{z-\mathrm{i}\epsilon}. \tag{A4.6}$$

By using Eqs.(4.8)-(4.10), Eq. (A4.1) can be written as

$$\begin{aligned}
& S_{\boldsymbol{p}_\mathrm{f},\boldsymbol{p}_\mathrm{i}} - \delta(\boldsymbol{p}_\mathrm{f}-\boldsymbol{p}_\mathrm{i}) \\
= \; & <\chi_\mathrm{f}|V_\mathrm{atom}|\chi_\mathrm{i}> + <\chi_\mathrm{f}|V_\mathrm{atom}GV_\mathrm{atom}|\chi_\mathrm{i}> + <\chi_\mathrm{f}|V_\mathrm{atom}GV_\mathrm{atom}GV_\mathrm{atom}|\chi_\mathrm{i}> + \cdots \\
& + <\chi_\mathrm{f}|V_\mathrm{atom}GV_\mathrm{dress}|\chi_\mathrm{i}> + <\chi_\mathrm{f}|V_\mathrm{dress}GV_\mathrm{atom}|\chi_\mathrm{i}> \\
& + <\chi_\mathrm{f}|V_\mathrm{atom}GV_\mathrm{dress}GV_\mathrm{dress}|\chi_\mathrm{i}> + <\chi_\mathrm{f}|V_\mathrm{atom}GV_\mathrm{atom}GV_\mathrm{dress}|\chi_\mathrm{i}> \cdots \\
& + <\chi_\mathrm{f}|V_\mathrm{dress}|\chi_\mathrm{i}> + <\chi_\mathrm{f}|V_\mathrm{dress}GV_\mathrm{dress}|\chi_\mathrm{i}> + \cdots .
\end{aligned} \tag{A4.7}$$

The second line of this equation represents the S-matrix elements which depend only on V_atom, the third and fourth lines show the S-matrix elements which contain both V_atom and V_dress, and the fifth line represents the S-matrix elements which depend only on V_dress. In the Zon's model, which adopts the first Born approximation, only the terms $<\chi_\mathrm{f}|V_\mathrm{atom}|\chi_\mathrm{i}>$ and $<\chi_\mathrm{f}|V_\mathrm{dress}|\chi_\mathrm{i}>$ are included. By adopting the low-frequency approximation used in the Kroll-Watson approximation (Section 2.1.2) [67], the second line of this equation can be written as

$$\begin{aligned}
& <\chi_\mathrm{f}|V_\mathrm{atom}|\chi_\mathrm{i}> + <\chi_\mathrm{f}|V_\mathrm{atom}GV_\mathrm{atom}|\chi_\mathrm{i}> + <\chi_\mathrm{f}|V_\mathrm{atom}GV_\mathrm{atom}GV_\mathrm{atom}|\chi_\mathrm{i}> + \cdots \\
= \; & \sum_n \delta(E_{\boldsymbol{p}_\mathrm{f}} - E_{\boldsymbol{p}_\mathrm{i}} - n\hbar\omega) J_n(\xi)\Big(<\phi_\mathrm{f}|V_\mathrm{atom}|\phi_\mathrm{i}> \\
& + <\phi_\mathrm{f}|V_\mathrm{atom}GV_\mathrm{atom}|\phi_\mathrm{i}> + <\phi_\mathrm{f}|V_\mathrm{atom}GV_\mathrm{atom}GV_\mathrm{atom}|\phi_\mathrm{i}> + \cdots \Big),
\end{aligned} \tag{A4.8}$$

with

$$<\phi_\mathrm{f}|V_\mathrm{atom}|\phi_\mathrm{i}> = -2\pi\mathrm{i}\int \mathrm{d}\boldsymbol{r}\phi^*_{\boldsymbol{p}^*_\mathrm{f}}(\boldsymbol{r})V_\mathrm{atom}(\boldsymbol{r})\phi_{\boldsymbol{p}^*_\mathrm{i}}(\boldsymbol{r}), \tag{A4.9}$$

$$<\phi_\mathrm{f}|V_\mathrm{atom}GV_\mathrm{atom}|\phi_\mathrm{i}> = -2\pi\mathrm{i}\int\int \mathrm{d}\boldsymbol{r}\mathrm{d}\boldsymbol{r}'\phi^*_{\boldsymbol{p}^*_\mathrm{f}}(\boldsymbol{r})V_\mathrm{atom}(\boldsymbol{r})G(\boldsymbol{r};\boldsymbol{r}')V_\mathrm{atom}(\boldsymbol{r}')\phi_{\boldsymbol{p}^*_\mathrm{i}}(\boldsymbol{r}'), \tag{A4.10}$$

$$\begin{aligned}
<\phi_\mathrm{f}|V_\mathrm{atom}GV_\mathrm{atom}GV_\mathrm{atom}|\phi_\mathrm{i}> \; = \; & -2\pi\mathrm{i}\int\int\int \mathrm{d}\boldsymbol{r}\mathrm{d}\boldsymbol{r}'\mathrm{d}\boldsymbol{r}''\phi^*_{\boldsymbol{p}^*_\mathrm{f}}(\boldsymbol{r})V_\mathrm{atom}(\boldsymbol{r}) \\
& \times G(\boldsymbol{r};\boldsymbol{r}')V_\mathrm{atom}(\boldsymbol{r}')G(\boldsymbol{r}';\boldsymbol{r}'')\phi_{\boldsymbol{p}^*_\mathrm{i}}(\boldsymbol{r}''),
\end{aligned} \tag{A4.11}$$

where $\hbar\omega$ is the photon energy, J_n is the Bessel function of the first kind, ξ is defined by Eq. (4.23), $\phi_{\boldsymbol{p}}$ is the plane wave without laser fields which is defined by Eq. (3.4), $\boldsymbol{p}^*_\mathrm{i}$ and $\boldsymbol{p}^*_\mathrm{f}$ are

defined by Eqs. (2.30) and (2.31), respectively, and $G(\boldsymbol{r};\boldsymbol{r}')$ is the Green function defined by

$$G(\boldsymbol{r};\boldsymbol{r}') = \lim_{\epsilon\to+0}\int \mathrm{d}\boldsymbol{p}\frac{\phi_{\boldsymbol{p}}(\boldsymbol{r})\phi^*_{\boldsymbol{p}}(\boldsymbol{r}')}{E_{\boldsymbol{p}} - E_{\boldsymbol{p}^*_{\mathrm{i}}} - \mathrm{i}\epsilon}. \tag{A4.12}$$

On the right-hand-side of Eq. (A4.10), the terms in the parenthesis represent the successive S-matrix elements under the Born approximation for the elastic scattering by the potential V_{atom} without laser fields. Therefore, the left-hand-side of Eq. (A4.10) can approximately be expressed by the following equation,

$$\begin{aligned} & < \chi_{\mathrm{f}}|V_{\mathrm{atom}}|\chi_{\mathrm{i}} > + < \chi_{\mathrm{f}}|V_{\mathrm{atom}}GV_{\mathrm{atom}}|\chi_{\mathrm{i}} > + < \chi_{\mathrm{f}}|V_{\mathrm{atom}}GV_{\mathrm{atom}}GV_{\mathrm{atom}}|\chi_{\mathrm{i}} > + \cdots \\ = \quad & -2\pi\mathrm{i}\sum_n \delta(E_{\boldsymbol{p}_{\mathrm{f}}} - E_{\boldsymbol{p}_{\mathrm{i}}} - n\hbar\omega)J_n(\xi)\frac{1}{4\pi^2\hbar m_{\mathrm{e}}}f_{\mathrm{ex}}, \end{aligned} \tag{A4.13}$$

where f_{ex} is an exact scattering amplitude for the elastic scattering by V_{atom} without laser fields. This means that by the substitution of the first Born amplitude f_{atom} in Eq. (4.26) with the exact amplitude (f_{ex}) obtained by the partial-wave analysis (Eq. (4.33)), the S-matrix elements which represent the higher-order Born effect of the scattering by V_{atom},

$$< \chi_{\mathrm{f}}|V_{\mathrm{atom}}GV_{\mathrm{atom}}|\chi_{\mathrm{i}} > + < \chi_{\mathrm{f}}|V_{\mathrm{atom}}GV_{\mathrm{atom}}GV_{\mathrm{atom}}|\chi_{\mathrm{i}} > + \cdots, \tag{A4.14}$$

are effectively included in the simulation. Because, as discussed in the introduction of Chapter 4 (Fig. 77), the amount of the deformation of the electron density distribution ($\Delta\rho(\boldsymbol{r})$) by the laser field used in this study is much smaller compared with the electron density distribution without laser fields ($\rho^0(\boldsymbol{r})$), the strength of V_{dress} is weaker than that of V_{atom} and the higher-order Born terms which depend on V_{dress} are neglected in the simulation in Section 4.2.1.

The second-order Born terms which are not included in the simulation are expressed as

$$< \chi_{\mathrm{f}}|V_{\mathrm{atom}}GV_{\mathrm{dress}}|\chi_{\mathrm{i}} > + < \chi_{\mathrm{f}}|V_{\mathrm{dress}}GV_{\mathrm{atom}}|\chi_{\mathrm{i}} > + < \chi_{\mathrm{f}}|V_{\mathrm{dress}}GV_{\mathrm{dress}}|\chi_{\mathrm{i}} > . \tag{A4.15}$$

Because the strength of V_{dress} is weaker than that of V_{atom}, the contribution of the third term in this formula could be negligibly small compared with the contributions from the first and the second terms. In what follows, I derive concrete expressions for $< \chi_{\mathrm{f}}|V_{\mathrm{atom}}GV_{\mathrm{dress}}|\chi_{\mathrm{i}} >$ and $< \chi_{\mathrm{f}}|V_{\mathrm{dress}}GV_{\mathrm{atom}}|\chi_{\mathrm{i}} >$.

$$\begin{aligned} & < \chi_{\mathrm{f}}|V_{\mathrm{atom}}GV_{\mathrm{dress}}|\chi_{\mathrm{i}} > \\ = \quad & -\frac{\mathrm{i}}{\hbar}\frac{1}{\mathrm{i}\hbar}\int \mathrm{d}\boldsymbol{p}''\int \mathrm{d}\boldsymbol{r}\int \mathrm{d}t\int \mathrm{d}\boldsymbol{r}'\int \mathrm{d}t' \\ & \times\chi^*_{\boldsymbol{p}_{\mathrm{f}}}(\boldsymbol{r},t)V_{\mathrm{atom}}(\boldsymbol{r})\chi_{\boldsymbol{p}''}(\boldsymbol{r},t)\Theta(t-t')\chi^*_{\boldsymbol{p}''}(\boldsymbol{r}',t')V_{\mathrm{dress}}(\boldsymbol{r}',t')\chi_{\boldsymbol{p}_{\mathrm{i}}}(\boldsymbol{r}',t') \end{aligned} \tag{A4.16}$$

In a similar way as that in Appendix 3,

$$
\begin{aligned}
& < \chi_{\rm f}|V_{\rm atom}GV_{\rm dress}|\chi_{\rm i} > \\
= & -\frac{\rm i}{\hbar}\frac{1}{{\rm i}\hbar}\frac{1}{(2\pi\hbar)^3}\int {\rm d}\boldsymbol{p}''\Big(\int {\rm d}\boldsymbol{r}V_{\rm atom}(\boldsymbol{r})\exp\Big(\frac{\rm i}{\hbar}(\boldsymbol{p}''-\boldsymbol{p}_{\rm f})\cdot\boldsymbol{r}\Big)\Big) \\
& \times\int {\rm d}t'\Big(\int {\rm d}t\Theta(t-t')\exp\Big(\frac{\rm i}{\hbar}(E_{\boldsymbol{p}_{\rm f}}-E_{\boldsymbol{p}''})t\Big)\exp\Big(-\frac{\rm i}{\hbar}(\boldsymbol{p}''-\boldsymbol{p}_{\rm f})\cdot\boldsymbol{\alpha}_0\sin\omega t\Big)\Big) \\
& \times\int {\rm d}\boldsymbol{r}'\chi^*_{\boldsymbol{p}''}(\boldsymbol{r}',t')V_{\rm dress}(\boldsymbol{r}',t')\chi_{\boldsymbol{p}_{\rm i}}(\boldsymbol{r}',t') \\
= & -\frac{\rm i}{\hbar}\frac{1}{{\rm i}\hbar}\frac{1}{(2\pi\hbar)^3}\sum_{m=-\infty}^{\infty}\int {\rm d}\boldsymbol{p}''\Big(\int {\rm d}\boldsymbol{r}V_{\rm atom}(\boldsymbol{r})\exp\Big(\frac{\rm i}{\hbar}(\boldsymbol{p}''-\boldsymbol{p}_{\rm f})\cdot\boldsymbol{r}\Big)\Big)J_m\Big(\frac{\boldsymbol{p}''-\boldsymbol{p}_{\rm f}}{\hbar}\cdot\boldsymbol{\alpha}_0\Big) \\
& \times\int {\rm d}t'\Big(\int {\rm d}t\Theta(t-t')\exp\Big(\frac{\rm i}{\hbar}(E_{\boldsymbol{p}_{\rm f}}-E_{\boldsymbol{p}''}-m\hbar\omega)t\Big)\Big) \\
& \times\int {\rm d}\boldsymbol{r}'\chi^*_{\boldsymbol{p}''}(\boldsymbol{r}',t')V_{\rm dress}(\boldsymbol{r}',t')\chi_{\boldsymbol{p}_{\rm i}}(\boldsymbol{r}',t') \\
= & -\frac{\rm i}{\hbar}\frac{1}{{\rm i}\hbar}\frac{1}{(2\pi\hbar)^3}\sum_{m=-\infty}^{\infty}\int {\rm d}\boldsymbol{p}''\Big(\int {\rm d}\boldsymbol{r}V_{\rm atom}(\boldsymbol{r})\exp\Big(\frac{\rm i}{\hbar}(\boldsymbol{p}''-\boldsymbol{p}_{\rm f})\cdot\boldsymbol{r}\Big)\Big)J_m\Big(\frac{\boldsymbol{p}''-\boldsymbol{p}_{\rm f}}{\hbar}\cdot\boldsymbol{\alpha}_0\Big) \\
& \times\int {\rm d}t'\lim_{\epsilon\to+0}\frac{\hbar}{\rm i}\frac{\exp[-{\rm i}(E_{\boldsymbol{p}_{\rm f}}-E_{\boldsymbol{p}''}-m\hbar\omega)t'/\hbar]}{E_{\boldsymbol{p}_{\rm f}}-E_{\boldsymbol{p}''}-m\hbar\omega-{\rm i}\epsilon} \\
& \times\int {\rm d}\boldsymbol{r}'\chi^*_{\boldsymbol{p}''}(\boldsymbol{r}',t')V_{\rm dress}(\boldsymbol{r}',t')\chi_{\boldsymbol{p}_{\rm i}}(\boldsymbol{r}',t') \\
= & \frac{\rm i}{\hbar}\frac{1}{(2\pi\hbar)^6}\sum_{m=-\infty}^{\infty}\int {\rm d}\boldsymbol{p}''\Big(\int {\rm d}\boldsymbol{r}V_{\rm atom}(\boldsymbol{r})\exp\Big(\frac{\rm i}{\hbar}(\boldsymbol{p}''-\boldsymbol{p}_{\rm f})\cdot\boldsymbol{r}\Big)\Big)J_m\Big(\frac{\boldsymbol{p}''-\boldsymbol{p}_{\rm f}}{\hbar}\cdot\boldsymbol{\alpha}_0\Big) \\
& \times\lim_{\epsilon\to+0}\frac{1}{E_{\boldsymbol{p}_{\rm f}}-E_{\boldsymbol{p}''}-m\hbar\omega-{\rm i}\epsilon}\sum_{l=-\infty}^{\infty}J_l\Big(\frac{\boldsymbol{p}_{\rm i}-\boldsymbol{p}''}{\hbar}\cdot\boldsymbol{\alpha}_0\Big)\int {\rm d}t'\exp\Big(\frac{\rm i}{\hbar}(E_{\boldsymbol{p}_{\rm f}}-E_{\boldsymbol{p}_{\rm i}}-(l+m)\hbar\omega)t'\Big) \\
& \times\int {\rm d}\boldsymbol{r}'V_{\rm dress}(\boldsymbol{r}',t')\exp\Big(\frac{\rm i}{\hbar}(\boldsymbol{p}_{\rm i}-\boldsymbol{p}'')\cdot\boldsymbol{r}'\Big) \\
= & \frac{\rm i}{\hbar}\frac{1}{(2\pi\hbar)^6}\lim_{\epsilon\to+0}\sum_{n=-\infty}^{\infty}\sum_{m=-\infty}^{\infty}\int {\rm d}\boldsymbol{p}''J_m\Big(\frac{\boldsymbol{p}''-\boldsymbol{p}_{\rm f}}{\hbar}\cdot\boldsymbol{\alpha}_0\Big)J_{n-m}\Big(\frac{\boldsymbol{p}_{\rm i}-\boldsymbol{p}''}{\hbar}\cdot\boldsymbol{\alpha}_0\Big) \\
& \times\Big(\int V_{\rm atom}(\boldsymbol{r})\exp\Big(\frac{\rm i}{\hbar}(\boldsymbol{p}''-\boldsymbol{p}_{\rm f})\cdot\boldsymbol{r}\Big){\rm d}\boldsymbol{r}\Big)\frac{1}{E_{\boldsymbol{p}_{\rm f}}-E_{\boldsymbol{p}''}-m\hbar\omega-{\rm i}\epsilon} \\
& \times\int {\rm d}t'\exp\Big(\frac{\rm i}{\hbar}(E_{\boldsymbol{p}_{\rm f}}-E_{\boldsymbol{p}_{\rm i}}-n\hbar\omega)t'\Big)\int {\rm d}\boldsymbol{r}'V_{\rm dress}(\boldsymbol{r}',t')\exp\Big(\frac{\rm i}{\hbar}(\boldsymbol{p}_{\rm i}-\boldsymbol{p}'')\cdot\boldsymbol{r}'\Big). \qquad \text{(A4.17)}
\end{aligned}
$$

In a similar way, I obtain

$$
\begin{aligned}
& < \chi_{\rm f}|V_{\rm dress}GV_{\rm atom}|\chi_{\rm i} > \\
= \; & \frac{\rm i}{\hbar}\frac{1}{(2\pi\hbar)^6}\lim_{\epsilon\to+0}\sum_{n=-\infty}^{\infty}\sum_{m=-\infty}^{\infty}\int {\rm d}\boldsymbol{p}''J_{n-m}\Big(\frac{\boldsymbol{p}''-\boldsymbol{p}_{\rm f}}{\hbar}\cdot\boldsymbol{\alpha}_0\Big)J_m\Big(\frac{\boldsymbol{p}_{\rm i}-\boldsymbol{p}''}{\hbar}\cdot\boldsymbol{\alpha}_0\Big) \\
& \times\int {\rm d}t\exp\Big(\frac{\rm i}{\hbar}(E_{\boldsymbol{p}_{\rm f}}-E_{\boldsymbol{p}_{\rm i}}-n\hbar\omega)t\Big)\int {\rm d}\boldsymbol{r}V_{\rm dress}(\boldsymbol{r},t')\exp\Big(\frac{\rm i}{\hbar}(\boldsymbol{p}''-\boldsymbol{p}_{\rm f})\cdot\boldsymbol{r}\Big) \\
& \times\frac{1}{E_{\boldsymbol{p}''}-E_{\boldsymbol{p}_{\rm i}}-m\hbar\omega-{\rm i}\epsilon}\Big(\int V_{\rm atom}(\boldsymbol{r}')\exp\Big(\frac{\rm i}{\hbar}(\boldsymbol{p}_{\rm i}-\boldsymbol{p}'')\cdot\boldsymbol{r}'\Big){\rm d}\boldsymbol{r}'\Big). \qquad \text{(A4.18)}
\end{aligned}
$$

Bibliography

[1] N. F. Mott and H. S. W. Massey, *The theory of atomic collisions* (Clarendon Press, Oxford, 1965).

[2] P. G. Burke and J. Williams, Phys. Rep. **34**, 325 (1977).

[3] D. A. Kohl and L. Bartell, J. Cryst. Soc. Japan **5**, 2 (1963).

[4] L. Bartell and L. Brockway, Phys. Rev. **90**, 833 (1953).

[5] L. Brockway, Rev. Mod. Phys. **8**, 231 (1936).

[6] M. I. Davis, *Electron Diffraction in Gases* (Dekker, New York, 1971).

[7] D. Kohl and L. Bartell, J. Chem. Phys. **51**, 2891 (1969).

[8] D. A. Kohl and L. Bartell, J. Chem. Phys. **51**, 2896 (1969).

[9] M. De Crescenzi and M. N. Piancastelli, *Electron scattering and related spectroscopies* (World Scientific, Singapore, 1996).

[10] I. Hargittai and M. Hargittai, eds., *Stereochemical Applications of Gas-Phase Electron Diffraction* (VCH, New York, 1988).

[11] K. Yamanouchi, *Quantum Mechanics of Molecular Structures* (Springer, Heidelberg, 2012).

[12] C. Shank and E. Ippen, Appl. Phys. Lett. **24**, 373 (1974).

[13] R. L. Fork, C. H. Brito Cruz, P. Becker, and C. V. Shank, Opt. Lett. **12**, 483 (1987).

[14] M. J. Rosker, M. Dantus, and A. H. Zewail, J. Chem. Phys. **89**, 6113 (1988).

[15] M. Dantus, M. J. Rosker, and A. H. Zewail, J. Chem. Phys. **89**, 6128 (1988).

[16] T. S. Rose, M. J. Rosker, and A. H. Zewail, J. Chem. Phys. **88**, 6672 (1988).

[17] A. H. Zewail, Angew. Chem. Int. Edit. **39**, 2586 (2000).

[18] P. . M. Paul, E. Toma, P. Breger, G. Mullot, F. Augé, P. Balcou, H. Muller, and P. Agostini, Science **292**, 1689 (2001).

[19] M. Hentschel, R. Kienberger, C. Spielmann, G. A. Reider, N. Milosevic, T. Brabec, P. Corkum, U. Heinzmann, M. Drescher, and F. Krausz, Nature **414**, 509 (2001).

[20] G. Sansone, E. Benedetti, F. Calegari, C. Vozzi, L. Avaldi, R. Flammini, L. Poletto, P. Villoresi, C. Altucci, R. Velotta, S. Stagira, S. D. Silvestri, and M. Nisoli, Science **314**, 443 (2006).

[21] K. Schafer, B. Yang, L. DiMauro, and K. Kulander, Phys. Rev. Lett. **70**, 1599 (1993).

[22] P. B. Corkum, Phys. Rev. Lett. **71**, 1994 (1993).

[23] E. Goulielmakis, M. Schultze, M. Hofstetter, V. S. Yakovlev, J. Gagnon, M. Uiberacker, A. L. Aquila, E. Gullikson, D. T. Attwood, R. Kienberger, F. Krausz, and U. Kleineberg, Science **320**, 1614 (2008).

[24] K. Zhao, Q. Zhang, M. Chini, Y. Wu, X. Wang, and Z. Chang, Opt. Lett. **37**, 3891 (2012).

[25] M. Drescher, M. Hentschel, R. Kienberger, M. Uiberacker, V. Yakovlev, A. Scrinzi, T. Westerwalbesloh, U. Kleineberg, U. Heinzmann, and F. Krausz, Nature **419**, 803 (2002).

[26] M. Uiberacker, T. Uphues, M. Schultze, A. J. Verhoef, V. Yakovlev, M. F. Kling, J. Rauschenberger, N. M. Kabachnik, H. Schröder, M. Lezius, K. L. Kompa, H. G. Muller, M. J. J. Vrakking, S. Hendel, U. Kleineberg, U. Heinzmann, M. Drescher, and F. Krausz, Nature **446**, 627 (2007).

[27] G. Sansone, F. Kelkensberg, J. Pérez-Torres, F. Morales, M. F. Kling, W. Siu, O. Ghafur, P. Johnsson, M. Swoboda, E. Benedetti, F. Ferrari, F. Lépine, J. L. Sanz-Vicario, S. Zherebtsov, I. Znakovskaya, A. L'Huillier, M. Y. Ivanov, M. Nisoli, and M. J. J. Vrakking, Nature **465**, 763 (2010).

[28] F. Calegari, D. Ayuso, A. Trabattoni, L. Belshaw, S. De Camillis, S. Anumula, F. Frassetto, L. Poletto, A. Palacios, P. Decleva, J. B. Greenwood, F. Martïn, and M. Nisoli, Science **346**, 336 (2014).

[29] H. Mashiko, S. Gilbertson, C. Li, S. D. Khan, M. M. Shakya, E. Moon, and Z. Chang, Phys. Rev. Lett. **100**, 103906 (2008).

[30] E. J. Takahashi, P. Lan, O. D. Mücke, Y. Nabekawa, and K. Midorikawa, Phys. Rev. Lett. **104**, 233901 (2010).

[31] F. Ferrari, F. Calegari, M. Lucchini, C. Vozzi, S. Stagira, G. Sansone, and M. Nisoli, Nat. Photon. **4**, 875 (2010).

[32] G. Sansone, L. Poletto, and M. Nisoli, Nat. Photon. **5**, 655 (2011).

[33] E. J. Takahashi, P. Lan, O. D. Mücke, Y. Nabekawa, and K. Midorikawa, Nat. Commun. **4** (2013).

[34] P. Carpeggiani, P. Tzallas, A. Palacios, D. Gray, F. Martín, and D. Charalambidis, Phys. Rev. A **89**, 023420 (2014).

[35] Z. Chang, *Fundamentals of attosecond optics* (CRC Press, Boca Raton, 2011).

[36] J. C. Williamson, J. Cao, H. Ihee, H. Frey, and A. H. Zewail, Nature **386**, 159 (1997).

[37] P. Baum, J. Manz, and A. Schild, Sci. China Ser. G **53**, 987 (2010).

[38] H.-C. Shao and A. F. Starace, Phys. Rev. Lett. **105**, 263201 (2010).

[39] G. Mourou and S. Williamson, Appl. Phys. Lett. **41**, 44 (1982).

[40] R. Srinivasan, V. A. Lobastov, C.-Y. Ruan, and A. H. Zewail, Hel. Chim. Acta. **86**, 1761 (2003).

[41] N. Mason, Rep. Prog. Phys. **56**, 1275 (1993).

[42] D. Andrick and L. Langhans, J. Phys. B **9**, L459 (1976).

[43] A. Weingartshofer, J. K. Holmes, G. Caudle, E. M. Clarke, and H. Krüger, Phys. Rev. Lett. **39**, 269 (1977).

[44] R. Kanya, Y. Morimoto, and K. Yamanouchi, Phys. Rev. Lett. **105**, 123202 (2010).

[45] C. J. Joachain, N. J. Kylstra, and R. M. Potvliege, *Atoms in intense laser fields* (Cambridge University Press, Cambridge, 2011).

[46] A. D. Bandrauk, E. Aubanel, and J. Gauthier, *Molecules in laser fields* (Dekker, New York, 1994).

[47] J. Posthumus, Rep. Prog. Phys. **67**, 623 (2004).

[48] F. Byron Jr and C. Joachain, J. Phys. B **17**, L295 (1984).

[49] E. Weigold and I. McCarthy, *Electron momentum spectroscopy* (Kluwer Academic/Plenum Publishers, New York, 1999).

[50] M. Takahashi, Bull. Chem. Soc. Jpn. **82**, 751 (2009).

[51] K. A. Kouzakov, Y. V. Popov, and M. Takahashi, Phys. Rev. A **82**, 023410 (2010).

[52] C. Höhr, A. Dorn, B. Najjari, D. Fischer, C. Schröter, and J. Ullrich, Phys. Rev. Lett. **94**, 153201 (2005).

[53] I. E. McCarthy and E. Weigold, Phys. Rep. **27**, 275 (1976).

[54] J. A. Wheeler and R. Wildt, Astrophys. J. **95**, 281 (1942).

[55] L. Schlessinger and J. Wright, Phys. Rev. A **20**, 1934 (1979).

[56] C. G. Morgan, Rep. Prog. Phys. **38**, 621 (1975).

[57] F. Linder, in *Electron-molecule scattering*, edited by S. Brown (Wiley, New York, 1979) pp. 107–145.

[58] M. H. Mittleman, *Introduction to the theory of laser-atom interactions* (Plenum, New York, 1982).

[59] A. Weingartshofer and C. Jung, in *Multiphoton lonization of Atoms*, edited by S. L. Chin (Academic Press, Canada, 1984) pp. 155–187.

[60] F. H. Faisal, *Theory of multiphoton processes* (Plenum, New York, 1986).

[61] R. Kanya, Y. Morimoto, and K. Yamanouchi, in *Progress in Ultrafast Intense Laser Science*, edited by K. Yamanouchi, G. Paulus, and D. Mathur (Springer International Publishing, Switzerland, 2014) pp. 1–16.

[62] L. Rosenberg, Adv. Atom. Mol. Phys. **18**, 1 (1982).

[63] M. Gavrila and M. Wiel, Comments. At. Mol. Phys. **8**, 1 (1978).

[64] N. Mason, Contemp. Phys. **30**, 449 (1989).

[65] C. Joachain, Laser Chem. **11**, 273 (1991).

[66] F. Ehlotzky, A. Jaroń, and J. Kamiński, Phys. Rep. **297**, 63 (1998).

[67] N. M. Kroll and K. M. Watson, Phys. Rev. A **8**, 804 (1973).

[68] L. B. Madsen, *Strong Field Dynamics: Scattering and Multiphoton Ionization*, Ph.D. thesis, Institute of Physics and Astronomy, University of Aarhus (1998).

[69] R. Kanya, Y. Morimoto, and K. Yamanouchi, Rev. Sci. Instrum. **82**, 123105 (2011).

[70] C. J. Joachain, *Quantum Collision Theory* (North-Holland, Amsterdam, 1975).

[71] W. H. Press, S. A. Teukolsky, W. T. Vetterling, and B. P. Flannery, *Numerical recipes 3rd edition: The art of scientific computing* (Cambridge university press, Cambridge, 2007).

[72] F. Bunkin and M. Fedorov, Sov. Phys. JETP **22**, 844 (1966).

[73] W. Gordon, Z. Phys. **40**, 117 (1926).

[74] D. Volkov, Z. Phys **94**, 250 (1935).

[75] G. B. Arfken and H. J. Weber, *Mathematical Methods For Physicists International Student Edition* (Academic press, London, 2005).

[76] M. Abramowitz and I. A. Stegun, *Handbook of mathematical functions*, Vol. 1 (Dover, New York, 1972).

[77] H. Krüger and C. Jung, Physical Review A **17**, 1706 (1978).

[78] M. H. Mittleman, Phys. Rev. A **19**, 134 (1979).

[79] E. J. Kelsey and L. Rosenberg, Phys. Rev. A **19**, 756 (1979).

[80] J. Bergou and F. Ehlotzky, Phys. Rev. A **33**, 3054 (1986).

[81] P. Krstić and D. Milošević, J. Phys. B **20**, 3487 (1987).

[82] N. Kylstra and C. Joachain, Phys. Rev. A **60**, 2255 (1999).

[83] A. Weingartshofer, J. Holmes, J. Sabbagh, and S. Chin, J. Phys. B **16**, 1805 (1983).

[84] D. Andrick and L. Langhans, J. Phys. B **11**, 2355 (1978).

[85] L. Langhans, J. Phys. B **11**, 2361 (1978).

[86] A. Weingartshofer, E. Clarke, J. Holmes, and C. Jung, Phys. Rev. A **19**, 2371 (1979).

[87] D. Andrick and H. Bader, J. Phys. B **17**, 4549 (1984).

[88] H. Bader, J. Phys. B **18**, L235 (1985).

[89] H. Bader, J. Phys. B **19**, 2177 (1986).

[90] B. Wallbank, J. Holmes, and A. Weingartshofer, J. Phys. B **20**, 6121 (1987).

[91] B. Wallbank, V. Connors, J. Holmes, and A. Weingartshofer, J. Phys. B **20**, L833 (1987).

[92] B. Wallbank, J. Holmes, S. MacIsaac, and A. Weingartshofer, J. Phys. B **25**, 1265 (1992).

[93] B. Wallbank and J. Holmes, Phys. Rev. A **48**, R2515 (1993).

[94] B. Wallbank and J. Holmes, J. Phys. B **27**, 1221 (1994).

[95] B. Wallbank and J. Holmes, J. Phys. B **27**, 5405 (1994).

[96] B. Wallbank and J. Holmes, J. Phys. B **29**, 5881 (1996).

[97] B. Wallbank and J. Holmes, Can. J. Phys. **79**, 1237 (2001).

[98] D. Nehari, J. Holmes, K. Dunseath, and M. Terao-Dunseath, J. Phys. B **43**, 025203 (2010).

[99] M. Musa, A. MacDonald, L. Tidswell, J. Holmes, and B. Wallbank, J. Phys. B **43**, 175201 (2010).

[100] B. A. deHarak, L. Ladino, K. B. MacAdam, and N. L. S. Martin, Phys. Rev. A **83**, 022706 (2011).

[101] Y. Morimoto, R. Kanya, and K. Yamanouchi, J. Chem. Phys. **140**, 064201 (2014).

[102] B. A. deHarak, B. Nosarzewski, M. Siavashpouri, and N. L. S. Martin, Phys. Rev. A **90**, 032709 (2014).

[103] K. Nobusada and K. Yabana, Phys. Rev. A **70**, 043411 (2004).

[104] C. Cornaggia, Phys. Rev. A **54**, R2555 (1996).

[105] A. Hishikawa, A. Iwamae, and K. Yamanouchi, Phys. Rev. Lett. **83**, 1127 (1999).

[106] J. Sanderson, A. El-Zein, W. Bryan, W. Newell, A. Langley, and P. Taday, Phys. Rev. A **59**, R2567 (1999).

[107] H. Hasegawa, A. Hishikawa, and K. Yamanouchi, Chem. Phys. Lett. **349**, 57 (2001).

[108] A. Iwasaki, A. Hishikawa, and K. Yamanouchi, Chem. Phys. Lett. **346**, 379 (2001).

[109] P. Allen and L. E. Sutton, Acta Crystallogr. **3**, 46 (1950).

[110] J. H. Callomon, E. Hirota, T. Iijima, K. Kuchitsu, and W. Lafferty, (1987).

[111] K. Kuchitsu, *Structure of free polyatomic molecules: basic data* (Springer, Berlin, 1998).

[112] J. McQuarrie and D. Simon, *Physical Chemistry: A Molecular Approach* (University Science Books, Sausalito, 1997).

[113] A. Jablonski, F. Salvat, and C. Powell, National Institute of Standards and Technology, Gaithersburg, Maryland **20899**, 22 (2003).

[114] M. Fink and A. C. Yates, At. Data **1**, 385 (1969).

[115] M. Fink and J. Ingram, At. Data **4**, 129 (1972).

[116] J. A. Ibers and W. C. Hamilton, eds., *International tables for X-ray crystallography* (International Union of Crystallography by the Kynoch Press, 1974).

[117] H. Kleinpoppen and M. McDowell, eds., *Electron and photon interactions with atoms* (Plenum, New York, 1976).

[118] J.-C. Zheng, L. Wu, and Y. Zhu, J. Appl. Cryst. **42**, 1043 (2009).

[119] R. Jansen, F. De Heer, H. Luyken, B. Van Wingerden, and H. Blaauw, J. Phys. B **9**, 185 (1976).

[120] R. Jansen and F. De Heer, J. Phys. B **9**, 213 (1976).

[121] D. A. Kohl and L. Bartell, J. Cryst. Soc. Japan **17**, 277 (1975).

[122] M. Fink, K. Jost, and D. Herrmann, Phys. Rev. A **12**, 1374 (1975).

[123] D. Herrmann, K. Jost, J. Kessler, and M. Fink, J. Chem. Phys. **64**, 1 (1976).

[124] I. Shimamura and K. Takayanagi, *Electron-molecule collisions* (Plenum Press, New York, NY, 1984).

[125] V. Schomaker and R. Glauber, Nature **170**, 290 (1952).

[126] L. Bartell, L. Brockway, and R. Schwendeman, J. Chem. Phys. **23**, 1854 (1955).

[127] Y. Morino, Y. Nakamura, and T. Iijima, J. Chem. Phys. **32**, 643 (1960).

[128] F. Salvat, A. Jablonski, and C. J. Powell, Com. Phys. Comm. **165**, 157 (2005).

[129] A. H. Zewail, Annu. Rev. Phys. Chem. **57**, 65 (2006).

[130] G. Sciaini and R. D. Miller, Rep. Prog. Phys. **74**, 096101 (2011).

[131] F. Carbone, P. Musumeci, O. Luiten, and C. Hebert, Chem. Phys. **392**, 1 (2012).

[132] S. A. Aseyev, P. M. Weber, and A. A. Ischenko, J. Anal. Sci. Methods Instrum. **3**, 30 (2013).

[133] R. D. Miller, Ann. Rev. Phys. Chem **65**, 583 (2014).

[134] P. Baum, J. Phys. B **47**, 124005 (2014).

[135] A. Ishchenko, S. Aseyev, V. N. Bagratashvili, V. Y. Panchenko, and E. A. Ryabov, Phys.-Usp. **57**, 633 (2014).

[136] J. R. Helliwell and P. M. Rentzepis, eds., *Time-resolved diffraction* (Oxford University Press, Oxford, 1997).

[137] A. H. Zewail and J. M. Thomas, *4D electron microscopy: imaging in space and time* (Imperial College Press, London, 2010).

[138] A. A. Ischenko and S. A. Aseyev, *Advances in Imaging and Electron Physics, Volume 184, Time-Resolved Electron Diffraction: For Chemistry, Biology and Materials Science* (Elsevier, USA, 2014).

[139] C. Davisson and L. H. Germer, Phys. Rev. **30**, 705 (1927).

[140] H. Mark and R. Wierl, Naturwissenschaften **18**, 205 (1930).

[141] A. Ischenko, V. Golubkov, V. Spiridonov, A. Zgurskii, A. Akhmanov, M. Vabischevich, and V. Bagratashvili, Appl. Phys. B **32**, 161 (1983).

[142] S. Williamson, G. Mourou, and J. C. M. Li, Phys. Rev. Lett. **52**, 2364 (1984).

[143] B. J. Siwick, J. R. Dwyer, R. E. Jordan, and R. D. Miller, Science **302**, 1382 (2003).

[144] M. Harb, R. Ernstorfer, C. T. Hebeisen, G. Sciaini, W. Peng, T. Dartigalongue, M. A. Eriksson, M. G. Lagally, S. G. Kruglik, and R. D. Miller, Phys. Rev. Lett. **100**, 155504 (2008).

[145] R. Ernstorfer, M. Harb, C. T. Hebeisen, G. Sciaini, T. Dartigalongue, and R. D. Miller, Science **323**, 1033 (2009).

[146] G. Sciaini, M. Harb, S. G. Kruglik, T. Payer, C. T. Hebeisen, F.-J. M. zu Heringdorf, M. Yamaguchi, M. Horn-von Hoegen, R. Ernstorfer, and R. D. Miller, Nature **458**, 56 (2009).

[147] P. Zhou, C. Streubühr, M. Ligges, T. Brazda, T. Payer, F. M. zu Heringdorf, M. Horn-von Hoegen, and D. Von der Linde, New J. Phys. **14**, 103031 (2012).

[148] P. Baum, D.-S. Yang, and A. H. Zewail, Science **318**, 788 (2007).

[149] M. Eichberger, H. Schäfer, M. Krumova, M. Beyer, J. Demsar, H. Berger, G. Moriena, G. Sciaini, and R. D. Miller, Nature **468**, 799 (2010).

[150] S. Wall, B. Krenzer, S. Wippermann, S. Sanna, F. Klasing, A. Hanisch-Blicharski, M. Kammler, W. G. Schmidt, and M. Horn-von Hoegen, Phys. Rev. Lett. **109**, 186101 (2012).

[151] M. Gao, C. Lu, H. Jean-Ruel, L. C. Liu, A. Marx, K. Onda, S.-y. Koshihara, Y. Nakano, X. Shao, T. Hiramatsu, G. Saito, H. Yamochi, R. R. Cooney, G. Moriena, G. Sciaini, and R. J. D. Miller, Nature **496**, 343 (2013).

[152] V. R. Morrison, R. P. Chatelain, K. L. Tiwari, A. Hendaoui, A. Bruhács, M. Chaker, and B. J. Siwick, Science **346**, 445 (2014).

[153] F. Carbone, P. Baum, P. Rudolf, and A. H. Zewail, Phys. Rev. Lett. **100**, 035501 (2008).

[154] H. Jean-Ruel, M. Gao, M. A. Kochman, C. Lu, L. C. Liu, R. R. Cooney, C. A. Morrison, and R. D. Miller, J. Phys. Chem. B **117**, 15894 (2013).

[155] S. Tokita, M. Hashida, S. Inoue, T. Nishoji, K. Otani, and S. Sakabe, Phys. Rev. Lett. **105**, 215004 (2010).

[156] T. Van Oudheusden, P. Pasmans, S. Van Der Geer, M. De Loos, M. Van Der Wiel, and O. Luiten, Phys Rev. Lett. **105**, 264801 (2010).

[157] S. Manz, A. Casandruc, D. Zhang, Y. Zhong, R. Loch, A. Marx, T. Hasegawaa, L. C. Liu, S. Bayesteh, H. Delsim-Hashemi, M. Hoffmann, M. Felber, M. Hachmann, F. Mayet, J. Hirscht, S. Keskin, M. Hada, S. Epp, K. Flottmann, and R. J. D. Miller, Faraday Discuss. (Accepted) (2014).

[158] E. Fill, L. Veisz, A. Apolonski, and F. Krausz, New J. Phys. **8**, 272 (2006).

[159] P. Baum and A. H. Zewail, Proc. Natl. Acad. Sci. USA **104**, 18409 (2007).

[160] A. Gliserin, A. Apolonski, F. Krausz, and P. Baum, New J. Phys. **14**, 073055 (2012).

[161] P. Hansen, C. Baumgarten, H. Batelaan, and M. Centurion, Appl. Phys. Lett. **101**, 083501 (2012).

[162] P. Baum and A. H. Zewail, Chem. Phys. **366**, 2 (2009).

[163] J. D. Ewbank, W. L. Faust, J. Y. Luo, J. T. English, D. L. Monts, D. W. Paul, Q. Dou, and L. Schäfer, Rev. Sci. Instrum. **63**, 3352 (1992).

[164] J. Williamson, M. Dantus, S. Kim, and A. Zewail, Chem. Phys. Lett. **196**, 529 (1992).

[165] H. Ihee, V. A. Lobastov, U. M. Gomez, B. M. Goodson, R. Srinivasan, C.-Y. Ruan, and A. H. Zewail, Science **291**, 458 (2001).

[166] R. C. Dudek and P. M. Weber, J. Phys. Chem. A **105**, 4167 (2001).

[167] R. Srinivasan, J. S. Feenstra, S. T. Park, S. Xu, and A. H. Zewail, Science **307**, 558 (2005).

[168] K. Hoshina, K. Yamanouchi, T. Ohshima, Y. Ose, and H. Todokoro, J. Chem. Phys. **118**, 6211 (2003).

[169] P. Reckenthaeler, M. Centurion, W. Fuß, S. A. Trushin, F. Krausz, and E. E. Fill, Phys. Rev. Lett. **102**, 213001 (2009).

[170] C. J. Hensley, J. Yang, and M. Centurion, Phys. Rev. Lett. **109**, 133202 (2012).

[171] J. Charles Williamson and A. H. Zewail, Chem. Phys. Lett. **209**, 10 (1993).

[172] J. Hastings, F. Rudakov, D. Dowell, J. Schmerge, J. Cardoza, J. Castro, S. Gierman, H. Loos, and P. Weber, Appl. Phys. Lett. **89**, 184109 (2006).

[173] P. Musumeci, J. Moody, C. Scoby, M. Gutierrez, H. Bender, and N. Wilcox, Rev. Sci. Instrum. **81**, 013306 (2010).

[174] R. Li, W. Huang, Y. Du, L. Yan, Q. Du, J. Shi, J. Hua, H. Chen, T. Du, H. Xu, and C. Tang, Rev. Sci. Instrum. **81**, 036110 (2010).

[175] Y. Murooka, N. Naruse, S. Sakakihara, M. Ishimaru, J. Yang, and K. Tanimura, Appl. Phys. Lett. **98**, 251903 (2011).

[176] P. Zhu, J. Cao, Y. Zhu, J. Geck, Y. Hidaka, S. Pjerov, T. Ritschel, H. Berger, Y. Shen, R. Tobey, J. P. Hill, and X. J. Wang, Appl. Phys. Lett. **103**, 071914 (2013).

[177] P. Baum and A. H. Zewail, Proc. Natl. Acad. Sci. USA **103**, 16105 (2006).

[178] P. Zhang, J. Yang, and M. Centurion, New J. Phys. **16**, 083008 (2014).

[179] T. Brabec and F. Krausz, Rev. Mod. Phys. **72**, 545 (2000).

[180] F. X. Kärtner, ed., *Few-cycle laser pulse generation and its applications*, Vol. 95 (Springer, 2004).

[181] S. Miura, T. Ando, K. Ootaka, A. Iwasaki, H. Xu, T. Okino, K. Yamanouchi, D. Hoff, T. Rathje, G. G. Paulus, M. Kitzler, A. Baltuška, G. Sansone, and M. Nisoli, Chem. Phys. Lett. **595**, 61 (2014).

[182] K. Hedberg, L. Hedberg, D. S. Bethune, C. Brown, H. Dorn, R. D. Johnson, and M. De Vries, Science **254**, 410 (1991).

[183] D. Schooss, M. N. Blom, J. H. Parks, B. V. Issendorff, H. Haberland, and M. M. Kappes, Nano Lett. **5**, 1972 (2005).

[184] D. A. Wann, P. D. Lane, H. E. Robertson, T. Baše, and D. Hnyk, Dalton Trans. **42**, 12015 (2013).

[185] D. Strickland and G. Mourou, Opt. Commun. **55**, 447 (1985).

[186] A. Stingl, R. Szipöcs, M. Lenzner, C. Spielmann, and F. Krausz, Opt. Lett. **20**, 602 (1995).

[187] D. E. Spence, P. N. Kean, and W. Sibbett, Opt. Lett. **16**, 42 (1991).

[188] G. Cheriaux, B. Walker, L. Dimauro, P. Rousseau, F. Salin, and J. Chambaret, Opt. Lett. **21**, 414 (1996).

[189] Z. Zhang, T. Yagi, and T. Arisawa, Appl. Opt. **36**, 3393 (1997).

[190] J. Jiang, Z. Zhang, and T. Hasama, J. Opt. Soc. Am. B **19**, 678 (2002).

[191] F. Verluise, V. Laude, Z. Cheng, C. Spielmann, and P. Tournois, Opt. Lett. **25**, 575 (2000).

[192] P. Tournois, Opt. Commun. **140**, 245 (1997).

[193] E. Treacy, IEEE J. Quantum Electron. **5**, 454 (1969).

[194] C. Iaconis and I. A. Walmsley, Opt. Lett. **23**, 792 (1998).

[195] R. Trebino, *Frequency-Resolved Optical Gating: The Measurement of Ultrashort Laser Pulses: The Measurement of Ultrashort Laser Pulses*, Vol. 1 (Springer, New York, 2000).

[196] Y. Morimoto, *Observation of Laser-Assisted Electron-Atom and Electron-Molecule Scatterings in Femtosecond Intense Laser Fields*, Master's thesis, Department of Chemistry, School of Science, the University of Tokyo (2012).

[197] G. Scoles, D. Bassi, U. Buck, and U. Valbusa, *Atomic and molecular beam methods*, Vol. 1 (Oxford University Press, New York, 1988).

[198] A. Zecca, G. Karwasz, and R. Brusa, Phys. Rev. A **46**, 3877 (1992).

[199] M. Born and E. Wolf, *Principles of optics: electromagnetic theory of propagation, interference and diffraction of light* (Cambridge University Press, Cambridge, 1999).

[200] B. J. Siwick, A. A. Green, C. T. Hebeisen, and R. Miller, Opt. Lett. **30**, 1057 (2005).

[201] C. T. Hebeisen, R. Ernstorfer, M. Harb, T. Dartigalongue, R. E. Jordan, and R. Dwayne Miller, Opt. Lett. **31**, 3517 (2006).

[202] C. T. Hebeisen, G. Sciaini, M. Harb, R. Ernstorfer, T. Dartigalongue, S. G. Kruglik, and R. Miller, Opt. Exp. **16**, 3334 (2008).

[203] M. Dantus, S. B. Kim, J. C. Williamson, and A. H. Zewail, J. Phys. Chem **98**, 2782 (1994).

[204] H. Park, Z. Hao, X. Wang, S. Nie, R. Clinite, and J. Cao, Rev. Sci. Instrum. **76**, 083905 (2005).

[205] S. Schäfer, W. Liang, and A. H. Zewail, New J. Phys. **13**, 063030 (2011).

[206] O. Jagutzki, A. Cerezo, A. Czasch, R. Dorner, M. Hattas, M. Huang, V. Mergel, U. Spillmann, K. Ullmann-Pfleger, T. Weber, H. Schmidt-Böcking, and G. D. W. Smith, IEEE Trans. Nucl. Sci. **49**, 2477 (2002).

[207] T. Shimanouchi, *Tables of Molecular Vibrational Frequencies Consolidated. Volume I* (National Bureau of Standards: Washington, DC, 1972).

[208] P. Limão-Vieira, M. Horie, H. Kato, M. Hoshino, F. Blanco, G. García, S. J. Buckman, and H. Tanaka, J. Chem. Phys. **135**, 234309 (2011).

[209] M. Nagashima, S. Konaka, and M. Kimura, Bull. Chem. Soc. Jpn. **55**, 28 (1982).

[210] J. Geiger, Z. Phys. **181**, 413 (1964).

[211] R. Bonham and T. Iijima, J. Chem. Phys. **42**, 2612 (1965).

[212] R. A. Bonham and M. Fink, *High energy electron scattering* (Van Nostrand Reinhold, 1974).

[213] R. Buckingham, Proc. Roy. Soc. A **160**, 94 (1937).

[214] T. N. Olney, N. Cann, G. Cooper, and C. Brion, Chem. Phys. **223**, 59 (1997).

[215] M. H. Mittleman and K. M. Watson, Physical Review **113**, 198 (1959).

[216] F. Salvat, Phys. Rev. A **68**, 012708 (2003).

[217] M. Adibzadeh and C. E. Theodosiou, Atomic Data and Nuclear Data Tables **91**, 8 (2005).

[218] H. Daimon, T. Kondow, and K. Kuchitsu, J. Phys. Soc. Jpn. **52**, 84 (1983).

[219] P. G. Burke and C. J. Joachain, *Theory of Electron-Atom Collisions: Part One: Potential Scattering* (Plenum, New York, 1995).

[220] B. H. Bransden and C. J. Joachain, *Physics of atoms and molecules*, 2nd Ed. (Peerson Education, 2003).

[221] G. H. Ho, Chem. Phys. **226**, 101 (1998).

[222] J. Ying and K. Leung, J. Chem. Phys. **100**, 7120 (1994).

[223] J. Küpper, S. Stern, L. Holmegaard, F. Filsinger, A. Rouzée, A. Rudenko, P. Johnsson, A. V. Martin, M. Adolph, A. Aquila, S. c. v. Bajt, A. Barty, C. Bostedt, J. Bozek, C. Caleman, R. Coffee, N. Coppola, T. Delmas, S. Epp, B. Erk, L. Foucar, T. Gorkhover, L. Gumprecht, A. Hartmann, R. Hartmann, G. Hauser, P. Holl, A. Hömke, N. Kimmel, F. Krasniqi, K.-U. Kühnel, J. Maurer, M. Messerschmidt, R. Moshammer, C. Reich, B. Rudek, R. Santra, I. Schlichting, C. Schmidt, S. Schorb, J. Schulz, H. Soltau, J. C. H. Spence, D. Starodub, L. Strüder, J. Thøgersen, M. J. J. Vrakking, G. Weidenspointner, T. A. White, C. Wunderer, G. Meijer, J. Ullrich, H. Stapelfeldt, D. Rolles, and H. N. Chapman, Phys. Rev. Lett. **112**, 083002 (2014).

[224] M. P. Minitti, J. M. Budarz, A. Kirrander, J. Robinson, T. J. Lane, D. Ratner, K. Saita, T. Northey, B. Stankus, V. Cofer-Shabica, J. Hastings, and P. M. Weber, Faraday Discuss. **171**, 81 (2014).

[225] M. Meckel, D. Comtois, D. Zeidler, A. Staudte, D. Pavičić, H. Bandulet, H. Pépin, J. Kieffer, R. Dörner, D. Villeneuve, and P. Corkum, Science **320**, 1478 (2008).

[226] C. I. Blaga, J. Xu, A. D. DiChiara, E. Sistrunk, K. Zhang, P. Agostini, T. A. Miller, L. F. DiMauro, and C. Lin, Nature **483**, 194 (2012).

[227] J. Xu, C. I. Blaga, K. Zhang, Y. H. Lai, C. Lin, T. A. Miller, P. Agostini, and L. F. DiMauro, Nat. Commun. **5** (2014).

[228] R. Boll, D. Anielski, C. Bostedt, J. Bozek, L. Christensen, R. Coffee, S. De, P. Decleva, S. Epp, B. Erk, L. Foucar, F. Krasniqi, J. Küpper, A. Rouzée, B. Rudek, A. Rudenko, S. Schorb, H. Stapelfeldt, M. Stener, S. Stern, S. Techert, S. Trippel, V. M. J. J, J. Ullrich, and D. Rolles, Phys. Rev. A **88**, 061402(R) (2013).

[229] M. Kazama, T. Fujikawa, N. Kishimoto, T. Mizuno, J.-i. Adachi, and A. Yagishita, Phys. Rev. A **87**, 063417 (2013).

[230] V. Typke, M. Dakkouri, and H. Onerhammer, J. Mol. Struct. **44**, 85 (1978).

[231] Y. S. Kim, W. K. Kang, and K.-H. Jung, J. Chem. Phys. **105**, 551 (1996).

[232] A. Tehlar and H. Wörner, Mol. Phys. **111**, 2057 (2013).

[233] G. Öhrwall, P. Karlsson, M. Wirde, M. Lundqvist, P. Andersson, D. Ceolin, B. Wannberg, T. Kachel, H. Dürr, W. Eberhardt, and S. Svensson, J. Electron Spectrosc. Relat. Phenom. **183**, 125 (2011).

[234] C. Jauregui, J. Limpert, and A. Tünnermann, Nat. Photon. **7**, 861 (2013).

[235] C. J. Saraceno, C. Schriber, F. Emaury, O. H. Heckl, C. R. Baer, M. Hoffmann, K. Beil, C. Kränkel, M. Golling, T. Südmeyer, and U. Keller, Appl. Sci. **3**, 355 (2013).

[236] A. A. Eilanlou, Y. Nabekawa, M. Kuwata-Gonokami, and K. Midorikawa, Jpn. J. Appl. Phys. **53**, 082701 (2014).

[237] J. Brons, V. Pervak, E. Fedulova, D. Bauer, D. Sutter, V. Kalashnikov, A. Apolonskiy, O. Pronin, and F. Krausz, Opt. Lett. **39**, 6442 (2014).

[238] D. Irimia, D. Dobrikov, R. Kortekaas, H. Voet, D. A. van den Ende, W. A. Groen, and M. H. Janssen, Rev. Sci. Instrum. **80**, 113303 (2009).

[239] C. Neidel, J. Klei, C.-H. Yang, A. Rouzée, M. J. J. Vrakking, K. Klünder, M. Miranda, C. L. Arnold, T. Fordell, A. L'Huillier, M. Gisselbrecht, P. Johnsson, M. P. Dinh, E. Suraud, P.-G. Reinhard, V. Despré, M. A. L. Marques, and F. Lépine, Phys. Rev. Lett. **111**, 033001 (2013).

[240] M. J. Frisch, G. W. Trucks, H. B. Schlegel, G. E. Scuseria, M. A. Robb, J. R. Cheeseman, G. Scalmani, V. Barone, B. Mennucci, G. A. Petersson, H. Nakatsuji, M. Caricato, X. Li, H. P. Hratchian, A. F. Izmaylov, J. Bloino, G. Zheng, J. L. Sonnenberg, M. Hada, M. Ehara, K. Toyota, R. Fukuda, J. Hasegawa, M. Ishida, T. Nakajima, Y. Honda, O. Kitao, H. Nakai, T. Vreven, J. A. Montgomery, Jr., J. E. Peralta, F. Ogliaro, M. Bearpark, J. J. Heyd, E. Brothers, K. N. Kudin, V. N. Staroverov, R. Kobayashi, J. Normand, K. Raghavachari, A. Rendell, J. C. Burant, S. S. Iyengar, J. Tomasi, M. Cossi, N. Rega, J. M. Millam, M. Klene, J. E. Knox, J. B. Cross, V. Bakken, C. Adamo, J. Jaramillo, R. Gomperts, R. E. Stratmann, O. Yazyev, A. J. Austin, R. Cammi, C. Pomelli, J. W. Ochterski, R. L. Martin, K. Morokuma, V. G. Zakrzewski, G. A. Voth, P. Salvador, J. J. Dannenberg, S. Dapprich, A. D. Daniels, Ö. Farkas, J. B. Foresman, J. V. Ortiz, J. Cioslowski, and D. J. Fox, "Gaussian 09, revision a. 1. wallingford, ct," Gaussian Inc. Wallingford CT 2009.

[241] L. Martins, F. de Souza, G. Ceolin, F. Jorge, R. de Berrêdo, and C. Campos, Comput. Theo. Chem. **1013**, 62 (2013).

[242] S. Shibata, H. Sekiyama, K. Tachikawa, and M. Moribe, J. Mol. Struct. **641**, 1 (2002).

[243] J. I. Gersten and M. H. Mittleman, Phys. Rev. A **13**, 123 (1976).

[244] M. H. Mittleman, Phys. Rev. A **14**, 1338 (1976).

[245] M. H. Mittleman, Phys. Rev. A **16**, 1549 (1977).

[246] M. H. Mittleman, Phys. Rev. A **18**, 685 (1978).

[247] M. H. Mittleman, Phys. Rev. A **21**, 79 (1980).

[248] B. Zon, Sov. Phys. JETP **73**, 128 (1977).

[249] K. Deguchi, H. Taylor, and R. Yaris, J. Phys. B **12**, 613 (1979).

[250] A. Lami and N. Rahman, J. Phys. B **14**, L523 (1981).

[251] A. Lami and N. Rahman, J. Phys. B **16**, L201 (1983).

[252] E. Beilin and B. Zon, J. Phys. B **16**, L159 (1983).

[253] A. Dubois, A. Maquet, and S. Jetzke, Phys. Rev. A **34**, 1888 (1986).

[254] M. Dörr, C. Joachain, R. Potvliege, and S. Vučić, Phys. Rev. A **49**, 4852 (1994).

[255] D. Charlo, M. Terao-Dunseath, K. Dunseath, and J. Launay, J. Phys. B **31**, L539 (1998).

[256] M. Terao-Dunseath and K. Dunseath, J. Phys. B **35**, 125 (2002).

[257] I. Rabadán, L. Méndez, and A. Dickinson, J. Phys. B **27**, L535 (1994).

[258] S. Geltman, Phys. Rev. A **51**, R34 (1995).

[259] S. Varró and F. Ehlotzky, Phys. Lett. A **203**, 203 (1995).

[260] L. Madsen and K. Taulbjerg, J. Phys. B **28**, 5327 (1995).

[261] C. Chen and F. Robicheaux, J. Phys. B **29**, 345 (1996).

[262] S. Geltman, Phys. Rev. A **53**, 3473 (1996).

[263] A. Cionga, L. Dimou, and F. Faisal, J. Phys. B **30**, L361 (1997).

[264] D. B. Milosevic and F. Ehlotzky, J. Phys. B **30**, 2999 (1997).

[265] A. Jaroń and J. Kamiński, Phys. Rev. A **56**, R4393 (1997).

[266] N. Kylstra and C. Joachain, Phys. Rev. A **58**, R26 (1998).

[267] J. Sun, S. Zhang, Y. Jiang, and G. Yu, Phys. Rev. A **58**, 2225 (1998).

[268] M. Bouzidi, A. Makhoute, D. Khalil, A. Maquet, and C. Joachain, J. Phys. B **34**, 737 (2001).

[269] K. Dunseath and M. Terao-Dunseath, J. Phys. B **37**, 1305 (2004).

[270] I. Rabadán, L. Méndez, and A. Dickinson, J. Phys. B **29**, L801 (1996).

[271] J. D. Jackson, *Classical electrodynamics* (Wiley, New York, 1998).

[272] J. K. Nagle, J. Am. Chem. Soc. **112**, 4741 (1990).

[273] M. H. Mittleman and K. M. Watson, Phys. Rev. **113**, 198 (1959).

[274] S. Nakazaki, K. Berrington, W. Eissner, and Y. Itikawa, J. Phys. B **30**, 5805 (1997).

[275] M. Stott and E. Zaremba, Phys. Rev. A **21**, 12 (1980).

[276] K. Ishida, Y. Morimoto, R. Kanya, and K. Yamanouchi, (in preparation) .

[277] N. Mason and W. Newell, J. Phys. B **20**, L323 (1987).

[278] B. Wallbank, J. Holmes, L. Le Blanc, and A. Weingartshofer, Z. Phys. D **10**, 467 (1988).

[279] N. Mason and W. Newell, J. Phys. B **22**, 777 (1989).

[280] B. Wallbank, J. Holmes, and A. Weingartshofer, Phys. Rev. A **40**, 5461 (1989).

[281] B. Wallbank, J. Holmes, and A. Weingartshofer, J. Phys. B **22**, L615 (1989).

[282] N. Mason and W. Newell, J. Phys. B **23**, L179 (1990).

[283] B. Wallbank, J. Holmes, and A. Weingartshofer, J. Phys. B **23**, 2997 (1990).

[284] S. Luan, R. Hippler, and H. Lutz, J. Phys. B **24**, 3241 (1991).

[285] B. Wallbank, J. Holmes, and A. Weingartshofer, Can. J. Phys. **71**, 326 (1993).

[286] C. Höhr, A. Dorn, B. Najjari, D. Fischer, C. Schröter, and J. Ullrich, J. Electron Spectrosc. Relat. Phenom. **161**, 172 (2007).

[287] H. Ehrhardt, K. Jung, G. Knoth, and P. Schlemmer, Z. Phys. D **1**, 3 (1986).

[288] I. E. McCarthy and E. Weigold, Rep. Prog. Phys. **54**, 789 (1991).

[289] M. Mohan and P. Chand, Phys. Lett. A **65**, 399 (1978).

[290] P. Cavaliere, G. Ferrante, and C. Leone, J. Phys. B **13**, 4495 (1980).

[291] J. Banerji and M. Mittleman, J. Phys. B **14**, 3717 (1981).

[292] C. Joachain, P. Francken, A. Maquet, P. Martin, and V. Veniard, Phys. Rev. Lett. **61**, 165 (1988).

[293] P. Martin, V. Veniard, A. Maquet, P. Francken, and C. Joachain, Phys. Rev. A **39**, 6178 (1989).

[294] C. Joachain, A. Makhoute, A. Maquet, and R. Taieb, Z. Phys. D **23**, 397 (1992).

[295] D. Khalil, A. Maquet, R. Taïeb, C. Joachain, and A. Makhoute, Phys. Rev. A **56**, 4918 (1997).

[296] A. Makhoute, D. Khalil, A. Maquet, C. Joachain, and R. Taïeb, J. Phys. B **32**, 3255 (1999).

[297] A. A. Bulychev and K. A. Kouzakov, Eur. Phys. J. D **68**, 1 (2014).

[298] J. Ullrich, R. Moshammer, A. Dorn, R. Dörner, L. P. H. Schmidt, and H. Schmidt-Böcking, Rep. Prog. Phys. **66**, 1463 (2003).

[299] S. Ghosh Deb and C. Sinha, Eur. Phys. J. **60**, 287 (2010).

[300] A. Vollmer, R. Ovsyannikov, M. Gorgoi, S. Krause, M. Oehzelt, A. Lindblad, N. Mårtensson, S. Svensson, P. Karlsson, M. Lundvuist, T. Schmeiler, J. Pflaum, and N. Koch, J. Electron Spectrosc. Relat. Phenom. **185**, 55 (2012).

[301] R. Ovsyannikov, P. Karlsson, M. Lundqvist, C. Lupulescu, W. Eberhardt, A. Foehlisch, S. Svensson, and N. Mårtensson, J. Electron Spectrosc. Relat. Phenom. **191**, 92 (2013).

[302] M. Huth, C.-T. Chiang, A. Trützschler, F. O. Schumann, J. Kirschner, and W. Widdra, Appl. Phys. Lett. **104**, 061602 (2014).

[303] Y. K. Kim, K. K. Irikura, M. E. Rudd, M. A. Ali, P. M. Stone, J. Chang, J. S. R. A. Coursey, Dragoset, A. R. Kishore, K. J. Olsen, A. M. Sansonetti, G. G. Wiersma, D. S. Zucker, and M. A. Zucker, *NIST Electron-Impact Cross Sections for Ionization and Excitation*.

[304] H. Ehrhardt, K. Hesselbacher, K. Jung, and K. Willmann, J. Phys. B **5**, 1559 (1972).

[305] B. Lohmann, I. McCarthy, A. Stelbovics, and E. Weigold, Phys. Rev. A **30**, 758 (1984).

[306] M. Yamazaki, Y. Kasai, K. Oishi, H. Nakazawa, and M. Takahashi, J. Phys.: Conf. Ser. **488**, 012056 (2014).

[307] M. Takahashi, N. Watanabe, Y. Khajuria, Y. Udagawa, and J. Eland, Phys. Rev. Lett. **94**, 213202 (2005).

[308] S. Bellm, J. Lower, E. Weigold, and D. Mueller, Phys. Rev. Lett. **104**, 023202 (2010).

[309] X. Ren, T. Pflüger, S. Xu, J. Colgan, M. Pindzola, A. Senftleben, J. Ullrich, and A. Dorn, Phys. Rev. Lett. **109**, 123202 (2012).

[310] H. Stapelfeldt and T. Seideman, Rev. Mod. Phys. **75**, 543 (2003).

[311] P. Francken, Y. Attaourti, and C. Joachain, Phys. Rev. A **38**, 1785 (1988).

[312] J. Itatani, F. Quéré, G. L. Yudin, M. Y. Ivanov, F. Krausz, and P. B. Corkum, Phys. Rev. Lett. **88**, 173903 (2002).

[313] F. Kirchner, A. Gliserin, F. Krausz, and P. Baum, Nat. Photon. **8**, 52 (2014).

[314] M. Drescher, M. Hentschel, R. Kienberger, G. Tempea, C. Spielmann, G. A. Reider, P. B. Corkum, and F. Krausz, Science **291**, 1923 (2001).

[315] R. Kienberger, E. Goulielmakis, M. Uiberacker, A. Baltuska, V. Yakovlev, F. Bammer, A. Scrinzi, T. Westerwalbesloh, U. Kleineberg, U. Heinzmann, M. Drescher, and F. Krausz, Nature **427**, 817 (2004).

[316] B. Barwick, D. J. Flannigan, and A. H. Zewail, Nature **462**, 902 (2009).

[317] S. T. Park, M. Lin, and A. H. Zewail, New J. Phys. **12**, 123028 (2010).

[318] A. Yurtsever, R. M. van der Veen, and A. H. Zewail, Science **335**, 59 (2012).

[319] A. Makhoute, D. Khalil, M. Zitane, and M. Bouzidi, J. Phys. B **35**, 957 (2002).

Acknowledgments

First, I would like to thank my supervisor, Prof. Kaoru Yamanouchi for giving me an opportunity to work in his group and invaluable guidance throughout the PhD study. I would also like to thank my secondary supervisor, Dr. Katsumi Midorikawa for his support and helpful discussions. I am deeply indebted to Dr. Reika Kanya from whom I learned all my experimental skills.

I would like to thank Mr. Kakuta Ishida for his help in conducting experiments, constructing the apparatus, and building power supplies. I am grateful to Mr. Takao Yamazaki and Mr. Hideaki Tanaka for their assistance in constructing the ultrahigh vacuum chamber, and Mr. Takashi Hiroi for his assistance in conducting performance tests of the apparatus for the (e,2e) experiment. I wish to express my gratitude to other members in Prof. Yamanouchi's group.

I acknowledge the financial support from the Japan Society for the Promotion of Science.

Last but most importantly, I would like to thank my parents.